Local moisture distribution in a mortar paste by ex-situ and in-situ MRI : Application to the understanding of the drying process

Maxime van Landeghem

DISSERTATION ZUR ERLANGUNG DES AKADEMISCHEN GRADES EINES DOKTORS DER NATURWISSENSHAFTEN

THESE DE DOCTORAT

Spécialité : Physique
Ecole doctorale : La Physique de la Particule à la Matière Condensée

Maxime VAN LANDEGHEM

Zur Erlangung des akademischen Grades **eines Doktors des Naturwissenshaften von der Fakultät für Mathematik, Informatik und Naturwissenschaften der Rheinisch-Westfälischen Technischen Hochschule Aachen**

Pour obtenir le grade de **Docteur de l'Université Pierre et Marie Curie**

Title :

Local moisture distribution in a mortar paste by ex-situ and in-situ MRI : Application to the understanding of the drying process

Defense scheduled on November 23rd, 2011

Before a jury composed of :

Prof. Bernhard Blümich	PhD supervisor	RWTH, Aachen
Dr. Peter Blümler	examiner	Universität Mainz
Prof. Christian Bonhomme	Chair	UPMC, Paris
Dr. Jean-Baptiste d'Espinose de Lacaillerie	PhD supervisor	ESPCI, Paris
Dr. Paul-Henri Guering	invited	Saint-Gobain Recherche, Aubervilliers
Dr. Geneviève Guillot	reviewer	Université de Paris Sud, Orsay
Prof. Frank Haarmann	reviewer	RWTH, Aachen
Dr. Jean-Pierre Korb	reviewer	Ecole Polytechnique, Palaiseau
Prof. Marcel Liauw	Chair	RWTH, Aachen
Dr. Joël Mispelter	invited	Institut Curie, Orsay

Titre :
Distribution locale de l'eau dans un mortier par IRM ex-situ et in-situ : application à la compréhension des processus de séchage.

Résumé
L'élaboration de matériaux cimentaires aux propriétés extrêmes en terme de tenue mécanique, de durabilité, voire de perméabilité, nécessite la compréhension précise du développement de leur structure poreuse. L'aspect non destructif de l'Imagerie par Résonance Magnétique (IRM) en fait une méthode de choix pour l'étude de la distribution et des transferts hydriques au sein de ces matériaux. Cependant, le caractère multi-échelle de ce matériau et la présence d'impuretés paramagnétiques requièrent des performances particulières en termes d'intensité de gradient de champ magnétique et de rapidité d'acquisition. C'est dans cet objectif que nous avons développé deux techniques IRM complémentaires. Le STRAFI permet de suivre, au laboratoire, l'effet des conditions de température et d'humidité sur la distribution d'eau à travers le matériau mais également sur l'évolution de sa structure poreuse, élément décisif pour les performances de ce dernier. La NMR-MOUSE™, version bas champ mais portative de l'IRM, permet un suivi du séchage des matériaux cimentaires directement sur-site, ce qui en fait un outil de choix dans un contexte industriel. Enfin, la mise au point d'une méthode d'analyse multi-dimensionnelle dans les milieux poreux nous a permis de mettre en évidence les constantes de temps impliquées dans l'échange de matière entre les différents types de pores présents dans le matériau, ce qui permet d'obtenir des informations sur sa porosité et la connectivité de ses pores.
Mots clés : IRM, champ inhomogène, STRAFI, NMR-MOUSE, échange

Title :
Local moisture distribution in a mortar paste by ex-situ and in-situ MRI : Application to the understanding of the drying process.

Abstract
The development of high performance cementitious materials in terms of mechanical properties, sustainability and permeability requires a good understanding of their porous structure. As a non-destructive tool, Magnetic Resonance Imaging (MRI) is a method of choice for studying water distribution and hydric transfer throughout the material. However, due to a pore-size distribution over a few orders of magnitude and the presence of paramagnetic impurities, MRI applied to these materials requires the use of high magnetic field gradient systems and fast acquisition rates. For this purpose, we developed two techniques. Performed ex-situ, STRAFI allows to follow the effect of temperature and humidity on the water distribution within the material but also its impact on the porous structure and thus on the material performances expected. The NMR-MOUSE™, acting at low field and being portable, allows us to follow the drying of cementitious materials directly on-site. As such, it appears as an interesting tool for industrial use. Finally, the implementation of a method to understand multi-site exchange NMR experiments in porous media allowed us to quantify the exchange rates involved between various pores within the materials, which provides information about the porosity and connectivity of the porous structure.
Keywords : MRI, inhomogeneous field, STRAFI, NMR-MOUSE, exchange

Thèse en cotutelle effectuée conjointement dans les laboratoires :

Institut für Technische und Makromolekulare Chemie
RWTH Aachen
Worringer Weg 1
D-52056 Aachen
Deutschland

et

Science et Ingénierie de la Matière Molle, UMR 7615
ESPCI
10 rue Vauquelin
75 231 Paris cedex 05
France

ACKNOWLEDGEMENTS

First of all, I would like to thanks my supervisors Bernhard Blümich and Jean-Baptiste d'Espinose for guidance and goodwill during my PhD. It was a real pleasure to work within their labs and I learnt a lot there.

Many thanks to Saint-Gobain Recherche for financial support, especially to Guillaume Counil, Myriam Guérin, Hélène Gascon and Paul-Henri Guering for motivating and supporting me.

I would like to thank also the jury for accepting to evaluate this work, their advice and supports to improve this manuscript.

I wish to warmly thank B. Bresson. He was always there to help me and share his knowledges about NMR and porous media. His commitment allows me to bring the experiments forward even when I was not there.

My thanks to J. Mispelter and D. Petit for helping me to design coils.

My thanks to J.-P. Korb for sharing with me his knowledges about the investigation of porous media by NMR.

My thanks to the "Argentinian" team (Federico, Juan and Ernesto) for their help on the instrumentation of NMR.

My thanks to F. Lequeux and C. Frétigny for sharing with me their experience of physics.

I would like to thanks all my colleagues from the PPMD lab especially Céline, Astrid, Aurélie, Julien and Damien and from the ITMC lab especially Agnes for making the life fun even when experiments do not work.

My thanks to Ludovic for learning me how to design and make my own mechanics.

Last but not least, I would like to thank my family and friends for their support, my father, my sister and most of all my wife who has always believed in me.

To my mother...

Résumé long

L'IRM pour l'étude des matériaux de construction

Introduction

Le Viaduc de Millau, les tours de la Défense ou encore le pont de Normandie sont autant d'infrastructures qui ont nécessité l'utilisation de matériaux cimentaires aux propriétés extrêmes en terme de résistance et de durabilité. Bien que très largement utilisés, certaines questions subsistent. La difficulté dans l'étude de ces matériaux poreux vient de la largeur sur laquelle s'étend la distribution de taille de pore. Ainsi le ciment est un matériau multi-échelle dont les propriétés dépendent aussi bien de la structure des pores nanométriques que de la présence de fissures à l'échelle millimétrique. Devant ce matériau, qui de plus est opaque, peu de méthodes permettent de l'étudier et ce de manière non-destructive. L'une d'entre elle est l'imagerie par résonance magnétique (IRM) du proton.

Principe de l'IRM

Le principe de l'IRM du proton est le suivant. En présence d'un champ magnétique, la levée de dégénérescence des niveaux d'énergie du spin du proton conduit à l'apparition d'une aimantation macroscopique. En appliquant un champ radiofréquence à l'aide d'une antenne, il est possible de modifier cette aimantation. L'expérience consiste alors à mesurer le retour de cette aimantation à son état d'équilibre. Ce retour est caractérisé par deux types de paramètres : sa fréquence de précession et ses temps de relaxation transversale et longitudinale. La mesure de la fréquence de précession est couramment utilisée pour caractériser l'environnement chimique du spin considéré. L'écart de la fréquence mesurée par rapport à la fréquence de référence est appelé déplacement chimique. Quant à eux, les temps de relaxation dépendent de l'environnement physico-chimique du spin considéré. Le temps de relaxation longitudinal (T_1) correspond au temps de retour à l'équilibre thermodynamique des niveaux d'énergie. Le temps de relaxation transversale (T_2) correspond à une perte de cohérence des spins induit par un échange d'énergie. Ainsi, la présence par exemple d'un centre paramagnétique à proximité du proton conduit à un T_2 court. En plus de ces effets, l'expérience d'IRM permet, en outre, une localisation spatiale grâce à l'ajout de gradients de champ magnétique se superposant au champ principal.

IRM en champ de fuite

Un système d'IRM conventionnel ne peut être utilisé directement pour l'étude des matériaux cimentaires. La raison à cela vient du caractère extrêmement court de leur temps de relaxation, s'étendant de la dizaine de microsecondes à la milliseconde. Il en résulte, dans l'espace de Fourier, un élargissement des raies tel que le gradient de champ magnétique permettant d'obtenir l'encodage est souvent insuffisant pour obtenir une bonne résolution. D'autre part, les bobines de gradients utilisées dans les machines IRM étant pulsés, le temps d'établissement du gradient de champ est trop long comparé à la durée du signal du ciment (T_2). Face à ces problèmes, on se propose d'utiliser un gradient statique très intense. Celui-ci peut-être obtenu en exploitant le gradient naturel qui entoure les aimants permanents. On se propose d'utiliser ce principe sous deux déclinaisons, une version haut champ appelée STRAFI (STRay Field Imaging) et une version bas champ appelée MOUSE (Mobile Universal Surface Explorer). L'objectif de la thèse est d'instrumenter ces deux outils complémentaires afin d'étudier la structuration et le séchage des matériaux cimentaires.

Conception et fabrication d'antennes IRM adaptée à l'étude des matériaux cimentaires

Introduction

La présence d'impuretés paramagnétiques (principalement du fer) dans les ciments en fait un matériau difficile à étudier par IRM du fait de ses temps de relaxation qui sont particulièrement courts. Outre une technique d'imagerie rapide impliquant un gradient de champ intense, il est nécessaire que l'antenne (ou sonde) utilisée soit elle-même rapide. En d'autres termes, il faut qu'elle soit à la fois efficace et qu'elle ait des temps morts courts. D'autre part, utilisée pour exciter des tranches fines (quelques centaines de micromètres typiquement), elle doit générer un champ radio-fréquence homogène à travers la tranche sélectionnée. Enfin, elle doit être compatible avec une symétrie de révolution de façon à pouvoir être utilisée dans l'expérience de STRAFI. Pour satisfaire tous ces points nous avons été amenés à réaliser nous-même notre sonde.

Adaptation d'impédance faible bruit

L'objectif premier d'une sonde RMN quelle qu'elle soit est de générer un champ magnétique radio-fréquence. Cette fonction est réalisée par un composant appelé "résonateur" de type principalement inductif. Pour être efficace, le résonateur dont l'impédance est principalement imaginaire doit être adaptée à l'impédance caractéristique du spectromètre RMN qui est purement résistif, conventionnellement égale à 50 Ω. Cela est rendu possible grâce à l'insertion du résonateur dans un circuit de type RLC résonant. A sa fréquence de résonance, ce circuit a la propriété d'avoir une partie imaginaire nulle et une partie réelle de l'ordre de la dizaine de kΩ. Bien que purement réelle, la partie réelle d'un tel circuit ne satisfait pas aux conditions d'adaptation d'impédance. Comme l'ajout de résistances est proscrit pour des raisons de bruit, il est nécessaire d'ajouter à ce circuit une capacité supplémentaire. Celle-ci permet de placer à la fréquence où la partie réelle est égale à 50 Ω un zéro sur la partie imaginaire. Cette procédure, bien que simple en théorie, est délicate à mettre en oeuvre car elle nécessite la connaissance des caractéristiques électriques de tous les composants, souvent biaisées par des effets parasites dus à la présence de l'échantillon. Ainsi, on utilise des condensateurs dont la capacité est variable de façon à réaliser l'adaptation d'impédance et ce quel que soit l'échantillon.

Conception de résonateurs

Pour être utilisable dans une expérience de STRAFI, le résonateur doit être compatible avec une géométrie cylindrique et permettre d'exciter efficacement une fine tranche (typiquement quelques centaines de microns) de l'échantillon. Dans cette optique, on a comparé différents types de géométrie de résonateur et proposé d'utiliser une bobine de type "Bolinger". Cette géométrie est basée sur une distribution de fils verticaux placés sur un cercle, ces fils étant parcourus par un courant direct ou inverse. A courant égal, plus le nombre de fils est grand plus le champ magnétique est important et plus l'inductance du résonateur est importante. A priori, il semble donc intéressant d'utiliser un grand nombre de fils. Cependant, ce serait oublier que l'amplificateur d'un spectromètre RMN est, en général, une source de puissance, produit de la tension par l'intensité. Ainsi, afin d'obtenir un champ magnétique créé le plus intense possible, il est nécessaire, à puissance donnée, de minimiser la tension délivrée et de maximiser l'intensité. Cela nécessite la conception d'un résonateur dont l'inductance soit minimale de façon obtenir un courant maximal et éviter tout risque de claquage. L'optimum entre le nombre du fils du résonateur, la valeur du champ magnétique généré par celui-ci, et la tension aux bornes des condensateur minimale conduit à la conception d'un résonateur fait de 8 fils. En pratique, les fils sont remplacés par des bandes cuivrées ("strips") permettant de diminuer l'inductance tout

en améliorant l'homogénéité du champ magnétique créé. En effet, à la fréquence de travail (137 MHz), du fait de l'effet de peau, le champ radio-fréquence se propage uniquement sur la première dizaine de microns du conducteur. Ainsi, à section de cuivre égale, il est plus favorable en terme d'inductance d'avoir de larges bandes de cuivre que des fils plus fins.

Mise en place d'une expérience de STRAFI

Principe de l'expérience

Munis d'une sonde adaptée à l'étude par STRAFI, nous avons implémenté cette technique sur notre aimant supraconducteur 7 T situé à l'ESPCI. La beauté de cette technique réside dans le fait que contrairement à l'IRM conventionnelle qui exploite l'utilisation de bobines de gradients pulsés pour réaliser des images, ici le gradient de champ magnétique utilisé pour l'encodage de l'espace est celui existant naturellement dans le champ de fuite des aimants supraconducteurs. Le principe est le suivant. L'échantillon est placé dans la zone de gradient intense à l'aide d'un moteur pas à pas. Une impulsion radio-fréquence permet d'exciter une tranche de l'échantillon. La géométrie de la tranche sélectionnée est déterminée par la fréquence de l'impulsion et sa durée. Le signal RMN de cette même tranche est alors collecté. Enfin, le moteur pas à pas permet de déplacer l'échantillon de façon à exciter une autre tranche. Un profil unidimensionnel construit point à point est alors obtenu. Dans toute l'expérience, la sonde est fixe par rapport à l'aimant supraconducteur, seul l'échantillon bouge. L'automatisation de cette expérience de RMN non conventionnelle nécessite l'interfaçage et la synchronisation du spectromètre RMN et du moteur pas à pas. Par ailleurs, de façon à pouvoir suivre la construction du profil en temps réel, nous avons mis en place un système de traitement des données également synchronisé avec l'acquisition RMN.

Détermination de la position optimale

Outre l'interfaçage des différents éléments constitutifs de l'expérience de STRAFI, la difficulté de la mise en place de cette expérience concerne la détermination de la zone où le gradient est intense selon une direction (z) et homogène dans le plan perpendiculaire (xy). Ce plan permettant d'obtenir une résolution optimale est appelé plan STRAFI. En l'absence de données précises concernant la géométrie de l'aimant supraconducteur, nous avons proposé une procédure permettant de trouver la zone optimale. Celle-ci consiste à déterminer la position pour laquelle le développement de Taylor du champ au voisinage de l'axe s'annule pour les premiers ordres. A partir de la mesure du champ magnétique sur l'axe de l'aimant, il est alors possible de déterminer analytiquement la position du plan STRAFI. La position de ce plan est ensuite vérifiée expérimentalement en déplaçant un spot de crème dans le plan xy à différentes cotes z et en mesurant sa fréquence de résonance, directement proportionnelle au champ. La position optimale est atteinte, lorsque la variation du champ avec la position du spot est linéaire. Reste à corriger le défaut d'alignement entre le plan de l'échantillon et le plan STRAFI. Cette correction est effectuée en mesurant la variation en fréquence induite par la révolution d'un spot de crème décalé par rapport à l'axe. Un système de goniomètres permet dès lors d'ajuster le plan de l'échantillon de telle sorte qu'il soit parallèle au plan STRAFI et permettre ainsi la meilleure résolution possible. Cette procédure nous a permis d'obtenir une résolution de 5 μm sur des échantillons de 10 millimètres de large. La limitation rencontrée par cette méthode concerne la stabilité du montage vis à vis de la température. En effet, lors de la variation d'un degré de la température de la pièce, une tige métallique d'une vingtaine de centimètres correspondant à la hauteur des positionneurs utilisés, s'allonge ou se rétrécit d'une distance typique de plusieurs microns. En pratique, pour l'étude des matériaux cimentaires, cette résolution est largement suffisante. En effet, le caractère très court de leur temps de relaxation (typiquement de quelques dizaines de microsecondes à quelques millisecondes) conduit à une limitation intrinsèque de la

résolution. Par exemple, une résolution de 5 μm obtenue dans un gradient de 50 T/m nécessite un T_2 d'au moins une centaine de microsecondes.

IRM bas champ unilatérale

Présentation de la MOUSE

Bien qu'extrêmement intéressante pour l'étude des matériaux cimentaires, l'expérience de STRAFI présente néanmoins un inconvénient. La mesure est nécessairement effectuée ex-situ. Cela signifie que la dimensionnement de l'échantillon doit être compatible avec la taille de la sonde utilisée, ce qui limite son usage aux échantillons de 20 millimètres de diamètre et quelques centimètres de haut. Pour pallier cette limitation un capteur unilatéral (MOUSE) a été développé. Bien que moins performant en terme de rapidité et de sensibilité, ce capteur bas champ présente le double avantage d'être mobile et unilatéral. Sa conception à l'aide d'aimants permanents et sa taille réduite ($40 \times 40 \times 40$ cm^3 typiquement) en font un capteur portable pouvant être directement utilisé sur site. D'autre part, son caractère unilatéral permet, de manière non destructive, de scanner un mur jusqu'à 20 millimètres de profondeur. Son principe est très proche de celui décrit précédemment en faisant une version bas champ de l'expérience de STRAFI. Il est constitué d'un agencement de 4 aimants permettant de générer dans une zone de l'espace située à 25 millimètres au-dessus de la surface des aimants un gradient uniforme dans la direction verticale z et homogène dans le plan perpendiculaire (xy). L'excitation de l'échantillon est assurée par une bobine dite de "surface" placée à la surface des aimants et permettant de conserver le caractère unilatéral du capteur. Enfin, de façon analogue à l'expérience de STRAFI, la MOUSE est placée sur un moteur pas à pas permettant de réaliser un profil point par point. Comparé au STRAFI, Le gradient de champ magnétique de la MOUSE est 7 fois moins intense et le champ 10 fois plus faible. Elle est accompagnée d'un spectromètre de taille réduite (typiquement la taille d'une unité centrale de bureau) commandé par un ordinateur portable.

Fourier MOUSE

Un inconvénient de ce système qui se veut simple et robuste réside en son système de positionnement qui doit être synchronisé avec l'acquisition du signal RMN. Pour pallier cette difficulté et en vue de l'étude de couches minces (quelques millimètres) nous avons développé un nouveau capteur. Le principe de ce capteur toujours unilatéral repose sur l'exploitation d'un gradient réduit permettant d'exciter des tranches épaisses de plusieurs millimètres tout en assurant une résolution suffisante (25 μm typiquement). L'aimant a une géométrie de type aimant en U à laquelle ont été ajoutés des petits aimants subsidiaires de façon à corriger naturellement les inhomogénéités de ce type d'aimant. Ce procédé rappelle la façon dont étaient rendus homogènes les premiers aimants utilisés pour la RMN. Ces petits aimants appelés aimants de shim ont deux actions sur le champ généré par l'aimant en U initial. Ils permettent de réduire le gradient selon l'axe vertical (d'un facteur 10 typiquement), tout en contrôlant les variations latérales du champ magnétique de façon à maintenir une résolution suffisante. La position des aimants de shim déterminée numériquement nécessite un ajustement de façon à prendre en compte les défauts d'usinage des aimants et leurs inhomogénéités de polarisation. Pour cela, ils sont placés sur des positionneurs permettant de les déplacer dans les 3 directions de l'espace indépendamment les uns des autres. L'optimisation du champ magnétique est réalisée en trois étapes. Tout d'abord, celui-ci est scanné en enregistrant la fréquence de résonance d'un spot de crème déplacé au-dessus du capteur. Les mouvements des aimants de shim nécessaires pour corriger les imperfections du champ sont alors déterminés numériquement. Les aimants de shim sont alors déplacés et le processus recommence. La difficulté réside dans le fait que le mouvement d'un aimant de shim dans une direction donnée, modifie en général le champ magnétique dans les 3 directions de l'espace. Ainsi, ce processus itératif nécessite le mouvement d'un aimant de shim

donné plusieurs fois de suite pour parvenir à la configuration optimale. En utilisant ce procédé itératif, nous sommes parvenus à obtenir une résolution de 25 μm sur des tranches excitées de 2 millimètres. Le profil de l'échantillon est alors obtenu de la manière suivante. Une impulsion radio-fréquence comportant une bande passante suffisante pour exciter une tranche de 2 mm à la surface de l'échantillon est émise. Le profil est obtenu en réalisant simplement la transformée de Fourier du signal RMN enregistré. On obtient alors un profil continu de l'échantillon, et ceci sans avoir besoin de le déplacer. Avec cet aimant, on peut donc réaliser des expériences de RMN multi-dimensionnelles classiques (T_1-T_2, T_2-T_2 ou encore D-T_2) tout en profitant d'une dimension supplémentaire qui est la localisation spatiale.

Application de l'IRM en champ de fuite à l'étude des matériaux cimentaires

Dans cette partie, on propose de détailler une expérience réalisée avec chacun des appareils utilisés de façon à mettre en évidence leur intérêt pour l'étude des matériaux cimentaires.

Types de protons présents dans la pâte cimentaire

La première partie de notre thèse a consisté à mettre au point des instruments dérivés de l'IRM de façon à les adapter à l'étude des matériaux cimentaires. Comme on l'a vu, un paramètre clé de ces matériaux est leur temps de relaxation transverse T_2. En réalité, il s'agit plutôt d'une famille de paramètres car ces matériaux ne présente pas un unique temps de relaxation mais une distribution rendant compte des différents états sous lesquels on peut trouver l'eau. Grossièrement, on peut trouver trois types de protons. Les protons solides sont les protons issus de la réaction chimique d'hydratation de la poudre de ciment avec l'eau. Ces protons, présents sous forme d'hydrates (C−S−H ou CH), ne sont pas évaporables et ont un temps de relaxation transverse très court (de l'ordre de la dizaine de microseconde). Les méthodes que nous avons développé (STRAFI et MOUSE) ne sont pas sensibles à ces protons qui relaxent trop vite. La deuxième famille de protons est situé dans les nanopores des gels de C−S−H. Ces protons qui sont en interaction forte avec la surface des gels ont un T_2 de l'ordre de la centaine de microseconde. Le STRAFI permet l'étude de ces protons. Cependant, ce temps de relaxation reste trop court pour être vu par la MOUSE. Enfin, la troisième catégorie de proton concerne l'eau libre des pores. Ce type d'eau est particulièrement sensible aux effets de séchage ainsi qu'aux conditions de température et d'humidité extérieures au matériau. Leur T_2 varie selon la taille des pores de plusieurs dixièmes à plusieurs dizaines de millisecondes. Ces protons peuvent donc être vus soit par le STRAFI, soit par la MOUSE.

Suivi de l'hydratation par STRAFI

Le STRAFI permet une étude localisée du développement de la structure poreuse du ciment en fonction du temps d'hydratation. La procédure employée est la suivante. A chaque point du profil, une mesure du T_2 est effectuée. La décroissance enregistrée est extrapolée par une décroissance de type double exponentielle décroissante, les facteurs pré-exponentiels évalués correspondant alors aux populations d'eau libre et d'eau dans les nanopores respectivement. L'étude d'un échantillon ouvert sur le dessus permet de mettre en évidence un effet de séchage qui se caractérise par l'obtention de profils inclinés dus à une évaporation d'eau plus facile au voisinage de la surface ciment/air que plus profond dans l'échantillon. L'étude de l'évolution de ce profil au cours du temps d'hydratation permet d'estimer à 4h, le temps à partir duquel une structure poreuse apparaît limitant ainsi la réhomogénéisation de la concentration d'eau libre sur toute la hauteur de l'échantillon. Une étude plus fine du type d'eau impliqué dans le processus de séchage montre qu'il s'agit d'une perte d'eau libre. Proche de la surface, on assiste donc à

une désaturation des pores, tandis que l'eau dans les nanopores semble très peu affecté par l'effet de séchage dans les conditions de température (20^{o}C) et d'humidité (30% rH) utilisées. Dans ce cas, il est donc raisonnable de penser que le développement de la structure poreuse du matériau est peu affecté par le séchage. D'autre part, on a constaté qu'outre cet effet, la cinétique de développement de la structure poreuse est peu affecté le séchage. En effet, l'apparition de la population correspondant à l'eau des nanopores suit la même dynamique que ce soit en surface de l'échantillon de ciment que plus en profondeur. Ainsi, l'utilisation du STRAFI nous permet, de manière indépendante et spécifique, résolue dans l'espace et dans le temps, de suivre l'évolution de l'eau libre et de l'eau des nanopores dans une pâte de ciment en cours d'hydratation.

Influence de la température vue par la MOUSE

On l'a vu, l'immense avantage de la MOUSE est son aspect portatif qui en fait un instrument de choix pour des études sur site. Par exemple, il est particulièrement aisé de la placer directement dans une chambre climatique de type commerciale afin d'étudier l'effet de la température et de l'humidité sur la prise du ciment. Le ciment peut être alors préparé dans un bécher quelconque et placé directement sur la MOUSE pour y être scanné. Il faut rappeler que la MOUSE n'est sensible qu'aux temps de relaxation longs. En d'autre termes, la MOUSE apparaît comme un filtre naturel permettant de suivre exclusivement la distribution d'eau libre dans l'échantillon. Conséquence de l'étude réalisée par le STRAFI, elle apparaît donc particulièrement adaptée à l'étude des effets de séchage.
On a donc utilisé la MOUSE pour étudier à humidité relative fixée (60 %), l'effet de la température dans la gamme 5^{o}C - 60^{o}C. Comme avec le STRAFI, on effectue une mesure de type T_2 mais cette fois, on réalise une extrapolation avec une seule exponentielle comme la MOUSE n'est sensible qu'à une seule des populations d'eau. En dessous de 20^{o}C, on constate que les profils sont plats quelque soit le temps d'hydratation. Cela montre que pour cette gamme de température, l'on a une redistribution homogène de l'eau libre par les forces capillaires sur tout l'échantillon. On est dans un régime dit funiculaire, c'est à dire que l'on a un film continu d'eau tout au long de l'échantillon. Cependant, au-delà de 25^{o}C, on constate que le profil commence à s'incliner aux longs temps d'hydratation. Cela traduit le fait qu'aux temps longs la microporosité est telle que les forces capillaires ne sont plus suffisantes pour redistribuer l'eau de manière homogène le long de l'échantillon et contre-balancer ainsi le séchage. La cinétique de redistribution de l'eau étant trop lente on passe alors à un régime de type pendulaire où le film d'eau n'est plus continu le long de l'échantillon mais peut être parfois rompu.

Echange RMN multi-site

Principe de l'expérience d'échange

Jusqu'à présent, nous avons supposé que les populations d'eau étaient indépendantes les unes des autres. Cependant, à un site est associé une amplitude et un temps de relaxation. En pratique, les molécules ne sont pas statiques et des molécules peuvent s'échanger d'un site à l'autre. Pour visualiser l'échange de matière d'un site à l'autre, il est possible de réaliser une expérience RMN dite d'échange. Cette expérience se déroule en trois étapes. Tout d'abord, une période dite de préparation permet d'encoder la position des protons. En d'autre termes, les protons sont étiquetés en fonction de leur appartenance à un site. Cette période est ensuite suivie d'une période dite de mélange. Pendant ce temps, on laisse le système évoluer librement. Les protons ont donc la possibilité de passer d'un site à l'autre. Enfin, une période de lecture permet de déterminer la position des protons à l'issu du temps de mélange. Le résultat de cette expérience est une carte 2D dont on réalise l'inversion numérique de Laplace. Cette inversion est un point délicat dans l'expérience qui explique que cette méthode date seulement d'une dizaine d'années. En effet, la difficulté vient du fait que contrairement à la transformée de Fourier pour

laquelle le produit scalaire fonctionne bien, la famille des exponentielles complexes formant une base, ce n'est pas le cas de la famille des exponentielles décroissantes. L'inversion numérique de Laplace est en réalité une méthode de minimisation dont la limite vient du nombre important de paramètres notamment dans le cas à deux dimensions. Pour pallier cette difficulté et pouvoir réaliser l'inversion sur un ordinateur de bureau, une méthode basée sur une décomposition préalable des données 2D en valeurs singulières a été proposée. La carte de corrélation 2D obtenue après inversion présente, en général, des pics sur la diagonale principale et parfois des pics hors diagonaux. La présence des pics hors diagonaux est la signature d'un échange de matière entre les sites.

Effet de l'échange sur la mesure des T_2

Cette expérience d'échange est basée sur une hypothèse importante : l'échange de matière n'a lieu que durant la période de mélange. Ainsi, on suppose que la valeur des temps de relaxation mesurée n'est pas biaisée par l'échange. En réalité, la valeur des T_2 mesurée est nécessairement biaisée par l'échange. En effet, la perte de matière d'un site du fait de l'échange entraine une décroissance supplémentaire du signal réduisant ainsi le temps de relaxation apparent. Pire, lorsque l'échange est trop rapide par rapport à la mesure, le temps de relaxation observé est un temps de relaxation moyen. Ainsi, un temps de relaxation peut parfois cacher la présence de deux ou plusieurs sites en échange rapide. Cet effet peut être facilement montré par des simulations numériques. Plus important, l'intensité des pics est elle-même affectée par l'échange. Ainsi, lorsqu'une expérience de mesure de temps de relaxation est réalisée, les populations obtenues peuvent être biaisées par un effet d'échange.

Expérience d'échange T_2-T_2

Pour prendre en compte l'effet d'échange, il est nécessaire d'utiliser des séquences RMN 2D telles que celle décrite précédemment. La présence d'un pic d'échange fournit une information importante sur le système étudié mais reste souvent qualitative. Nous avons donc proposé une méthode pour déterminer les constantes d'échanges mises en jeu et prendre en compte leur effet sur les populations et les temps de relaxation mesurés. Cette méthode repose sur l'extrapolation de données expérimentales par simulation numérique. Le modèle utilisé prenant en compte les valeurs de T_2 et les populations non affectées par l'échange, notre méthode permet, en plus de l'obtention des paramètres cinétiques de l'échange, l'obtention des populations et des temps de relaxation et ce de manière non biaisée.

Notre méthode nous a permis en particulier de montrer que l'absence de pic d'échange ne signifie pas nécessairement une absence d'échange, mais simplement que les paramètres expérimentaux choisis (notamment la valeur du temps de mélange) ne permettent pas de le voir. En outre, une étude numérique nous a permis de proposer une origine à l'obtention de cartes de corrélation non symétriques souvent rencontrées expérimentalement. Cette dissymétrie peut provenir d'une asymétrie de l'échange entre deux sites consécutifs. Si un échange plus rapide dans un sens que dans l'autre peut conduire à des cartes de corrélations non symétriques. Cependant, il est à noter que cela n'est possible qu'en présence de plus de deux sites. En effet, la conservation totale de matière impose que dans le cas à deux sites A et B, la constante d'échange soit la même entre A et B qu'entre B et A. En théorie, lorsque des pics d'échange sont présents, la figure géométrique obtenue en considérant les deux pics diagonaux et les deux pics d'échange est un carré. Cependant, expérimentalement, on trouve que ce carré est souvent déformé. Une analyse numérique prenant en compte le bruit expérimental nous a permis de proposer une explication pour cette déformation.

Enfin, pour valider notre méthode, nous avons étudié un système modèle constitué d'un empilement de billes de silice de 500 nanomètres de diamètre. La méthode de synthèse utilisée (réaction de Stöber) nous a assuré une mono-dispersité nécessaire à notre système modèle dis-

cret à deux sites (les protons libres dans les pores et les protons en interaction avec la silice). L'extrapolation des données expérimentales effectuée à différents temps de mélange nous a permis de déterminer les proportions de chacune des populations d'eau et la constante de temps de l'échange, paramètre physique pertinent. La réelle limitation de notre méthode réside en le fait que le nombre de paramètres à évaluer varie de manière quadratique avec le nombre de sites. En outre, elle suppose une distribution discrète du nombre de sites ce qui est, en pratique, rarement le cas.

Contents

INTRODUCTION

Cements, concretes and mortars are used in huge quantities across the world. The use of cement with a composition comparable to the one we know dates from the Romans[1]. They mixed lime (calcium hydroxide) and pozzolana (source of silica), a volcanic ashes of Mount Vesuvius with water. This mixture of calcium, silica and water is still the basis of modern industrial cement. It leads to the formation of a calcium silicate hydrate gel (called C−S−H) which is the main binder of cement pastes. The Romans relied on the geology of their environment to make cement. Artificial production was not possible as this requires high temperature processes that were not achievable on a large scale before the industrial period. Knowledge of hydraulic cement was then lost during the Middle Ages, to be rediscovered during the 18th century by the British engineer John Smeaton seeking a durable material with which to rebuild the Eddystone Lighthouse on the coast of Cornwall after frequent failures due to the harshness of the location. For some years, cement was produced by burning a naturally occurring mixture of lime and clay. This discovery was fundamental in enabling the start of production on an industrial scale. Because the raw materials were used in their natural mix, their chemical composition varied widely and therefore so did the performance of the final material. In 1824, Joseph Aspdin patented a cement that he called Portland due to the similarity in colour with the stone quarried on the Isle of Portland. The Aspdin method of producing cement was based on a careful proportioning of limestone and clay, their pulverisation and mixing, cooking in a kiln to obtain a clinker and grinding again. This basic process is, with some optimisation, still the one used today.

Figure 1: Picture of the ”Viaduc de Millau”.

Although cements, concretes and mortars, are incredibly widely used, new cement types and additives are still being developed to meet the requirements of new challenging projects.

[1]Source : http://www.understanding-cement.com/history.html

One example is the "Viaduc de Millau" which is incredibly thin despite its length and height thanks to the use of high performance concretes (see Figure 1). Another example is the use of a new generation of mortars such as the ones proposed by Saint-Gobain Weber and Saint-Gobain Maxit which combine various properties (insulation, waterproofing, low thermal conductivity, ...) in the same product. These porous materials are characterized by a pore size distribution encompassing a range which extends over more than three orders of magnitude (nanometer to micrometer scale). This very wide range makes the study of these materials difficult.

Among the available methods, only a few are non destructive. One of these techniques is proton Magnetic Resonance Imaging (MRI). The purpose of this method is to follow the concentration and the states of water. It is particularly interesting in the case of building materials as water plays a major role in their performances. However, this promising method has a major drawback when applied to industrial materials. Fast relaxing species such as protons close to paramagnetic centers can hardly be seen. For example, in cements, the concentration of paramagnetic impurities can reach a few percents, which has a drastic effect on the relaxation times. Thus, it is necessary to push the limits of classical MRI to make it suitable for the study of cements. To achieve this, we propose to use a particular MRI method called STRAy Field Imaging (STRAFI). This technique is suitable for the study of fast relaxing systems and can provide micrometer resolution. However, STRAFI is only suitable for ex-situ measurements. Thus, in combination with this method, we also propose to use the MObile Universal Surface Explorer (MOUSE) which is less sensitive to fast relaxing species but has the major advantage of being mobile, which means that it can be brought on-site and perform in-situ measurements.

As we have seen, in the study of building materials, the key is the ability of measuring very short relaxation times (from a few milliseconds to a few microseconds typically). More than a fast method, a sensitive MRI probehead with very short dead times is required. That is why, we are going to present, at first, how MRI coils can be designed and optimized for the study of mortars by STRAFI and the MOUSE. Indeed, these two methods are non conventional and require customized probeheads. Then, we will present what is STRAFI and how such an experiment can be implemented. In particular, we will show how to reach the limits of this technique in terms of resolution and speed of measurement. Afterwards, we will present the MOUSE and an evolution of the classical MOUSE called the Fourier MOUSE. This new type of MOUSE dedicated to the measurement of the first millimeters of a surface has the advantage of avoiding any electrical positioning system, which makes it even more mobile. Once these tools are defined, we will apply them to the study of building materials. The idea is to monitor the hydration and the drying through the water concentrations and the distribution of relaxation rates which are an image of the various sites of water. Finally, we will present a method to analyse the dynamic of water in porous media. This method consist in correlating the relaxation time distribution at two various instants and observe how protons go from one site to the other. We show that by a numerical study, it is possible not only to evidence an exchange between sites but also to extract an exchange rate which is the meaningful parameter as it depends on the geometry of the porous structure.

INSTRUMENTATION

Chapter 1

NMR probe design

Nuclear Magnetic Resonance in grossly inhomogeneous field such as in STRAFI or when using the NMR-MOUSE™ leads to the excitation and detection of spins localized in a very small region. In addition to this, protons involved in the chemistry of building materials have short relaxation times. Therefore, sensitive coils exhibiting short dead times are required. Coil designs must also match the geometry of the experiment. For example, in STRAFI experiment, the geometry is cylindrical, whereas the NMR-MOUSE™, as it is single-sided, requires the use of a surface coil. Due to these constraints, classical NMR probes appeared not suitable and it seems necessary to develop our own probes. After presenting the basics of NMR probehead electronics, we propose various designs adapted to our problem.

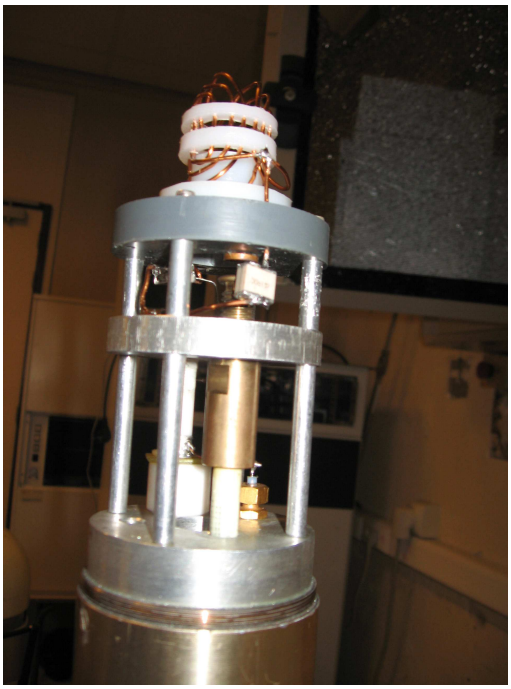

Figure 1.1: Picture of one of our home-made customized probehead

1.1 Electrokinetics of NMR probes

1.1.1 Introduction

Usually, the NMR probe is both used as an emitter to tilt the spin magnetization and as a receiver to detect the magnetic flux induced by the precession of the nuclear magnetization coming back to its equilibrium state. The probe is then connected to a duplexer which directs the signal either from the power amplifier(Tx) to the probe or from the probe to the preamplifier (Rx). Even if some alternative methods exist like the use of Josephson junctions [MTM+02], for the last fifty years the generation and detection of the magnetic flux has mainly been performed using an inductive coil. However, this simple way has a major drawback. Its impedance is mainly inductive, which does not match the impedance of conventional spectrometers which usually exhibit a pure resistive 50 ohms impedance. This chapter focuses on the way of converting the impedance of the probe coil into a purely resistive 50 Ω one.

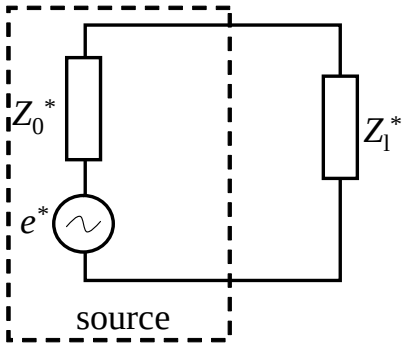

Figure 1.2: Equivalent circuit for a Thévenin generator and a load

1.1.2 Impedance adaptation

From an electrical point of view, the spectrometer and the probe can be modelled as a complex Thévenin generator defined by its parameters e and Z_0 and a complex load Z_l (see Figure 1.2). One should notice that the probe behaves as a load during the transmitting pulses while it behaves as a source when receiving and transmitting back to the spectrometer the signal generated by the precession of the spins. Ideally, one wants to maximize the transmission of the power to the probe when the radiofrequency pulse is emitted and avoid any reflection of the NMR signal transmitted from the probe to the receiver. The object of the following calculation is to determine the impedance of the load which is required to optimize the energy transfer. We consider a source whose internal impedance Z_0 is known. The dissipated power P_l in the load can be written as

$$P_l = \frac{1}{2}\Re(U_l\overline{I_l}) \tag{1.1}$$

where U and I are the complex voltage and current.

$$I = \frac{e}{Z_0 + Z_l} \tag{1.2}$$

$$U = \frac{eZ_l}{Z_0 + Z_l} \tag{1.3}$$

Then, the power becomes:

$$P_l = \frac{1}{2}\,\Re\Big[\frac{eZ_l}{Z_0+Z_l}\overline{\Big(\frac{e}{Z_0+Z_l}\Big)}\Big] \tag{1.4}$$

$$P_l = \frac{1}{2}\frac{|e|^2}{|Z_0+Z_l|^2}\,\Re(Z_l) \tag{1.5}$$

where the overline means the complex conjugate. The dissipation of the power in the load (ie the transmission of the power to the probe) can be maximized in two steps. First, the modulus $|Z_0+Z_l|$ can be lowered by nullifying the imaginary part of Z_0+Z_l. In this case, the imaginary part of Z_0 and Z_l are of opposite sign and Z_0+Z_l is purely real. The second step is to find the real part R_l of Z_l which minimize P_l:

$$\frac{\mathrm{d}P_l}{\mathrm{d}R_l} = \frac{1}{2}\frac{|e|^2(R_0-R_l)}{(R_0+R_l)^3} = 0 \tag{1.6}$$

where R_0 is the real part of Z_0. This derivative can be easily cancelled by choosing $R_l = R_0$.

To conclude, to maximize the transmission of the power to the load, one must choose a load whose impedance is the complex conjugate of the impedance of the source. As conventionally, the impedance of sources, loads and transmission lines within a spectrometers are purely resistive impedance of 50 Ω, it is necessary to adapt NMR probes to 50 Ω.

1.1.3 RLC circuits

In an NMR experiment, a magnetic field needs to be generated. An efficient way is to use a coil. However, the impedance of a coil is mainly inductive (L) and slightly resistive (R). Thus, its impedance is not adapted, ie not suitable for an optimized transfer of energy between the spectrometer and the sample. Somehow, this impedance must be converted into a real 50 Ω one without adding any noise to the signal.

To compensate the inductance of the coil and convert it into a 50 Ω load, it is necessary to add components with non zero imaginary parts which are capacitors and eventually inductors. Henceforth, the NMR probe appears as a RLC circuit. Some properties of RLC circuits are going to be reviewed here. It exists two types of RLC circuit depending if the capacitor is in parallel or in series with the inductance (see Fig. 1.3).

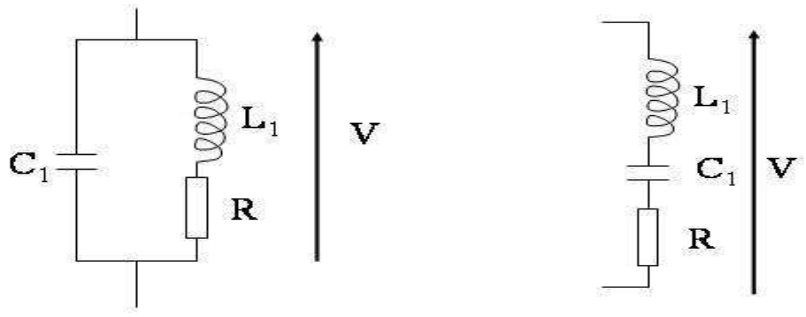

A) B)

Figure 1.3: A) Parallel RLC circuit. B) Series RLC circuit

A convenient representation of the parallel RLC circuit is through its impedance whereas, in series RLC circuits, the calculations are easier when the admittance is considered. The impedance Z of the parallel RLC circuit and the admittance Y of the series RLC circuit can be written as:

$$Z = -\frac{\jmath(R+\jmath L_1\omega)}{RC_1\omega+\jmath(L_1C_1\omega^2-1)} \tag{1.7}$$

$$Y = \frac{\jmath C_1\omega}{1-L_1C_1\omega^2+\jmath RC_1\omega} \tag{1.8}$$

Z and Y are both complex and to get an idea of their frequency dependence, it is necessary to estimate the parameters of the circuit elements. The inductance L of a typical $l = 1$ cm long solenoid coil with $N = 5$ turns and a diameter of 5 mm can be obtained using the following formula:

$$L = \frac{\mu N^2 S}{l} \approx 60\,\mathrm{nH} \tag{1.9}$$

Taking as an example a resonance frequency f_0 of 250 MHz, the capacitor C_1 which achieves the resonance condition can be estimated through the relation :

$$L_1C_1(2\pi f_0)^2 = 1 \tag{1.10}$$

One finds $C_1 = 8$ pF. Considering that the resistance of the coil has the typical value of $0.2\,\Omega$, the impedance and admittance of the parallel and series RLC circuits can be plotted around the resonance frequency f_0 (see Figure 1.4).

In this figure, we can notice that, at f_0, the real part of the impedance (resp. the admittance) of the parallel RLC circuit (resp. series RLC circuit) reaches its maximum whereas the imaginary part is equal to zero. So, at the resonance frequency, the impedance (resp. the admittance) is purely real, but still, its value (30 $k\Omega$ in the parallel case and 5 Ω^{-1} in the series case) is far from matching the 50 Ω of the spectrometer. In this case, the reflection coefficient ρ estimated by the formula :

$$\rho = \frac{Z_2 - Z_1}{Z_1 + Z_2} \tag{1.11}$$

where Z_1 and Z_2 are the impedances of the source and the load, is 0.997 in the parallel case and -0.992 in the series case. Therefore, almost no power is transmitted to the probe but also almost none of the signal induced by the spins goes to the spectrometer in this configuration. As a consequence, a RLC circuit is not sufficient and needs to be modified.

1.1.4 The quality factor

As we have just seen, the RLC circuit exhibits a large variation of the real part of its impedance near the resonance. This variation depends a lot on the quality factor Q. Its expression for RLC circuits is well known:

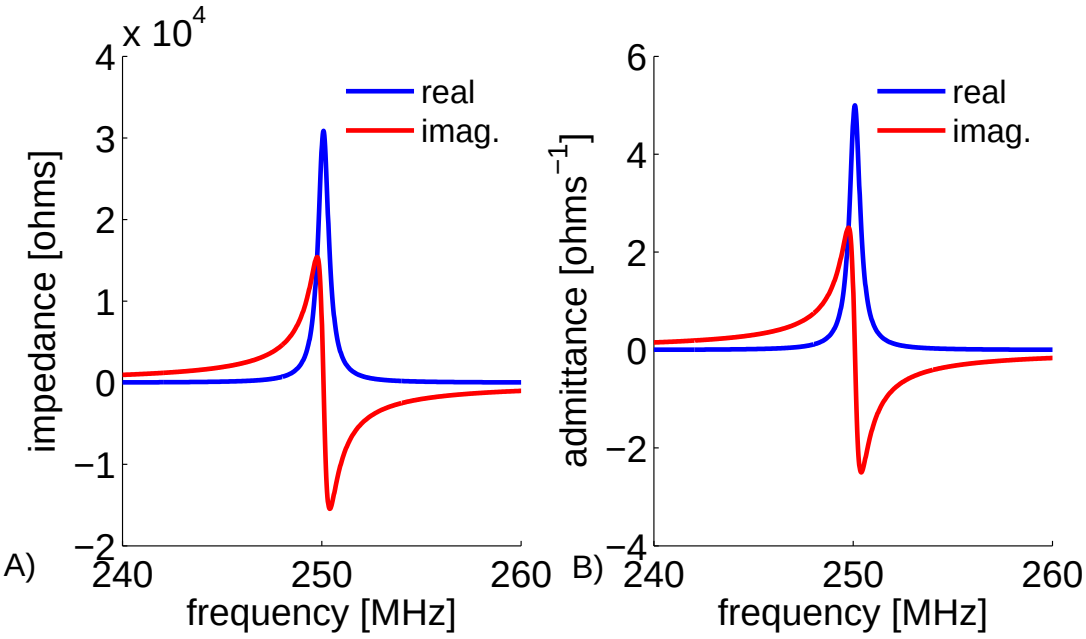

Figure 1.4: A) Impedance of a parallel RLC circuit. B) admittance of a series RLC circuit (right) near resonance. $f_0 = 250$ MHz.

$$Q_{\text{series}} = \frac{1}{R}\sqrt{\frac{L}{C}} \tag{1.12}$$

$$Q_{/\!/} \cong \frac{1}{RC\omega_0} = \frac{L\omega_0}{R} \tag{1.13}$$

In an NMR probe, the quality factor of the RLC circuit is typically a few hundreds (450 in our example). The higher the quality factor is, the higher is the real part of the impedance of the circuit at resonance. So, at first sight, the quality factor could be lowered to adjust the real part of the RLC circuit to 50 Ω. To do so, only the value of the resistor can be modified as the value of the inductance is fixed by the coil and the value of the capacitor is fixed by the resonance frequency (see Eqn. 1.10). To decrease of the quality factor in order to achieve the matching the real part of the impedance to 50 Ω, requires an increase of the resistor by a typical factor of 1000.

In NMR, the signal induced inside the coil by spins is very small (a few microvolts typically). Thus, a high signal to noise ratio (SNR) must be kept. One source of noise is the thermal motion of the electrons inside the resistor. This electron motion leads to a current which results in a voltage proportional to the resistor because of the Ohm law. From thermodynamics considerations, one can show that this is a white noise with a zero mean value and a mean square value (expressed in Volts) given by

$$\sigma_R = \sqrt{4k_B T R \Delta f} \tag{1.14}$$

where k_B is the Boltzmann's constant, T the temperature of the probe and Δf the bandwidth of the NMR receiver. From the previous expression, the important point is that σ_R is proportional to the square root of the resistor. As a consequence, to match the impedance of the RLC circuit to 50 Ω by increasing the resistor by a factor 1000 is not acceptable as it would increase the thermal noise by a factor 30.

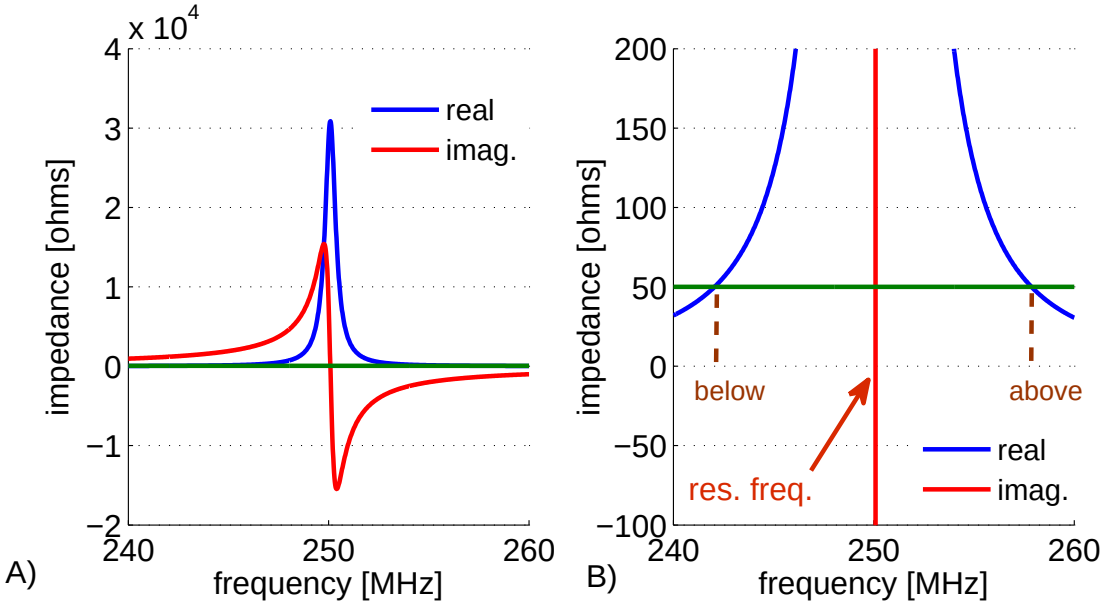

Figure 1.5: A) Impedance of a parallel RLC circuit. B) Zoom in the region where the resistive part is equal to 50 Ω

1.1.5 Matching by adding an imaginary impedance

As we have seen previously, the coil which is used to generate the magnetic field needs to be adapted to the 50 Ω output of the NMR spectrometer. As its impedance is mainly imaginary, we added a capacitor to cancel this part at the resonance frequency. This leads to a RLC circuit which exhibits a large real part at the resonance due to a high quality factor. In Figure 1.5B , we made a zoom around the resonance frequency. One can notice that the real part of the impedance goes rapidly from a value much lower than 50 Ω to a value much higher than 50 Ω and then goes back to a value close to zero. Thus, there are two particular frequency values where the real part of the impedance is equal to 50 Ω. The idea is to add below one of these two positions a zero on the imaginary part. This is performed by adding purely reactive components (inductance or capacitor). Table 1.1 shows for each type of RLC circuit (parallel or in series) which component is required to cancel the reactive part at the two points where the real part is equal to 50 Ω (below or above the resonance frequency).

Table 1.1: Matching component versus used RLC circuit

RLC circuit type	//	series
below res. freq.	capacitor in series	inductance in //
above res. freq.	inductance in series	capacitor in //

At first sight, there are four cases to consider depending if the RLC circuit is parallel or series and if the matching is achieved using an extra capacitor or inductance. In practice, the procedure is the same for each of them. First, a capacitor is placed in series or in parallel with the coil to adjust the resonance frequency using Eqn. 1.10. Then, a second reactive component is added to cancel the imaginary part at the frequency (the working frequency f_w) where the real part of the created RLC circuit is equal to 50 Ω, so that the following equations are verified:

$$\Re(Z(f_{\mathrm{w}})) = 50\ \Omega \quad (1.15)$$
$$\Im(Z(f_{\mathrm{w}})) = 0 \quad (1.16)$$

In practice, the inductance of the coil can vary slightly from one experiment to the other. Indeed, it depends directly on the magnetic permeability μ of the sample and on the filling factor of the coil. To overcome this difficulty, the matching and tuning components are slightly variable to precisely satisfy the matching conditions.

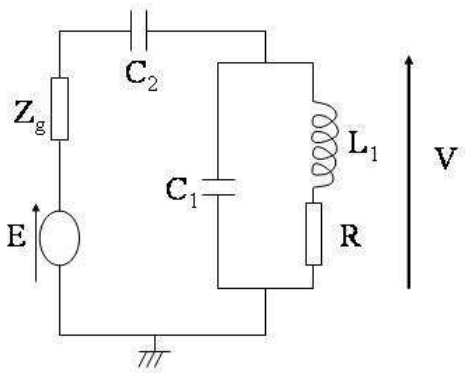

Figure 1.6: Parallel RLC circuit in series with a matching capacitor (so-called "tank" circuit).

Let us apply this procedure to the example of a parallel RLC circuit where a second capacitor in series is added to match the probe at the frequency f_w (pulsation ω_w). This case is one of the most common and is called a "tank circuit". It consists of two variable capacitors added to tune and match the circuit. This case is preferred in practice as it requires only the use of variable capacitors.

The inductance of the coil L_1 is assumed to be known (equal to 60 nH to follow the previous example) and the values of the two capacitors C_1 (called tuning capacitor) and C_2 (matching capacitor) are calculated to achieve the impedance matching (see Fig. 1.6). The complex impedance Z of such a circuit is :

$$Z = \left((\jmath L_1 \omega_{\mathrm{w}} + R) \mathbin{/\!/} \frac{1}{\jmath C_1 \omega_{\mathrm{w}}} \right) + \frac{1}{\jmath C_2 \omega_{\mathrm{w}}} \quad (1.17)$$

The real part and the imaginary part can be easily separated and are set to verify Eqns 1.15 and 1.16:

$$\Re(Z(f_0)) = \frac{R}{(1 - L_1 C_1 \omega_{\mathrm{w}}^2)^2 + R^2 C_1^2 \omega_{\mathrm{w}}^2} = 50\,\Omega \quad (1.18)$$
$$\Im(Z(f_0)) = -\frac{\omega_{\mathrm{w}}(-L_1 + L_1^2 C_1 \omega_{\mathrm{w}}^2 + R^2 C_1)}{(1 - L_1 C_1 \omega_{\mathrm{w}}^2)^2 + R^2 C_1^2 \omega_{\mathrm{w}}^2} - \frac{1}{\omega_{\mathrm{w}} C_2} = 0 \quad (1.19)$$

Equation 1.18 exhibits two solutions $C_1^{\pm}$ for the capacitor C_1. They correspond to the two points below and above the resonance frequency of the RLC circuit (see Fig. 1.5):

$$C_1^{\pm} = \frac{L_1\omega_w \pm \sqrt{(R/50)(R^2 + L_1^2\omega_w^2 - 50R)}}{\omega_w(L_1^2\omega_w^2 + R^2)} \tag{1.20}$$

Let us choose the solution C_1^- and substitute it in the equation 1.19. This leads to the following solutions :

$$C_1^- = \frac{L_1\omega_w - \sqrt{(R/50)(R^2 + L_1^2\omega_w^2 - 50R)}}{\omega_w(L_1^2\omega_w^2 + R^2)} \tag{1.21}$$

$$C_2 = \frac{\left(1 - L_1C_1^-\omega_w^2\right)^2 + R^2(C_1^-)^2\omega_w^2}{\omega_w^2(L_1(1 - L_1C_1^-\omega_w^2) - R^2C_1^-)} \tag{1.22}$$

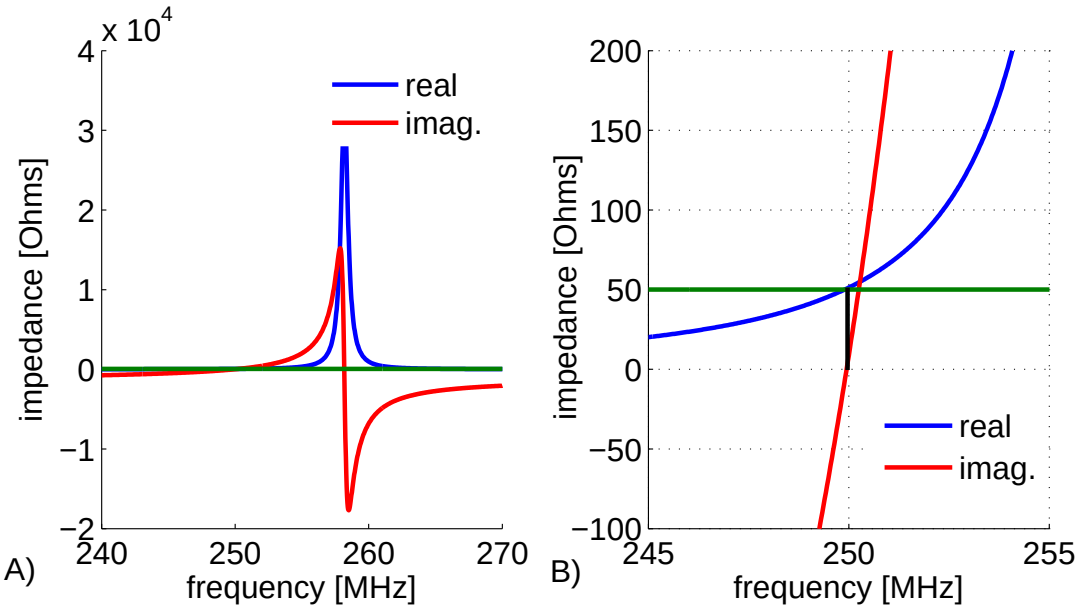

Figure 1.7: A) Real part and imaginary part of a parallel RLC circuit in series with a capacitor to achieve a matching at 250 MHz. B) Zoom around the working frequency.

With the value of inductance and resistor we used previously, to match the circuit at the working frequency of 250 MHz, C_1 must be equal to about 6 pF and C_2 to 1 pF. Figure 1.7 displays the variation of the real part and the imaginary part of the matched circuit. At the working frequency, the real part is equal to 50 Ω and an additional zero is added to the imaginary part.

1.1.6 Inductive matching

1.1.6.1 Introduction

Until here, we presented the classical method to tune and match the probe. As we have seen, the idea is to add reactive components in parallel or series to cancel the imaginary part at the frequency where the real part is equal to 50 Ω. An alternative method consists on using perfect transformers. The idea is to transform the impedance of the resonator such as it appears like a 50 Ω load from the spectrometer. This method is presented as it is the one implemented in the NMR-MOUSE™ we used during the present thesis work. However, this circuit was not implemented by ourselves so we only briefly outline its principle.

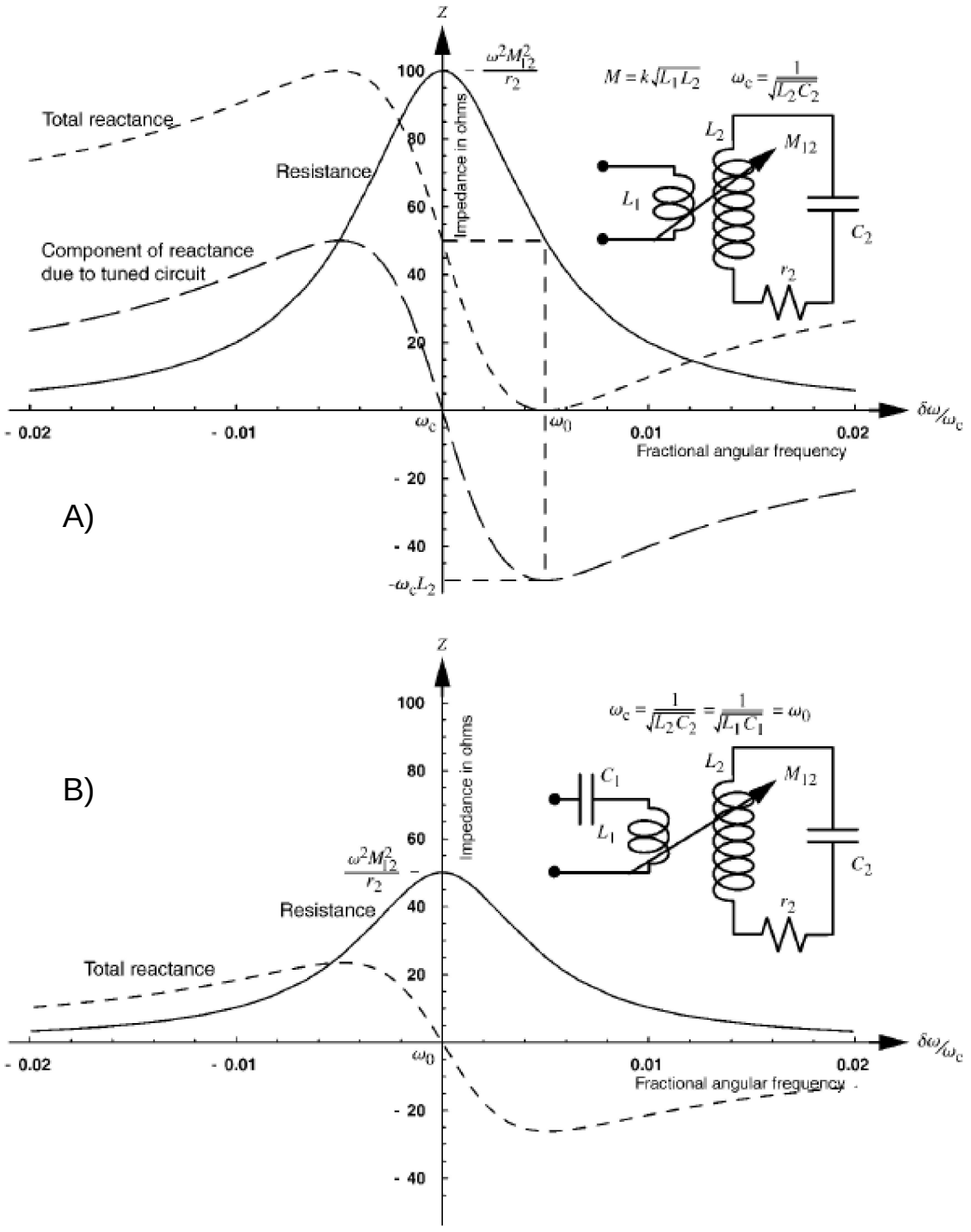

Figure 1.8: A) Circuit for inductive matching with a coupling loop. B) Circuit for inductive matching with a tuned coupling loop (reproduced from [HT02].)

1.1.6.2 Principle

This method consists in coupling the coil with a second loop [DBR+85, KLLC88, HT02]. The circuit is splitted into two parts (see Fig. 1.8). As in the method presented previously, the first step is to add a capacitor C_2. The RLC circuit obtained is similar to the one in section 1.1.3. The resonance frequency $f_c = \omega_c/2\pi$ of this circuit is adjusted to the operating frequency. Then, a coupling loop transforms the inductance of the coil. From the spectrometer, the inductance

appears to be much lower as the mutual M of the coupling coil and the initial coil plays now the role of the inductance of the initial coil. At this point, two designs are possible. In the first case (Fig. 1.8A), the situation is comparable to the one of classical tank circuit. At ω_c, the impedance of the real part is higher than 50 Ω. Thus, the matching is performed by adjusting the value of the mutual M whose effect is to shift the imaginary impedance curve vertically. The idea is the same as in the classical circuits described previously. The distance between the coupling coil and the coil is varied until a zero appears at the frequency where the resistive part is equal to 50 Ω. In the case of Fig. 1.8B, the procedure is slightly different. As the coupling coil is tuned with an additional capacitor C_1, the matching condition is achieved by adjusting the value of C_1 such as the real part of the impedance is equal to 50 Ω at the resonance frequency $f_c = \omega_c/2\pi$. In this case, the operating frequency is the same as the resonance frequency $f_c = \omega_c/2\pi$ of the RLC circuit $r_2C_2L_2$.

1.1.7 Power, voltage, current : from pulse duration to electric losses

1.1.7.1 The importance of voltage minimisation

In NMR, a 90° pulse magnetization tilt is obtained by adjusting the pulse duration and power. As stray field experiments require the use of short pulses to excite large bandwidths, the emitted power must be large. More precisely, the magnetic field generated by the probe must be large, which means a large current flowing through it. As the emitted power is limited by the specification of the amplifier (1 kW typically), it is necessary to ensure that for a given power, the current contribution is maximum and the voltage minimum. This limits the electric field and dielectric losses within the sample and avoids any arcing within the probe which would deteriorate the efficiency of the pulse. To achieve this, the geometry of the coil and the circuit must be finely designed.

1.1.7.2 Shape of the wires in the coil

Advantage of using thick wires

The inductance of wires varies as $\ln(1/r)$ where r is the radius of the wire. This means that the bigger the wire, the smaller is the inductance of the coil. As the impedance of the coil is proportional to its inductance, the voltage at the output of the coil is proportional to the logarithm of the inverse of the radius of the coil. Thus, to minimize the voltage, it is favourable to use thick wires.

Skin effect

In NMR, relatively high fields are used, typically between 0.5 T for low fields to 20 T for the largest fields. This corresponds to quite high resonance frequencies for the protons (20 MHz to 1 GHz). At these frequencies, the propagation of radiofrequency waves is submitted to the so-called skin effect. Due to this effect, high frequency waves only propagates at the surface of the conductors down to a distance δ called the skin depth:

$$\delta = \sqrt{\frac{1}{\pi\, f\, \mu\, \sigma}} \tag{1.23}$$

where f is the frequency of the radiofrequency current, μ the magnetic permeability and σ the electric conductivity. The skin depth on copper varies from 15 μm at 20 MHz to 2 μm at 1 GHz. Thus, instead of thick wires where most of the internal copper is unused, it is favourable to use conductors exhibiting a large surface such as wide copper strips.

Numerical application

Let us consider for example a 1 cm long strip with a width of 1.5 mm and a thickness of 30 μm. Its inductance at a typical frequency of 100 MHz can be easily computed using a software like FastHenry™ [KSW11] : 6.2 nH. If one considers the equivalent wire with the same cross section, this corresponds to a radius of 120 μm. Taking into account the skin effect, the inductance can be estimated to 8.3 nH using the formula for high frequency provided by Grover [Gro46]. This corresponds to a decrease of 34% of the inductance for a similar resistance when going from a wire to a strip.

Double advantage of the copper strip

As we have just seen, the copper strip is advantageous in terms of inductance minimisation. However another point concerns the parasitic capacitor between the wires in the coil. Indeed, it must be checked that these capacitors are really negligible at the working frequency so that the energy is really emitted to the sample and not dissipated through them. In other terms, the working frequency must be much lower than the resonance frequency of the coil seen as a whole RLC circuit to insure that it is in its inductive regime. To achieve this, the value of these parasitic capacitor can be limited by minimizing the surface which is facing other parts of the coil at different electrical potentials. This is naturally solved when using copper strips as the surfaces facing the others are already small due to the small thickness of the strip. Due to the advantages of copper strips we have presented here, we decide to use this wire geometry in the design of the coil we present later.

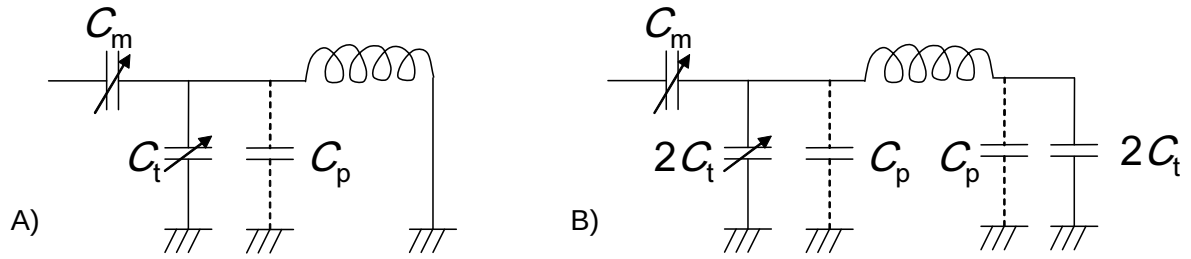

Figure 1.9: Sketch of impedance matching circuits for a non-symmetrical (A) and symmetrical (B) design.

1.1.7.3 Balancing the circuit

The parasitic capacitor between the wires and the ground through the sample plays a non negligible role. The effect of the sample can be evidenced by looking at the shift of the tuning of the probe when the sample is introduced in it. To avoid this, Mispelter [MLB06] suggests to symmetrize the configuration of the circuit. In the non-symmetrical design (Figure 1.9A), the global tuning capacitor C_{T}, taking into account the parasitic capacitors, is:

$$C_{\mathrm{T}} = C_{\mathrm{t}} + C_{\mathrm{p}} \tag{1.24}$$

where C_t and C_p are the tuning and parasite capacitors. Whereas in the symmetrical configuration (Figure 1.9B):

$$C_{\mathrm{T}} = \frac{2C_{\mathrm{t}} + C_{\mathrm{p}}}{2} = C_{\mathrm{t}} + \frac{C_{\mathrm{p}}}{2} \tag{1.25}$$

Thus, in the symmetrical case, the parasite capacitor is lowered by a factor of 2 and the intrinsic resonance frequency is shifted only by a factor of about $\sqrt{2}$. As a consequence, the current flowing through the parasitic capacitor is diminished and the corresponding losses are expected to be smaller. Besides, the electric field inside the coil is also lowered by a factor of two, so the voltage at the output of the coil is expected to be smaller.

Until here, we have seen the use of splitting the tuning capacitor. Murphey-Boesch and Koretsky [MBK83] studied the effect of also splitting the matching capacitor. In that configuration both ends of the coil are connected to the same capacitor (see Figure 1.10). As the current flowing through these two capacitors is the same, then, the voltages with respect to the ground at the two coil ends are the same but of opposite phases. This reduces the electrical field and the voltage amplitudes.

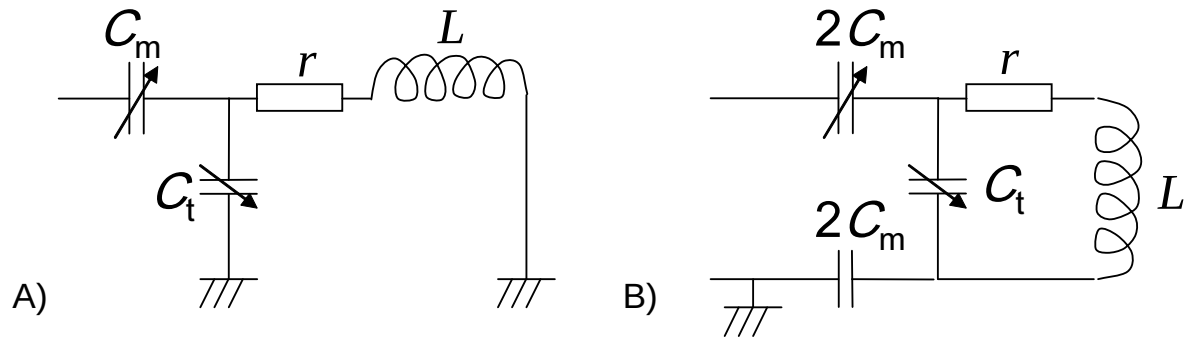

Figure 1.10: A) Sketch of a basic matching circuit (tank circuit). B) Sketch of a balance matching circuit.

In practice, the circuit we presented in Figure 1.9B already incorporates a balance with the matching capacitor as both ends of the coils are connected to a capacitor. This is the electrical configuration we used in our home-made probes.

1.1.7.4 Advantages and drawbacks of having a low resistance

As we have seen before, it seems to be always favourable to have a resistance as low as possible to minimize the thermal noise. This leads to a high quality factor and high sensitivity. However, a high quality factor has also some bad effects. In particular, the power sent to the the probe is quite large (a few Watts to a few thousands of Watts). So, before being able to record any NMR signal, this large amount of energy has to be absorbed. As this is the resistive parts which mainly dissipates the energy, a significant amount of time might be necessary before being able to record any signal when the resistance is too low. Consequently, when the life time of the NMR signal is very short (smaller than 100 μs typically), a high quality factor may lead to too large dead times. Adding small resistors can help to decrease the dead time, but at the expense of SNR.

Another drawback of having a very high quality factor is that the voltage generated inside the probe is very high. An electronic simulation software like LTSpice™ [Eng11] allows to calculate intensities and voltages at various nodes of a circuit. The circuit which is simulated is the one of Figure 1.10A with $C_\mathrm{m} = 6$ pF, $r = 0.2\,\Omega$, $L = 60$ nH and $C_\mathrm{t} = 1$ pF. When a moderate input power of 10 W is applied, the voltage at the ends of C_t reaches already 4.1 kV. The consequence is that special capacitors able to hold this order of magnitude of voltages are required. Besides, with such voltages, arcing may occur anyway within the circuit, which will make the probe inefficient. One solution can be to add small resistance values. For example, a resistance twice larger leads to a peak voltage twice lower for the same power at the input. Of course, the consequence is that the contribution of the thermal noise is also increased.

1.2 Coil design

So far, we focused on probeheads from a theoretical point of view. We presented example of circuits adapted to the impedance of the spectrometer. Let us now show our practical realizations.

1.2.1 Introduction

This part concerns mainly the probe realized for the STRAFI experiment as the NMR-MOUSE™ we used was already equipped with a coil. In a STRAFI experiment (see chapter 2), the profile of a sample is measured step by step. At each position, only a thin slice (typically 100 μm) is excited and then, the sample is moved along the depth direction to image the next slice and complete the profile. Thus, from a geometrical point of view, the coil must exhibit both a cylindrical geometry to allow the motion of the sample and be as close as possible to the sample to obtain a good SNR. In addition to this, the design of the coil must take into account the intrinsic limitation of the RF amplifier and the voltage limit of the capacitors. So, in our simulation, we will limit the input power to 1 kW which corresponds to the maximum output power of our RF amplifier. Moreover, to avoid any arcing, we will also limit the voltage at the output of each of the components to 1 kV. This is a typical value for commercial capacitors. The object of this section is to propose a coil design which fulfills all these requirements and provides the highest possible magnetic field amplitude.

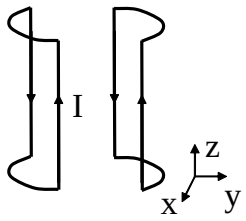

Figure 1.11: Sketch of a "saddle" coil.

1.2.2 Which type of coil?

The radiofrequency field must be homogeneous over the selected slice in the xy plane and generated by a resonator with a cylindrical geometry around the z axis. This constrains drastically the design of the coil and only few geometries fulfill this conditions:

- The "Bolinger" coils are made of vertical wires positioned on a circle. The idea of this coil is to imitate the ideal cosinusoidal distribution of current required to obtain an homogeneous magnetic field in the circle. The so-called "saddle" coil is a particular case of the "Bolinger" coils. The distribution is made by four wires positioned at $\pi/6$, $5\pi/6$, $-\pi/6$ and $-5\pi/6$ (see Fig. 1.11). This simple geometry has been used for years now [Gar51, GM70] and is quite easy to achieve. However, the generated field is only homogeneous in the central part of the coil. To improve it, wires must be added.

- The "Alderman-Grant" coil [AG79] is formed by two H shaped copper sheets wounded on a cylinder. In this case, the magnetic field is created by the current distribution along the copper sheets. What is remarkable in this configuration is that the inductance of the resonator is lower than a "Bolinger" coil of equivalent size, which makes it interesting especially at high frequencies.

- The last configuration we can think of is the "birdcages". They were introduced by Hayes [HES+85] and have been modelled by Tropp [Tro89]. They consist of a linear network wounded around a cylinder. The idea is to change the phase of the current in each "leg" of the "birdcage" by adding capacitors in such a way that the inductive fields add up inside the resonator but cancel each other outside. The end result is a very homogenous RF field inside the resonator. This geometry is used especially to image larger volumes.

From these three cases, we decided a priori to use a Bolinger like coil. Indeed, it seems to correspond the best to our problem of exciting a thin slice of a large radius. The other coils having a large sensitive volume would lead in our case to the reception of noise coming from areas outside our region of interest. During his PhD work, Javelot [Jav94] proposed an original method to improve the homogeneity of the field generated by saddle coils. Here, we compare the solution of Javelot and the cosine imitation of Bolinger, then, we propose a practical realization of the theoretical calculations.

1.2.3 Validation of the use of magnetostatics equations

To design coils, magnetic fields must be evaluated. This calculation would be much easier if we could consider that magnetostatic laws were valid and if the phase of the current did not have to be taken into account. The purpose of this section is thus to validate the use of the Biot-Savart law at our working frequencies (below 1GHz).

The equation valid at any frequency is the Maxwell-Gauss equation:

$$\mathbf{div}\,\vec{B} = 0. \tag{1.26}$$

So, a potential vector $\vec{A}$ can be introduced such as $\vec{B} = \overrightarrow{\mathbf{rot}}\,\vec{A}$. This potential vector can be written as a function of the retarded current density $\vec{J}$ [GH91]:

$$\vec{A} = \frac{\mu_0}{4\pi}\int \frac{\vec{J}\left(\vec{r}, t - \frac{r}{c}\right)}{r}\mathrm{d}V \tag{1.27}$$

where $\vec{r}$ is the distance between the point where we want to evaluate the field and one point of the source. c is the speed of light. The integral is on the source (here the wires) of volume V. The magnetic field $\vec{B}$ can be deduced from 1.27:

$$\vec{B} = \overrightarrow{\mathbf{rot}}\,\vec{A} = \overrightarrow{\mathbf{rot}}\left[\frac{\mu_0}{4\pi}\int \frac{\vec{J}\left(\vec{r}, t - \frac{r}{c}\right)}{r}\mathrm{d}V\right]. \tag{1.28}$$

Then, by using, the mathematical relationship:

$$\overrightarrow{\mathbf{rot}}(\rho\cdot\vec{V}) = \rho\cdot\overrightarrow{\mathbf{rot}}\vec{V} - \vec{V}\wedge\overrightarrow{\mathbf{grad}}\rho\,, \tag{1.29}$$

where ρ is a scalar and $\vec{V}$ a vector, the magnetic field can be expressed as:

$$\vec{B} = \frac{\mu_0}{4\pi}\int\left(\frac{1}{r}\overrightarrow{\mathbf{rot}}\left[\vec{J}\left(\vec{r}, t - \frac{r}{c}\right)\right] - \vec{J}\left(\vec{r}, t - \frac{r}{c}\right)\wedge\overrightarrow{\mathbf{grad}}\left(\frac{1}{r}\right)\right)\mathrm{d}V. \tag{1.30}$$

Using the following relationship [GH91]:

$$\overrightarrow{\mathbf{rot}}\left[\vec{J}\left(\vec{r},t-\frac{r}{c}\right)\right]=-\frac{\partial\vec{J}}{\partial t}\wedge\overrightarrow{\mathbf{grad}}\left(t-\frac{r}{c}\right)=\frac{1}{c}\frac{\partial\vec{J}}{\partial t}\wedge\vec{r}, \tag{1.31}$$

and combining it with Eqn. 1.30, the magnetic field can be written as [Jef90]:

$$\vec{B}=\frac{\mu_0}{4\pi}\int\left(\frac{1}{r^2}\,\vec{J}\left(\vec{r},t-\frac{r}{c}\right)\wedge\vec{r}+\frac{1}{c\,r}\frac{\partial\vec{J}}{\partial t}\left(\vec{r},t-\frac{r}{c}\right)\wedge\vec{r}\right)\mathrm{d}V. \tag{1.32}$$

This formula exhibits the magnetic field evolution when the current is time dependent.

In order to evaluate the effect of the time dependence of the current, let us use a Taylor expansion of $\vec{J}\left(\vec{r},t-\frac{r}{c}\right)$ close to time t:

$$\vec{J}\left(\vec{r},t-\frac{r}{c}\right)=\vec{J}(\vec{r},t)-\frac{r}{c}\frac{\partial\vec{J}}{\partial t}(\vec{r},t)+\frac{1}{2}\left(\frac{r}{c}\right)^2\frac{\partial^2\vec{J}}{\partial t^2}(\vec{r},t)+\cdots \tag{1.33}$$

So, Eqn. (1.32) becomes:

$$\vec{B}=\frac{\mu_0}{4\pi}\int\left[\vec{J}(\vec{r},t)-\frac{1}{2}\left(\frac{r}{c}\right)^2\frac{\partial^2\vec{J}}{\partial t^2}(\vec{r},t)\right]\wedge\frac{1}{r^2}\,\vec{r}\,\mathrm{d}V. \tag{1.34}$$

The first term is the same as in the Biot-Savart law and the second one is the perturbation term. It scales with the dimensionless parameter $\left(\frac{r}{cT}\right)^2$. By choosing $r=2$ cm and $T=5\,10^{-9}$ s ($f=200$ MHz), the ratio $\left(\frac{r}{cT}\right)^2$ is equal to $2\,10^{-4}\ll 1$. This validates a posteriori the use of the Biot and Savart law.

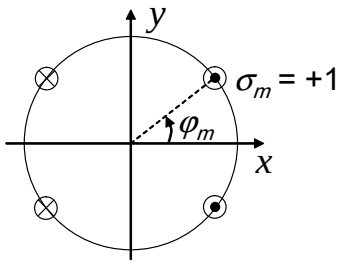

Figure 1.12: Configuration of the wires to model a "saddle" coil.

1.2.4 The coils of "Bolinger" type

Here, we start by presenting a theoretical approach proposed by Javelot [Jav94] where the position of the wires is optimized in order to zero the terms of the magnetic field Taylor development of order higher than order 0. Then, we will present the approach adopted by Bolinger [BPL89] and compare both of them.

1.2.4.1 Theoretical approach

The situation of the Biot-Savart law for an infinite wire

As we have seen in the previous paragraph, classical equations of magnetostatics can be used as the regime is quasi stationary. The elementary component of the "Bolinger" type coils is a straight wire. Let us consider a wire positioned on a unit circle and calculate the magnetic field creating inside the circle using the Biot-Savart law. The wire location is defined by its vector $\vec{r}_m = e^{\jmath\,\varphi_m}$ and it is supplied with a constant current $\sigma_m I$. It produces at the point $\vec{r}$ a field $\vec{B}_m(\vec{r})$:

$$\vec{B}_m(\vec{r}) = \frac{\mu_0 \sigma_m I}{4\pi} \int_{wire} \frac{(\vec{r} - \vec{r}_m) \wedge \mathrm{d}\vec{l}}{|\vec{r} - \vec{r}_m|^3} \tag{1.35}$$

$\sigma_m = \pm 1$ is the direction of the current.

In Cartesian coordinates, $\mathrm{d}\vec{l}$ and $\vec{r} - \vec{r}_m$ can be written as:

$$\mathrm{d}\vec{l} = \begin{vmatrix} 0 \\ 0 \\ \mathrm{d}z\,\vec{u}_z \end{vmatrix} \quad , \quad \vec{r} - \vec{r}_m = \begin{vmatrix} (x - a_m)\,\vec{u}_x \\ (y - b_m)\,\vec{u}_y \\ z\,\vec{u}_z \end{vmatrix}$$

with $\vec{r}_m = (a_m, b_m, 0)$ and $\vec{r} = (x, y, z)$.

Then, the integration of equation 1.35 leads to :

$$\vec{B}_m(\vec{r}) = \frac{\mu_0\,\sigma_m I}{2\pi\big[(x - a_m)^2 + (y - b_m)^2\big]} \begin{vmatrix} (y - b_m)\,\vec{u}_x \\ -(x - a_m)\,\vec{u}_y \\ 0 \end{vmatrix}$$

To simplify this expression, Zupančič and Pirš [ZP76] suggested to introduce the complex variable $\underline{B^\star_m}$:

$$\underline{B^\star_m} = \frac{\mu_0\,\sigma_m I}{2\pi} \frac{1}{(a_m + \jmath\, b_m) - (x + \jmath\, y)} \tag{1.36}$$

with $\underline{B^\star_m} = \vec{B}_{m\,y} + \jmath\,\vec{B}_{m\,x}$.

Then, if we define $\tilde{z}_m = a_m + \jmath\, b_m$ and $\tilde{z} = x + \jmath\, y$, the previous equation can be written:

$$\underline{B^\star_m} = \frac{\mu_0\,\sigma_m I}{2\pi\,\tilde{z}_m} \frac{1}{1 - \frac{\tilde{z}}{\tilde{z}_m}} \tag{1.37}$$

As the wires are supposed to be on a unit circle and we want to calculate the field inside this circle, the following relation is necessarily true:

$$\left| \frac{\tilde{z}}{\tilde{z}_m} \right| < 1, \tag{1.38}$$

so that $\underline{B^\star_m}$ can be developed into a power series:

$$\underline{B^\star_m} = \frac{\mu_0\,\sigma_m I}{2\pi\,\tilde{z}_m} \sum_{n=0}^{\infty} \left(\frac{\tilde{z}}{\tilde{z}_m} \right)^n = \frac{\mu_0\,\sigma_m I}{2\pi} \sum_{n=0}^{\infty} \tilde{z}^n e^{-\jmath\,(n+1)\,\varphi_m} \tag{1.39}$$

with $\tilde{z}_m = e^{\jmath\,\varphi_m}$.

Field generated by a single saddle coil

When an ensemble of h wires is located on the unit circle, then the total complex magnetic field $\underline{B^T}(\tilde{z})$ is:

$$\underline{B^T}(\tilde{z}) = \frac{\mu_0 I}{2\pi} \sum_{m=1}^{h} \sigma_m \sum_{n=0}^{\infty} \tilde{z}^n e^{-\jmath\,(n+1)\,\varphi_m} = \frac{\mu_0 I}{2\pi} \sum_{n=0}^{\infty} \tilde{z}^n \sum_{m=1}^{h} \sigma_m e^{-\jmath\,(n+1)\,\varphi_m} \tag{1.40}$$

In the "saddle" coil configuration, $h = 4$ and the pairs (φ_k, σ_k) defining the configuration are:

$$(\varphi_k, \sigma_k) \in \{(\varphi_m; +1), (-\varphi_m; +1), (\pi - \varphi_m; -1), (\pi + \varphi_m; -1)\} \tag{1.41}$$

This quadruplet is only defined by the angle φ_m. In this configuration, one can write:

$$\underline{B^T}(\tilde{z}) = \frac{\mu_0 I}{2\pi} \sum_{n=0}^{\infty} \tilde{z}^n \sum_{l=1}^{4} \sigma_l \, e^{-\jmath\,(n+1)\,\varphi_l} \tag{1.42}$$

$$= \frac{\mu_0 I}{\pi} \sum_{n=0}^{\infty} \tilde{z}^n \big(1 - e^{-\jmath\,(n+1)\,\pi}\big) \cos\big[(n+1)\,\varphi_m\big] \tag{1.43}$$

In the previous equation, one can notice that since each odd term is zero, $\underline{B^T}(\tilde{z})$ can be written as:

$$\underline{B^T}(\tilde{z}) = \frac{2\mu_0 I}{\pi} \sum_{p=0}^{\infty} \tilde{z}^{2p} \cos\big[(2p+1)\varphi_m\big]. \tag{1.44}$$

The q saddle coils case

If we now consider q quadruplets, the resulting field $\underline{B^T}(\tilde{z})$ is the sum over the q quadruplets:

$$\underline{B^T}(\tilde{z}) = \frac{2\mu_0 I}{\pi} \sum_{p=0}^{\infty} \tilde{z}^{2p} \sum_{m=1}^{q} \cos\big[(2p+1)\varphi_m\big]. \tag{1.45}$$

In order to homogenize the field, each order should be zero except the order one. This is equivalent to solving the following system of equations:

$$\Big(\sum_{m=1}^{q} \cos\big[(2p+1)\varphi_m\big] \Big)_{p \in \mathbb{N}^\star} = 0 \tag{1.46}$$

The resolution of this system is a bit tedious and has been fully developed in the Javelot PhD thesis [Jav94].

Numerical determination

Depending on the number of saddle coils which are considered, solving the previous system, for instance with MAPLE™, may provide more than one solution. This makes sense since the method consists in cancelling the high order terms of the Taylor development of the field but there was no constraint on the upper value of the magnetic field generated. Thus, it is necessary to sort the solutions and choose the one which corresponds to the highest magnetic field value.

The selection of the best configuration is performed by comparing the magnitude of the magnetic field created at the center of the coil of each solution assuming the current flowing through the wires is the same. For $q = [\![1; 5]\!]$, the best solution is displayed in Figure 1.14.

1.2.4.2 Comparison with the cosine imitation

Cosine imitation by discrete wires

Smythe [Smy67] showed that the ideal current distribution required to obtain the best field homogeneity is a cosine dependence of the amplitude. Bolinger et al. [BPL89] proposed to imitate the cosine distribution by discrete current wires in such a way that their projection along the diameter is equally separated (see figure 1.13). Depending on the number of wire pairs, the distance of the last segments (up or down) is the same length (Fig. 1.13A) or only the half (Fig. 1.13B) of the other segments.

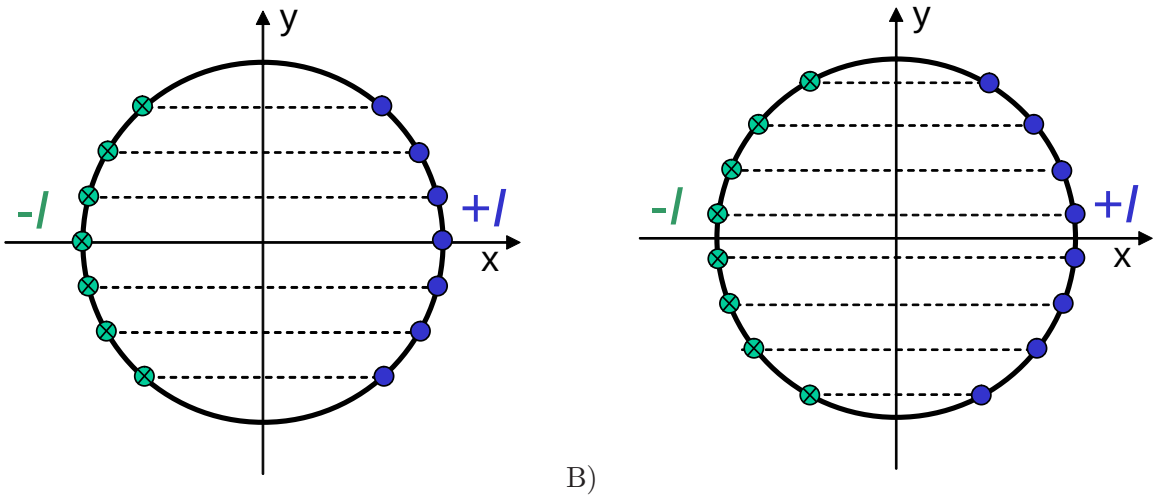

A) B)

Figure 1.13: Positioning of wires in a cosine distribution for an even number of wire pairs (A) and for an odd one (B).

Comparison of the field homogeneity of the cosine imitation and Javelot's analytical minimization.

First, both methods do not provide the same angles. In order to compare the magnetic field generated by multiple saddle coils, following either Javelot's approach (analytical minimisation) or a cosine imitation, the magnetic field was simulated using MATLAB™ in both cases. Assuming the wires were two centimeters high, placed on a circle with a radius of one centimeter, using the Biot-Savart law (Eqn. 1.35), the magnetic field is computed in a plane positioned at middle height of the wires. The results are displayed in Figure 1.14. To apprehend the field homogeneity in each case, three isofields are displayed: the same value as in the middle of the coil (0% in green) and two at $\pm 5\%$ (red or blue) of the central value. The wires are also represented by blue crosses or red points depending on the direction of the current.

First one should notice that both approaches provide comparable results in terms of homogeneity except in the case of a single saddle coil. In that case, the analytical minimisation

provides a result which is the complementary angle of the one expected from cosine imitation (30°). For all other cases (more than one saddle coil), the density of isofield lines at 0 % is much higher for the analytical minimisation than with the cosine imitation. This is consistent with the method used. Therefore, we expect the field to be more homogeneous in the configuration obtained by analytical minimization. This is confirmed by the plots in Figure 1.15 where the steps between the isofield lines is reduced to 0.5%. In this case, the region of homogeneous field appears 40% smaller (in diameter) in the cosine imitation. However the criteria of ±5% is acceptable especially in the presence of a gradient and except in the single saddle case, the diameter of the sample which can be introduced inside the resonator within ±5% of the value of the central magnetic field value is comparable in both cases (see Figure 1.16).

1.2.4.3 Probe simulation

Introduction

So far, the geometry of the coil was taylored to optimize the magnetic field homogeneity over the volume of interest. Two methods were identified : either a calculation based on an analytical minimization performed by Javelot and a cosine imitation proposed by Bolinger. According to the previous study, the two methods exhibit similar performances against our criteria in terms of field homogeneity. However, to finish this study, it is necessary to estimate the inductance of the corresponding coils in order to calculate the corresponding capacitors and inductors required to tune and match the coil following the procedure presented at section 1.1. Besides, it is necessary to determine which configuration exhibits the highest amplitude given the specification of the amplifier we used (1 kW) and the fact that the voltages applied to the capacitors must be limited to 1 kV to avoid arcing.

Inductance estimation

In order to determine voltages and currents in the NMR probe circuit, an estimation of the inductance of the coils designed in the previous section is required. To achieve this, the software Fasthenry™ from the Kamon's group [KSW11] was used. In agreement with paragraph 1.1.7.2, instead of using copper wires, copper strips 1.5 mm wide and 30 μm thick (thickness of commercial copper scotch) were used. Multiple saddle coils were built by adding straight segments for the vertical wires and by decomposing the wires linking the vertical wires into shorter segments (see Figure 1.17A). Then, the inductances were estimated at the frequency of 137 MHz. The results are displayed on Figure 1.17B. This figure shows that the inductances of 1 to 4 saddle coils calculated for the analytical minimisation and the cosine imitation are similar. Only for the case $q = 5$, do they differ significantly.

Whole probe simulation

Once the inductances of coils are known, they can be integrated into a circuit similar to the one of Figure 1.9. The tuning and matching capacitors were calculated using the program accompanying the book of Mispelter [MLB06] and assuming a typical quality factor value of 150. This program provides as an output the capacitor values in the symmetrical and non-symmetrical cases (see section 1.1.6). The results are compiled in Table 1.2. As we have seen before, the values of the capacitors in the symmetric case are about twice larger than in the non-symmetric case. Thus, we expect the voltage at the output of the tuning capacitor to be twice lower. From now, we will consider only the symmetric case. The object of the following section is to calculate the current in the coil to determine which coil configuration generates the highest magnetic field.

angles	analytical minimization	cosine type

φ_1
60
30

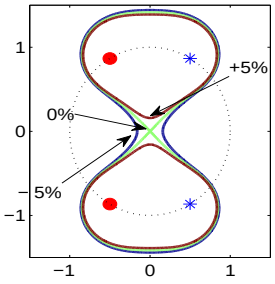

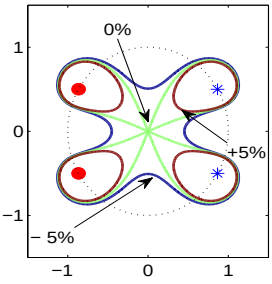

φ_1	φ_2
12	48
14.5	48.6

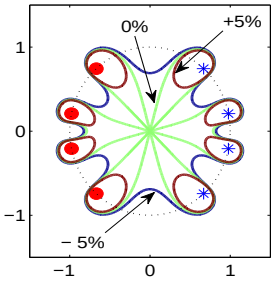

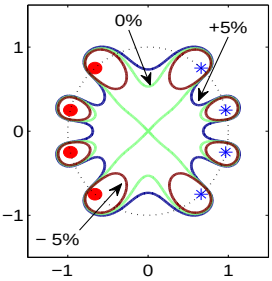

φ_1	φ_2	φ_3
11.7	26.9	56.1
9.6	30	56.4

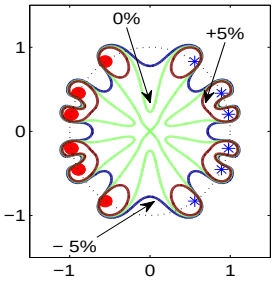

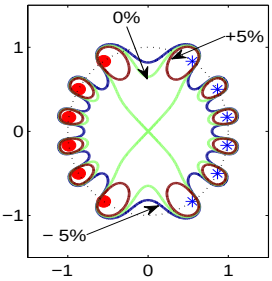

φ_1	φ_2	φ_3	φ_4
0.9	24.9	35.1	60.9
7.2	22	38.7	61

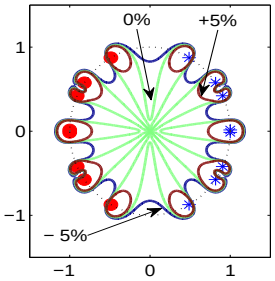

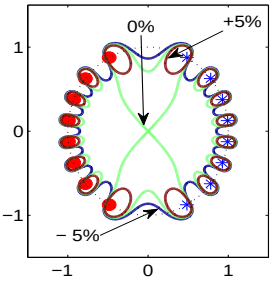

φ_1	φ_2	φ_3	φ_4	φ_5
5.7	21.4	35.1	55.9	87.1
5.7	17.5	30	44.4	64.2

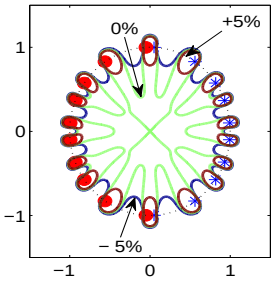

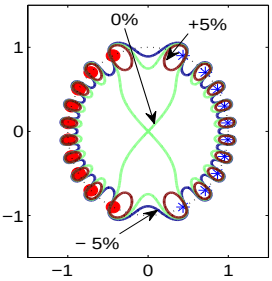

Figure 1.14: Angles allowing the optimum field homogeneity versus the number of saddle coils according the analytical minimization of Javelot (upper values) or an imitation of the cosine distribution (lower values). On the right, are displayed the corresponding field maps. The isofield lines are at ± 5%

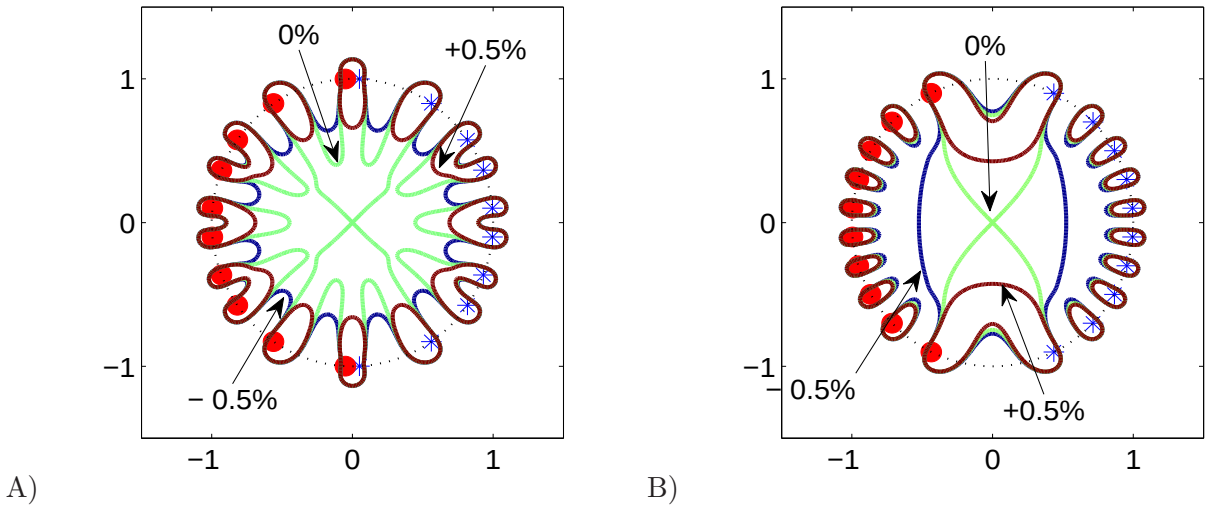

A) B)

Figure 1.15: Field map in the 5 saddle coil case with an isofield step of 0.5% following the analytical minimisation (A) and the cosine imitation (B).

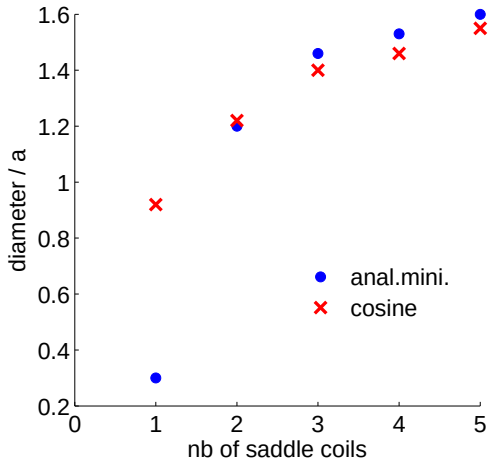

Figure 1.16: Maximum diameter (normalized by the radius of the coil a) of a circular sample which can be introduced within the ±5% isofield.

Simulation for a given input power

To compare the various multiple saddle coils, let us assume that the input power P at the entrance of the probe tuned and matched to $Z = 50\,\Omega$ using Table 1.2, is equal to 100 W. This power can be easily converted to a peak to peak voltage U_{pp} of 200 V :

$$P = \frac{U_{\mathrm{rms}}^2}{Z} = \frac{U_{\mathrm{pp}}^2}{8\,Z}. \tag{1.47}$$

Then, using a electronic simulation program such as LTspice™ [Eng11], currents and voltages at various nodes of the circuit can be easily computed.

The simulation was performed around the frequency of 137 MHz which is our working frequency in the STRAFI experiment. The results of this simulation are compiled on Figure 1.18A. This plot provides on the left axis the value of the magnetic field deduced from the current

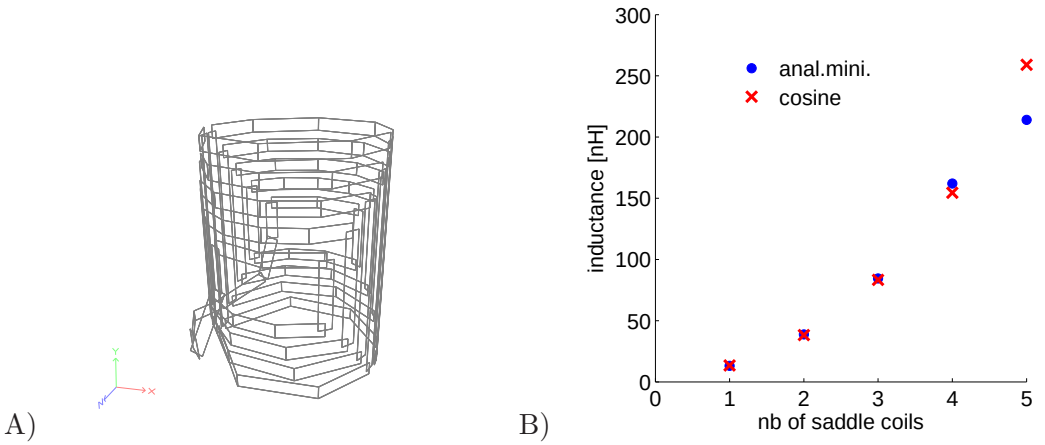

Figure 1.17: A) Drawing of a cosine type five saddle coil using the drawing package of FastModel™ [KSW11]. B) Inductances of the multiple saddle coils calculated with Fasthenry™ [KSW11].

Table 1.2: Inductance of the multiple saddle coils calculated following the previous theoretical considerations and using a classical cosine distribution. The value of the capacitors required to adapt the coil for both the symmetric and non symmetric configuration are provided. Inductances are in nH and capacitors in pF. The values of the capacitors was calculated using a program attached with the book of Mispelter [MLB06] and assuming a quality factor of 150.

	anal.mini.						cosine					
		non sym.		sym.				non sym.		sym.		
n	L	C_T	C_M	C_T	C_S	C_M	L	C_T	C_M	C_T	C_S	C_M
1	13.1	99	4	198.5	206	8.5	13.4	96.8	4	194	201.4	8.4
2	38.8	32.5	2.3	69.6	65	4.7	38.2	33	2.4	66	70.7	4.8
3	84.5	14.4	1.6	32	29	3	83.3	14.6	1.6	29.3	32.4	3.2
4	162	7.2	1.1	14.4	16.7	2.3	154.5	7.6	1.2	15.2	17.5	2.3
5	214	5.3	1	10.6	12.6	2	259	4.3	0.9	8.6	10.4	1.8

flowing through the inductor computed by LTspice™. We see that for the same input power, the magnetic field generated becomes larger when the number of saddle increases. The current in the resonator (not plotted here) decreases with the number of saddle coil but this decrease is overcome by the fact that a multiple saddle coil is more efficient when the number of wires increases. The effect is similar for the voltage at the output of the tuning capacitor. It is important to notice that this voltage is already higher than 1 kV in the case of 3 saddle coils, which is not compatible with our criteria to keep the voltage at the output of capacitors below 1 kV to avoid arcing.

Simulation with a limit on the voltage of the tuning capacitor

In this paragraph, we performed the same simulation as before, but instead of imposing the input power, we vary the input power until the voltage at the output of the tuning capacitor is equal to 1 kV. Of course, we take into account the fact that the input power cannot be higher than 1 kW. The results are displayed in Figure 1.18B. This curve exhibits an optimum value for the magnetic field generated. The highest magnetic field is obtained in the two saddle-coil case. In this case, the input power is about 500 W and the voltage at the output of the capcitors

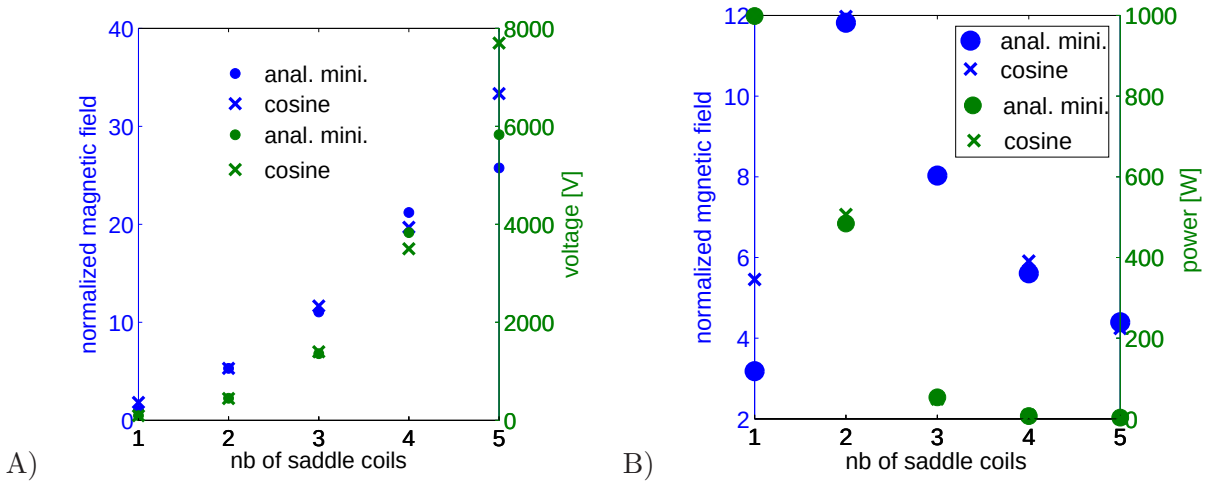

Figure 1.18: A) Magnetic field generated by multiple saddle coils and voltage at the output of the tuning capacitor assuming an input power of 100 W. B) Magnetic field generated by multiple saddle coils and input power assuming the voltage at the output of the tuning capacitor is 1 kV.

smaller than 1 kV. This result is valid for the analytical minimization configuration as well as for the cosine imitation. The values of the amplitude of the magnetic field obtained by both approaches are similar.

1.2.4.4 Practical realization

In the previous section, we have shown that the analytical minimisation of Javelot [Jav94] and the cosine imitation of Bolinger [BPL89] provide similar result in terms of magnetic field intensity. However, as the first one seems to give a better homogeneity, we decided to build a two saddle coils following the method of Javelot.

Mechanical details

The coil is made of 3 mm copper strips cut from a commercial 30 μm thick copper tape. First, a pattern is printed on a tracing paper (see Fig. 1.19) and then the copper strips are cut with a cutter. They are positioned and stuck around a glass cylinder. This glass cylinder goes through the whole probe as a guide for the sample and also isolates the electrical part of the probe when humidity and temperature are regulated. This home-made probe was designed by ourselves and machined in our mechanical workshop. A picture of this probe is given in Figure 1.20A. A tube of titanium (not displayed here) was used as a shielding for the probe.

Figure 1.19: Pattern used to make the copper strip. The strips are 3 mm wide and the pattern is 15 mm high. After being cut, the pattern is stuck around a glass tube.

Electrical characterization

The inductance of the coil was found equal to 52 nH and the quality factor 92. This is slightly larger than the value expected from the simulation of the equivalent coil using FastHenry™ (38.3 nH) [KSW11]. This difference may be explained by the fact that the wires connecting the coil to the capacitors are not taken into account in the calculation of the inductance.

The electrical circuit is the one presented in Figure 1.20B. Using the program attached to the book of Mispelter [MLB06], the values of the expected symmetrizing, tuning and matching capacitance are 51, 47 and 5.3 pF respectively. In practise, we used 40 pF for the symmetrizing capacitance, 35 pF in series with a variable capacitor between 1 and 10 pF for the tuning capacitance and 5 pF in parallel with a variable capacitor between 1 and 10 pF for the matching capacitance. The fixed capacitors were manufactured by American Technical Ceramics™ and the variable capacitors by Voltronics™. The difference to the values expected can be explained by the presence of parasitic capacitance with the shielding and the load which shifts the tuning frequency towards the low frequencies.

A) 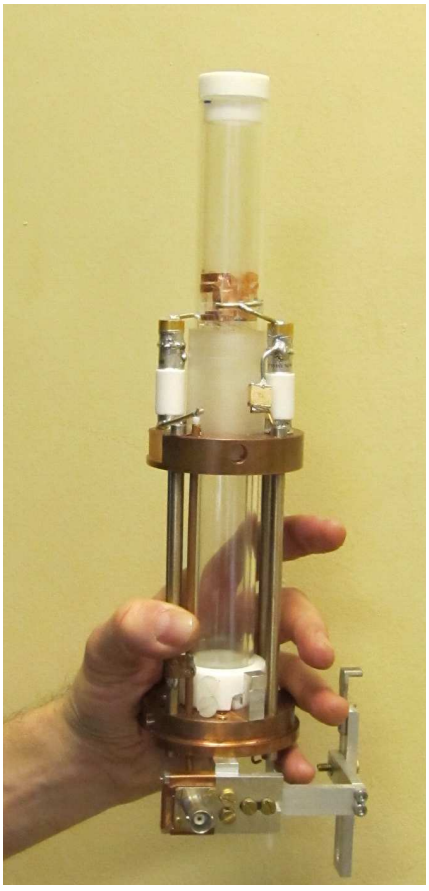

B) 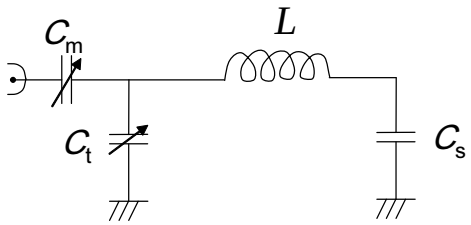

Figure 1.20: A) Picture of our STRAFI probe. B) Schematic of the symmetric electrical circuit used.

Conclusion

A fundamental aspect in the success of an NMR experiment is the ability to emit large radiofrequency pulses and collect the small signals induced by spin precession immediately thereafter. Furthermore, STRAFI requires the use of particular coil geometries. It must fit the cylindrical geometry as a classical MRI probe, but must have solid state NMR probe specifications. All these constraints fully justify the present study. Indeed, in this chapter after recalling the basics of NMR probe circuits, we presented a new probe design adapted to STRAFI. Based on this probe, it is possible to implement the STRAFI in auspicious circumstances as will be shown in the next chapter.

Bibliography

[AG79] D.W. Alderman and D.M. Grant. *J. Magn. Reson.*, 36(3):447–451, 1979.

[BPL89] L. Bolinger, M.G. Prammer, and J.S. Leigh. *J. Magn. Reson.*, 81(1):162–166, 1989.

[DBR+85] M. Decorps, P. Blondet, H. Reutenauer, J.P. Albrand, and C. Remy. *J. Magn. Reson.*, 65(1):100–109, 1985.

[Eng11] M. Engelhardt, 2011. `http://www.linear.com/designtools/software/`.

[Gar51] M.W. Garrett. *J. Appl. Phys.*, 22(9):1091–1107, 1951.

[GH91] D. J. Griffiths and M. A. Heald. *Am. J. Phys.*, 59(2):111–117, 1991.

[GM70] D.M. Ginsberg and J. Melchner. *Rev. Sci. Instrum.*, 41(1):122–123, 1970.

[Gro46] F.W. Grover. *Inductance Calculations*. D. Van Nostrand Company, Inc, 1946.

[HES+85] C.E. Hayes, W.A. Edelstein, J.F. Schenck, O.M. Mueller, and M. Eash. *J. Magn. Reson.*, 63(3):622–628, 1985.

[HT02] D.I. Hoult and B. Tomanek. *J. Magn. Reson.*, 15(4):262–285, 2002.

[Jav94] S. Javelot. *Réalisation d'un dispositif utilisant la RMN pour caractériser les écoulements multiphasiques*. PhD thesis, Université de Paris VI, 1994.

[Jef90] O.D. Jefimenko. *American Journal of Physics*, 58(8):505, 1990.

[KLLC88] L.P. Kuhns, M.J. Lizac, S.H. Lee, and M.S. Conradi. *J. Magn. Reson.*, 78(1):69–76, 1988.

[KSW11] M. Kamon, C. Smithhisler, and J. White, 2011. `http://www.fastfieldsolvers.com/`.

[MBK83] J. Murphey-Boesch and A.P. Koretsky. *J. Magn. Reson.*, 54(3):526–532, 1983.

[MLB06] J. Mispelter, M. Lupu, and A. Briguet. *NMR Probeheads for Biophysical and Biomedical Experiments*. Imperial College Press, 2006.

[MTM+02] R. McDermott, A.H. Trabesinger, M. Muck, E.L. Hahn, A. Pines, and J. Clarke. *Science*, 295(5563):2247–2249, 2002.

[Smy67] W.R. Smythe. *Static and Dynamic Electricity*. McGraw-Hill, 1967.

[Tro89] J. Tropp. *J. Magn. Reson.*, 82(1):51–62, 1989.

[ZP76] I. Zupančič and J. Pirš. *J. Phys. E: Sci. Instrum.*, 9(1):79–80, 1976.

Chapter 2

Stray Field Imaging

To perform a STRAFI experiment on superconductive magnets and achieve high resolutions the magnetic field must be uniform in the plane orthogonal to the gradient direction. Otherwise, the resonant slice is not planar and the profile resolution is compromised. After some theoretical considerations, we will explain how we measured the magnetic field and found the right position to perform STRAFI experiments with high resolution.

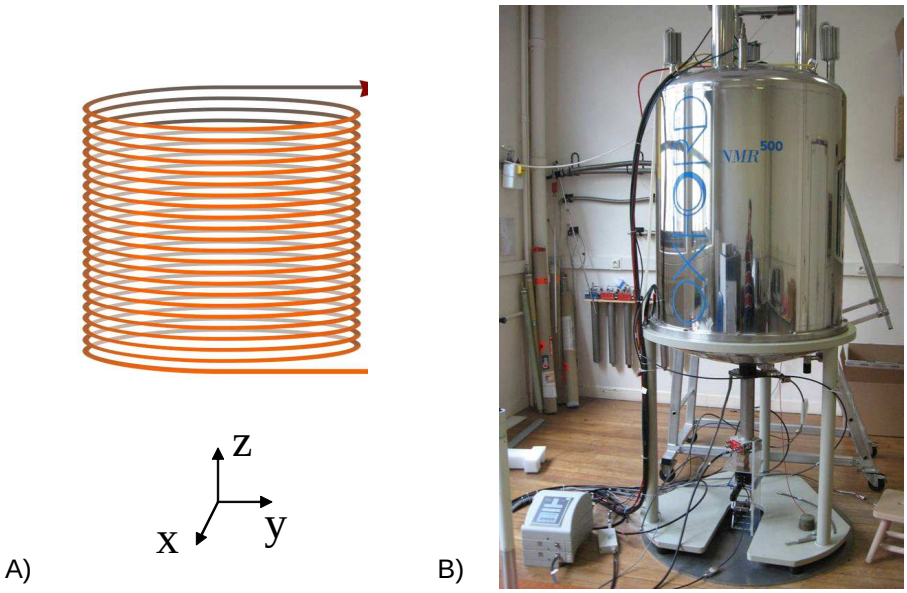

Figure 2.1: A) Sketch of a superconductive magnet. B) Picture of a STRAFI experiment on the 11.7 T superconductive magnet at the ESPCI. Note that the experiments conducted within the course of this thesis where actually performed on a 7 T magnet.

2.1 Introduction

2.1.1 A short introduction to MRI

Magnetic Resonance Imaging (MRI) [Lau73, MG74] is now used worldwide as a routine medical diagnostics tool. The attractiveness of this method is the use of three dimensional pulsed field gradients in order to scan k-space. After multi-dimensional Fourier transformation, three dimensional images are obtained with a typical resolution of 100 μm, and even in the range of 10 μm in the most favorable cases [UCC10].

2.1.1.1 Magnetic field and Larmor frequency

All Nuclear Magnetic Resonance arises from the following assertion. When placed in a magnetic field of strength B, due to a splitting in its energy levels known as the Zeeman effect, a particle with a net spin can absorb a photon of frequency $\nu = \omega/2\pi$. This frequency depends on the gyromagnetic ratio γ of the particle:

$$\nu = \frac{\omega}{2\pi} = \frac{\gamma B}{2\pi}. \tag{2.1}$$

The beauty of this equation is that the map between ω and B is bijective. This means that spins feeling the magnetic field B are only sensitive to the frequency ν.

2.1.1.2 Semi-classical description

In the case of independent spin $\frac{1}{2}$ nuclei, the motion of the ensemble of spins may always be described in terms of the precession of the spin magnetization vector $\vec{M}$. In such a model, $\vec{M}$ obeys the following equation:

$$\frac{\mathrm{d}\vec{M}}{\mathrm{d}t} = \gamma\, \vec{M} \times \vec{B} \tag{2.2}$$

The solution to this equation corresponds to a precession of the magnetization at a rate ω given by Eqn. 2.1. When the magnetization $\vec{M}$ is located in a plane xy orthogonal to the magnetic field $\vec{B}$, the solution $\vec{M}(t)$ of Eqn. 2.2 can be written as

$$\vec{M}(t) = M_0\big(\cos(\omega t) + \imath \sin(\omega t)\big) \tag{2.3}$$

In complex notation, this becomes:

$$\vec{M}(t) = M_0 \exp(\imath\omega t) \tag{2.4}$$

2.1.1.3 Space encoding

If one wants to encode space, it sounds natural to make the field vary with respect to space. Then, Equation 2.1 becomes :

$$\omega(\vec{r}) = 2\pi\nu(\vec{r}) = \gamma B(\vec{r}) \tag{2.5}$$

Thus, to excite the spins located at position $\vec{r}$, feeling the magnetic field $B(\vec{r})$, the radio-frequency pulse must have the frequency $\nu(\vec{r})$.

Obviously, to obtain a bijective relation between the resonance frequency and the space coordinate, one must also choose a bijective relationship between the magnetic field and the space coordinate. The simplest way to follow is to impose a linear relationship through a uniform gradient $\vec{G}$:

$$B(\vec{r}) = \vec{G}\cdot\vec{r} + \vec{B}_0 \tag{2.6}$$
$$\omega(\vec{r}) = \gamma\vec{G}\cdot\vec{r} + \omega_0 \tag{2.7}$$

Using a linear relationship between the space coordinate ($\vec{r}$) and the magnetic field has another advantage. A given bandwidth $\Delta\omega$ will always correspond to the same volume in space, wherever this bandwidth is centered. This is in part why the linear relationship is the most commonly used.

2.1.1.4 Conjugate space reconstruction

Let us consider the nuclear spins at position $\vec{r}$ in the sample, occupying a small element of volume $\mathrm{d}V$. If the local spin density is $\rho(\vec{r})$, then, there will be $\rho(\vec{r})\mathrm{d}V$ spins in this element. Following Eqn. 2.4, the NMR signal $\mathrm{d}S(\vec{G},t)$ arising from this element is:

$$\mathrm{d}S(\vec{G},t) \propto \rho(\vec{r})\mathrm{d}V\exp[\imath\omega(\vec{r})\,t] \tag{2.8}$$

For simplicity, we neglect the constant of proportionality in the previous equation and use a rotating frame at the frequency $\nu_0 = \omega_0/2\pi$ defined in Eqn. 2.7. In that case, the previous equation becomes:

$$\mathrm{d}S(\vec{G},t) = \rho(\vec{r})\mathrm{d}V\exp[\imath\gamma\vec{G}\cdot\vec{r}\,t]. \tag{2.9}$$

The signal amplitude $S(t)$ is obtained by integrating over the whole volume:

$$S(t) = \iiint \rho(\vec{r})\exp[\imath\gamma\vec{G}\cdot\vec{r}\,t]\mathrm{d}\vec{r} \tag{2.10}$$

This sum of oscillating terms has the form of a Fourier transformation. To make this more obvious, Mansfield [MG74] introduced the concept of a reciprocal space vector, $\vec{k}$, given by

$$\vec{k} = \frac{\gamma\vec{G}\,t}{2\pi} \tag{2.11}$$

Using this notation, Eqn. 2.10 can be rewritten

$$S(\vec{k}) = \iiint \rho(\vec{r}) \exp[\imath 2\pi \vec{k} \cdot \vec{r}] \mathrm{d}\vec{r} \tag{2.12}$$

Thus, the quantity of interest, $\rho(\vec{r})$, appears as the Fourier transform of the signal $S(\vec{k})$:

$$\rho(\vec{r}) = \iiint S(\vec{k}) \exp[-\imath 2\pi \vec{k} \cdot \vec{r}] \mathrm{d}\vec{k} \tag{2.13}$$

2.1.1.5 2D imaging

Equation 2.12 tells us that to obtain a full three dimensional image, the k-space must be sampled properly in the three directions. In practice, a conventional 2D image is obtained in two steps. First, a selective pulse allows to select only a slice of the sample. Second, the excited sample being reduced to a plane, the two dimensional k space remaining is sampled. Then, a 2D Fourier transformation is performed on the collected data and a 2D image of the slice is obtained.

Slice selection

The principle behind slice selection is explained by Eqn. 2.7. Slice selection is achieved by applying a one-dimensional, uniform magnetic field gradient during the period that the RF pulse is applied. A uniform magnetic field gradient oriented along the z direction allows to spread the resonance frequencies of spins along z:

$$\omega(z) = \gamma G_z \, z + \omega_0 \tag{2.14}$$

Then, the application of a sinc radiofrequency pulse of pulsation ω_0 and duration T allows to select the bandwidth $\Delta\omega(z) = 4\pi/T$ centered around ω_0 in the Fourier domain. This corresponds to the excitation of spins located in the slice Δz such as

$$\Delta z = \frac{\Delta\omega}{\gamma \, G_z} = \frac{2\pi\Delta\nu}{\gamma G} = \frac{4\pi}{\gamma \, G_z \, T}. \tag{2.15}$$

From this equation, two statements can be inferred. First, the higher is the gradient, the better is the resolution. Second, any phenomena increasing the intrinsic bandwidth $\Delta\omega$ will lead to a loss in resolution.

k-space sampling

The slice selection allows to excite only a plane of spins. At this point, Eqn. 2.12 is thus reduced to a two dimensional integral:

$$S(k_x, k_y) = \iint \rho(x, y) \exp[\imath 2\pi (k_x \, x + k_y \, y)] \mathrm{d}x\mathrm{d}y \tag{2.16}$$

The proper reconstruction of $\rho(x, y)$ requires the sampling of k_x and k_y given by

$$k_x = \frac{\gamma G_x \, t_x}{2\pi} \tag{2.17}$$

$$k_y = \frac{\gamma G_y \, t_y}{2\pi} \tag{2.18}$$

As $\vec{k}$ is the conjugate of the vector $\vec{r}$, high spatial resolution requires the sampling of high values of $\vec{k}$. The previous pair of equation shows that this can be achieved either by using high gradient values or long experimental times. This is an important issue when studying materials with short NMR signal lifetimes.

There are many MRI sequences which can be used to strategically fill the k-space. Some of them are reported in the book from Callaghan [Cal91, Blü00]. They all rely on the control of times $(t_x \, ; \, t_y)$ through the use of pulsed field gradients.

2.1.2 Solid state magnetic resonance imaging

2.1.2.1 From MRI to STRAFI

Although the technique presented in the previous section is very efficient in providing images of soft materials like living tissues [LKK$^+$01], the use of pulsed field gradients is less suitable in materials science. For example, when Mansfield and Grannell [MG74] used a test sample built from camphor with a proton resonance line width of 7.5 kHz, they were faced with a problem. To separate resonances arising from different spatial locations, they had either to use a very strong magnetic field gradient or the resonances had first to be narrowed. Mansfield and Granell followed the second option using multiple pulse line narrowing sequences. On the contrary, the STRAy Field Imaging (STRAFI) method originally proposed by Samoilenko [SAS88] circumvents some of the limitations of conventional MRI by using the high static magnetic field gradients surrounding conventional super-conducting NMR or MRI magnets.

2.1.2.2 Solids with short T_2's have limited resolution

In MRI, the spatial resolution Δz results from the frequency resolution $\Delta z = 2\pi\Delta\nu/\gamma G$ (Eqn. 2.15). In soft biological tissues, due to molecular motion, the relaxation times are long enough (typically of the order of the millisecond to the second) to allow resolutions of a few tens of micrometers. On the contrary, in rigid solids, the T_2's can be as short as a few microseconds, which limits considerably the sharpness of the bandwidth $\Delta\nu = 1/\pi T_2$. As matter of fact, for protons in rigid solids, the relaxation is dominated by the dipole-dipole interaction [PMRZ94]. One can show that in solid systems, the linewidth $\Delta\nu_{\text{dipole}}$, following the notations of Abragam [Abr60], is [MN98]:

$$\Delta\nu_{\text{dipole}} \approx \frac{\mu_0 \gamma^2 \hbar}{8\pi^2 r_{ij}^3} \approx \frac{1}{\pi \, T_2} \tag{2.19}$$

The subscript i and j denote the ith and jth nuclei which are separated by r_{ij}. Typically, $\Delta\nu_{\text{dipole}}$ varies from 1 kHz to 100 kHz. This directly impacts the resolution :

$$\Delta z_{\text{dipole}} = \frac{2\pi}{\gamma G}\Delta\nu_{\text{dipole}} \approx \frac{\mu_0 \gamma \hbar}{4\pi r_{ij}^3 G_z} \tag{2.20}$$

We shall notice that the relative effect of the dipolar coupling can be lowered by using large magnetic field gradients.

Effect of magnetic susceptibility on T_2

Despite dipolar coupling, the shortness of T_2 has multiple origins. The first one has to do with magnetic susceptibilities. In heterogeneous samples (like porous media), the magnetic susceptibility changes throughout the sample. This leads to localized sample-induced magnetic field gradients. Henceforth, the magnetic field gradient becomes the sum of the external gradient and the sample induced gradient which is not known. As a first consequence, Eqns. 2.7 and 2.15 break down and the local field distorsion leads to artefacts in the magnetic resonance image and thus limits the resolution to $\Delta z_{\text{suscept}}$. Callaghan [Cal90] calculated analytically this effect for simple geometries (glass sphere and cylinders with various orientation against the magnetic field).

Diffusion reduced the effective T_2

The second origin is linked to diffusion which leads to a reduce effective T_2. Indeed, the self diffusion of species inside a static gradient leads to a random phase shift of spins, which shorten drastically the T_2's [KRZ92, KRZ94] and thus the resolution. A specific case will be treated later at section 3.2.4.3.

Gradient requirements to overcome the loss of resolution in rigid solids

Let us assume that one wants to image a solid whose T_2 is 30 μs, with a resolution of 10 μm, which is close to the best resolution achieved in biological tissue. Equations 2.19 and 2.20 shows that the broadening in frequency is such that it requires the use of a 50 T/m gradient to be resolved. This is far from the typical gradient intensity obtained using pulsed field gradient systems (typically 10^{-1} T/m). Besides, this value must be reached within a time much shorter than T_2, which is again not achievable with conventional pulsed field gradient systems whose rising time is around 100 T/m/s. Due to these constraints, when imaging rigid solids, the classical way of filling the k-space as presented at section 2.1.1.5 using pulsed field gradient is not possible. Instead, large static gradients combined with slice selection imaging methods must be used. Such gradients can be found in the stray field surrounding superconducting magnets.

2.1.3 Principle

The beauty of this method resides in the simplicity of its principle: to take advantage of the strong field gradient of the edge of superconducting magnets to achieve high resolution through slice selection. The detailed principle is fully described by McDonald and al. [McD97, MN98, MBM06].

2.1.3.1 Slice selection

Stray field imaging is a sensitive slice magnetic resonance imaging technique developed by Samoilenko [SAS88]. As in conventional MRI slice selection, a radio frequency pulse is used to excite spins within a narrow slice of the sample orthogonal to the magnetic field gradient. This slice selection is the direct application of Equation 2.15. By adjusting the duration (and the shape) of the radio frequency pulse, a bandwidth $\Delta\nu$ is selected. Because of the univocal relationship between the bandwidth and the space through the gradient, a slice of thickness Δz is thus selected. The principle of slice selection is summarized in Figure 2.2.

2.1.3.2 Profile completion

Once a slice has been selected, the resulting magnetisation intensity is immediately recorded as a direct measurement of the total magnetisation in the slice. Following each measurement, as the gradient is static, the sample is mechanically moved through the sensitive slice by a step

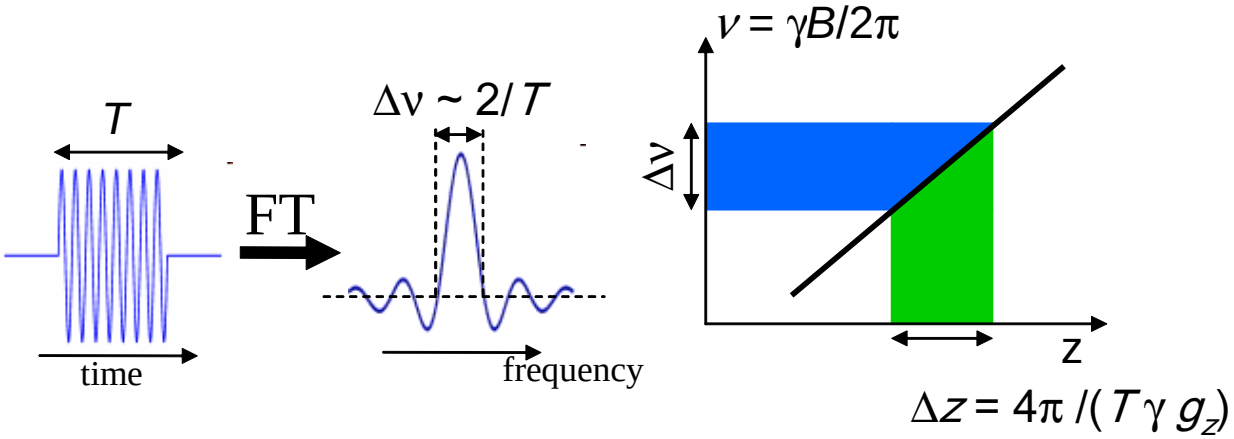

Figure 2.2: Principle of the slice selection. A pulse of duration T excites spins resonating within the bandwidth $\Delta\nu$, which, because of the gradient, are located within the slice Δz.

equal to the size of one slice and the process is repeated for the next slice (see Figure 2.3). In this way, a profile of the sample is built up in the gradient direction.

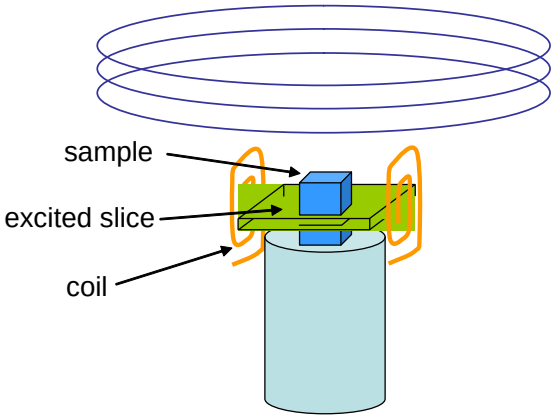

Figure 2.3: Sketch of the STRAFI experiment

2.1.4 Advantages and limitations

From a purely practical stand point, STRAFI appears like a simple inexpensive imaging tool which can be implemented on any existing solid-state spectrometer, even if some additional methods of precisely positioning the sample and synchronising the NMR acquisition and the sample adjustment are required. Besides the strong value of G_z, one of the main advantages, in comparison with any pulsed field gradient, is that the fringe field gradient is extremely stable. Whereas gradient pulses often require one to several hundred of microseconds to stabilize, which is a significant interval in comparison with the T_2's of most solids, no time is needed in STRAFI experiments and data acquisition is only delayed by the coil and receiver dead time. However, this fixed gradient is clearly not an advantage anymore as soon as T_2's become long enough to allow the use of pulsed gradients. Indeed, the fact that this method is coupled with a mechanical motion makes it much slower and very hard to implement in the case of imaging in more than one dimension.

2.1.5 Pulse sequences

While in conventional MRI the slice-selective gradient can be immediately followed by a refocusing gradient, this is obviously impossible in STRAFI. This problem combined with the fact that T_2^*'s are very short and the dead time is non zero, the FID following a pulse cannot be seen. Therefore, it is necessary to use multiple pulse sequences to create echoes to detect the signal away from the dead time.

2.1.5.1 The solid-echo train

The train is generated by the sequence $90^\circ_x - \tau - (90^\circ_y - \tau - echo - \tau)_n$, where 90°_x means a 90° pulse of relative phase along x and τ is a time interval (see Figure 2.4). First, one should notice that all pulses are of the same length so that the width of the selected slice is kept constant. Besides, one should notice that due to finite pulse lengths and the strong gradient, the nuclei experienced only approximate true 90° rotations. Indeed, most of the nuclei sees an effective magnetic field which is not in the xy plane. The recorded intensities are thus a complex function of the experimental parameters and exhibit strong amplitude modulations. For example, it is generally observed in STRAFI experiments that the second echo has a greater amplitude than the first. Benson et al. [BM95] and Bain and al. [BR96] quantitatively explained this modulation. For example, they showed that in absence of T_2 relaxation, the ratio of the intensities of the first four echoes is : $1 - 3/2 - 3/2 - 11/8$. Besides, in this sequence special phase cycling is necessary to subtract stimulated spin echoes.

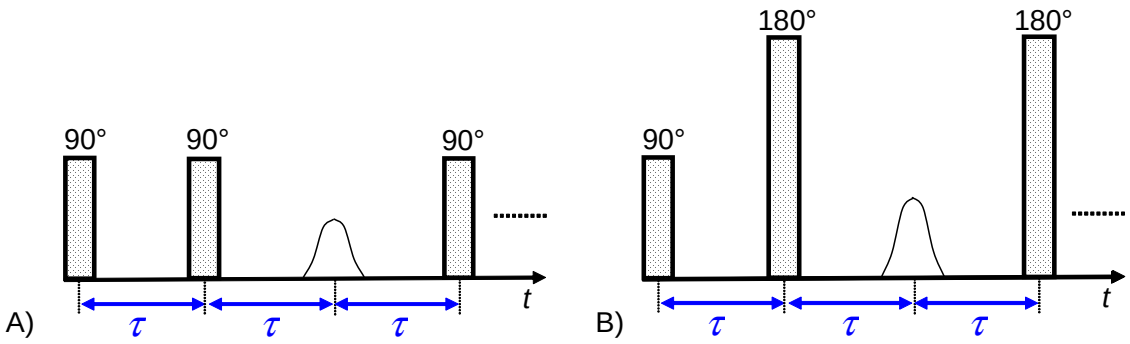

Figure 2.4: A) Sketch of the solid-echo train. B) Sketch of the CPMG echo train.

2.1.5.2 The CPMG train

When neglecting pulse width, the train is generated by the sequence $90^\circ_x - \tau - (180^\circ_{x,y} - \tau - echo - \tau)_n$ (see Figure 2.4). In this sequence, uniform slice selection is preserved by the use of a 180° pulse of twice the 90° amplitude, rather than twice its length. Thus, the frequency bandwidth of the two pulses is identical. Hürlimann [HG00], Song [Son02] and Goelman [GP95] have calculated analytical expressions for the CPMG echo amplitudes, including T_2 effects as well as diffusion. This is a robust method which can be applied even in systems with strong internal gradients. However, we shall notice that as in the previous sequence, the first echo of the train must be removed as its amplitude is much lower than the others.

2.2 Theoretical considerations

Because in STRAFI the profile is performed along a single axis and the G_z gradient is so strong, the resolution is actually not limited by the bandwidth of the pulse but mainly by the

curvature of the selected slice. As a consequence, the ideal slice must be planar. In what follows, this planar slice is called the STRAFI plane.

2.2.1 Existence of a STRAFI plane

The existence of a flat slice region is not immediately obvious but can be grasped as follows: near the axis of the magnet coil, the lines of constant field are concave close to the magnet whereas, they are convex further away (see Figure 2.5). By continuity, and because of the cylindrical symmetry of the field, an intermediate region must exist where the constant field lines are planar. This region can be precisely located by numerical simulations when the magnetic field is well known.

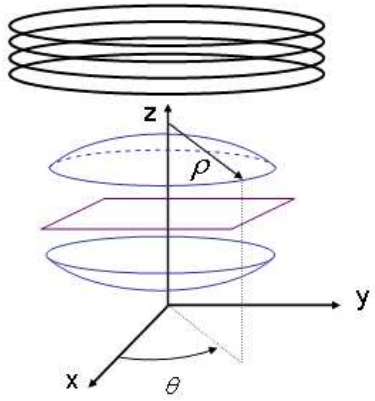

Figure 2.5: Sketch of isofield lines and the ideal plane (purple)

2.2.2 The single-loop case

A single loop of radius a travelled by a current I is first considered as a relevant example. Because of the cylindrical geometry, the magnetic induction can be decomposed in its axial and radial components H_z and H_ρ [Dur53]:

$$H_z(\rho,z) = \frac{I\,k}{4\pi\sqrt{a\,\rho}}\left[\tau_1(k)+\frac{a^2-\rho^2-z^2}{(a-\rho)^2+z^2}\tau_2(k)\right] \tag{2.21}$$

$$H_\rho(\rho,z) = \frac{I\,k\,z}{4\pi\,\rho\sqrt{a\,\rho}}\left[-\tau_1(k)+\frac{a^2+\rho^2+z^2}{(a-\rho)^2+z^2}\tau_2(k)\right] \tag{2.22}$$

where τ_1 and τ_2 are Legendre elliptic integrals of the first and second kind of modulus k:

$$k=\sqrt{\frac{4\,a\,\rho}{(a+\rho)^2+z^2}} \tag{2.23}$$

Figure 2.6 shows the numerical computation of the lines of constant field generated by a loop of radius a perpendicular to the z direction. In this figure, one can easily see that, at a distance of about z/a = 0.6 from the center of the coil, the curvature of the constant field lines changes sign. This means that near this position, the lines of constant field are flat and perpendicular to the z axis.

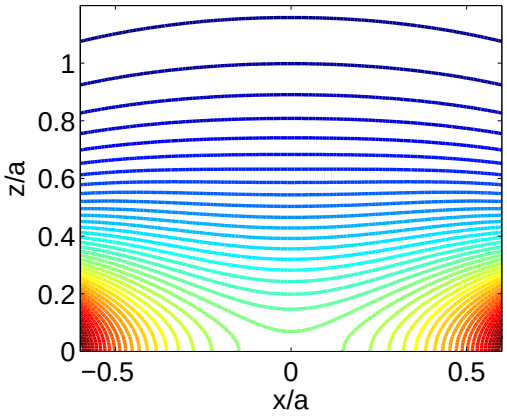

Figure 2.6: Map of equally spaced constant field lines induced by a loop computed according to equations 2.21 and 2.22.

2.2.3 Theoretical localization of the STRAFI plane

Beyond this simple example and in the general case, the position where this change of curvature takes place can be approached analytically through an expansion of the magnetic field around the z axis. The magnetic induction obeys the following Maxwell equation:

$$\vec{\mathrm{rot}}\vec{H} = 0 \tag{2.24}$$

Therefore, the magnetic induction can be derived from a scalar potential V^*. Close to the z axis, this potential can be developed in Taylor series near $\rho = 0$. Considering the cylindrical geometry and Equation 2.24, one can show that [Dur53]:

$$V^*(\rho,z) = V^*(0,z) - \frac{\rho^2}{4}\frac{\mathrm{d}^2V^*(0,z)}{\mathrm{d}z^2} + \ldots + \frac{(-1)^n}{(n)^2}\left(\frac{\rho}{2}\right)^{2n}\left(\frac{\mathrm{d}}{\mathrm{d}z}\right)^{2n}V^*(0,z) + \ldots \tag{2.25}$$

As $\vec{H} = -\vec{\mathrm{grad}}V^*$, the axial and radial components H_z and H_ρ of the magnetic induction can be easily obtained :

$$H_z(\rho,z) = \underline{H}(0,z) - \frac{\rho^2}{4}\frac{\mathrm{d}^2\underline{H}(0,z)}{\mathrm{d}z^2} + \ldots + \frac{(-1)^n}{(n)^2}\left(\frac{\rho}{2}\right)^{2n}\left(\frac{\mathrm{d}}{\mathrm{d}z}\right)^{2n}\underline{H}(0,z) + \ldots \tag{2.26}$$

$$H_\rho(\rho,z) = -\frac{\rho}{2}\frac{\mathrm{d}\underline{H}(0,z)}{\mathrm{d}z} + \ldots + \frac{(-1)^n}{n(n-1)}\left(\frac{\rho}{2}\right)^{2n-1}\left(\frac{\mathrm{d}}{\mathrm{d}z}\right)^{2n-1}\underline{H}(0,z) + \ldots \tag{2.27}$$

where $\underline{H}(\rho,z)$ is the modulus of the field. Note that by symmetry, $H_\rho(0,z) = 0$ and thus $\underline{H}(0,z) = H_z(0,z)$.

At this point, one should keep in mind that in NMR, spins are sensitive to the modulus of the magnetic field which makes them rotate at the Larmor frequency. Thus, to get a planar selected slice, the radial variation of the modulus of the field must be zero. It is often claimed that the highest resolution is obtained at the inflection point of the modulus of the magnetic field, namely at the position $z_{\mathrm{inflexion}}$ where:

$$\frac{\mathrm{d}^2\underline{H}(0,z_{\text{inflexion}})}{\mathrm{d}z^2}=0 \tag{2.28}$$

Equations 2.26 and 2.27 show this is not strictly true. Certainly, at this point, the z component of the induction is radially constant up to fourth order. However, at the inflection point, the absolute value of the first derivative (the first term of the radial component of the induction) is not only non zero but even at its maximum. Thus, one must consider the development of the square modulus of the induction:

$$H_\rho^2+H_z^2 = \underline{H}^2(0,z)+\rho^2\left[-\frac{1}{2}\underline{H}(0,z)\frac{\mathrm{d}^2\underline{H}(0,z)}{\mathrm{d}z^2}+\frac{1}{4}\left(\frac{\mathrm{d}\underline{H}(0,z)}{\mathrm{d}z}\right)^2\right] \tag{2.29}$$

$$+\frac{\rho^4}{16}\left[\left(\frac{\mathrm{d}^2\underline{H}(0,z)}{\mathrm{d}z^2}\right)^2+\frac{1}{2}\underline{H}(0,z)\frac{\mathrm{d}^4\underline{H}(0,z)}{\mathrm{d}z^4}-\frac{\mathrm{d}\underline{H}(0,z)}{\mathrm{d}z}\frac{\mathrm{d}^3\underline{H}(0,z)}{\mathrm{d}z^3}\right]+\ldots \tag{2.30}$$

To obtain the highest possible resolution on a large sample (ρ as large as possible), the second order term has to be zero. So, rather than trying to fulfill Eqn. 2.28, one should look instead for the position z_0 defined as the solution of the differential equation:

$$-\frac{1}{2}\underline{H}^2(0,z_0)\frac{\mathrm{d}^2\underline{H}(0,z_0)}{\mathrm{d}z^2}+\frac{1}{4}\left(\frac{\mathrm{d}\underline{H}(0,z_0)}{\mathrm{d}z}\right)^2=0 \tag{2.31}$$

where $\underline{H}(0,z)$ is a function of the magnet geometry.

2.2.4 Application to a single loop

This position can be easily identified for simple geometries where this function $H(0,z)$, that is the induction on the z axis, is well known. In our illustrative case of the simple loop, the induction on the loop axis is :

$$\underline{H}(0,z)=\frac{I\,a^2}{2(z^2+a^2)^{\frac{3}{2}}} \tag{2.32}$$

In that case, the solution to Eqn. 2.31 is:

$$z_0=\frac{\sqrt{10}}{5}a\approx 0.632\,a \tag{2.33}$$

which is significantly different from the location of the inflexion point:

$$z_{\text{inflexion}}=\frac{1}{2}a \tag{2.34}$$

Yet, for a single loop, the gradient at z_0 is still 95% of its maximum value located at the inflexion point. This means that by positioning the sample at z_0 instead of at the inflexion point, it is still possible to benefit from a large gradient but with a much better resolution.

2.2.5 Validity of the field expansion

The position of the STRAFI plane was obtained analytically for the particular case of a single loop. However, to derive Eqn. 2.31, one shall insist on the fact that no particular constraint was put on the geometry of the superconducting coil except the assumption of a cylindrical symmetry. Consequently, this equation stands even for more complex geometries like the ones of NMR or MRI superconducting magnets. It is thus concluded that the optimum position for a STRAFI experiment is not the inflexion point. Another important conclusion is that, to determine the position of the STRAFI plane, the sole requirement is the knowledge of the modulus of the magnetic field along the main axis of the magnet. This knowledge can be easily obtained experimentally by moving a sample along the z axis and measuring its NMR Larmor frequency.

2.3 Implementation

2.3.1 Introduction

In principle, any spectrometer equipped for broadband solid-state NMR may be adapted for the implementation of STRAFI. The superconducting magnet we used is the wide bore 7 Tesla magnet of a Brucker Avance III spectrometer. Only purely mechanical additions are required for sample positioning and manipulation. However, for convenience and to reduce the measurement time, it is necessary to synchronize the NMR acquisition and the sample adjustment. Besides, as in any experiment, it is good to have the possibility to process the data in real time in order to adjust the parameters without waiting for the end of the whole experiment. To achieve this, the hardware architecture must be modified.

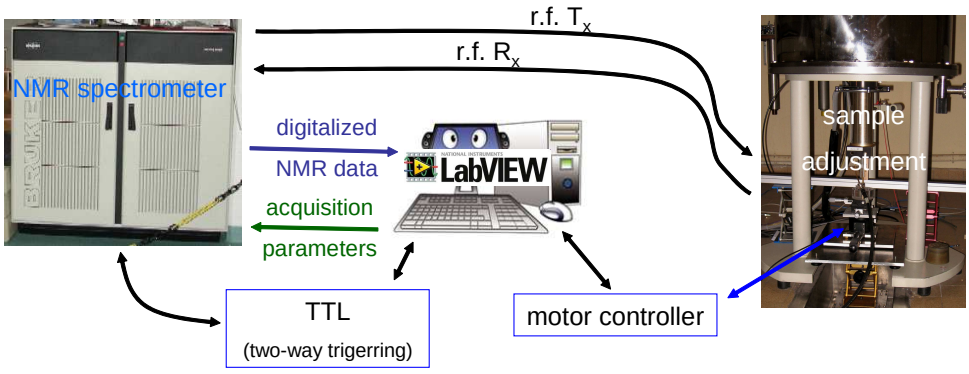

Figure 2.7: Sketch of the instrumental implementation to synchronize NMR acquisition and sample positioning.

2.3.2 Synchronisation of acquisition and sample adjustment

The Bruker Avance III™ spectrometer has TTL inputs and outputs triggers to communicate with outside hardware and thus allows the synchronization of the sample motion. A sketch of the synchronization set up is given in Figure 2.7. It is based on a Labview™ program which controls the motion of the stepper motor and the NMR acquisition. The NMR program was modified to wait for a TTL pulse before starting its acquisition and emit one when the acquisition is over. The Labview™ program runs on an external computer. It controls the motor displacement and triggers the NMR acquisition through an acquisition card. The complete procedure is sketched in Figure 2.8.

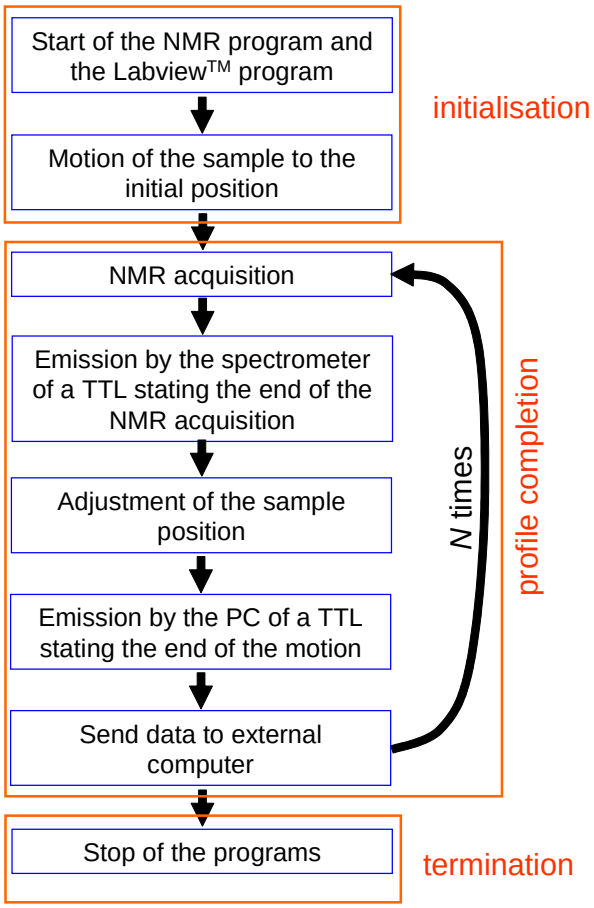

Figure 2.8: Steps of the synchronized procedure to acquire a $N + 1$ point profile.

2.3.3 Real-time data processing

The Bruker™ spectrometer is controlled through the Topsin™ software. Although this software is very powerful for classical NMR experiment (spectrum analysis, solid-state NMR, temperature monitoring...), it is clearly not adapted to STRAFI. Indeed, even simple but relevant operation like echo summing or echo integration cannot be performed with it. This means that the "correctness" of the choice of the experimental parameters cannot be assessed until the full experiment is completed and the data exported and processed by an external software, which is definitely not efficient and time wasting. To overcome this difficulty, a Labview™ program was developed to be able to control externally Topsin™ in order to collect and process the data in real-time (see sketch in Figure 2.9). Before each experiment, the meaningful parameters are converted into Topsin™ parameters. Then, during the measurement, Labview™ periodically collects data from the console, process and displays them. This is particularly important when the signal amplitude is very low and the dynamic sum of all the echoes is necessary to monitor the signal. Another example concerns the measurement of diffusion coefficient. In this experiment, one delay must be changed and this must be done manually in Topspin™ which is time wasting and risky when the number of measured point is large. With our procedure, the parameters required by Topspin™ are generated automatically and the real-time processing allows us to see the build-up of the diffusion curve in real-time as the experiment proceeds.

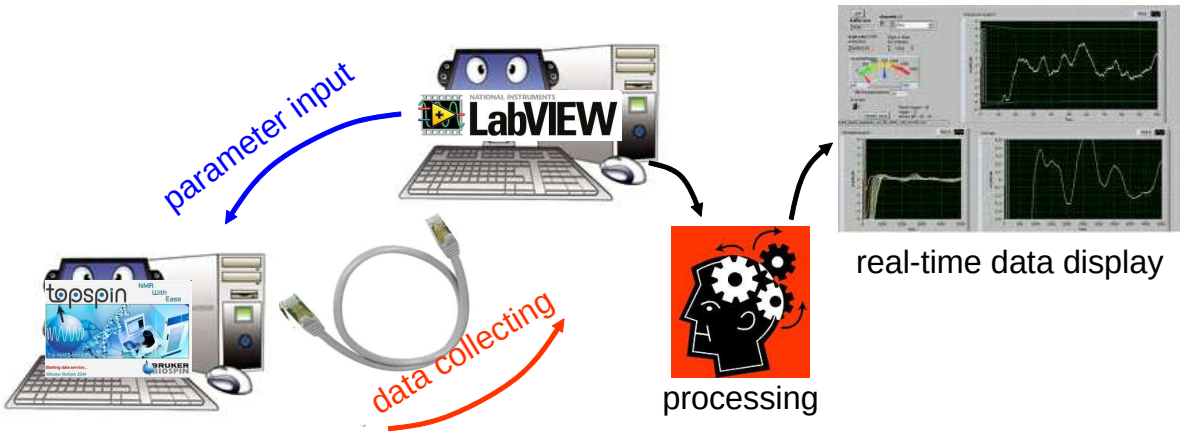

Figure 2.9: Principle of the system to control externally Topspin™ and process the data in real-time.

2.4 Mapping of the axial component of the field

2.4.1 Introduction

The first attempts to map the field were based on the use of a Hall effect sensor. However, this method was rapidly given up as it was too approximative. Instead, direct mapping by NMR was preferred. This method is the same as NMR spectroscopy but used in the other way around. In spectroscopy, the magnetic field is known and the frequency offset measured is interpreted in terms of chemical shift. Conversely, when the field is not known and a sample of a given species is moved inside the magnet, its change of frequency provides a map of the magnetic field. For spectroscopy, advanced electronics and methods to analyse the chemical shifts very precisely have been developed. Thus, one can benefit from them to map the field very finely.

2.4.2 Experimental setup

A commercial NMR static probehead was modified for that purpose (see Fig. 2.10). The resonator was replaced by a small horizontal solenoid. The tuning and matching circuit was modified in order to measure the magnetic field in the range of interest (40 to 280 MHz).

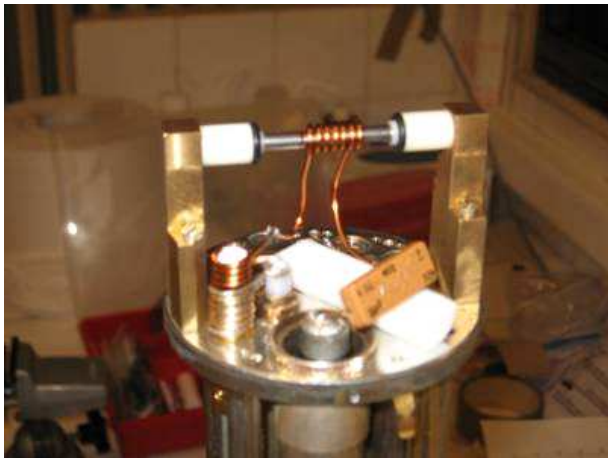

Figure 2.10: Picture of the NMR probehead used to map the magnetic field

The sample was a 2 mm^3 piece of polyethylacrylate (PEA). To measure the magnetic field, the following procedure was followed. A given excitation frequency was chosen. The spectrometer was set to emit a Hahn echo with a pulse length of 3 μs and an echo time of 53 μs. The repetition time was 0.5 second. No scan was accumulated and only the last acquisition was displayed (so-called **gs** mode) to follow in real time the change in amplitude of the NMR signal. Then, the probe was moved along the z axis until the maximum of proton the signal was reached. Then, the position was recorded, a new frequency was chosen and the procedure re-iterated. The results are compiled in Figure 2.11.

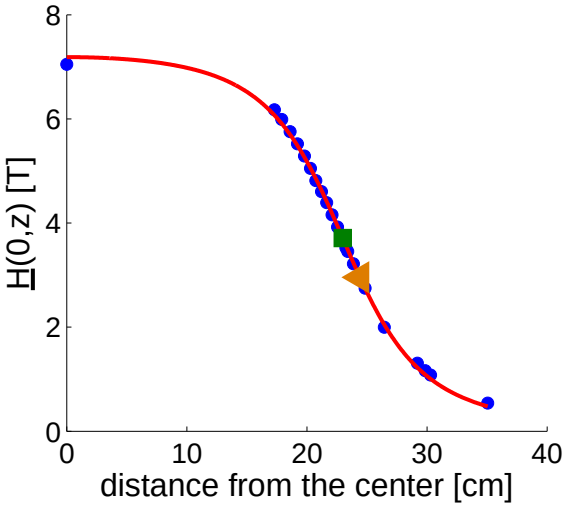

Figure 2.11: Magnetic field along the z axis of the superconducting magnet (points) and fitting with a solenoid model (line). The square represents the inflexion point and the triangle the theoretical position of the STRAFI plane of the solenoid model.

2.4.3 Theoretical determination of the STRAFI plane

According to the conclusion of the theoretical section above, the differential equation 2.31 must be solved to determine where in the stray field the resolution is the highest. For this purpose, the experimental values of the dependence of the modulus of the magnetic induction with the axial position must be reduced to a functional form. The exact geometry of a given superconducting magnet is generally not known by its users. Still, it is reasonable to approximate its magnetic induction by the one delivered by a simple solenoid magnetic induction. Accordingly the magnetic induction can be modelled by the following form [Dur53]:

$$\underline{H}(0,z) = \frac{I}{2p}\left[\frac{N\cdot p/2 + z}{\sqrt{a^2 + (N\cdot p/2 + z)^2}} + \frac{N\cdot p/2 - z}{\sqrt{a^2 + (N\cdot p/2 - z)^2}}\right] \tag{2.35}$$

Again, usually, the parameters I (the current), p (the path of the helix defining the solenoid), a (its radius) and N (the number of turns) are not known (see Figure 2.12). Furthermore, it must be understood that, the exact geometry of the superconducting magnet might not be a simple solenoid and that these parameters only represent effective physical quantities. They have to be obtained by fitting this functional form to the experimental values (see the solid line of Figure 2.11). Then, the solution to Eqn. 2.31 for this function effectively describing the induction was searched numerically. For the magnet of the present study, the STRAFI plane

was found at 24.4 cm from the center of the magnet (see Figure 2.11). The corresponding field strength and gradients at the STRAFI position were 2.97 T and 50.4 T / m respectively (to be compared to 3.7 T and 53.6 T / m at the inflexion point which was located at 23.0 cm).

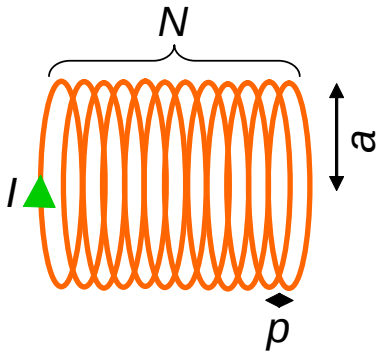

Figure 2.12: Sketch of a solenoid. The solenoid is defined by the parameter N (number of turns), a (the radius) and p the path of the helix defining the solenoid). A current I is flowing through it.

2.5 Mapping of the radial component of the field

Like in the previous case, proton NMR was used to map the field in the lateral direction and find the optimum STRAFI plane. The experimental procedure is however slightly more elaborate.

2.5.1 Experimental aspects

2.5.1.1 Experimental procedure

Starting from the approximate position of the STRAFI plane obtained as explained above, the radial component of the magnetic field was mapped by moving a thin sample in the radial direction and recording its change in frequency. The sample used was a 2 mm wide spot of beauty cream between two glass slides. The interest of this beauty cream is that the wetting properties of the glass by this emulsion results in the spontaneous formation of a film with a well-defined thickness of 20 μm over an extension of a few millimeters. The aim of this procedure is to record the curvature of the magnetic field in the radial direction (see Figure 2.5). If the sample is too close to the inside of the magnet, then the constant field lines are concave and we expect the resonance frequency to increase with the radial component (see Fig. 2.6). On the other hand, if we observe a frequency decrease, this means that the constant field lines are convex and that the sample is too far away from the center of the magnet. Thus, the shape of the recorded map tells us if the STRAFI plane must be search deeper inside the magnet or further out.

2.5.1.2 Experimental setup

The method described in the previous paragraph sounds promising but needs some experimental adjustments to be implemented. First, to see a change in frequency when the sample is moved, the excited slice must be much bigger than the size of the thickness of the sample. With an expected gradient of 50 T/m (ie $\approx$ 2 kHz/μm), 20 μm corresponds to 40 kHz. This means that to localize the sample, the selected slice must be at least 100 μm (200 kHz). Thus, the probe must be able to provide pulse length of 5 μs. Moreover, as the sample must be moved

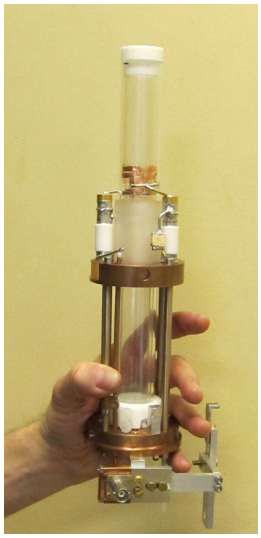

Figure 2.13: Picture of our STRAFI probe. The compatibility with the cylindrical geometry is preserved so the probe can be fixed and the sample move freely inside the glass tube.

both in the radial and the axial directions, the coil must be wide and open in the axial direction. Based on the study of the previous chapter, we used a home-made probe made of 2 saddle coils (see Figure 2.13) and fixed it against the superconducting magnet. The sample is placed at the top of a rod which transmits the motion from the stepper motor. In this particular design, the sample can be moved independently from the coil which is fixed at the STRAFI plane location. In addition to the stepper motor which provides the motion in the axial direction, two additional linear positioning stages were added to translate the rod in the x and y directions (see Figure 2.14).

As far as the pulse sequences used to map are concerned, we use a CPMG sequence in order to increase the signal to noise ratio. As we were interested in the frequency of the middle of the thin sample and not its internal structure, we used short echo time (40 μs) and a train of 256 echoes.

2.5.2 Radial mapping of the magnetic field

Figure 2.15 shows the result of the radial mapping of the field at various z positions around 24 cm from the center in the superconducting magnet. For each frequency, the thin sample was first positioned on the axis of the magnet. Then, it was radially moved and its frequency change recorded. Note that the curvature inversion between Figure 2.15 and Figure 2.5 is only due to a different representation. The position where the curvature is zero was located at 137 MHz which corresponds to a magnetic field of 3.20 T. There, the gradient was 47 T/m (2.01 kHz/μm). It is remarkable that this position was only 5 mm higher than the approximate position predicted by simply measuring the magnetic field along the z axis as exposed in the previous section. Even if the frequency where the isofields are planar is now determined, the curves were still tilted due to a misalignment of the the STRAFI plane with respect to the one within which the sample was moved.

2.6 Alignment of the sample

One of the key points of the STRAFI experiment concerns the resolution that can be obtained on a wide sample. Consequently, the next step to reach the ideal configuration depicted in Figure 2.3 is to correct the tilt between the sample holder and the STRAFI plane.

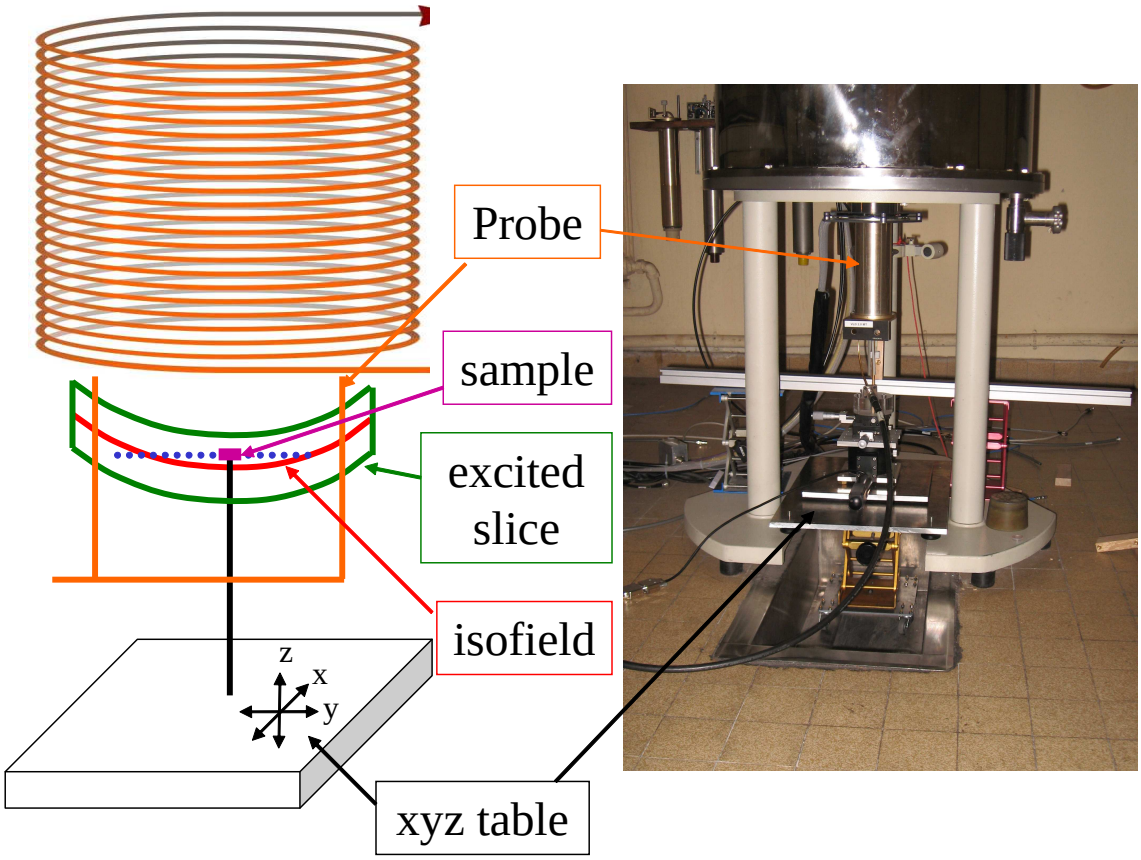

Figure 2.14: Sketch (left) and picture (right) of the setup for the mapping of the magnetic field

2.6.1 Experimental procedure

The working frequency is the one determined in the previous section to minimize the curvature of the field, namely 137 MHz. The method used to adjust the sample holder tilt is the following. A "spot" of cream (2 mm diameter and 20 μm of thickness) is placed off-center on a rotational stage with an axis roughly perpendicular to the STRAFI plane (see Figure 2.16). The spot is then brought within the STRAFI plane using a vertical stage. The signal of the spot is obtained with an 8 μs pulse duration which corresponds to an excited slice of 60 μm. It has been seen previously that changing the z position of the spot relative to the STRAFI selected slice induces a change of its resonance frequency. The frequency shift (in the kiloHerz range) as a function of the angle described by the rotational stage is then recorded. If there were no tilt between the plane of rotation of the sample and the STRAFI plane, the rotation would induce no z position variation of the spot and thus no frequency shift. The vertical stage axis, placed on a two axis goniometer was thus tilted to minimize the frequency dependence upon rotation of the sample. Proceeding iteratively, one should ideally reach a situation where the STRAFI plane fixed by the position of the superconducting magnet is aligned with the sample plane.

2.6.2 Effective alignment

The first steps of this procedure allows to reach rapidly resolution of a few tens of micrometers over one centimeter. To go further, the goniometers allowing to tilt the rod must be both precise and stable. Indeed, a resolution of 10 μm (ie less than 20 kHz of variation in the frequency) over

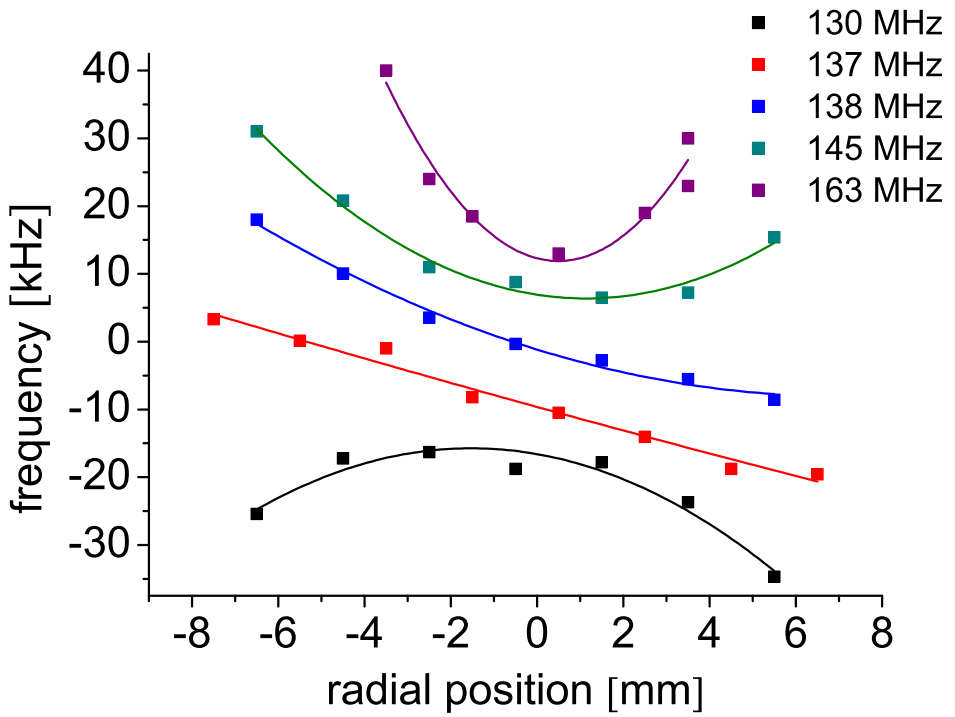

Figure 2.15: Radial mapping of the magnetic field. This plot clearly exhibits the change of sign in the curvature of the field below and above 137 MHz.

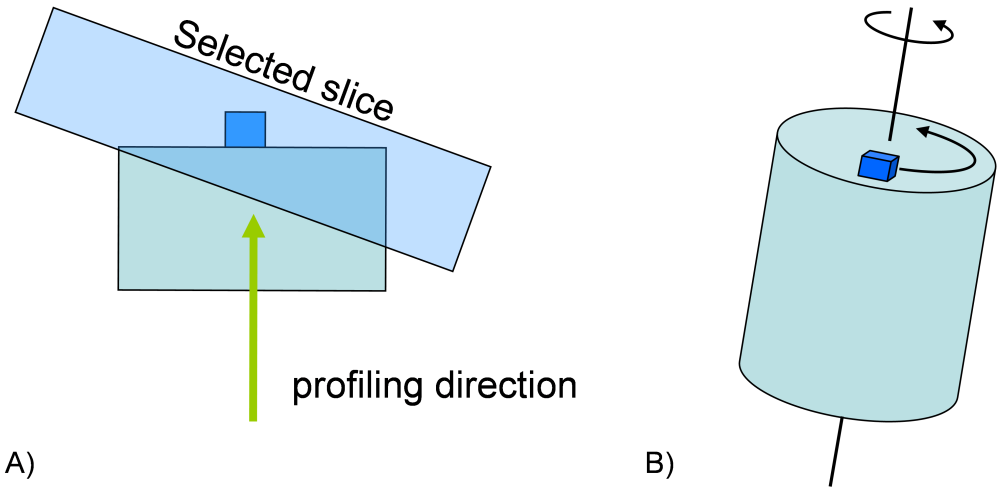

Figure 2.16: A) Sketch of the tilt between the sample plane and the STRAFI plane. B) Experimental method to measure the tilt between these two planes.

a one centimeter wide sample corresponds to a tilt of only 0.03° between the sample plane and the STRAFI plane.

The best resolution achieved is exhibited in Figure 2.17. In this figure, the frequency dependence of the spot moving on a circle of 2 cm is 15 kHz. The value of the gradient whose magnitude is 2.01 kHz/μm yields a resolution of 4.25 μm on a 1 cm wide sample. This resolution probably constitutes a limit beyond which other experimental complications arise, such as

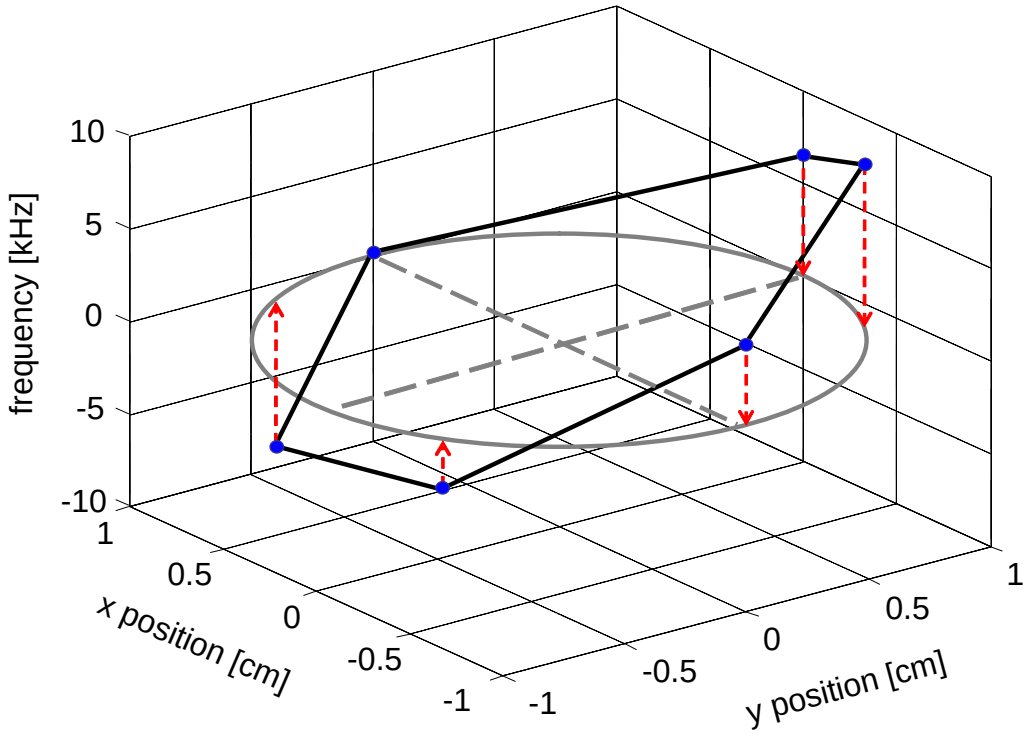

Figure 2.17: Frequency shift (kHz) of an off-centered cream "spot" (1 mm diameter, 20 μm thickness) versus the position of the sample holder. The position of the spot is one centimeter from the centre. The tilt angle between the STRAFI plane and the sample plane is 8.10^{-4} rad.

the precision of the goniometers or the thermal expansion of the experimental set up. The 30 centimeter long brass rod sees its length varying of about 6 μm when the temperature change of a single Celcius degree (dilatation coefficient of about $20 \cdot 10^{-6}$ K^{-1}).

2.7 Resolution test

2.7.1 Resolution with cream films

2.7.1.1 The advantage of cream films

The phantoms used to test the resolution were made of cream films pressed between glass plates. The interesting feature of these test samples is that the planarity of the glass plates is well below micrometric specifications. Furthermore, the thickness of the cream films is remarkably constant and reproducible as it is fully determined by its glass wetting properties, regardless of variations in the preparation procedure. The lateral extension of the films can be varied at will by controlling the amount of cream deposited between the glass plates. With this configuration, it is possible to check the resolution on a centimeter-wide sample.

2.7.1.2 Bilayer sample

Figure 2.18 (A) displays the profile of a bilayer sample made with three 1 cm diameter glass plates. A first off-centered cream "spot" layer (3 mm diameter) was pressed between the two first plates and a second 1 cm wide cream layer was pressed between the second and the third plate (Figure 2.18 (B)). The first peak corresponded to the wide layer. The intensities were not equal as they reflect the different volumes of the intersection of the STRAFI plane with

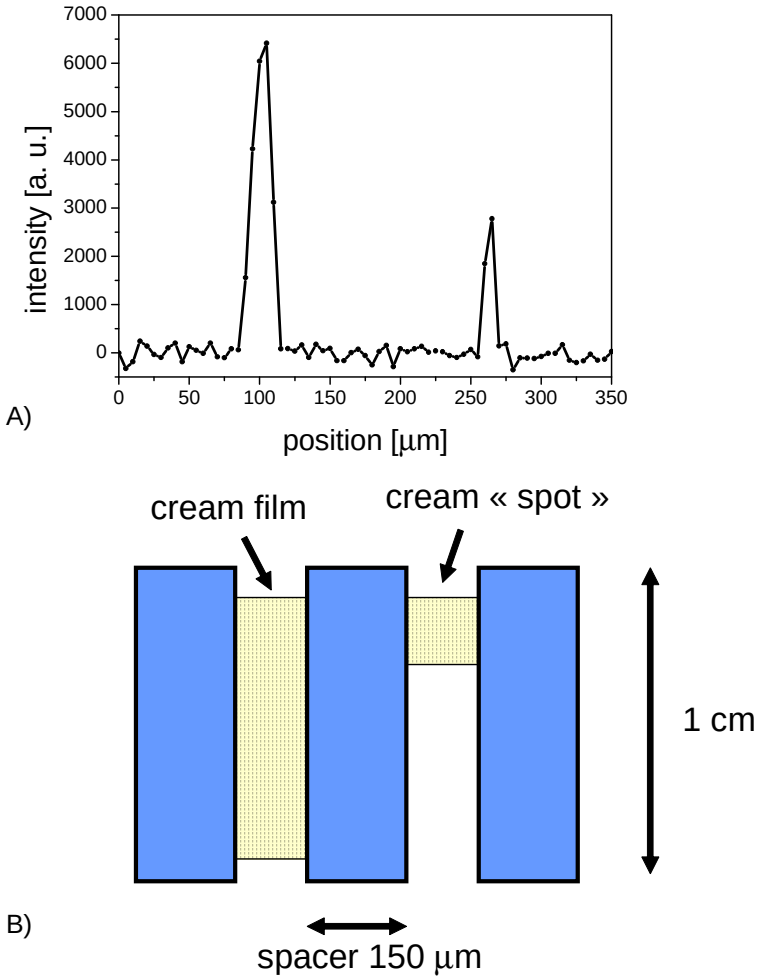

Figure 2.18: A) Step by step (5 μm step) profile of a bilayer phantom two cream films separated by a 150 micrometer glass plate. The NMR sequence is a CPMG detection train of 512 echoes with an echo time of 49 μs. The repetition time was 0.5 s and 64 scans were accumulated for each of the 70 points of the profile leading to a total experimental time of 37 min. B) Schematic (not to scale) of the bilayer phantom profiled in (A). The first film is 1 cm wide.

the successive layers of the sample, and thus depended on the diameter of the two layers (1 cm versus 3 mm). To acquire the profile, the z-axis motor was moved step by step in increments of 5 μm . Taking into account the magnitude of the gradient (50.4 T/m), the square pulse of duration 100 μs excited a 5 μm thick slice. The two layers are separated by a distance of 150 μm corresponding to the thickness of the intermediate glass plate. Each cream layer is 10 μm thick. In Figure 2.18 (A), one can see that the resolution defined as the thickness of the sample interface is 5 μm, which is consistent with the resolution expected from the map of Figure 2.17.

2.7.1.3 Resolution with thicker samples

It must be recognized that profiling with a step by step motion has the definite advantage of allowing to profile a sample not only with very small steps but also over a large range (a few cm). As an illustration, the profile of a sample made of as many as seven 1 cm wide layers of cream films separated by 150 μm thick glass slides was recorded (Figure 2.19 A). It was done step by step with a step size of 10 μm and over a range of 3 mm. Figure 2.19 B displays a more precise profile of part of the multilayer sandwich at the position 21.18 mm, which was obtained with a

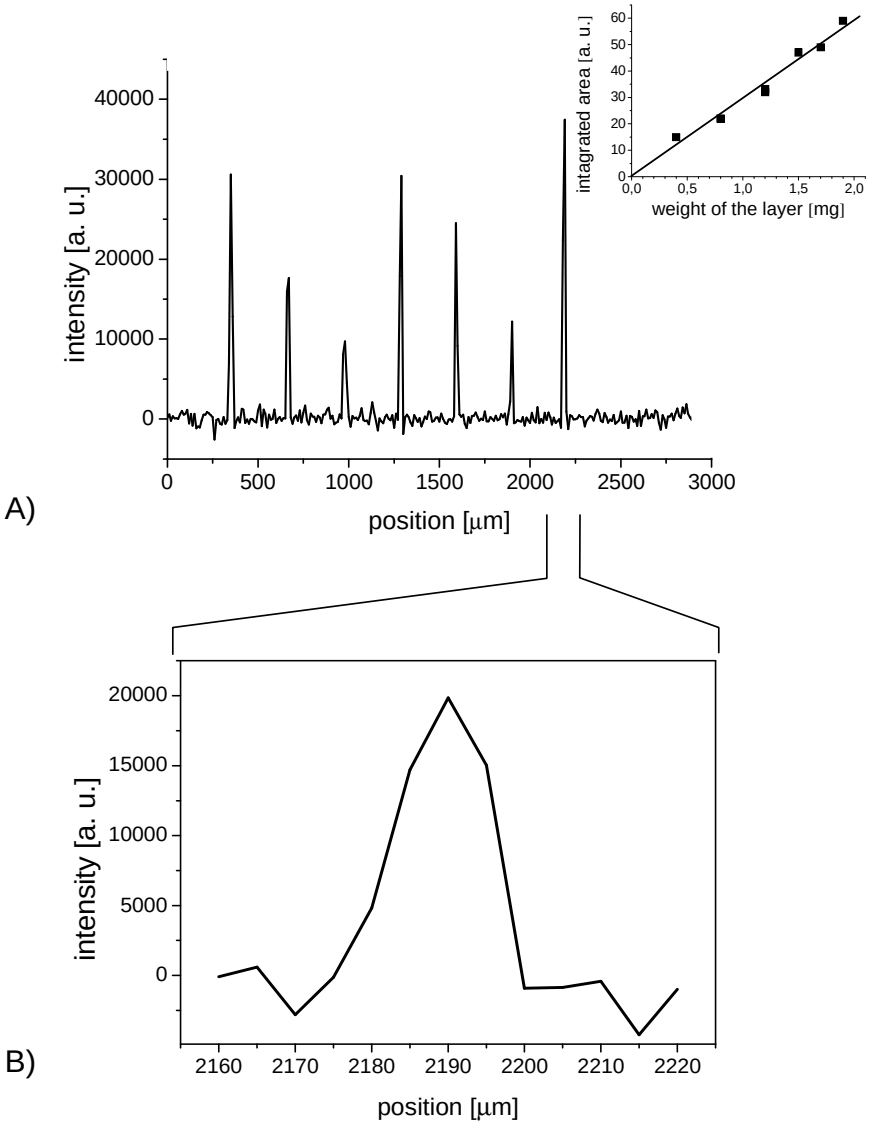

Figure 2.19: A) Step by step profile of a thin film cream multilayer. Each 1 cm wide film is separated by a glass plate of 150 μm thickness. The step is 10 μm. Inset : Correlation between the integrated area of each peak and the weight of the corresponding cream layer. B) Step by step profile of the 7th peak of the multilayer. The step size is 5 μm .

finer step size of 5 μm and a pulse duration of 100 μs . It is thus shown that it is indeed possible to obtain a complete profile on a large scale while maintaining, when needed, a resolution of 5 micrometers. Let us emphasize that the amplitude variations were not artifacts but reflected the actual lateral extensions of the films. The amount of cream in each layer can be appreciated by measuring their weights. As shown in the inset of Figure 2.19 A, for each peak, the integrated intensities correlated well with the weight of the corresponding layers.

2.7.2 Combining STRAFI and Fourier imaging

To check that the resolution obtained by Fourier Imaging is indeed similar to the one obtained by step-by-step motion, the corresponding experiment was performed on the same type of bilayer cream sample. Again, in this experiment, the sample was kept at a fixed position in the STRAFI plane in contrast to all previous results obtained by moving the object with a stepper motor. The

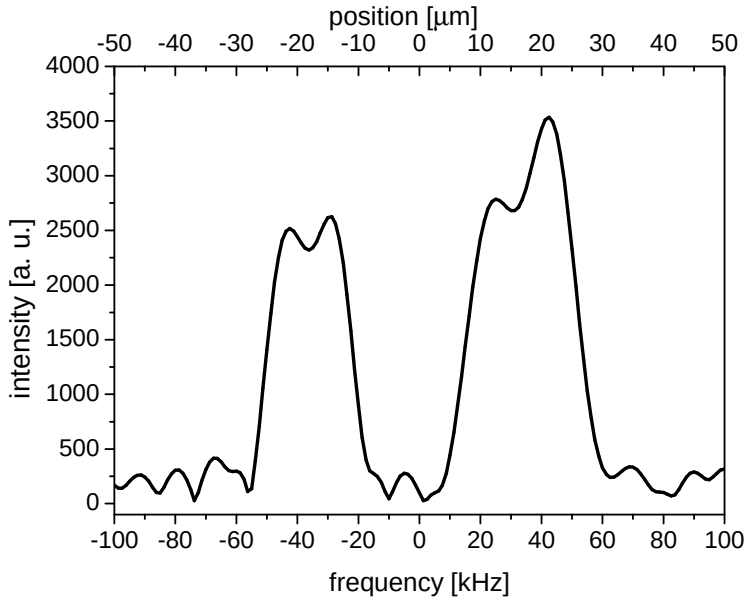

Figure 2.20: Profile of a bilayer made of two thin films separated by a thin spacer of 20 microns. This profile was obtained by computing the Fourier transform of the sum of the 256 first echoes of a CPMG detection train. The pulse length was of 4 μs and the repetition time 0.5 s. To avoid any effect of the acquisition window on the resolution, the acquisition time was set to 200 μs leading to a resolution of 5 kHz (2.5 μm) in the Fourier domain.

limitation of the observation window of the Fourier transform profile arises from the intensity of the gradient. With a gradient magnitude of 2.01 kHz/μm, a hard pulse of 4 μs excites a slice of 125 μm. This allows the observation of a bilayer made of two thin films separated by a thin spacer of 20 μm. Zero-filling up to 1024 points followed by a Fourier transformation provided the profile of Figure 2.20. Compared to the other plots, the profile appears smoother, which is an effect of the zero-filling. Then, it is easier to deduce the resolution from the derivative of the curve. A width of 10 kHz was obtained in the derivative of the profile, corresponding to a resolution of 5 μm . It is thus verified that the same 5 μm resolution can be obtained, either with soft pulses and step-by step sample motion, or by hard pulses and Fourier Imaging.

2.8 Resolution vs T_2

STRAFI has been developed to image fast relaxing species which cannot be observed by classical MRI. Here, we push the limit of STRAFI and show that a resolution of 5 μm can be achieved by correctly mapping the field and aligning the sample. However, the price to pay is the use of long pulses (to reduce the slice thickness) or long acquisition times (to obtain spectral/spatial resolution), which limits the shortness of T_2's which can be observed.

2.8.1 Intrinsic T_2 limitation

As presented previously, the observation of a slice with a resolution ϵ requires a frequency resolution of at least $\gamma G\epsilon$. With a gradient $G = 50$ T/m and $\epsilon = 5$ μm, this correspond to a frequency resolution of 10 kHz.

However, the NMR signal is intrinsically limited by the relaxation time T_2. This means that spectra are inevitably convoluted by a Lorentzian with Full Width at Half Maximum (FWHM) of $1/\pi T_2$, leading to a loss of resolution. The plot of Fig. 2.21 displays the resolution which can

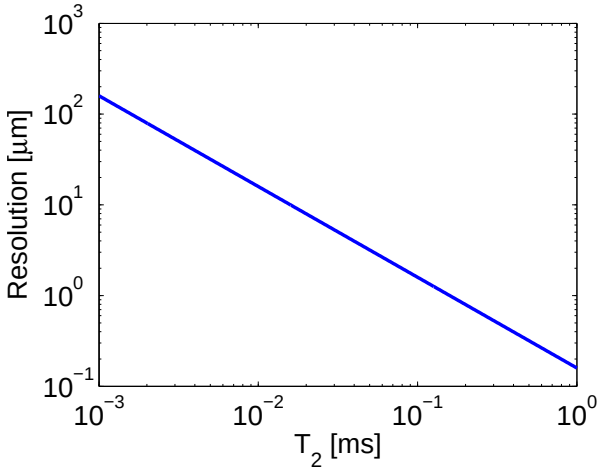

Figure 2.21: Intrinsic resolution versus T_2 assuming a gradient of 50 T/m.

theoretically be achieved for a given T_2. In particular, T_2's smaller than 32 μs would lead to a broadening larger than a frequency resolution of 10 kHz and so to a loss of resolution.

2.8.2 Pulse sequences for high resolution

2.8.2.1 Introduction

In the previous section, we showed that the relaxation time T_2 limits the resolution as it leads to a broadening in the Fourier domain. However, in STRAFI, the NMR signal cannot be measured directly and it is necessary to use echo pulse sequences. This significantly increases the effective minimum T_2 which can be measured for a given resolution. Here, we present a few pulse sequences designed for the high resolution measurement of fast relaxing materials. In this part, we will assume that the resolution one wants to achieve is 5 μm. Besides, we impose that the pulse sequence including the acquisition time cannot last larger than T_2. Finally, all dead times are neglected in this theoretical study.

2.8.2.2 Thin slice selection

In STRAFI, the resolution is usually directly given by the thickness of the selected slice (Eqn. 2.15). Thus, a pulse length $T = 100$ μs is required to excite a 5 μm thick slice. If we take as a rule of thumb that the shortest achievable time between pulses cannot be shorter than the pulse length, at best the top of the echo occurs $4 \times T$ after the beginning of the Hahn echo sequence (see Fig. 2.22A). As a consequence, T_2 must be at least 400 μs to be measured with this resolution and this sequence.

2.8.2.3 Long acquisition time

As we have seen in the paragraph 2.7.2, that instead of making thin slices, it is possible to make short pulses and use an acquisition time t_{acq} long enough (100 μs in our case) to achieve the 5 μm resolution by performing a Fourier transformation of the echo (see Fig. 2.22B). To achieve this, it is necessary to have a delay of $t_{acq}/2$ between the two pulses. Finally, by neglecting the pulse widths, $1.5 \times t_{acq}$ separates the first pulse and the last acquired point, which corresponds to 150 μs. Thus, using this sequence, 5 μm resolution is achieved only if T_2 is not shorter than 150 μs.

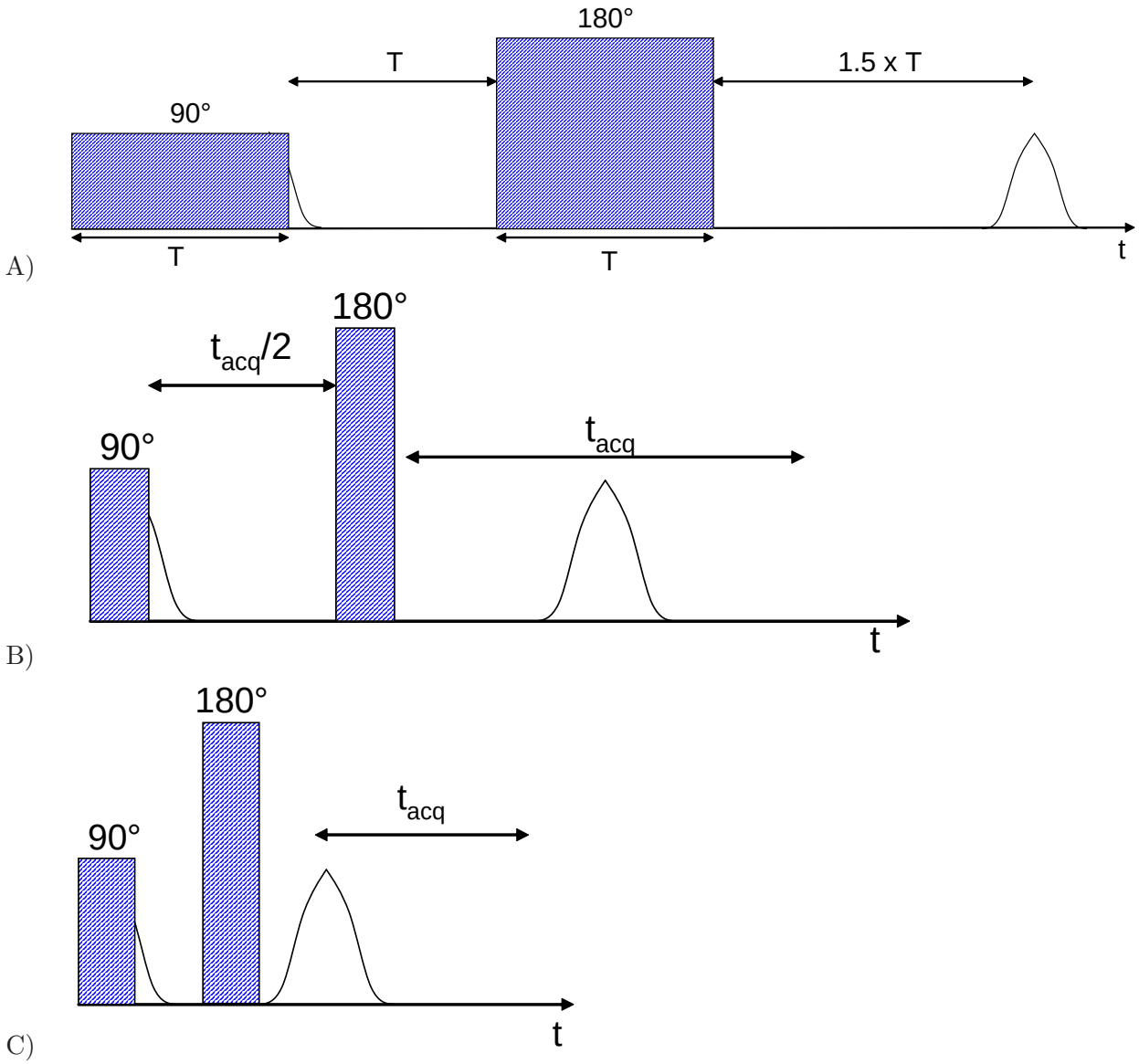

Figure 2.22: A) Pulse sequence for thin slice selection. B) Pulse sequence for long acquisition time. C) Pulse sequence for half echo recording.

2.8.2.4 Using echo symmetry

The duration of the pulse sequence can be further lowered from the previous sequence by noticing that k-space is symmetric. Thus, only half of this space needs to be filled. This is a general property of real functions. Their Fourier transform is symmetric. This means that only half of the echo is needed to achieve the same resolution. So, the previous sequence can be reduced to the one displayed on Fig. 2.22C. In this case, the acquisition lasts t_{acq} but as the echo is completed by symmetry, the effective acquisition time is $2 \times t_{\mathrm{acq}}$. Thus, using this sequence, if one considers that the delay between the two pulses is 5 μs (the order of magnitude of the dead time) and that $t_{\mathrm{acq}} = 50$ μs, a T_2 as short as 60 μs can be measured with a resolution of 5 μm. A comparison of the three sequences presented here is given in Figure 2.23.

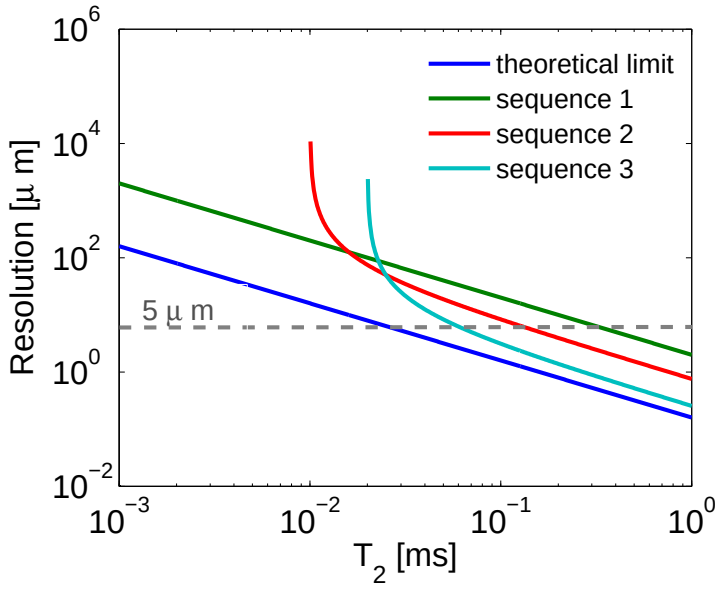

Figure 2.23: Resolution versus the shortest T_2 which can be achieved with the corresponding resolution. We compare the theoretical limit with the three sequences we proposed.

Conclusion

In this chapter, we presented the implementation of the STRAFI experiment on a standard solid state NMR system. First, we showed through a theoretical calculation how the knowledge of the magnetic field profiles along the axis of the magnet allows us to locate the STRAFI plane which provides the best resolution. Then, we proposed a method to localize finely this plane. This plane is found at a magnetic field corresponding to a resonance frequency of 137 MHz. A resolution better than 5 μm over 1 cm is then achieved by implementing an alignment procedure of the sample plane against the STRAFI plane. The main drawback of this experimental setup is that the STRAFI plane is found to be inside the bore of the superconducting magnet. This means that samples must fit a 20 mm wide cylinder. Thus, although materials with T_2 values as short as a 60 microseconds can be imaged with a resolution better than 10 μm, measurements are necessarily ex-situ. To overcome this difficulty, in parallel with STRAFI, we developed low field single-sided NMR sensors. These sensors are mobile and allow in-situ measurements. Thus, a wall does not need to be cut and can be scanned as such. The price to pay with these tools is a lower sensitivity of fast relaxing species. However, they provide valuable information which can be completed by STRAFI. The next chapter presents the development and the implementation of single-sided sensors for drying and dessication studies of mortar pastes.

Bibliography

[Abr60] A. Abragam. *Principles of Nuclear Magnetism*. Oxford Science Publications, 1960.

[Blü00] B. Blümich. *NMR Imaging of Materials*. Oxford Science Publications, 2000.

[BM95] T.B. Benson and P.J. Mcdonald. *J. Magn. Reson., Ser. B*, 112(3):17–23, 1995.

[BR96] A.D. Bain and E.W. Randall. *J. Magn. Reson., Ser. A*, 123(1):49–55, 1996.

[Cal90] P. T. Callaghan. *J. Magn. Reson.*, 87(2):304–318, 1990.

[Cal91] Paul T. Callaghan. *Principles of Nuclear Magnetic Resonance Microscopy*. Oxford Science Publications, 1991.

[Dur53] E. Durand. *Electrostatique et Magnétostatique*. Masson & Cie, 1953.

[GP95] G. Goelman and M.G. Prammer. *J. Magn. Reson.*, 113(1):11–18, 1995.

[HG00] M.D. Hürlimann and D.D. Griffin. *J. Magn. Reson.*, 143(1):120–135, 2000.

[KRZ92] P. Kinchesh, E.W. Randall, and K. Zick. *J. Magn. Reson.*, 100(2):411–415, 1992.

[KRZ94] P. Kinchesh, E.W. Randall, and K. Zick. *Magn. Reson. Imaging*, 12(2):305–307, 1994.

[Lau73] P.C. Lauterbur. *Nature*, 242:190–191, 1973.

[LKK+01] S.C. Lee, K. Kim, S. Kim, J.H. Yi, S.W. Kim, K.S. Ha, and C. Cheong. *J. Magn. Reson.*, 150(2):207–213, 2001.

[MBM06] J. Mitchell, P. Blumler, and P.J. McDonald. *Prog. Nucl. Magn. Reson. Spectrosc.*, 48(4):161–181, 2006.

[McD97] P.J. McDonald. *Prog. Nucl. Magn. Reson. Spectrosc.*, 30:69–99, 1997.

[MG74] P. Mansfield and P.K. Grannell. *J. Phys. C: Sold State Phys.*, 7(24):L457–L462, 1974.

[MN98] P.J. McDonald and B. Newling. *Rep. Prog. Phys.*, 61(11):1441–1493, 1998.

[PMRZ94] K.L. Perry, P.J. McDonald, E.W. Randall, and K. Zick. *Polymer*, 35(13):2743–2748, 1994.

[SAS88] A.A. Samoilenko, D.Y. Artemov, and A.L. Sibel'dina. *JEPT Letter*, 47(7):417–419, 1988.

[Son02] Y.-Q. Song. *J. Magn. Reson.*, 157(1):82–91, 2002.

[UCC10] J.F.P. Ullmann, G. Cowin, and S.P. Collin. *J. Morphol.*, 271(12):1446–1456, 2010.

Chapter 3

Mobile Single-Sided MRI

As both the sensitivity and the spectral resolution increase with the magnetic field, magnets tend to grow larger and larger. As a consequence, the relocation of these high field magnets is nearly impossible and samples necessarily need to be brought to the magnet. This is acceptable for samples that can be easily moved but for many application, this is not the case. Thus, there is a need for mobile tools which can be brought on site to perform the measurements. A typical example is the oil industry. Well-logging tools are required to evaluate the amount of oil which can be extracted from a geological formation.

Figure 3.1: Picture of the NMR-MOUSE™ used to scan the lock of Hohenwarthe (Germany).

The second drawback of high-field NMR tools is the fact that they can measure only samples which fit into the magnet. This comes from the fact that it is much easier to create homogeneous magnetic field in a closed magnet geometry. To enter into the bore of the magnet, samples must have a reasonable size compatible with the geometry of the magnet. Otherwise, they must be cut and the non-destructive aspect of this technique is lost. For example, walls cannot be scanned as they clearly do not fit whatever size a close geometry magnet could have. To overcome this difficulty, single-sided tools have been developed. The original idea was proposed by Jackson et al. [JBH80]. It consisted in generating a magnetic field relatively homogeneous outside the magnet. Then, the geometry was improved to fit particular applications such as the detection of moisture in building materials, soil and food. The single-sided tool family can be divided into two. The first is known as "sweet spot" tools. The idea is to generate a remote homogeneous field away from the surface of the magnet [CJ80, FJ02, MMCB05, PH02, MCD$^+$06, PCB07]

with a sub-ppm resolution to measure NMR spectra. The second makes use of a field profile which varies linearly with the distance from the sensor surface [BPC08, GAB+99]. The NMR-MOUSE™ belongs to the second family.

It exists several single-sided magnets designed to generate a magnetic field with an inhomogeneity dominated by a constant gradient G_0 perpendicular to the magnet surface [BPC08]. Considerable effort has been spent to improve the uniformity of this static gradient by tailoring the magnet geometry. So far, the best performance has been obtained with arrays generating large G_0 values [Pra03, PCB05, RLS+05, CCH06]. An example of this is the Profile NMR-MOUSE™, which uses a magnet constructed from an array of blocks that includes variables of control that can be adjusted to cancel the lateral field variations at a particular distance from the sensor surface. Although a large static gradient is convenient to achieve high resolution even in fast relaxing materials, it limits the thickness of the slice that can be excited to just a few hundred micrometers. The reason for this is the finite bandwidth that an rf circuit can excite ($\sim$ 200 kHz). Several attempts have been implemented to profile a larger depth range. One possibility is to reduce the quality factor Q of the rf circuit simply to excite a broader bandwidth [RLS+05]. This however, is achieved at the expenses of considerable sensitivity and rf power. Another alternative is to use a mechanical [PCB05, MMM+07] or electronic [Pra03] slice repositioning system. The price paid in these cases is an increase of the experimental time because the profile is measured point by point. Furthermore, the mechanical aspect weights down the experimental set-up.

Although the approach described above has demonstrated to be the most efficient one to reach large depths and maximum resolution, it has some disadvantages when it is applied to profile just a few millimeters at medium resolution. This situation is faced, for example, when open sensors are used to profile human skin, where the region of interest lies within the first two millimeters from the body surface, and a resolution better than 20 to 30 μm does not reveal finer structural details because the wavy pattern observed at the layer interfaces smoothes the profile. In such a case the experiment would considerably benefit from a sensor generating a gradient low enough to allow full excitation of the region of interest, but still offering reasonable uniformity to achieve the required depth resolution. First, the precise positioning system needed to move the sensitive slice across the object can be eliminated. Second, as all the points in the profile are acquired simultaneously in one excitation shot, without moving the sensor, the measurement time can be shortened. Third, measurements of liquid-like samples performed in a low gradient are less affected by molecular diffusion, usually responsible for considerable shortening of CPMG signals.

In this chapter, we first present the NMR-MOUSE™ we used to follow the drying and hydration of cementitious materials (see chapter 4). Then, we detail the building of a new sensor based on a reduced, but highly uniform static magnetic field gradient. This sensor allows us to profile a sample over 2 mm with a resolution of 25 μm without any repositioning system.

3.1 NMR-MOUSE™

3.1.1 Introduction

Single-sided sensors can be seen as low field version of STRAFI (see chap. 2). The strength of the static gradient generated by single-sided magnets is comparable to the one in STRAFI experiments (a few tens of T/m typically), but the lateral gradients of small magnets are comparable to the main gradient and result in a poor resolution. Several attempts have been made to increase the gradient uniformity over a large depth range [Pra01, CB03, PCB04, Pra03], by tailoring the magnet geometries. However, a resolution better than half a millimeter was hard to achieve. The idea of these magnets was to generate planes of constant field strength over large depth range. Following this philosophy, slices can be detected at various heights simply by electronically switching the tuning frequency. However, this apparently simple approach has intrinsic limitations. First, as the bandwidth of the coil is limited (200 kHz typically), the tuning frequency of the coil must vary during the experiment. For example, Prado [Pra03] adopted the strategy of using relays to change the tuning frequency of the coil. Second, a systematic bias is introduced as longitudinal decay times may be frequency dependent and when the static field varies because of diffusion through the gradient. Therefore, people went back to the original technique where a flat sensitive slice is generated at a single depth. Then, the sample profile is completed by changing the relative position of the sample with respect to the sensitive slice, keeping the excitation frequency constant [PCB05].

Among the existing single-sided sensors using this principle, one of the first is the MObile Universal Surface Explorer (MOUSE) [ESBB96, BBE+98]. The original design consisted of two semicylindrical permanent magnets embedded in a iron yoke with a small gap between them (Fig. 3.2A). This first design was updated to a design based on square magnets [PCB05] (Fig. 3.2B). Marble et al. [MMCB05, MMCB06] proposed a design based on an array of four magnets embedded in a iron yoke and covered by steel pole pieces (see Fig. 3.2C,D). These pole pieces are designed to finely homogenize the magnetic field. The main drawback of this geometry comes from the fact that the relative position of the magnets cannot be changed after their assembly. Thus, the inhomogeneities inherent to the manufacturing of the magnets cannot be compensated. A similar principle has been proposed by Paulsen et al. [PBG+08]. Their design allows the adjustment of the field by rotating the magnets (see Fig. 3.2E,F). The Surface GARField is another of the available single-sided sensors. From its original design [GAB+99] (see Fig. 3.2G), it was modified to a single-sided sensor [MAMM07] (see Fig. 3.2H). Its design can be seen as an open Halbach magnet array [Hal81]. The periodic positioning of the magnets allows to generate over the sensor a field of constant magnitude (but not of constant direction) in a plane parallel to the array. Finally, Chang et al. [CCH06] proposed a design based on the use of the fringe field of an Halbach magnet (see Fig. 3.2I).

3.1.2 Sensor design

The NMR-MOUSE™ is based on a U-shaped geometry. Two block magnets with opposite polarization are placed on an iron yoke [ESBB96]. In this configuration, the static field is parallel to its surface. The main point is that it can be combined with simple and efficient surface radiofrequency coils. In this geometry, due to the symmetry of the magnet along the y axis, the dependence of the field along this direction has only even terms in its Taylor expansion. As a function of the position, at the magnet surface, the field has a minimum at the center of the magnet ($y = 0$) and increases as the permanent magnet blocks are approached (see Fig. 3.3B). The field in the x direction is also an even function of x, but in this case, the field decreases when moving away from the center, reflecting the finite size of the magnet along x. This spatial

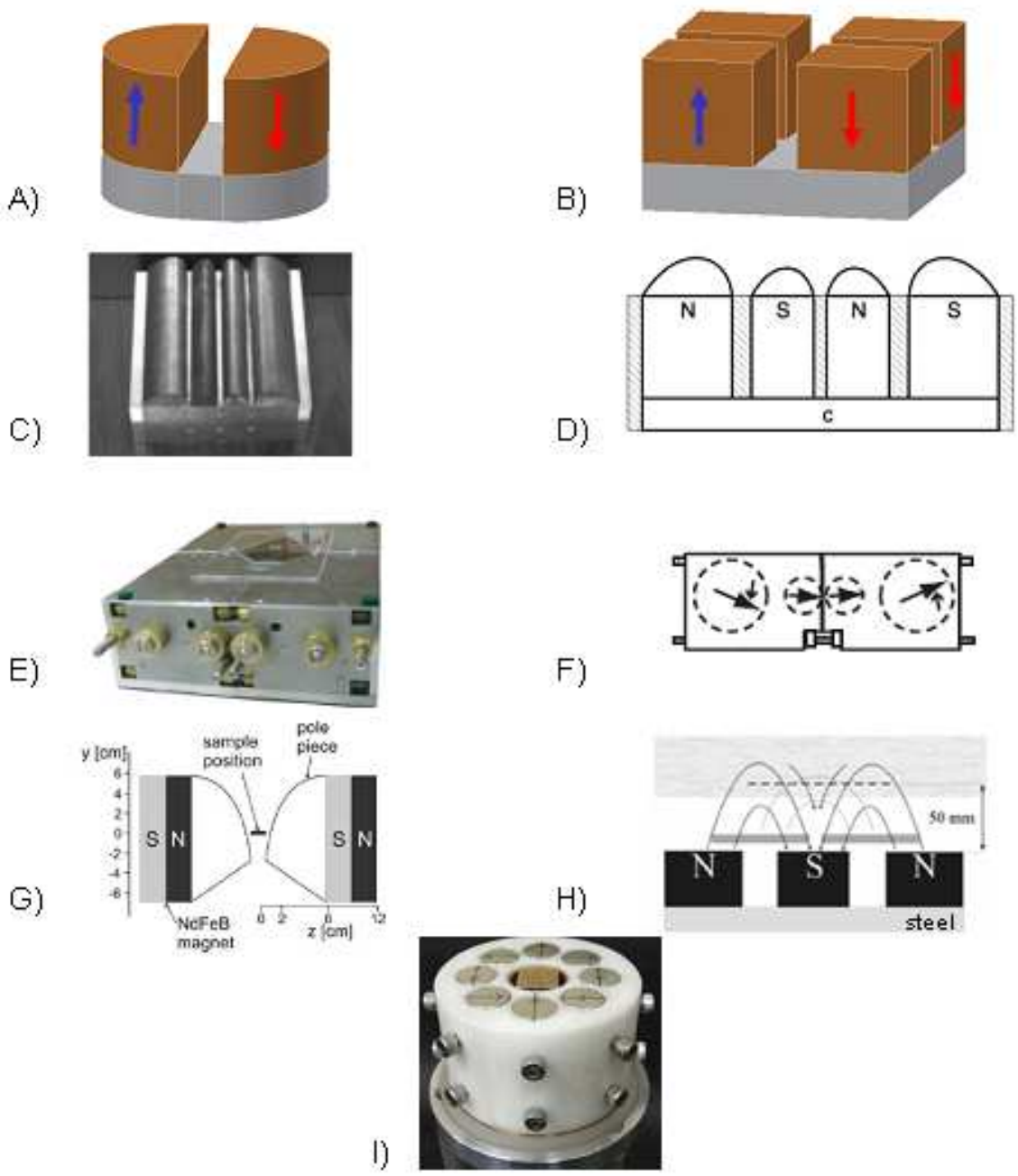

Figure 3.2: Short review of the most used single-sided sensor. A) is the original design of the NMR-MOUSE™ [ESBB96] and B) its current geometry [PCB05]. C) and D) are respectively a picture and a sketch of the single-sided sensor proposed by Marble et al. [MMCB05]. E) and F) correspond to the sensor proposed by Paulsen et al. [PBG+08] where the magnetic field can be adjusted by changing the orientation of the magnets. G) is the original design of the GARField [GAB+99] and H) its evolution towards a single-sided magnet [MAMM07]. I) corresponds to the idea of Chang et al. [CCH06] to use the fringe field of a Halbach array.

dependence gives rise to the well-known horse saddle shape of the magnetic field in the xy plane. It can formally be expressed by expanding the magnetic field $B_0(\vec{r})$ around $\vec{r}_0 = (0, 0, z_0)$ as

$$B_0(\vec{r}) = B_0 + G_z(z_0)(z - z_0) + \alpha_x(z)\, x^2 + \alpha_y(z)\, y^2 + \cdots \tag{3.1}$$

Further in the z direction (at a distance higher than the gap width), the field has a maximum at the center and decreases at higher y values (see Fig. 3.3B). This change of sign is the signature of the cancellation of the component α_y. To compensate α_x without increasing the size of the magnets, the solution proposed by Perlo et al. [PCB05] is to introduce a second gap d_s along x. Henceforth, the magnet has two natural degrees of freedom (namely the gaps along the x and y axis) which can be finely adjusted to tailor the magnetic field and achieves easily depth resolution of a few tens of micrometers.

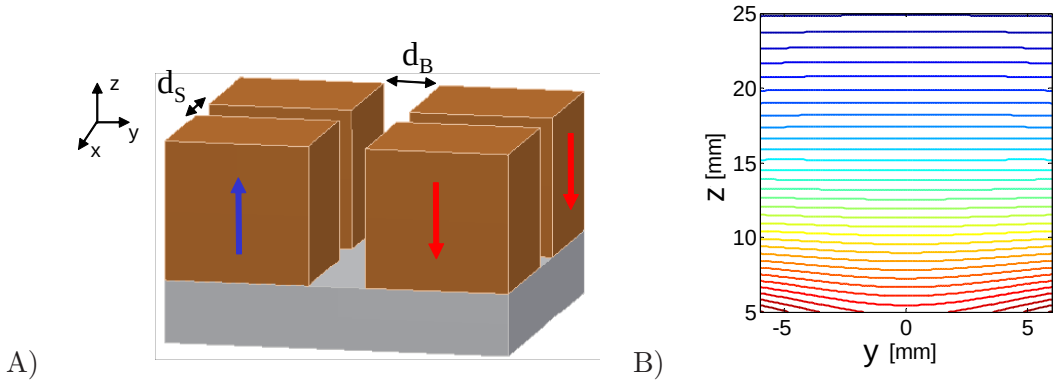

Figure 3.3: A) Sketch of the four magnet pieces in the design of the current NMR-MOUSE™. B) Contour line of the magnetic field over the magnet.

It is important to point out that the region where the isofields can be considered to be planar (formally $\alpha_x\, x\,,\ \alpha_y\, y \leq G_z$) is limited. It is of the same order of magnitude as the gap along the y axis. Beyond this limit, the lateral gradients increase drastically. As the object to be scanned often spread over the limits, the sensitive spot must be limited by using a proper radiofrequency surface coil. It varies from 1 cm^2 for the profile NMR-MOUSE™ whose sensitive layer is 5 mm above the surface of the magnet (PM5), to 5 cm for the one with a sensitive volume located at 25 mm over the magnets (PM25).

3.1.3 Radiofrequency coils

Coil circuits have been extensively discussed at chapter 1 so we will focus on what is probably the most important feature of these coils : their inductance must be kept as low as possible to reduce possible detuning due to loading changes during the scanning procedure. This is obtained by minimizing the number of turns of the surface coil and using preferably large copper strips than small wires. Two types of circuit are used. Either normal tank circuits as described in section 1.1.5, or coils with an inductive coupling (see section 1.1.6). Finally, resistances are introduced in parallel (on the order of a few kΩ) to the coil both to reduce the quality factor and the dead time. A low quality factor helps to minimize changes in the tuning frequency induced by load variations.

3.1.4 Positioning system

As the sensitive volume is at a fixed position compared to the magnet, it is necessary to reposition the sensitive slice with respect to the object, in order to complete the profile. In practice as the sample might be unmovable (a wall for example), it was chosen to reposition the magnet placed on a lift (see sketch of Fig. 3.4). This lift has a range at least equal to the

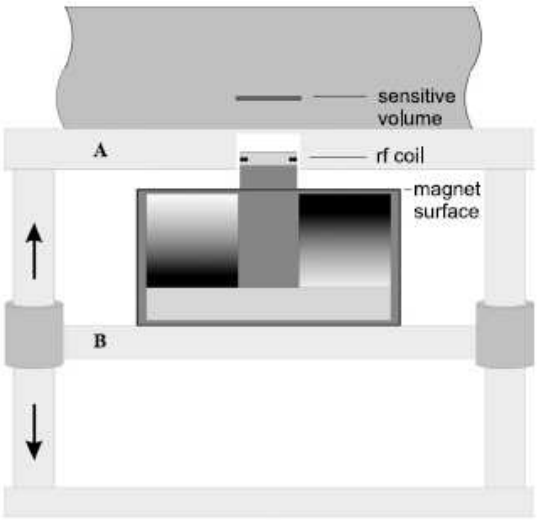

Figure 3.4: Schematic of the lift used to reposition the sensitive slice across the sample (from [PCB05]). The object is placed on top of the plate A, which is parallel to the movable plate B where the sensor is mounted. In this way, the surface of the object can be precisely aligned with the flat sensitive slice. The drawing also illustrates the positions of the sensitive slice, the RF coil that defines the sensor surface, and the magnet surface.

distance between the surface of the magnet and the sensitive slice. It contains a stepper motor which drives a screw to move the sensor up and down.

3.1.5 Pulse sequences

Initially, the two parameters which could be measured with this magnet were T_1 and T_2. T_2, for example, can be measured in a single shot using the Carr-Purcell-Meiboom-Gill (CPMG) sequence [CP54, MG58]. This sequence turns out to be very robust and still applicable in inhomogeneous field [GP95, CPB11, HG00]. T_1 cannot be measured in a single shot. The two sequences which are usually used to measure T_1 are the inversion [VWKP68] and the saturation [MHK71] recovery. These sequences exhibit some artefacts when used in inhomogeneneous field. The difficulties arise from the fact that it is impossible to achieve a full magnetization inversion or saturation across the full sample. Thus, the buildup curves present an offset [CPB11]. Whereas such single-echo sequences require, in general, a large number of scans which leads to long experimental times. CPMG detection following T_1 editing sequence reduces the measurement time.

As single-sided NMR is now better understood, more advanced methodologies have been developed. For example, self-diffusion coefficients can be easily measured [RCP$^+$06, CPB11]. The idea is to use a stimulated spin echo [Tan70] followed by a CPMG detection train. This method is fully described in appendix A. This sequence naturally leads to two dimensional sequences. Instead of using simply the CPMG train to increase the signal-to-noise ratio, it is possible to exploit this train by adding a second dimension to the experiment. This leads to the so-called D-T_2 experiment [HV02, HVF02]. The panel of two dimensional experiments has been extended to other distribution functions such as T_1-T_2 [EWJH91, SVH$^+$02, HV02] or even some exchange experiments such as diffusion-diffusion [CF04] and T_2-T_2 [MKMM05] correlation functions.

3.1.6 Flip angle adjustment

In order to preserve the thickness of the selected slice (or spectral bandwidth) we used a 180^o pulse of twice the 90^o amplitude, rather than twice its length. Thus, the RF power was set to a value close to the maximum (on the order of a few hundreds of watt) for the 180^o pulse and 6 dB below for the 90^o pulse. To adjust the flip angle, the pulse length was varied until the maximum of the echo signal was reached. Depending on the distance between the surface coil and the sample, the pulse length varies between 7 μs (sample at less than 5 mm from the surface of the coil) and 30 μs (sample at 25 mm from the coil).

3.1.7 Profile and resolution

The resolution is given by the combination of the magnitude of the quadratic terms of Eqn. 3.1 against the main gradient and the volume selected by the surface coil. The resolution of the NMR-MOUSE™ is usually around 50 μm, which is enough for most applications. However, a few microns of resolution can be reached by finely adjusting the position of the magnets [PCB05]. As an example, we measured the drying of a sample of Vycor glass with a pore size of about 5 μm. The sample has the shape of a 50 mm diameter, 5 mm thick pill. It was initially pumped at 10^{-2} mBar during 10 minutes to remove air. Afterwards, it was saturated with water. A layer of plastic was put around the sample to avoid any drying from the side. Then, the sample was placed on top of the profile NMR-MOUSE™ PM25, which was set inside a climate chamber (see Figure 3.5 (A)). The temperature was regulated at 25 °C and the humidity at 60 % rH. One profile was measured every 13 minutes. At each step a CPMG train was performed. Instead of summing the echo, each decay was fitted by an exponential decay in order to avoid any T_2 contrast in the profile. The amplitude of the exponential decay is exhibited in Figure 3.5 (B). Each solid line corresponds to one profile (the top is at the position 5 mm). The drying behaviour is consistent with what is found in the literature [BS90]. From a funicular regime where capillary forces allow to homogenize the water concentration over the sample (flat profiles), the drying switches to a pendular regime when the film of water becomes too thin. In that case, the sample is drying from top to bottom. This is evidenced by the last profiles measured whose amplitude is not constant over the whole sample but only on the bottom part.

3.2 Fourier MOUSE

3.2.1 Introduction

As we have already said in the introduction of this chapter, sensors using large static gradient have proven to be the most efficient to achieve micrometer scale resolutions [PCB05]. As the finite bandwidth of the coil limits the thickness of the slice which can be excited to a few hundreds of microns, a precise positioning system is required to profile a sample over a few millimeters. This often leads to long experimental times and the measurements of liquid like sample can be strongly affected by molecular diffusion. To avoid this, it is necessary to excite thicker slices, which means to reduce the magnetic field gradient. In previous attempts to reduce the gradient strength, the magnet geometry was optimized by setting as a constraint the gradient uniformity along the depth axis [MMCB06, GNMCB10]. By doing so, profiles of up to 8 mm could be measured without moving the magnet, but reasonable resolution of the order of 200 μm was only achieved in samples with limited lateral size [MMCB06]. In this case the maximum resolution was limited by the lateral field variations which, without adjustment, can be considerably larger than the variations caused by G_0. Besides compromising resolution, a reduction of G_0 is normally achieved at the expense of B_0 field strength. Then, taking into account that the SNR depends on the magnet parameters as SNR $\propto \frac{B_0^2}{G_0}$, where the inverse of the gradient quantifies the excited volume [CPB11], the field-optimization procedure can easily lead to considerable sensitivity loss.

A) 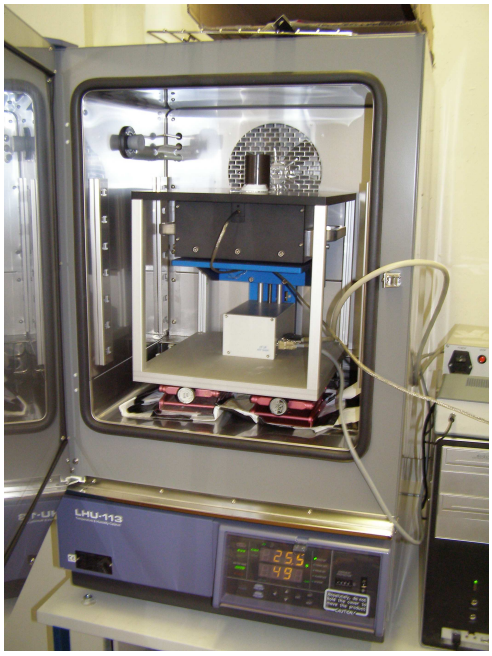

B) 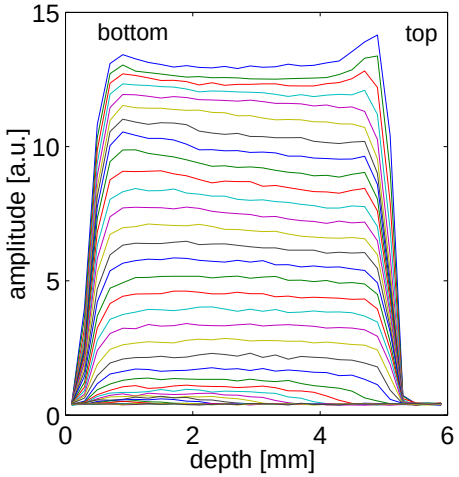

Figure 3.5: A) Picture of the profile NMR-MOUSE™ PM25 inside a climate chamber used to monitor the drying of Vycor glass. B) Drying of a Vycor glass made from 10 μm silica particles. The sample was initially saturated with water after 10 minutes of vacuum pumping. Each solid line corresponds to one profile. The completion of one profile over 6 mm by step of 200 μm requires 10 minutes using 8 scans per point and a repetition time of 2.5 s. The RF pulse duration was 12 μs. For each point, a CPMG detection train was performed using an echo time of 112 μs. The 800 echoes collected were fitted by an exponential decay to obtain the amplitude.

The above considerations show that when the gradient strength is reduced, a delicate trade-off between working depth, spatial resolution, and sensitivity is established.

Recently, it has been shown that the strongly inhomogeneous fields generated by single-sided magnets can be homogenized by including in the main magnet array small permanent magnet blocks forming a so called shim unit [PDC$^+$05, PCB06, PCB07]. By moving the magnets of the shim unit, linear and quadratic terms can be generated in a controlled manner to maximize the field homogeneity across the sensitive volume. This approach has proven to give enough precision to shim the field even to the sub ppm limit, demonstrating that it is possible to measure highly resolved NMR spectra in the stray field of open magnets [PCB07]. In this work we exploit the concept of mechanical field shimming to strongly reduce the magnetic field gradient along the depth direction while keeping efficient control of the lateral field variation and minimizing the loss in magnetic field strength. A sensor built following this approach allowed us to measure depth profiles over a range of two millimeters with a resolution of about 25 μm. As the full profile is obtained in one experiment by Fourier transforming the echo signal acquired in the presence of a static gradient of about 2 T/m, no repositioning system was required. The performance of the sensor is first demonstrated with phantom samples where sensitivity and resolution are quantified. Then it is used to measure human skin profiles in vivo. As in the presence of a low gradient the relaxation time T_2 can be measured without strong diffusion contamination, the sensor is useful to spatially resolve both T_2 and diffusion coefficients along the depth direction.

3.2.2 Sensor design

The sensor used for the present application consists of two units. The main unit is built from static magnet blocks generating the main magnetic field. The second one is the shim unit. It

consists of smaller movable magnets used to modify in a controlled manner the magnetic field generated by the main unit. By combining the two units, magnetic fields with different spatial variations can be generated depending on the application.

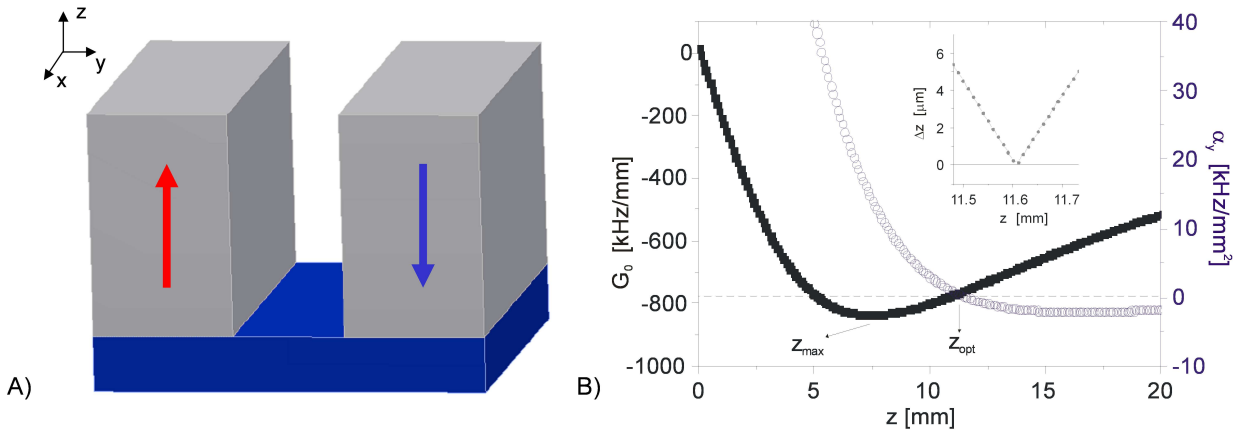

Figure 3.6: A) Sketch of a U-shaped magnet. Magnet blocks of SmCo magnetic material were used with dimensions of $140 \times 57 \times 80$ mm^3. Setting the central gap $g_y = 16$ mm a magnetic field of 0.42 T was generated at the working depth (z_{opt}). B) Coefficients characterizing the most important field inhomogeneities of the U-shaped magnet as a function of the depth. The left ordinate shows the gradient G_0 while the right ordinate measures the second derivative of the field α_y along the lateral direction y. Inset: upper bound for the resolution Δz calculated using Eq. (3.4). For each depth the G_0 value corresponds to the curve of solid squares and $\Delta B = \alpha_y \cdot R^2$ with α_y obtained from the open circles and $R = 5$ mm.

3.2.2.1 Main unit

There are several way to design magnets for unilateral NMR [BPC08]. For the present work a U-shaped geometry was chosen because of its excellent performance and simplicity. It consists of two permanent magnet blocks with anti-parallel polarizations placed on an iron yoke separated by a gap between them [PCB05, BBE$^+$98] (see Fig. 3.6A). The direction along the gap is called x, the direction across the gap y, and z is along the depth direction. All distances are measured in a coordinate system that has its origin at the geometric center of the magnet but with the xy plane at zero depth placed at the magnet surface. In good approximation, the magnetic field close to the magnet surface can be considered to be oriented along the y axis with its dominant gradient component G_0 along the depth direction.

Figure 3.6B (left axis, solid symbols) shows the dependence of $G_0 = \frac{\partial B_0}{\partial z}\,|_{(0,0,z)}$ of the U-shaped magnet as a function of the depth calculated for $x = y = 0$. Its non-uniformity is obvious. Starting from values close to zero at the magnet surface, the maximum absolute gradient value of about -20 T/m is reached at a distance $z_{\text{max}} = 7.5$ mm. At first sight, one might be tempted to choose the working region centered at z_{max} where the G_0 gradient along the z axis has the highest uniformity. However, the lateral spatial inhomogeneities of B_0 proportional to higher order derivatives of the field along x and y (ΔB) have critical effects on the image resolution. Indeed, close to the z axis, B_0 can be rewritten as a Taylor expansion:

$$B_0(x,y,z) = B_0 + \left.\frac{\partial B_0}{\partial z}\right|_{(0,0,z)}(z-z_0) + \left.\frac{\partial^2 B_0}{\partial x^2}\right|_{(0,0,z)}x^2 + \left.\frac{\partial^2 B_0}{\partial y^2}\right|_{(0,0,z)}y^2 + \\ + \left.\frac{\partial^2 B_0}{\partial x \partial y}\right|_{(0,0,z)}xy + \left.\frac{\partial^2 B_0}{\partial x \partial z}\right|_{(0,0,z)}xz + \left.\frac{\partial^2 B_0}{\partial y \partial z}\right|_{(0,0,z)}yz + \cdots \quad (3.2)$$

$$= B_0 + G_z(z-z_0) + \alpha_x\, x^2 + \alpha_y\, y^2 + \beta_{xy}\, xy + \beta_{yz}\, yz \quad (3.3)$$

Note that this equation is the same one as Eqn. 3.1 but to which we have added the cross-terms.

In a first approximation ΔB is considered to be dominated only by second order derivatives (quadratic and cross terms) neglecting contributions of 4-th or higher order terms. This is always true as long as the radius R delimiting the sensitive volume is much smaller than the magnet dimension. In addition, because of the symmetry of a U-shaped magnet, the variation of the field along x, close to the magnet surface, is smaller than the one observed along y. This variation can be further reduced by introducing a small gap along x with minimum influence on the field dependence along y [PCB05]. Under this condition the dominant contribution to ΔB comes from the term proportional to $\alpha_y = \frac{\partial^2 B_0}{\partial y^2}\,|_{(0,0,z)}$.

Figure 3.6B (right axis, open symbols) plots α_y as a function of depth s. At $z = z_{\max}$ the value of the second order coefficient is $\alpha_y \approx 0.35$ mT/mm^2 equivalent to 15 kHz/mm^2 for protons (from here on the latter frequency units will be used). This quadratic term defines a field deviation $\Delta B \approx 370$ kHz from the center ($y = 0$) to the border of the sensitive volume at $y = 5$ mm. Then, the isofields or lines of constant magnetic field at this particular depth are represented by curved lines. A different situation is found if the working depth is set at $z_{\text{opt}} > z_{\max}$. Here $\alpha_y = 0$ and then the isofields are parallel planes (at least close to the xy origin) since no deviation of the magnetic field is expected at the borders of the sensitive volume. In this situation the field profile is optimum to scan objects aligned with the magnet since sharp interfaces can be determined with maximum resolution. This situation is also observed in STRAFI experiments carried out in superconducting magnets [McD97, VLBBddL11], where the imaging plane is placed at a position different from the one corresponding to the maximum gradient in order to maximize the resolution. The best resolution Δz that can be achieved at a given depth can be calculated by converting the lateral field variation ΔB to space curvature via the main gradient strength G_0,

$$\Delta z = \frac{|\Delta B|}{|G_0|}. \quad (3.4)$$

The inset of Fig. 3.6B shows the values for Δz calculated using Eq. (3.4) for different depths around z_{opt}. Here, ΔB was evaluated at a radius $R = 5$ mm representing the border of the sensitive volume. The depth range shown in the figure corresponds to 200 kHz, which is the bandwidth excited by a typical resonance circuit built for this type of sensor without reducing the Q factor on purpose. The best resolution ($\Delta z = 0$) is determined by the zero crossing of the α_y curve at z_{opt}. Although the resolution degrades when moving away from z_{opt}, for the present U-shaped magnet Δz remains under 5 μm over the whole excited range. This resolution was experimentally achieved with a sensor having similar characteristics [PCB05]. The outstanding performance in terms of resolution around z_{opt} is obtained thanks to the zero crossing of α_y, but also because of the strength of the gradient. However, due to the large G_0 value, the thickness of the excited slice is at most 250 μm, requiring repositioning of the excited slice in order to measure a profile of the sample.

In the present work we modified the magnet geometry to reduce the value of G_0 in order to

excite a slice a few millimeters thick. Since in principle, ΔB is independent of the gradient value, in the optimization process followed to reduce G_0, the lateral field deviations become comparable or even dominate over the field deviation along the depth direction $\Delta z \cdot G_0$. According Eq. (3.4) this leads to large values of Δz. In order to obtain a resolution of a few tens of a micrometer over the whole slice thickness of 2-3 mm, it was necessary to reduce the value of ΔB keeping it as close to zero as possible within the slice thickness. To meet this condition it was necessary to include in the magnet design variables of control to reduce ΔB.

3.2.2.2 Shim unit

The use of movable magnets has proven to be of great assistance to reduce the field inhomogeneities of single-sided sensors. Following this concept the stray field of an open magnet could be shimmed to sub-ppm homogeneity, allowing the measurement of proton spectra from liquids outside the magnet [PCB07]. The working principle of this approach is based on reproducing the field inhomogeneities of the main magnet with the shim unit, while at the same time generating the smallest average field strength possible. By setting the polarization of the shim unit opposite to that of the main unit, the inhomogeneities of the main field can be corrected while the total field strength is maintained at an acceptable magnitude. An elementary shim unit block that satisfies these requirements is the one which has the geometry of the main unit but with different aspect ratio and smaller size. Depending on the required spatial dependence of the magnetic field, it can be necessary to combine more than one shim unit to achieve optimum performance. A detailed description of the shim unit can be found elsewhere [CPB11]. Here a brief description of the components and their main effects on B_0 are given.

The shim unit is designed following a numerical procedure which optimizes the magnetic field according to the specifications imposed by a particular application. In addition, the design needs to contemplate the fact that once the magnet array is built, the positions of the shim magnets need to be adjustable to allow correcting unavoidable inaccuracies in the polarization, size, and positioning of the magnet pieces. Small displacements of the magnet blocks around their optimum positions allow one to experimentally reach the performance calculated numerically.

To achieve a good performance the main magnet was furnished with two shim units and its original geometry was slightly modified:

- the first one is placed in the gap of the main unit at about 15 mm below the magnet surface. The strength of the gradient is adjusted by controlling the height of this shim unit relatively to the main magnet. However, the addition of this unit also reduces the magnitude of B_0, so its size and position must be chosen to minimize this effect.

- To cancel the lateral variations ΔB of the main magnetic field, a second shim unit mounted on top of the previous one is used. Generally its dimensions are smaller than the lower shim unit but its gap tends to be larger than the one of the main unit.

- In order to avoid spatial superpositions between the main magnet and the upper shim unit, the former was modified by removing the inner edges of the large magnets blocks (Fig. 3.7A). The grooves formed at those positions can be thought of as a third shim unit placed inside the main unit. Since the magnetizations of the main magnet and the third shim unit oppose each other, their associated fields cancel each other in the sensitive volume.

With this modified geometry of the main unit, an iterative optimization of the shim unit dimensions starts in order to reach the desired field profile.

Figure 3.7B shows the value for the gradient (left axis, solid symbols) and α_y (right axis,

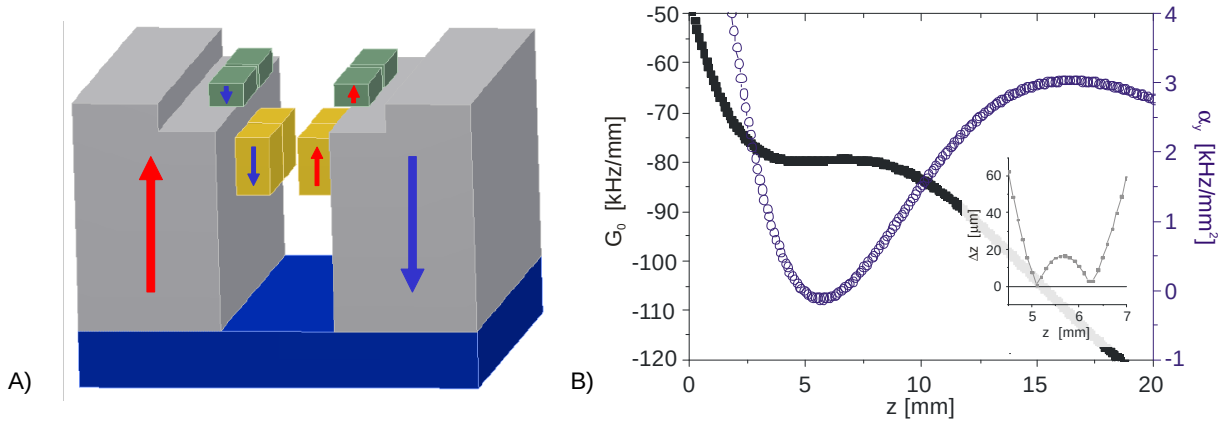

Figure 3.7: A) Drawing of the final sensor. The internal edges of the original U-shaped magnet have been removed and upper and lower shim units of block dimensions $30 \times 8 \times 12$ mm^3 and $38 \times 12 \times 20$ mm^3, respectively, have been added. The field generated at 6 mm from the surface is 0.21 T. B) Coefficients characterizing the most important field inhomogeneities of the sensor as a function of depth. The left ordinate shows the gradient G_0 while the right one measures the second derivative α_y of the field along the lateral direction y. Inset: upper bound for the resolution Δz calculated using Eq. (3.4). For each depth the G_0 value corresponds to the curve of solid squares and $\Delta B = \alpha_y \cdot R^2$ with α_y obtained from the curve of open circles and $R = 5$ mm.

open symbols) defined in Eqn. 3.3 as a function of depth for the optimized sensor. It can be appreciated that over a region 2.5 mm thick (range excited with a bandwidth of 200 kHz), centered at $z_0 = 5.75$ mm, the gradient was considerably reduced from about -20 T/m to -1.87 T/m (or equivalently -80 kHz/mm for hydrogen nuclei), and α_y has a minimum with two zero crossings in this depth range. The inset of this figure plots Δz calculated using Eq. (3.4) within the excited range. As before ΔB was evaluated at the borders of the lateral region with radius $R = 5$ mm for each particular depth. It can be seen that for almost a 2 mm range along z, the resolution is better than 25 μm. It degrades to reach ~ 50 μm at the limits of the slice at $z = 4.5$ mm and $z = 7$ mm.

3.2.3 Magnet construction

The magnet was built from SmCo blocks reproducing the geometry described in Fig. 3.7A. The main unit was placed on an iron yoke that defines a lateral dimension of 140×140 mm^2 and is 20 mm thick. Each of the main blocks is $140 \times 52 \times 80$ mm^3 and the size of the removed edge is $140 \times 14 \times 16$ mm^3. Two shim units, as described in the previous section, were placed within the main gap.

3.2.3.1 Practical shimming

Ideally, once the shim units are placed at the optimum calculated positions the spatial dependence of the magnetic field is expected to be the one shown in Fig. 3.7B. However, due to inaccuracies in the polarizations and sizes of the pieces (about 1%), and limited precision in the positions of the magnets in the array (a few hundred micrometers), the magnetic field achieved after assembling the components considerably deviates from the calculated one. To correct these imperfections, each of the shim magnets is mounted in a holder that can be moved along the three Cartesian directions in a controlled way by means of threaded bolts. Proper

movement of the shim magnets around their optimum positions allows to correct the magnetic field up to second order. By varying the height of the lower unit, the strength of the gradient can be adjusted. The displacement of the whole upper unit along x and y is used to correct linear inhomogeneities along these directions. In the same way, second order corrections along x and y are achieved by varying the gaps g_x and g_y, respectively. Further asymmetric movements of the upper shim magnets around the origin generate cross terms which are also necessary to homogenize the final magnetic field [CPB11].

Shimming of the magnet is an iterative process. One of the reasons for this is the non orthogonal nature of the control variables provided by the shim units. For example, when the gap g_y of the upper shim unit is adjusted to introduce a quadratic correction α_y, a small but non desired variation of the gradient G_0 is generated. To recover the original value of G_0 the height of the lower shim unit must be slightly modified. Each time after moving the shim magnets, the field was mapped by recording the resonance frequency of a point-like sample at each point of the whole sensitive volume. The sample voxel was made by pressing a small dot of cosmetic cream between two glass blades. The size of this small sample was about 2 mm in diameter and 30 μm thick. It was moved to scan planes over the surface rf coil at various positions z in order to measure a full 3D field map. To measure the field, the echoes generated by a CPMG sequence were first added and then Fourier transformed. The position of the line in the spectrum was measured to determine the resonance frequency and thus the magnetic field strength. After quantifying the coefficients of the terms describing the measured field map, the required magnet displacements were determined numerically. This iterative process was repeated until a small enough deviation from the target field distribution was achieved.

For the field scanning procedure a 15×15 mm^2 surface rf coil was built and fixed at the down side of a PC board positioned at adjustable distances from the magnet surface. As the rf field generated by the surface coil is inhomogeneous, the 90° pulse was set as the one that maximizes the signal of a sample layer larger than the size of the rf coil.

Figure 3.8 compares the field maps measured (left) and simulated (right) at 5, 6 and 7 millimeters above the shimmed magnet. The field difference between lines is 0.05 mT (2.125 kHz). This value was chosen because, given the gradient value, it corresponds to a depth variation of 25 μm. The agreement between simulated and experimental data is very good. Indeed, both exhibit a comparable large area (about 10×10 mm^2) of constant field in the xy plane over the 2 mm range along the z axis. By limiting the lateral extension of the coil to a 10×10 mm^2 square, profiles with a resolution of the order of 25 μm are expected to be measured. These maps are helpful to define the lateral size of the surface rf coil needed to excite the area of the sample where the desired resolution is achieved. In this case a two-turn rf coil (copper wire of 0.8 mm of diameter) with an outer lateral size of about 10×10 mm^2 was built. The coil was tuned at the frequency defined at $z_0 = 6$ mm in order to center the sensitive volume at this depth. A pulse length of 3 μs obtained with a 30 W rf power was used in most of the experiments reported in the present work. By placing the coil at $z_{\text{coil}} = 5$ mm from the magnet surface, a two millimeter thick region was excited. From now on all the depth measurements will be referred to the position of the rf coil, depth $= z - z_{\text{coil}}$.

Figure 3.9 shows the magnetic field along the z axis. The field plotted at each depth is an average over the sensitive area. It was measured by displacing along the depth direction a 30 μm thick layer larger than the rf coil. This plot shows that a very uniform gradient $G_0 = 2$ mT/mm is generated over the targeted 2 mm range. This is in good agreement with the gradient predicted by the simulations (see Fig. 3.7B).

3.2.3.2 Resolution tests

To measure the resolution over the 2 mm range, two types of experiments were performed. First, a semi-infinite step-like sample was measured at various depths from the magnet. Figure

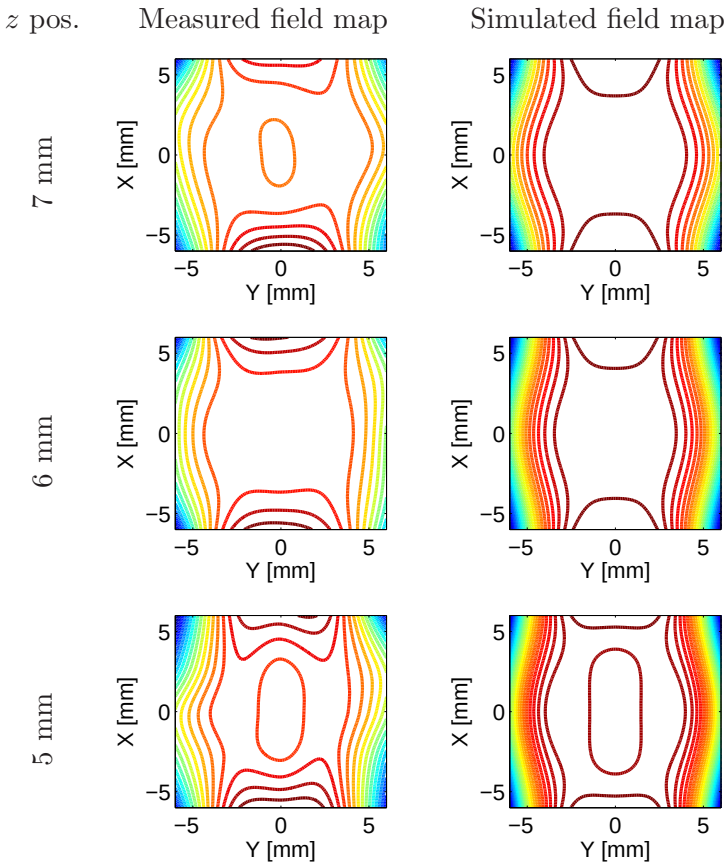

Figure 3.8: Magnetic field maps in the xy plane at various positions z. The left and right columns show the measured and simulated maps at 5, 6, and 7 mm from the magnet surface. The contour lines represents the lines of constant field at 0.05 mT (2.125 kHz). These maps were measured by recording the frequency changes of a $1 \times 1 \times 0.03$ mm^3 spot moved by step of 3 mm in a xy plane over the coil. A CPMG detection train of 1024 echoes with an echo time of 130 μs was performed. 64 scans and a recycle delay of 400 ms lead to an experimental time of 11 min to measure the 25 points of corresponding to the division of a 6×6 mm^2 square in step of 3 mm. After each point, the echoes of the CPMG decay are summed and the frequency is obtained by computing the Fourier transformation and considering its maximum.

3.10A shows the step profiles every 500 μm between 0 and 2 millimeters. The point-spread function (PSF) at the sample interface position can be simply obtained as the derivative of the step profiles [PCB05] (Fig. 3.10B). Then, calculating the line width at half-height of the PSF the resolution is obtained at each depth. In the central region (0.5 to 1.5 mm) the resolution is about 25 μm and it slowly degrades towards the borders of the sensitive volume located at 0 and 2 mm. The resolution at the borders is about 50 μm, in very good agreement with the values predicted from the simulation.

In a second experiment a 2 mm thick phantom sample made by stacking six water layers between glass blades was profiled. The layers of water are of the order of 150 μm thick and the glass blades are standard, 167 μm thick microscope cover glasses. The measured profile was then normalized by the profile of a homogeneous sample of water to account for the depth dependence of the coil sensitivity. The good resolution can be appreciated from the sharp edges of the layers, which get smoother at the borders of the sensitive volume (see Fig. 3.11).

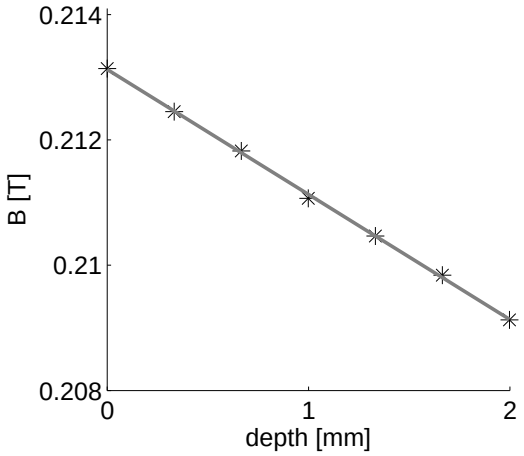

Figure 3.9: Magnetic field strength along the z axis measured by displacing a large but very thin sample. The field variation is highly linear, defining a gradient strength of about 2 mT/mm ($\approx$ 85 kHz/mm).

3.2.4 Sensitivity analysis

The results presented in the previous section show that with the present magnet design, a thick slice can be excited with relatively good spatial resolution. However, to reduce G_0 the intensity of the magnetic field B_0 also decreased. The purpose of the present section is to evaluate the SNR of the present sensor and compare it with a high-gradient system providing the same resolution in a similar lateral volume. In particular, from the available high-gradient systems the Profile NMR-MOUSE™ [PCB05] was chosen for reference since it has dimensions similar to the U-shaped magnet presented in this paper. The Profile NMR-MOUSE™ magnet has a gradient of 20 T/m, which is 10 times higher than the one generated by the present design, and a field strength of $B_0 = 0.4$ T, almost a factor two higher than that of the low-gradient sensor. In addition, both magnets use similar surface rf coils, making a direct comparison possible. For the present discussion we also assume that the relaxation time T_2 is much longer than the echo time of the CPMG sequence applied for signal detection. This situation is encountered in most liquid-like systems.

According to Richards and Hoult [HR76], the SNR ψ can be expressed as

$$\psi = \frac{K B_1^u V_\mathrm{s} \omega_0 B_0 N \gamma^2 \hbar^2 I(I+1)/(3k_\mathrm{B}T_\mathrm{s})}{\sqrt{4k_\mathrm{B}T_\mathrm{c}\Delta f R}}, \tag{3.5}$$

where K is a factor which characterizes the homogeneity of the rf field over the sample, ω_0 is the Larmor frequency and B_1^u is the field produced by a unit current over the volume V_s of the sample assuming it is homogeneous. N is the number of spins per unit of volume, γ is the gyromagnetic ratio, and T_s and T_c are the temperatures of the sample and coil, respectively. k_B is the Boltzmann's constant, $\hbar$ is Plank's constant, Δf stands for the frequency bandwidth, and R is the resistance of the circuit.

Considering that $\omega_0 = -\gamma B_0$, and since the value of the resistance R of the rf circuit is adapted to maintain its frequency bandwidth constant, it follows from Eq. (3.5) that the SNR is proportional to the square of the magnetic field B_0. This leads to a factor of almost 4 between the SNR for the high and low gradient systems. However, the bandwidth Δf across a slice of thickness ϵ is defined as $\Delta f = \gamma G \epsilon / 2\pi$, it follows that $\Delta f_{\mathrm{high}G} = 10 \Delta f_{\mathrm{low}G}$. Then, finally

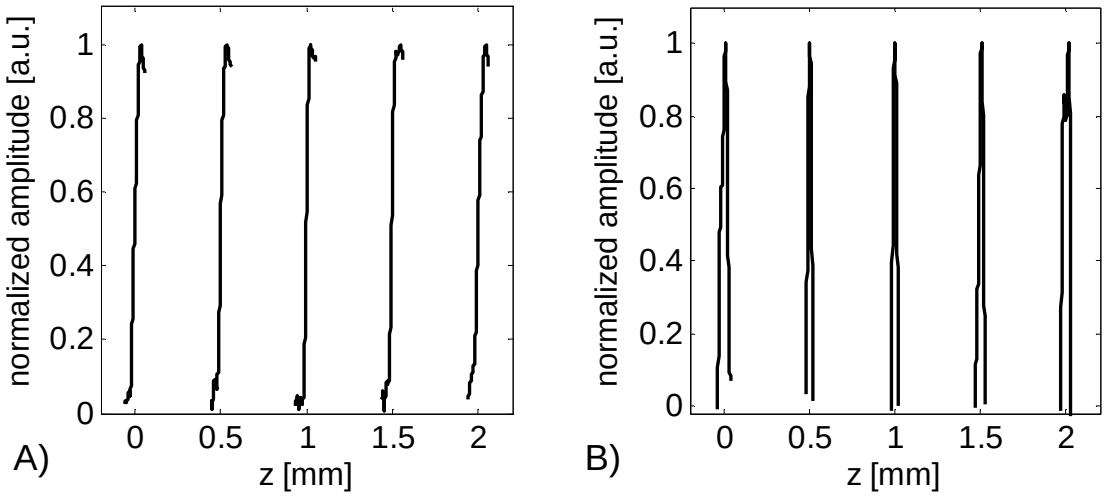

Figure 3.10: A) Profiles of a step sample positioned at different depths. B) Derivatives of the step profiles. The width measured at half height defines the resolution at the corresponding position z.

$$\psi_{\text{high}G} = \frac{4}{\sqrt{10}}\psi_{\text{low}G}. \tag{3.6}$$

where $\psi_{\text{high}G}$ and $\psi_{\text{low}G}$ correspond to the SNR of the high gradient and low gradient system respectively.

It should be noticed, nevertheless, that the high gradient system excites a slice thickness ten times thinner than the one obtained with the low gradient system. It is thus necessary to reposition the magnet ten times to cover the same spatial range. Consequently, the low gradient system can average 10 times more scans than the high gradient system during the same measurement time. Per unit of time, the SNR $\psi_{\text{high}G}$ and $\psi_{\text{low}G}$ of the two systems compare as

$$\psi_{\text{high}G} = (4/10)\psi_{\text{low}G}. \tag{3.7}$$

In the above consideration it is assumed that the signal is acquired using a Hahn echo sequence during a time $t_{\text{Acq}} = \frac{2\pi}{\gamma G \cdot \epsilon}$, from which it follows that $t_{\text{Acq}}^{\text{low}G} = 10\, t_{\text{Acq}}^{\text{high}G}$. The situation changes when a CPMG sequence is used, which is normally the case for single-sided profiling.

3.2.4.1 CPMG analysis neglecting dead-time effects

Assuming the NMR signal can be acquired immediately after the rf pulse (no dead-time), the shortest echo time t_{Emin} of the CPMG sequence corresponds to the acquisition time t_{Acq} required to obtained the resolution δz:

$$t_{\text{Emin}} = t_{\text{Acq}} = \frac{2\pi}{\gamma G \cdot \delta z}. \tag{3.8}$$

Since the CPMG train effectively collects echoes until a time $t = T_2$ where the signal has decayed up to a fraction 1/e of the initial value, the number of echoes that can be added is

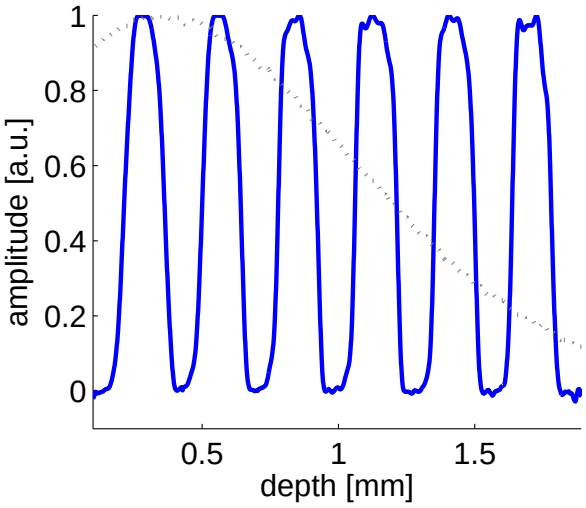

Figure 3.11: Profile of a phantom sample made of six layers of water 150 μm thick separated by microscope cover glasses. The dashed line corresponds to the normalization amplitude profile of the rf coil.

$$n_{\mathrm{E}} = \frac{T_2}{t_{\mathrm{E}}}. \tag{3.9}$$

Then, replacing t_{E} by Eq. 3.8

$$n_{\mathrm{Emax}} = \frac{\gamma G \cdot \delta z \cdot T_2}{2\pi}. \tag{3.10}$$

It follows from Eq. (3.10) that $n_{\mathrm{Emax}}^{\mathrm{high}G} = 10\, n_{\mathrm{Emax}}^{\mathrm{low}G}$. The effect of this on the SNR is that the reduction due to the bandwidth difference is recovered by the echo summation. Under this condition, the relation between the SNR of both systems is given by Eq. (3.6), evidencing the fact that both systems have similar performances in terms of sensitivity. The factor 4 coming from the field strength difference in favor of the high-gradient system is almost compensated by a factor $\sqrt{10}$ arising from the larger volume excited by the low-gradient system.

There are, however, two issues that were not taken into account in the evaluation. First, the unavoidable dead-time t_{d}, and second, the diffusion attenuation of the NMR signal in the presence of a static gradient. Since their influences are manifested in the recovery of the bandwidth, it is expected that the low gradient system becomes less affected by their effects than the high gradient system does.

3.2.4.2 CPMG analysis including dead-time effects

After an rf pulse is applied and to avoid saturation of the receiver, it is necessary to delay the signal acquisition until the voltage in the coil has decayed to a value compared with the one induced by the thermal noise. This delay time is usually called dead-time t_{d} and is present in all NMR experiments. Its influence in a CPMG sequence leads to a longer echo time (see Fig. 3.12A), and consequently Eq. (3.8) is modified to

$$t_{\mathrm{E}} = \frac{2\pi}{\gamma G \cdot \delta z} + 2 \cdot t_{\mathrm{d}}. \tag{3.11}$$

In this equation we have neglected once more the pulse length t_p, which is assumed to be of the order of a few μs. A typical value for the dead time is about $t_\mathrm{d} = 20$ μs. From Eq. (3.11) it can be seen that the effect of t_d is to increase the echo time t_E reducing the number of echoes that can be collected during T_2 (see Eq. (3.9)) by the ratio $\frac{t_\mathrm{Acq}}{t_\mathrm{E}}$ between the acquisition time and the echo time, defining

$$n_\mathrm{E} = n_\mathrm{Emax} \cdot \frac{t_\mathrm{Acq}}{t_\mathrm{E}} = n_\mathrm{Emax} \cdot \frac{1}{1 + \frac{2t_\mathrm{d}\gamma G \cdot \delta z}{2\pi}}. \tag{3.12}$$

For measurements where good resolution is required (long acquisition times), the dead time will be much shorter than the acquisition time and then $t_\mathrm{E} \rightarrow t_\mathrm{Acq}$, that is $n_\mathrm{E} \rightarrow n_\mathrm{Emax}$. On the other hand, when the measurement is conducted at low resolution, the effect of the dead time becomes rather large and may even dominate over the impact of t_Acq. Then $t_\mathrm{E} >> t_\mathrm{Acq}$, and $n_\mathrm{E} << n_\mathrm{Emax}$.

Figure 3.12B shows the behavior of the ratio $\frac{n_\mathrm{E}}{n_\mathrm{Emax}}$ as a function of resolution for both high- and low-gradient systems. The high-gradient system becomes highly affected by the dead-time and for poor resolutions (>200 μm) only 10% of the ideal number of echoes can be summed.

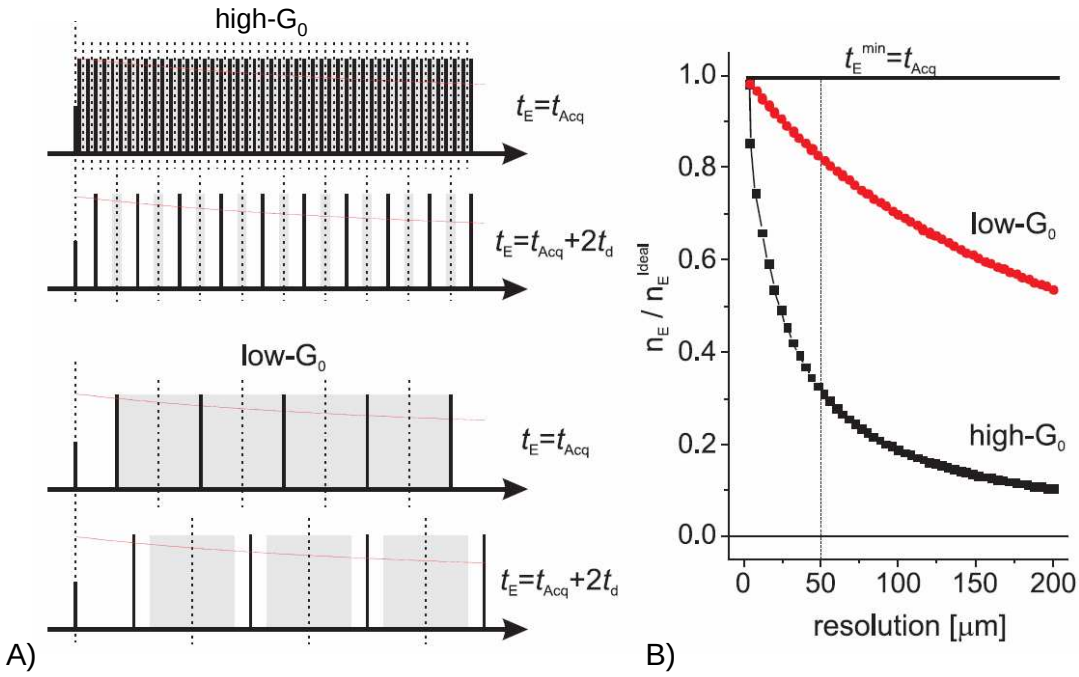

Figure 3.12: A) Schematics of the CPMG sequence. Long and short vertical black lines represent π and $\pi/2$ pulses, respectively. The light gray areas in between π pulses indicate the acquisition windows while the white regions represent the dead time intervals. B) Dead-time effects manifested in the ratio $n_\mathrm{E}/n_\mathrm{Emax}$ as a function of the resolution set for the NMR experiment. The number of echoes n_E is obtained from Eq. (3.12). For the computation of the maximum number of echoes Eq. (3.10) was used.

3.2.4.3 Diffusion effects

For most liquid-like samples the effects of molecular diffusion in the presence of high inhomogeneities of the magnetic field shorten the relaxation time T_2 measured with a CPMG sequence

[Cal91, Kim97]. The net effect is a reduced effective relaxation time $T_{2\text{eff}}$ which depends on the diffusion coefficient D of the sample, the gradient strength, and the echo time of the CPMG sequence. Neglecting off-resonance effects [Son02], $T_{2\text{eff}}$ can be expressed as [CP54] :

$$\frac{1}{T_{2\text{eff}}} = \frac{1}{T_2} + \frac{D\gamma^2 G^2}{12} t_{\text{E}}^2. \tag{3.13}$$

The analysis performed in the previous section corresponds to the case in which the decay of the signal due to diffusion (second term of the right hand side of Eq. (3.13)) can be neglected in comparison to $1/T_2$. In order to evaluate the performance of the low- and high-gradient sensors for samples in which this condition does not hold it is necessary to recalculate Eq.(3.9) replacing T_2 by $T_{2\text{eff}}$. Then, the effect of the dead time is accentuated for these samples because an increase of t_{E} due to t_{d} (Eq. (3.11)) reduces $T_{2\text{eff}}$. The maximum effective relaxation time $T_{2\text{eff}}^{\max}$ is reached in the limit of negligible dead time and pulse length, that is $t_{\text{E}} = t_{\text{Acq}}$, then

$$\frac{1}{T_{2\text{eff}}^{\max}} = \frac{1 + (D\gamma^2 G^2/12) T_2 t_{\text{Acq}}^2}{T_2}, \tag{3.14}$$

which, rewritten in terms of resolution through the expression for $t_{\text{Acq}} = \frac{2\pi}{\gamma G \cdot \delta z}$, becomes

$$\frac{1}{T_{2\text{eff}}^{\max}} = \frac{1}{T_2} + \frac{\pi^2 D}{3 \cdot (\delta z)^2}. \tag{3.15}$$

Then, for a given resolution δz, it can be seen that in this limit the effective relaxation time does not depend on the gradient magnitude. The expression of associated number of echoes that can be collected is thus similar to Eqn. 3.10:

$$n_{\text{Emax}} = \frac{\gamma G \cdot \delta z \cdot T_{2\text{eff}}^{\max}}{2\pi}. \tag{3.16}$$

Thus, we still have $n_{\text{Emax}}^{\text{high}G} = 10\, n_{\text{Emax}}^{\text{low}G}$, and the relation between the SNR of both systems is given by Eq. (3.6). When the value of the dead time becomes of the order or even larger than the acquisition time t_{Acq} (a situation corresponding to moderate or low spatial resolution), the effects of t_{d} on $T_{2\text{eff}}$ become important. This can be observed explicitly in the following expression, which is obtained by placing Eq. (3.11) into Eq. (3.13),

$$\frac{1}{T_{2\text{eff}}} = \frac{1 + (D\gamma^2 G^2/12) T_2 (t_{\text{Acq}} + 2t_{\text{d}})^2}{T_2}. \tag{3.17}$$

Then, inserting Eqs. (3.11) and (3.17) into Eq. (3.9) it is possible to calculate the number of real echoes that can be collected when both effects, diffusion and dead-time, are taken into account

$$n_{\text{E}} = n_{\text{Emax}} \cdot \frac{t_{\text{Acq}}}{t_{\text{E}}} \cdot \frac{T_{2\text{eff}}}{T_{2\text{eff}}^{\max}}. \tag{3.18}$$

Equation (3.18) shows that the shortening of $T_{2\text{eff}}$ introduced by t_d leads to an extra loss factor in n_E that increases when t_Acq becomes comparable with t_d (low resolution limit).

Figure 3.13A shows the ratio n_E/n_Emax as a function of the resolution when dead-time and the diffusion effects are taken into account. The two curves correspond to the low- and high-gradient systems. For a resolution of 50 μm, of the order of the one targeted in this work (see the vertical dashed line), the number of echoes that can be collected using a low gradient is much closer to the ideal situation (no dead-time) than what is obtained for large G_0. The improvement in SNR achieved with the low-gradient system compared to that of the high-gradient system is shown in Fig. 3.13B. For the resolution mentioned above the SNR of the present sensor improves by a factor of two.

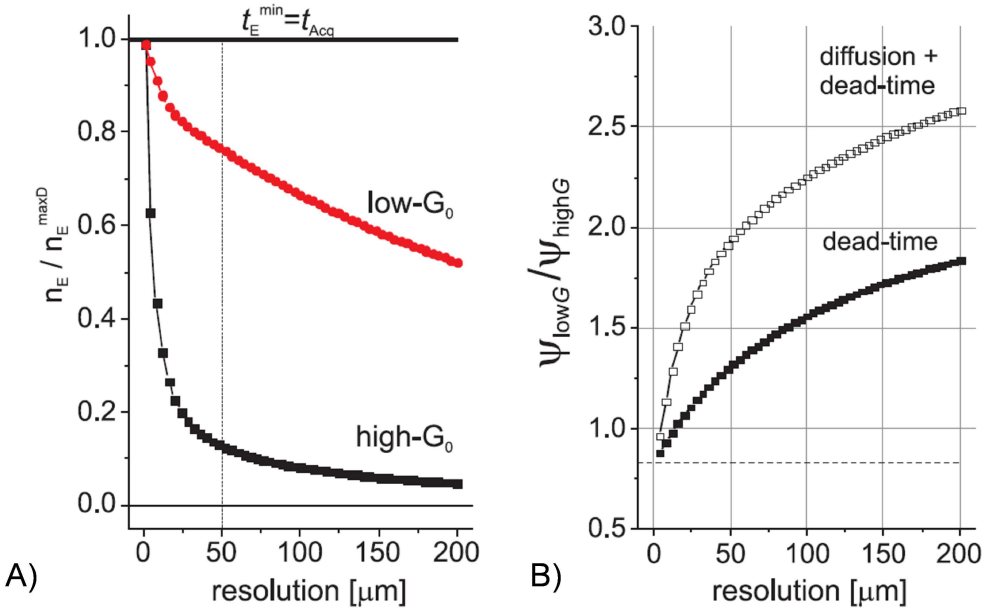

Figure 3.13: A) Effects of diffusion and dead-time manifested in the ratio n_E/n_Emax plotted as a function of the resolution set for the NMR experiment. The number of echoes n_E is calculated using Eq. (3.18). For the computation of the maximum number of echoes Eq. (3.16) was used. B) Ratio between the SNR of a low-gradient and a high-gradient system as a function of the resolution. Solid and open symbols correspond to the cases in which only the dead-time and diffusion plus dead-time effects are taken into account, respectively. The horizontal dashed line indicates the value $\sqrt{10}/4$ corresponding to the limit $t_\text{d} \to 0$. The diffusion coefficient of water ($D = 2 \cdot 10^{-9}\text{m}^2/\text{s}$) was used for this calculation.

3.2.5 Experiments and results

3.2.5.1 Spatially resolved T_2 and D measurements

In the presence of the low gradient generated by the sensor described in this paper 1D profiles can be straightforwardly obtained by Fourier transforming the echoes generated by a CPMG sequence. To enhance the SNR of the profile the echoes of the CPMG train can be added. Another strategy is to record the full echo decay and Fourier transform every echo independently to spatially resolve the CPMG decay along z. Then, by applying an inverse

Laplace transformation along the second dimension, the T_2-distribution is obtained at each depth.

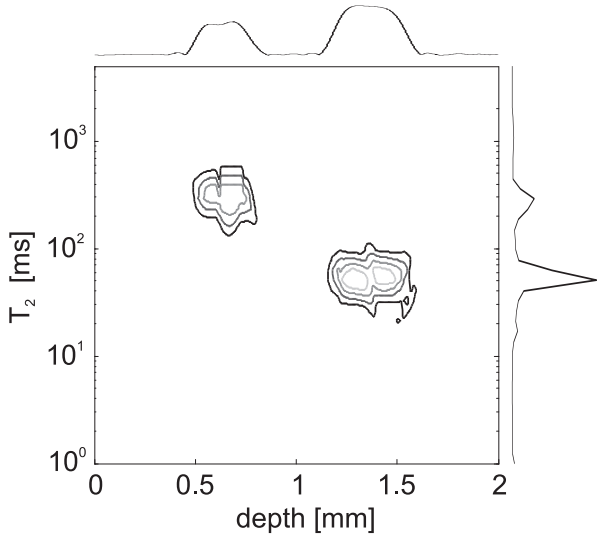

Figure 3.14: Depth-relaxation map corresponding to a bilayer phantom made of doped water and glycol. It was measured using a CPMG sequence composed of 460 echoes with $t_{\mathrm{E}} = 400$ μs. The spatial resolution was set to 100 μm by acquiring 80 points separated by a dwell time of 2 μs. The pulse length was 3 μs. 1024 scans were used with a repetition time of 1.0 s, defining a total experimental time of 17 min.

Besides T_2, the sensor can also be used to measure the molecular self-diffusion coefficient. For this purpose the stimulated-echo sequence (STE) is commonly used [RCP$^+$06, Kim97]. It encodes molecular displacement along the gradient direction in the amplitude of the stimulated echo. This sequence is combined with a CPMG echo train (STE-CPMG) to maximize sensitivity. Then, by Fourier transforming the added echoes and calculating the ILT [HV02] along the diffusion axis, the distribution of diffusion coefficients can be spatially resolved along the depth direction. If instead of summing up the CPMG echo train each echo is independently Fourier transformed, a 3D diffusion-relaxation-position correlation is obtained.

The performance of these methods is illustrated with measurements on a simple bilayer phantom. It is composed of glycol and water separated by two microscope cover glasses. These two components have different diffusion coefficients and T_2 relaxation times. Figure 3.14 shows the depth-relaxation map obtained from the CPMG echo train. Two spots are obtained at positions (0.6 mm ; 300 ms) and (1.4 mm ; 50 ms) corresponding to glycol and doped water respectively. The 1D projections along the depth and T_2 dimensions are also shown in the figure. A depth-diffusion map of the bilayer phantom is shown in Figure 3.15. In this plot, two peaks can clearly be identified as the glycol peak (0.6 mm ; $2 \cdot 10^{-10}\mathrm{m}^2/\mathrm{s}$) and the water peak (1.4 mm ; $3 \cdot 10^{-9}\mathrm{m}^2/\mathrm{s}$).

3D information regarding diffusion, relaxation, and depth can be obtained using the STE-CPMG sequence if the echoes are recorded independently. This method was applied to the bilayer phantom. To spatially resolve the Diffusion-T_2 correlation maps each echo is Fourier transformed, and a 2D ILT is computed on each 2D data set obtained at each particular position. Figure 3.16 shows the Diffusion-T_2 maps at the positions of each of the sample layers.

3.2.5.2 Measurements with low spatial resolution

For some applications in which bulk information is required [FJ02, MCD$^+$06, MMCB07], spatial resolution can be traded for sensitivity. If, for example, the acquisition time is set to 6

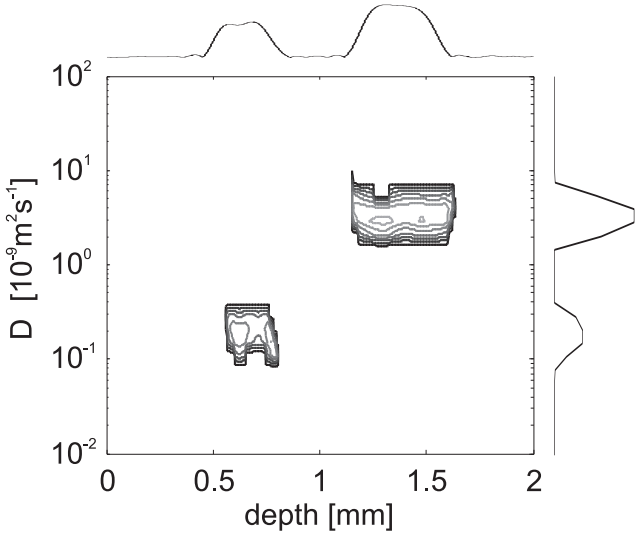

Figure 3.15: Depth-diffusion map corresponding to a bilayer phantom made of doped water and glycol. It was measured using a stimulated spin echo sequence where the diffusion encoding time was split into 48 steps logarithmically spaced between 108 μs to 629 μs and the evolution time was 5 ms. The signal was collected by a CPMG sequence composed of 460 echoes with $t_{\mathrm{E}} = 400$ μs. 16 scans were used with a repetition time of 1.0 s, defining a total experimental time of 12 min.

μs, corresponding to a resolution of the order of the thickness of the sensitive volume (2 mm), the sensitivity increases not only due to the larger integrated slice, but also because the echo time is considerably reduced. In this way, the diffusion contamination in the CPMG decay is reduced to maximize the duration of the CPMG echo train (see Eq. (3.13)). Under this conditions diffusion-relaxation maps can be measured with the STE-CPMG sequence with maximum sensitivity.

In the low resolution limit, the low gradient of the sensor allows to measure the relatively long relaxation times T_2 of liquid like samples. The range of T_2 values that is possible to cover depends on the echo time used in the sequence, which is set according to the spatial resolution that is needed. Figure 3.18A shows the measured T_2 as a function of the echo time for a water sample. It can be seen that as long as the echo time becomes larger, the T_2 value decreases reflecting the diffusion effects (Eqn. 3.13). It can be seen from Figure 3.18 that T_2 values of the order of 500 ms can be measured with the present magnet.

3.2.5.3 Application to the in-vivo profiling of human skin

The performance of the sensor in terms of resolution and sensitivity is suitable for studying human skin. Moreover, since it is possible to obtain a whole profile in a single scan, the measurement process becomes easy and fast which is important when working with patients.

Human skin tissue consists of several layers. The two most important ones are a superficial epithelial layer, the epidermis, and a deep connective tissue layer, the dermis. The epidermis is itself stratified beginning from the stratum basale, where the cells are generated, to the outer stratum corneum, where the cells are keratinised in a squamous structure. The dermis is subdivided in two layers, the thinner more superficial one that lies adjacent to the epidermis (papillare), and a deeper one known as the stratum reticulare. Finally, the hypodermis lies deep underneath the dermis and consists of adipose tissue. The hypodermis does allow the skin to move relatively freely over the underlying tissues. Depending on the part of the body, the thickness of the layers can vary from 20 μm to some millimeters [RQB$^+$91].

Figure 3.19 shows a typical depth-T_2 map measured at the palm of the hand. The T_2 distri-

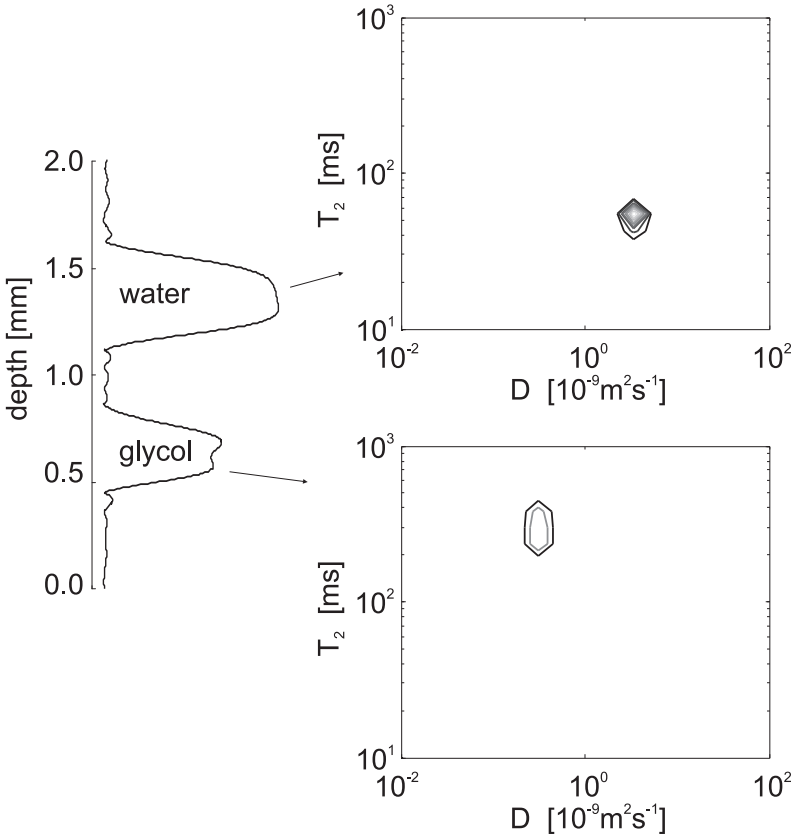

Figure 3.16: 3D diffusion-relaxation-profile correlation of a bilayer sample made of water and glycol. In the diffusion direction, 48 points were recorded and 700 echoes in the CPMG direction with $t_{\mathrm{E}} = 250$ μs. Finally, 512 scans were performed on each of the diffusion encoding points. This leads to a measure time of 7 hours.

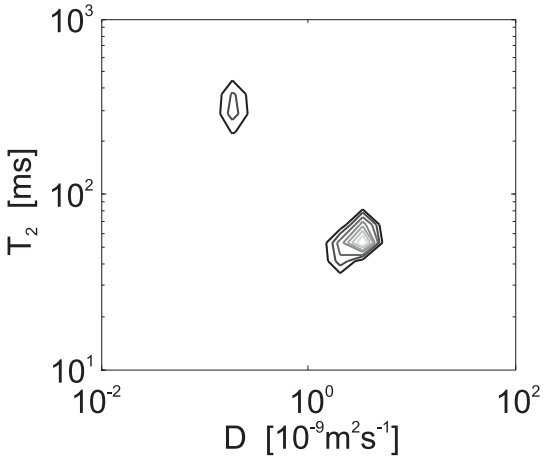

Figure 3.17: Diffusion-relaxation correlation on a bilayer sample made of water and glycol. In the diffusion direction, 48 points were recorded and 3000 echoes in the CPMG direction with $t_{\mathrm{E}} = 250$ μs. The measurement time was about 25 min.

bution measured at all depths is mono-modal with a center value characteristic for each layer. The first layer associated with the epidermis is approximately 200 μm thick and has short T_2 values of the order of 5 to 10 ms. It is followed by the dermis papillare, which has a thickness

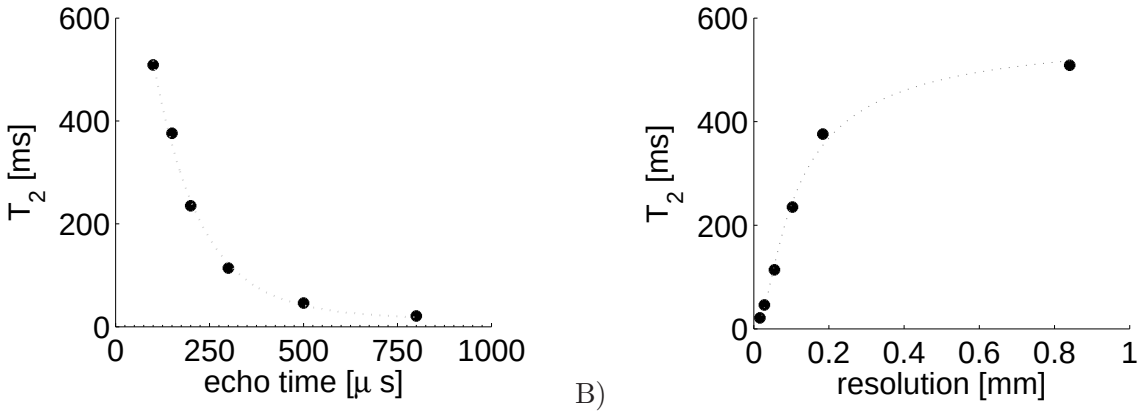

Figure 3.18: A) CPMG decay time as a function of the echo time for a tap water sample. B) CPMG decay time as a function of spatial resolution for a tap water sample.

comparable to the epidermis, but longer T_2 values of around 40 ms. Then, the third layer corresponding to the dermis reticulare is about 500 μm thick. It has a T_2 of about 20 ms which becomes longer when moving deeper into the body.

The last part of the profile, where the sensitivity is the lowest, corresponds to the beginning of the adipose tissue layer. It is important to notice that the diffusion contamination in the measured T_2 is negligible. This is so because the measured T_2 values are too short to be affected by diffusion as in free water, the CPMG decay recorded under the same conditions is fully due to diffusion attenuation and has a time constant of 100 ms (Fig. 3.18B). The T_2 relaxation times and the spatial structure obtained are in good agreement with previous single-sided measurements performed by stepping the sensor in order to record the whole profile [DJGM03, CPB06] and also are in accordance with high-field MRI experiments [RQB$^+$91].

For clinical applications it is convenient to reduce the total experimental time to the minimum. This can be achieved by compressing the T_2 dimension and use an average T_2 instead of the distribution as indicator. A robust parameter that can be used in this case is the so-called w function, which is calculated as the ratio of the sum of the last n_f to that of the first n_i echoes acquired with the CPMG sequence [CPB06]. Defining $s_n(t)$ as the signal corresponding to the n-th echo, we have for the w function

$$w(n_i, n_f) = \frac{\sum_{k\in\{n_\mathrm{f}\}} s_k(t)}{\sum_{m\in\{n_\mathrm{i}\}} s_m(t)}. \tag{3.19}$$

The thick solid line in Fig 3.19 shows the value of the w parameter spatially resolved along the depth direction. It was computed for n_i and n_f equal to 16 and 120, respectively. The profile was measured with a spatial resolution of 50 μm. It was achieved by setting the acquisition time per echo to 250 μs, and the echo time to 320 μs. By averaging 128 scans with a recycle delay of 300 ms, a total experimental time of the order of 30 seconds was defined. The behavior of the w function follows very well the maximum peak of the T_2 distribution, validating the use of the w parameter as a robust quantity well suited to characterize the tissue. By replacing the T_2 distribution by the w parameter sets a compromise between acquired information and experimental time.

It must be noted that due to the strong B_1 gradient the SNR of the profile degrades with depth. In order to measure the error along the profile, a series of w parameters was measured in the same spot of the palm of a volunteer. After each measurement the hand was removed from the magnet surface and kept in contact with air for a few minutes to avoid transpiration effects.

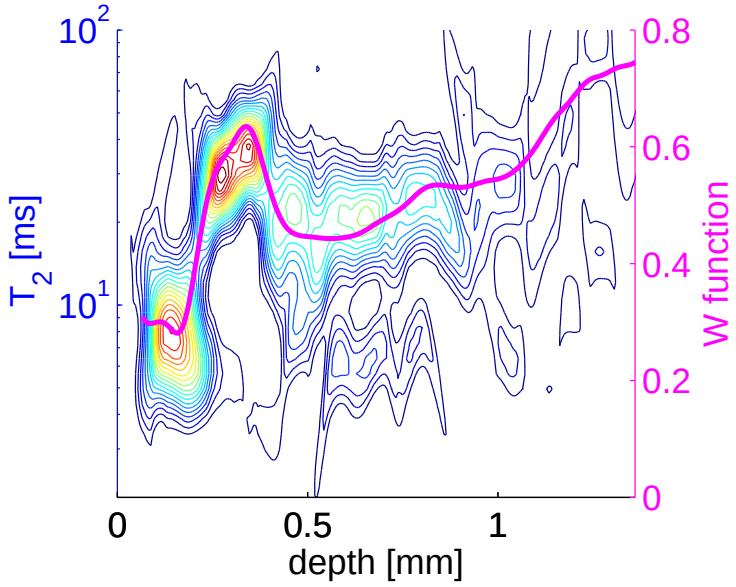

Figure 3.19: Depth-relaxation map of the skin tissue of the palm of the hand. The purple line corresponds to the w function (Eq. (3.19)). For the present T_2 distribution map 340 echoes were collected in the CPMG detection train where for each echo 128 complex points were acquired with a dwell time of 2 μs which sets a resolution of 50 μm. Using 2048 scans and a repetition time of 300 ms the total experimental time was 10 minutes. The w parameter was measured using 128 scans in 38 s.

A very thin cream layer of about 30 μm was pressed with a thin glass on top of the rf plate in order to set a reference for the initial position of the skin profile. The hand was then placed on top of the glass. The standard deviation measured in this way is about 1% at the skin surface reaching values of the order of 8% for the deepest points of the profile.

As a test, the w parameter was used to compare the skin profiles of various volunteers (male and female) of different ages and skin type. The results of these measurements are displayed on Figure 3.20. The main difference between the skin data of the measured people is the thickness of the epidermis.

Besides getting access to the T_2 of each layer, the diffusion coefficient can also be measured by implementing the STE-CPMG sequence described above. Figure 3.21 shows a 2D depth-diffusion map of the same spot for the same volunteer measured in Fig. 3.19. Within the first 200 μm two distinct diffusion coefficients can be identified. Then, the two values collapse into a single value for larger depths in the skin. At the surface of the skin (0 mm in the plot), the largest diffusion value is comparable to the self-diffusion coefficient of free water at 37°C [HHS00], the second one, almost two orders of magnitude smaller, is assumed to be restricted water and less movable biological tissue in the cells. Deeper in the skin, the diffusion coefficient is around $10^{-9}\mathrm{m}^2\,\mathrm{s}^{-1}$ with a monomodal distribution.

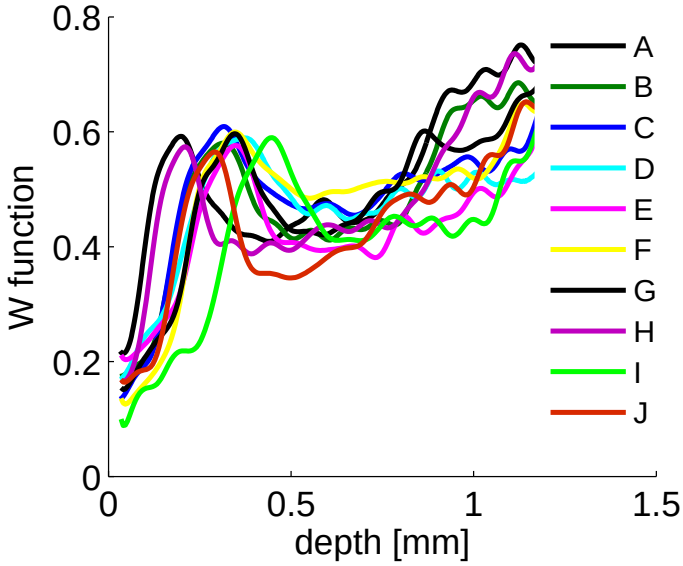

Figure 3.20: Depth profiles of the w parameter of the skin measured for various volunteers. While all profiles show the same pattern, the thickness of the layers varies considerably from volunteer to volunteer.

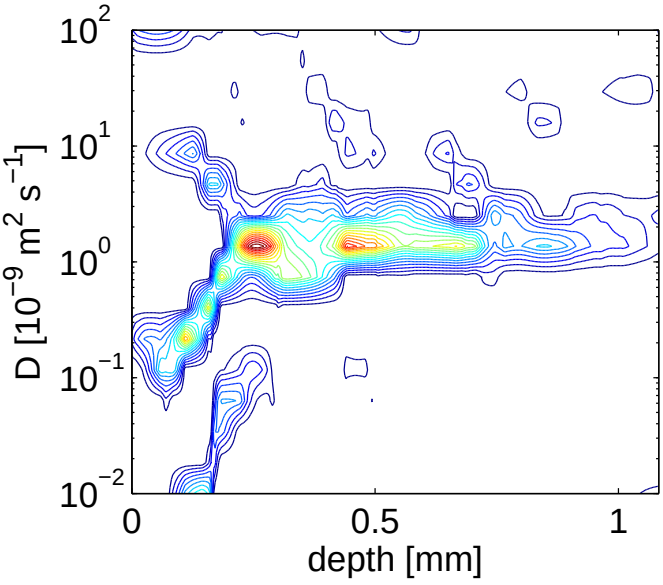

Figure 3.21: Depth-diffusion map corresponding to the skin tissue of the palm of a hand. A resolution of 100 μm was chosen to reduce the echo time (160 μs) and increase the SNR. Acquiring 128 scans for each diffusion encoding step with a recycle delay of 300 ms, 20 minutes were necessary to record the 32 encoding points in the diffusion direction. The evolution time in the stimulated spin echo was set to 5 ms.

Conclusion

In this part, we presented two single-sided sensors dedicated to the study of mortar dessication. Made from permanent magnets, these low cost portable sensors can be brought on-site to perform in-situ measurements. In particular, the existing NMR-MOUSE™ (PM25) was adapted to the study of rigid materials. We also developed a new magnet prototype. The idea was to generate a low but highly uniform static gradient in a 2 mm depth region by furnishing a conventional U-shaped magnet with small and movable permanent magnets. This approach allowed us to reduce the field gradient in one order of magnitude, keeping under control the lateral field variations across the excited layer. In this way, a 2 mm thick slice can be profiled with a spatial resolution of 25 μm without any slice repositioning.

Until here, the performance of each technique (low field and high field) was evidenced on phantoms and soft materials. In the next chapter, we report a study on the drying and dessication of cementitious material. We will combine the various techniques developed during this work and show which information can be extracted from each of them.

Bibliography

[BBE+98] B. Blümich, P. Blümler, G. Eidmann, A. Guthausen, R. Haken, U. Schmitz, K. Saito, and G. Zimmer. *Magn. Reson. Imaging*, 16(5-6):479–484, 1998.

[BPC08] B. Blümich, J. Perlo, and F. Casanova. *Progr. Nucl. Magn. Reson. Spectr.*, 52(4):197–269, 2008.

[BS90] C.J. Brinker and G.W. Scherer. *Sol-Gel Science : The Physics and Chemistry of Sol-Gel Processing*. Academic Press, 1990.

[Cal91] Paul T. Callaghan. *Principles of Nuclear Magnetic Resonance Microscopy*. Oxford Science Publications, 1991.

[CB03] F. Casanova and B. Blümich. *J. Magn. Reson.*, 163(1):38–45, 2003.

[CCH06] W.-H. Chang, J.-H. Chen, and L.-P. Hwang. *Magn. Reson. Imaging*, 24(8):1095–1102, 2006.

[CF04] P. T. Callaghan and I. Furó. *J. Chem. Phys.*, 120(8):4032–4038, 2004.

[CJ80] R.K. Cooper and J.A. Jackson. *J. Magn. Reson.*, 41(3):400–405, 1980.

[CP54] H.Y. Carr and E.M. Purcell. *Phys. Rev.*, 94(3):630–641, 1954.

[CPB06] F. Casanova, J. Perlo, and B. Blümich. *NMR Imaging in Chemical Engeneering*, chapter 2.4. Wiley-VCH Verlag, 2006.

[CPB11] F. Casanova, J. Perlo, and B. Blümich. *Single-Sided NMR*. Springer, 2011.

[DJGM03] M. Dias, Hadgraft J., P.M. Glover, and P.J. McDonald. *J. Phys. D:App. Phys.*, 36(4):364–368, 2003.

[ESBB96] G. Eidmann, R. Savelsberg, P. Blümler, and B. Blümich. *J. Magn. Reson., Ser. A*, 122(1):104–109, 1996.

[EWJH91] A.E. English, K.P. Whittall, M.L.G. Joy, and R.M. Henkelman. *Magn. Reson. Med.*, 22(2):425–434, 1991.

[FJ02] E. Fukushima and J.A. Jackson. Unilateral magnet having a remote uniform magnetic field region for nuclear magnetic resonance, 2002. US Patent, 6489872.

[GAB+99] P.M. Glover, P.S. Aptaker, J.R. Bowler, E. Ciampi, and P.J. McDonald. *J. Magn. Reson.*, 139(1):90–97, 1999.

[GNMCB10] J.C. Garcia-Naranjo, I.V. Mastikhin, B.G. Colpitts, and B.J. Balcom. *J. Magn. Reson.*, 207(2):337–344, 2010.

[GP95] G. Goelman and M.G. Prammer. *J. Magn. Reson.*, 113(1):11–18, 1995.

[Hal81] K. Halbach. *Nucl. Instrum. Methods Phys. Res.*, 187(1):109–117, 1981.

[HG00] M.D. Hürlimann and D.D. Griffin. *J. Magn. Reson.*, 143(1):120–135, 2000.

[HHS00] M. Holz, S.R. Heil, and A. Sacco. *Phys. Chem. Chem. Phys.*, 2(20):4740–4742, 2000.

[HR76] D.I. Hoult and R.E. Richards. *J. Magn. Reson.*, 24(1):71–85, 1976.

[HV02] M.D. Hürlimann and L. Venkataramanan. *J. Magn. Reson.*, 157(1):31–42, 2002.

[HVF02] M.D. Hürlimann, L. Venkataramanan, and C. Flaum. *J. Chem. Phys.*, 117(22):10223–10232, 2002.

[JBH80] J.A. Jackson, L.J. Burnett, and J.F. Harman. *J. Magn. Reson.*, 41(3):411–421, 1980.

[Kim97] R. Kimmich. *NMR Tomography Diffusometry Relaxometry*. Springer, 1997.

[MAMM07] P. J. McDonald, P.S. Aptaker, J. Mitchell, and M. Mulheron. *J. Magn. Reson.*, 185(1):1–11, 2007.

[McD97] P.J. McDonald. *Prog. Nucl. Magn. Reson. Spectrosc.*, 30:69–99, 1997.

[MCD+06] B. Manz, A. Coy, R. Dykstra, C.D. Eccles, M.W. Hunter, B.J. Parkinson, and P.T. Callaghan. *J. Magn. Reson.*, 183(1):25–31, 2006.

[MG58] S. Meiboom and D. Gill. *Rev. Sci. Instrum.*, 29(8):688–691, 1958.

[MHK71] J.L. Markley, W.J. Horsley, and M.P. Klein. *J. Chem. Phys.*, 55(7):3604–3605, 1971.

[MKMM05] P. J. McDonald, J. P. Korb, J. Mitchell, and L. Monteilhet. *Phys. Rev. E*, 72(1), 2005.

[MMCB05] A.E. Marble, I.V. Mastikhin, B.G. Colpitts, and B.J. Balcom. *J. Magn. Reson.*, 174(1):78–87, 2005.

[MMCB06] A.E. Marble, I.V. Mastikhin, B.G. Colpitts, and B.J. Balcom. *J. Magn. Reson.*, 183(2):228–234, 2006.

[MMCB07] A.E. Marble, I.V. Mastikhin, B.G. Colpitts, and B.J. Balcom. *J. Magn. Reson.*, 186(1):100–104, 2007.

[MMM+07] P. J. McDonald, J. Mitchell, M. Mulheron, P. S. Aptaker, J. P. Korb, and L. Monteilhet. *Cem. Concr. Res.*, 37(3):303–309, 2007.

[PBG+08] J.L. Paulsen, L.S. Bouchard, D. Graziani, B. Blümich, and Pines A. *PNAS*, 105(52):20601–20604, 2008.

[PCB04] J. Perlo, F. Casanova, and B. Blümich. *J. Magn. Reson.*, 166(2):228–235, 2004.

[PCB05] J. Perlo, F. Casanova, and B. Blümich. *J. Magn. Reson.*, 176(1):64–70, 2005.

[PCB06] J. Perlo, F. Casanova, and B. Blümich. *J. Magn. Reson.*, 180(2):274–279, 2006.

[PCB07] J. Perlo, F. Casanova, and B. Blümich. *Science*, 315(5815):1110–1112, 2007.

[PDC+05] J. Perlo, V. Demas, F. Casanova, C.A. Meriles, J. Reimer, A. Pines, and B. Blümich. *Science*, 308(5726):1279, 2005.

[PH02] Y.M. Pulyer and M.I. Hrovat. *IEEE Trans. Magn.*, 38(3):1553–1563, 2002.

[Pra01] P.J. Prado. *Magn. Reson. Imaging*, 19(3-4):505–508, 2001.

[Pra03] P.J. Prado. *Magn. Reson. Imaging*, 21(3-4):397–400, 2003.

[RCP+06] D.G. Rata, F. Casanova, J. Perlo, Demco D.E., and B. Blümich. *J. Magn. Reson.*, 180(2):229–235, 2006.

[RLS+05] S. Rahmatallah, Y. Li, H.C. Seton, I.S. Mackenzie, J.S. Gregory, and R.M. Aspden. *J. Magn. Reson.*, 173(1):23–28, 2005.

[RQB+91] S. Richard, B. Querleux, J. Bittoun, I. Idy-Peretti, O. Jolivet, E. Cermakova, and J.E. Lévêque. *Magn. Reson. Imaging*, 94(1):120–125, 1991.

[Son02] Y.-Q. Song. *J. Magn. Reson.*, 157(1):82–91, 2002.

[SVH+02] Y.-Q. Song, L. Venkataramanan, M.D. Hurlimann, M. Flaum, P. Frulla, and C. Straley. *J. Magn. Reson.*, 154(2):261–268, 2002.

[Tan70] J.E. Tanner. *J. Chem. Phys.*, 52(5):2523–2526, 1970.

[VLBBddL11] M. Van Landeghem, B. Bresson, B. Blümich, and J.-B. d'Espinose de Lacaillerie. *J. Magn. Reson.*, 211(1):60–66, 2011.

[VWKP68] R.L. Vold, J.S. Waugh, M.P. Klein, and D.E. Phelps. *J. Chem. Phys.*., 48(8):3831–3605, 1968.

APPLICATIONS

Chapter 4

Monitoring of drying and hydration of cementitious materials

In the instrumentation part, we presented two methods developed to study the drying and the hydration of cementitious materials. Before applying these techniques, we present briefly the physics and chemistry of cement and the available techniques to study it. We performed some measurements on building materials using these two techniques and correlated the results with the structure of the materials.

Figure 4.1: Picture of the application of a self smoothing mortar (from [Web11]). To get this property, some adjuvants are added to the basic composition of a mortar, which can modify its drying.

4.1 Cement basics

4.1.1 Cement chemistry

4.1.1.1 Chemistry nomenclature

Cement is such a particular material that it has its own chemical nomenclature. In practice, all the elements are described in term of oxides (see Table 4.1).

Table 4.1: Cement nomenclature and chemical notations.

Cement notation formula	Traditional formula	Name
C	CaO	Calcium oxide
S	SiO_2	Silica
A	Al_2O_3	Aluminium oxide
F	Fe_2O_3	Iron oxide
$\bar{S}$	SO_3	Sulphur oxide
H	H_2O	Water

Cement powder is a combination of oxides of calcium, silicon, aluminium and iron. Using the nomenclature in Table 4.1, the main components of Portland cement are C_3S and C_2S (tri-calcium and di-calcium silicate, also called Alite and Belite). The other phases are C_3A (tricalcium aluminate) and C_4AF (tetracalciumaluminoferrite). C_3S and C_2S represent 67 % of the content and are the two phases that develop the main strength during hydration forming a gel like calcium silicate hydrates (C−S−H) and calcium hydroxide ($Ca(OH)_2$ or "Portlandite"). Some additional materials such as gypsum ($C\bar{S}H_2$), flying ashes or silica smokes can be added to modify the properties of the cement.

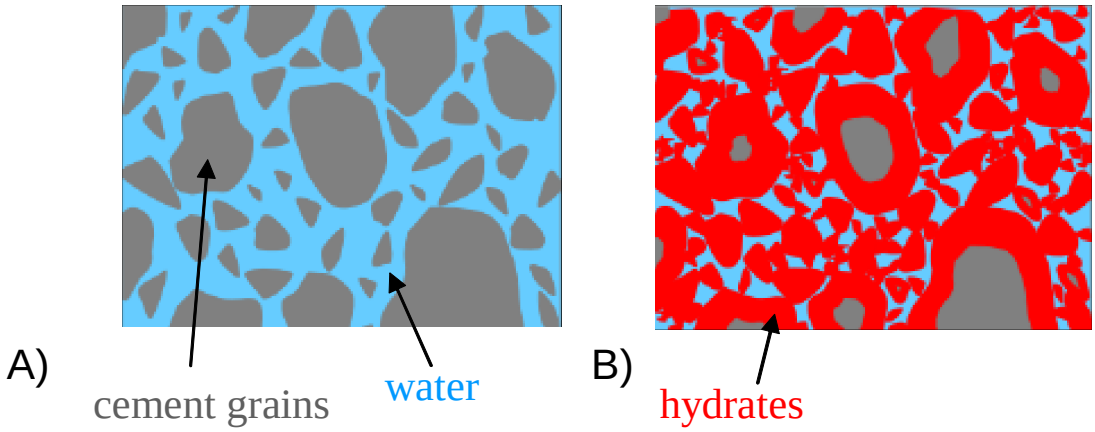

Figure 4.2: Sketch of cement grains before the hydration (A) and after (B). The outer layer of the grains dissolves, reacts with water and reprecipitates around the grain increasing its size and brings grains into contact.

4.1.1.2 Hydration chemistry

After mixing cement powder with water, there are two phenomena that happen together. One is hydration, which is the chemical reaction between the anhydrous cement and water. The other is the setting during which the paste becomes a solid. The soluble components present in the cement powder, when in contact with water, dissolve quickly, creating a saturated solution

from which the hydrates precipitate. The hydrates grow on the surface of the cement grain as long fibrillous structures which can eventually connect the grains to each other (see Figures 4.2 and 4.3). The fact that the specific volume of water is lower, on average, when in the hydrates than when in the free state causes the cement to be subject to chemical shrinkage during hydration, and therefore to be intrinsically and inevitably porous. The main chemical reactions in the hydration of cement are the hydration of C_3S and C_2S [Tay90]:

$$C_3S + (y + 3 - x)H_2O \longrightarrow C_xSH_y + (3 - x)CH$$

$$C_2S + (y' + 2 - x,)H_2O \longrightarrow C_{x'}SH_{y'} + (2 - x')CH$$

In parallel, the aluminates also hydrate. The main role of the gypsum is to slow down the aluminate hydration reaction at the early ages. This slowing of the reaction is necessary to keep the workability of cement paste (or concrete) for a time that allows casting.

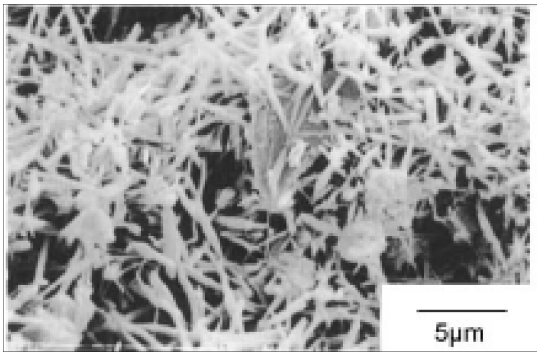

Figure 4.3: SEM picture of a hydrated sample after 180 minutes [SNID04].

4.1.1.3 C−S−H gels

The C−S−H gel is the most abundant reaction product (about 50% of the paste volume) and is also responsible for most of the engineering properties of cement paste [TJ08]. This is due to the fact that it forms a continuous layer that binds together the cement particles into a cohesive ensemble. As C−S−H gel grows outward from the cement particles, it develops an internal system of tiny pores, called gel pores, which are hundreds or thousands of times smaller than the so-called capillary pores. Although the liquid water in the gel pores is not part of the solid C−S−H phase in a chemical sense, it is physically isolated and thus cannot undergo further chemical reaction with the cement minerals. The porous C−S−H gel occupies significantly more volume than the original C_3S and C_2S mineral that it replaces. This causes the layers of C−S−H gel to expand outward and interconnect into a continuous phase. Thus, the cement paste first sets. As the hydration proceeds, it further hardens into a strong solid. Because the overall volume of the cement paste does not change significantly after mixing, the increase in the volume of solid phases causes the capillary pore system to decrease in volume and, if the ratio w/c is reasonably low, to become discontinuous. This decreases the permeability of the cement paste and it is more difficult for liquid water and dissolved ions to move through the pore system.

Table 4.2: Classification of pores in cement and water states according to [MM93].

	Type of Pore	Description	Size	Water
	Capillary pores	Medium	10nm - 10 μm	Evaporable Bulk Water
CSH	Gel Pores	Micropores	0.5 - 10 nm	Non-Evaporable Intermolecular Interactions
CSH	Interlayer Space	Molecular	$<$ 0.5 nm	Non evaporable Ionic/Covalent Bond
	Others	Microcracks	50 $\rightarrow$ 200 μm	Bulk water

4.1.2 Cement, a porous medium filled with water

4.1.2.1 The pore system

A typical pore size distribution for hardened cement encompasses a large range, extending from about a few nanometers to a few microns (see Table 4.2 [MM93]). The larger pores, ranging from 10 nm to 10 μm, are the residual unfilled spaces between cement grains, defined as capillary pores. The finest pores, ranging from approximately 0.5 nm to 10 nm, are called gel pores since they constitute the internal porosity of the C−S−H gel phase. While this is certainly a useful distinction, it should be kept in mind that the sizes of capillary and gel pores overlap, and the distribution of pore sizes in a cement paste is continuous. Internal features with dimensions of 0.5 nm or smaller are formed by the interlayer spaces of C−S−H gel. Various models explain this interlayer structure [Jen00, Non04, Ric08]. The C−S−H have a tobermorite-type layer structure. Each layer consists of central calcium and oxygen atoms sandwiched by silicate tetrahedral chains. Additional calcium and water are located in interlayer zones. A TEM picture and a sketch of this structure is displayed on Figure 4.4. Finally, some microcracks might occur during the hardening of cement, leading to micronic to millimetric pores filled with water.

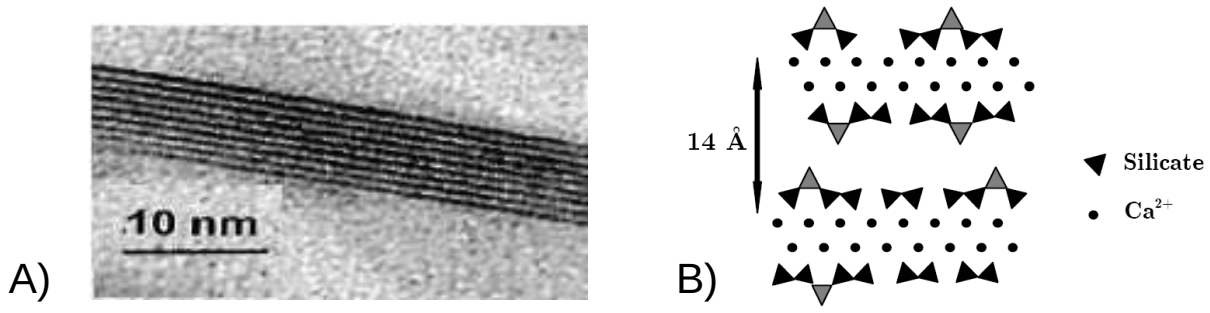

Figure 4.4: Layered structure of C−S−H from [Fra08]. A) TEM picture of a stack of C−S−H layers. B) Sketch of two layers of C−S−H.

4.1.2.2 Physical state of water in cement paste

The process of hydration can be seen as a progressive conversion of free (liquid) water in the capillary pores into bound water in the solid hydrated products. The water cannot simply be divided into bulk liquid water and chemically bound (structural) water. Indeed, the C−S−H gel phase also contains significant amounts of free and adsorbed water in its gel pores. Within its interlayer space, C−S−H also holds tightly bound water.

Liquid pore water

The water within a few molecular distances of a pore surface has properties very different from bulk liquid water. The first layer of molecules is physically adsorbed or hydrogen bounded on the surface, while the next few layers are aligned in a non-random way due to the polar nature of the water molecule. In the larger capillary pores the fraction of this "surface water" is negligible and on average the water maintains the properties of the bulk liquid. As the pore size decreases to the order of nanometers, the surface water becomes a significant fraction of the total water content. Thus, the physical properties of gel water (density, viscosity, ...) often differ from those of bulk water. For example, the rate of diffusion of surface water is significantly lower than that of bulk water. The reduced mobility of the surface water in a paste can be measured directly using NMR relaxometry, which is a important parameter in the determination of the pore size distribution [MKMM05, KMM$^+$07].

Interlayer water

The C−S−H structure contains in its interlayer a certain fraction of water that is more tightly bound than adsorbed on a gel pore surface. The traditional view of the C−S−H gel is based on a layered structure at the scale of tens of nanometers, because crystalline minerals with compositions similar to C−S−H gel have a layered structure [RFE99, BGT59, FRE98, Gir09, GddLS$^+$09] (see Fig. 4.4). The spaces between these layers can hold significant numbers of water molecules.

Structural water

This is the water that is chemically bound as hydroxyl groups in C−S−H

4.1.3 Classical techniques to study cements

The porous structure of cement is difficult to characterize. This is due to the very wide range (four orders of magnitude) over which the pore size distribution extends. Most of the methods are adapted to a particular range but very few cover this whole range.

4.1.3.1 Gas sorption

Gas sorption is the oldest and most widely used technique for measuring the surface area of porous materials. The physics and applications of gas sorption techniques are covered by Gregg and Sing [GS91]. Rarick et al. [RBJ94] reviewed the application of the gas sorption method to cement paste. Physical gas sorption is a volumetric method to measure the amount of gas adsorbed on the porous material surface. What is measured in practice with this technique is the mass of gas adsorbed as a function of the gas pressure. The analysis is based on the theory developed by Brunauer [BET38]. From the number of mole X of adsorbed gas, the specific surface area S of the porous medium can be deduced given the cross sectional area of a gas mole σ:

$$S = \frac{X\sigma}{m} \tag{4.1}$$

where m is the mass of adsorbed gas. Furthermore, from the pressure p, the Kelvin equation leads to an estimation of the radius r assuming cylindrical pores :

$$r = \frac{-2\,V_{\mathrm{mol}}\,\gamma_{\mathrm{vs}}}{R\,T\,\ln\left(p/p_0\right)} \tag{4.2}$$

where γ_{vs} is the surface tension at the vapour-solid interface, V_{mol} the molar volume of adsorbed gas, R the universal gas constant, T the temperature and p_0 the saturated vapour pressure. One of the drawbacks when using this technique on cementitious materials is that, it requires to desaturate the porosity, ie to dry the sample, which affects the C−S−H gel structure of cement [Par81].

4.1.3.2 Cryoporometry

Cryoporometry is based on the fact that the water restricted in pores freezes at a lower temperature than in the bulk. The melting-point depression ΔT of a liquid in a porous material according to the so-called Gibbs-Thomson equation is given by [VPK02]:

$$\Delta T = \frac{4\,\sigma_{cl}\,T}{a\,\Delta H_f\,\rho_c} \tag{4.3}$$

where T is the normal (bulk) melting temperature, a is the diameter of a cylindrical crystal, σ_{cl} is the crystal-liquid interfacial energy, ΔH_f is the bulk enthalpy of fusion and ρ_c is the density of the frozen liquid (crystal). Then, the proportion of liquid water and solid water is determined either by classical calorimetric method (measurement of the melting heat as a function of temperature) or by NMR [Der69, SRS93]. The main advantage of this method for cement compared to gas sorption is that it does not require any drying.

4.1.3.3 Mercury Intrusion Porosimetry

This technique is based on the fact that a non wetting liquid can enter the pores of a solid only under pressure. Mercury does not wet the paste and will only enter the pore system if it is forced in by an external pressure. The advantage of this is that the pressure required increases as the size of the pore decreases. Assuming cylindrical pores of size r the pressure p required is given by the Washburn equation [Was21]:

$$p = \frac{-2\,\gamma\,\cos(\theta)}{r} \tag{4.4}$$

where γ is the surface energy of the liquid and θ the contact angle. A plot of the intruded volume of mercury as a function of the external pressure thus gives an indication of the pore size distribution (how the total porosity is distributed among different size pores).

However, this technique has major drawbacks. First, the method measures the size of the pore throats and not the pore itself. Thus, when a large pore can only be accessed through a small opening, the entire volume accessed is registered as small porosity. Second, the data analysis assumes cylindrical pores and a constant contact angle while these assumptions are not strictly correct for cement paste [GM81]. Then, as with gas sorption, the drying treatment necessarily changes the pore structure. Finally, the fine structure of cement may be damaged by the large stresses needed to intrude the mercury.

4.1.3.4 Scanning Electron Microscopy (SEM)

Compared to the previous ones, this method is a direct technique. The sample is scanned with a high energy beam of electrons. Various parameters can be accessed if one looks at the secondary electrons [SG88] or backscattered electrons [SPPP87]. Secondary electrons provide morphological surface information whereas backscattered electrons (BSE) allows to spatially resolve the chemical composition.

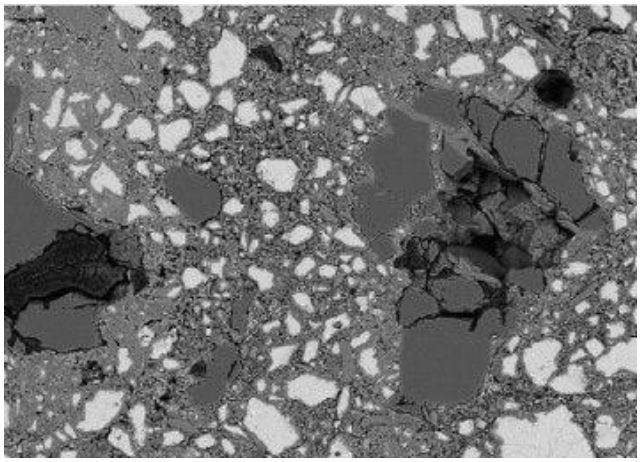

Figure 4.5: SEM-BSE image of cement from [HGGS07].

The main drawback of this method is its destructive feature. Indeed, during preparation, the sample must be dried, vacuumed and impregnated with a resin that fills the pores. After impregnation a careful polishing procedure is required to have good resolution. Additional limitations are the fact that giving a 2D section, SEM does not allow to determine the connectivity of the pores and it has a relatively limited range of applicability (greater than 500 nm) [TJ08].

4.1.3.5 Transmission Electron Microscopy (TEM)

This technique is based on the transmission of electrons through a thin section of material. Due to the very short wavelength of the electrons (a few picometers) at typical operating voltages of 200-300 kV, the diffraction is not a problem and the achievable resolution goes down to the subnanometric scale. This allows one, for example, to see the coherence domains of the C−S−H structure [VLYX96] (see Fig. 4.6). With this technique, the sample preparation is crucial and its thickness should not exceed a few nanometers. Although the sample conditioning may again affect the sample structure, this technique provides information on the structure at the nanoscale, which cannot be accessed directly by other techniques.

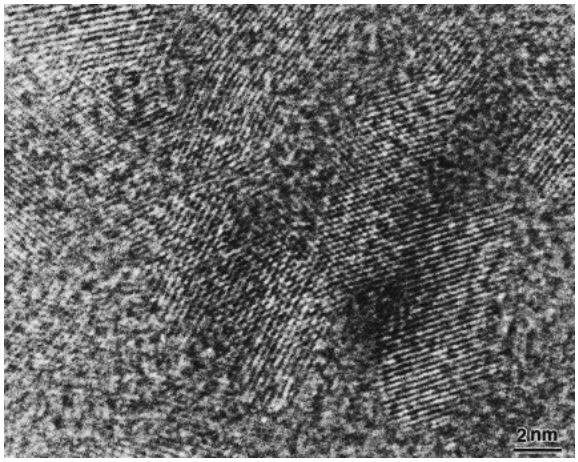

Figure 4.6: Coherence domain in C−S−H from [VLYX96].

4.1.4 Dynamic imaging techniques

In the methods presented in the previous section, either there was no space localization (gas sorption, cryoporometry, mercury intrusion porosimetry) or the sample preparation was such that no dynamic observation of the evolution of the cement was possible. In this part, we focus on two alternative techniques which solve this problem.

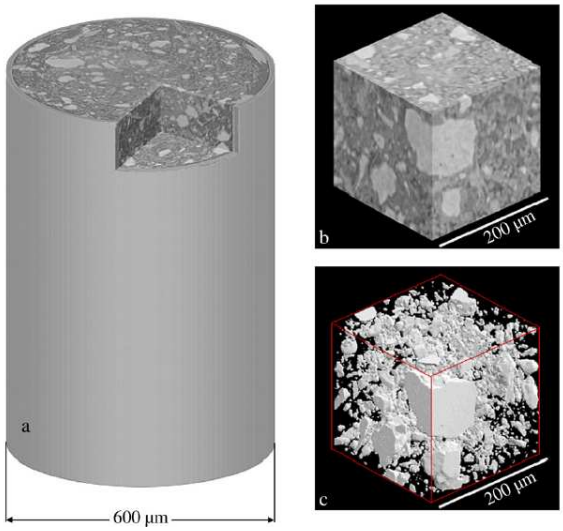

Figure 4.7: (a) 3 days old reconstructed sample, (b) volume of interest and (c) segmented cement fraction from [GSG+07].

4.1.4.1 X-ray microtomography

The principle of this method is based on a 3D computed reconstruction of a sample from 2D X-ray absorption data acquired at different angles around its axis of rotation. The higher the number of projections is, the better is the resolution of features in the reconstructed volume. The homogeneous 2D X ray beam is generated by a synchrotron and resolutions of about 1 μm can be reached on cement based materials. Bentz et al. [BQK+00] reported the first tomographic scans of cement pastes. The possibility to extract the microstructural development of cementitious materials and access to the real pore network that forms and its evolution with time make this technique very interesting [GSG+07].

The drawbacks of this method is the limitation of the resolution due to the relatively similar attenuation coefficients of pores and C−S−H relative to unreacted cement, which makes the pores hard to resolve. Another problem encountered here concerns sample preparation since it is very difficult to control the homogeneity and water to cement ratio in the very fine capillary tubes (0.5 mm wide) used. Moreover, the resolution of fine pores is only possible when the sample size is also small. For larger samples there would be lower transmission of X-rays therefore more attenuation problems as well as much longer acquisition times.

4.1.4.2 Magnetic Resonance Imaging

This is the method we study. We focus on this method in the next sections.

4.1.5 Mortars

Practically, cement is never used alone. It is used as a glue to bind together various elements (sand, rocks, concrete blocks, ...). Mortars are usually obtained by mixing cement or lime,

sand, water and some additives such as polymers or glass fibers. The proportion of each of these elements depends on the application (brick binding, crack filling, tiling, insulation, ...) and its environment. An overview of the applications is available on the website : `http://www.weber.fr/`.

4.2 MRI techniques to study cementitious materials

4.2.1 Introduction

Contrary to X ray tomography, MRI is not a direct method as it relies on the observation of protons of water molecules within the cement paste to deduce properties about the porous structure of the surrounding medium. However, it can be performed on a macroscopic scale and is very sensitive to water dynamics. The earliest report of the use of MRI in this context is by Gummerson et al. [GHH$^+$79].

Table 4.3: Water states in cement and the corresponding relaxation rates.

Type of pore	State of water	T_1	T_2
Capillary pores	Free water	> 10 ms	> 10 ms
Gel pores	Surface water	0.3-10 ms	0.3-10 ms
Interlayer space	Chemically bound water	> 100 ms	< 10 μs

4.2.2 States of water in cementitious materials

It is now well established that measurements of the proton NMR relaxation times T_2 and T_1 give access not only to the water content but also to the saturated pore-size distribution of a hydrating cement paste [BGM$^+$98, KMMM07a]. Numerous NMR experiments carried out at various frequencies (from kHz up to the MHz), are based on the following hypotheses [KMM$^+$07, KMMM07a, KMMM07b]:

1. Almost all the water molecules in a cement paste can be viewed as to belong to a pore distribution.

2. The water diffusion is sufficiently fast to reach the requirements of the biphasic fast exchange model that associates a given pore size to a measured overall relaxation time.

3. The method is quantitative provided a prior calibration of the paramagnetic sources of relaxation (Fe^{3+} and Mn^{2+}) is made by electronic spin resonance technique (ESR).

For all kinds of cement, it is now accepted that the paramagnetic impurities (Fe^{3+} and Mn^{2+}) at the surface of the pores control the relaxation rate of all the protons in the pore, even for white cement (with low concentration of Fe^{3+}) [MKMM05]. Of course, the structural hydroxyl groups within the layered structure of the C−S−H are not defined as a pore. This intralayer "proton species" is composed of the structural hydroxyl groups within the C−S−H and in the Portlandite CH. There are also hydroxyls and structural water in the calcium aluminate hydrates [Gir09], but we limit the present study to white cement where these phases are expected to contribute little to the total proton signal. Concerning the C−S−H interlayer water, it must be emphasized that it does not strictly belong to a pore as its removal irreversibly modifies the 1.4 nm "tobermorite-like" structure. Another important aspect is that the C−S−H gel is inherently nanoporous, and that, although the water confined in those very small pores (2 nm) is not strictly speaking "structural", its removal would imply the development of extreme capillary

pressures that would destroy the gel structure as well. This non-removable water confined in the nanopores of the C−S−H gel is called the C−S−H "gel" water. The rest of the cement paste water, in pores scaling from a few nanometers up to a few micrometers, is called the capillary water. The specificity of this type of water is that it can be reversibly removed without any destruction of the microstructure of the cement paste. The various kind of waters present and their associated relaxation rates are summarized in Table 4.3.

4.2.3 From the relaxation rates to the porous structure

For all kinds of cement, it is now accepted that the paramagnetic impurities at the surface of the pores control the NMR relaxation rate of all the water protons in the pore, even for white cement (with low concentration of Fe^{3+}) [MKMM05, VRM10]. The relaxation process is due to the water molecular diffusion within the pore, and transiently on the surface during a limiting time τ_s before returning into the bulk. During its stay onto the surface, the water molecule undergoes 2D diffusion on the pore surface with a characteristic correlation time τ_m and can enter the local ligand field of a paramagnetic impurity embedded within the pore wall. The magnetic interaction with the paramagnetic centers is the dominant contribution to the surface relaxation, even for cement with low Fe content. The surface residence time τ_s is very short compared to the NMR measurement time (fast exchange limit) so that for a given pore size, the overall relaxation rate $1/T_2^{\text{eff}}$ of water is an average of the bulk liquid relaxation rate $1/T_2^{\text{bulk}}$ and the enhanced surface relaxation rate, weighted according to the surface-to-volume ratio S/V of the pore [ZB57, BT79]:

$$\frac{1}{T_2^{\text{eff}}} = \frac{1}{T_2^{\text{bulk}}} + \rho\frac{S}{V} \tag{4.5}$$

where ρ is the surface relaxivity. Thus, the relaxation rate reflects potentially the pore size and morphology. For the complete pore network, the total experimental magnetic decay $S(t)$ is the superposition of the exponential decays T_2^i characteristics of each pore size i weighted by their relative population A_i:

$$S(t) = \sum_i A_i \exp\left(-\frac{t}{T_2^i}\right) \tag{4.6}$$

Therefore, in principle, NMR relaxation analysis can provide the relative abundance of each water populations in the cement paste (in the hydrates structure, in the C-S-H gel pores, in the capillary pores) and can even provide the corresponding pore size distribution [PPL+05, HJS94]. The problem is thus to recover the pore-size distribution from the NMR signal. The corresponding mathematical procedure is formally a Laplace inversion. This operation, a key-point of the analysis, was recently facilitated by the availability of stable multi-dimensional algorithms executable on desktop computers [VSH02]. In a typical white cement paste hydrated during a few days with a water/solid ratio of 0.4, the extraction of each T_2 component of the relaxation leads to a discrete distribution which ranges from 200 μs (smallest pore size, 2 nm) up to 1 s (free water, infinite pore size) [MKMM05] (see Table 4.4).

The same conclusions can be drawn for T_1 relaxation rates [FR08]. Even without a predictive model, some authors [GPC+00] have drawn precise conclusions about the evolution of each kind of water during the hydration of cement paste.

Table 4.4: T_2 values versus pore size in white cement paste (from [MKMM05]).

T_2 value	Pore size
200 μs	2 nm
1 ms	16 nm
50 ms	170 nm
200 ms	270 nm
1 s	free water

4.2.4 Diffusometry

Magnetic fields make spins rotate. In other words, magnetic fields shift the phase of spins by a quantity proportional to the amplitude of the magnetic field and its time of application. In presence of magnetic field gradients, as the amplitude of the magnetic field varies with the position, the phase shift experienced by spins is also a function of the position. Henceforth, when spins are moving randomly or diffusing through a magnetic field gradient, they explore regions with various magnetic field amplitudes and acquire random phase shifts. These phase shifts lead to an additional attenuation of the signal and can be seen as an additional relaxation rate which adds to the relaxation rate measured in homogeneous field. Then, it is possible to reverse the problem and from the measurement of the relaxation rates, deduce the diffusion coefficients assuming a model for the type of diffusion [Cal91, Kim97, RCP+06, Woe61]. Here, we present an NMR sequence which is often used in porous media analysis as well as some applications.

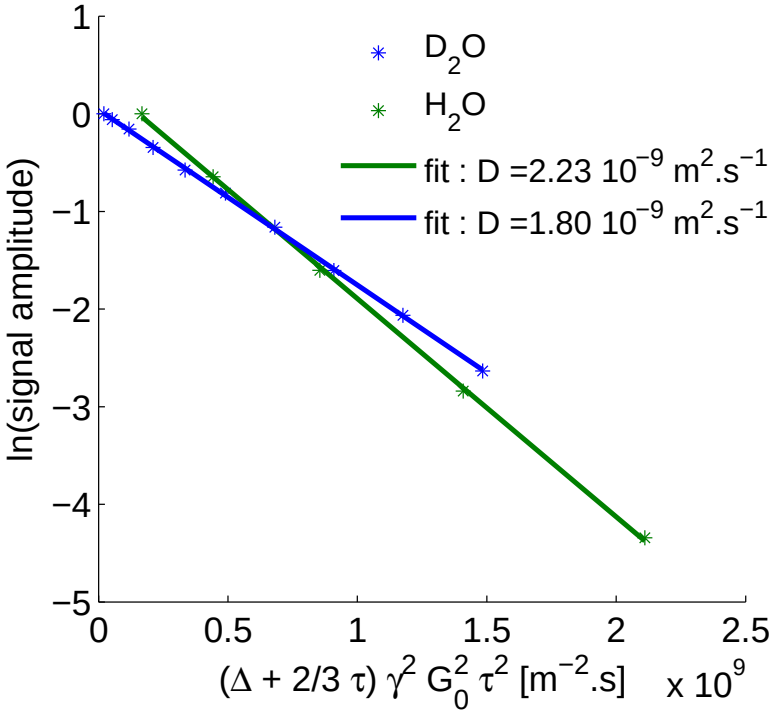

Figure 4.8: Diffusion measurements of normal and heavy water

4.2.4.1 Effect of diffusion on transverse and longitudinal relaxation rates

When using high magnetic field gradients, one should be aware that the impact of diffusion on both T_1 and T_2 measurements can already be seen at that echo times. In presence of diffusion, the loss of coherence from displacements in field gradients may be seen as an additional transverse relaxation rate. In the CPMG case, Equation 4.5 can be rewritten [Cal91] as:

$$\frac{1}{T_{2\,\mathrm{eff}}} = \frac{1}{T_{2\,\mathrm{bulk}}} + \rho_2 \frac{S}{V} + \frac{D\,\gamma\,G^2\,t_{\mathrm{E}}^2}{12} \tag{4.7}$$

where G is the magnetic field gradient and t_{E} the echo time associated with the CPMG train. In a large volume, T_1 is unaffected by diffusion, however, when narrow slices are excited, diffusive transport in and out of the slices modifies the apparent longitudinal relaxation time [NWN04].

4.2.4.2 Method to measure self-diffusion coefficients

The pulse sequence used is a stimulated spin echo. It consists of three 90° pulses. The first pulse flips the magnetization into the xy plane. After a duration τ (encoding time), a second 90° stores the magnetization along the z axis. Then, T_2 decay is stopped, the magnetization relaxes only with T_1 during a time Δ (evolution time). Finally, a third 90° pulse flips the magnetization back into the xy plane and an echo arises at time τ following the last pulse.

Because spins diffuse, they move randomly through the gradient. Therefore, they progressively loose their coherence and the amplitude of the stimulated echo is affected. It is possible to calculate theoretically the attenuation of the echo. The whole calculation is written in Appendix A, so we only recall the final expression :

$$\frac{I}{I_0} = \frac{1}{2} \exp\left(-\gamma^2 G^2 D \tau^2 \left\{ \frac{2}{3}\tau + \Delta \right\} - \frac{2\tau}{T_2} - \frac{\Delta}{T_1} \right) \tag{4.8}$$

For the condition $\Delta \ll T_1$ and $\tau \ll T_2$, the previous equation becomes independent of both, T_1 and T_2:

$$\frac{I}{I_0} = \frac{1}{2} \exp\left(-\gamma^2 G^2 D \tau^2 \left\{ \frac{2}{3}\tau + \Delta \right\} \right) \tag{4.9}$$

So, by plotting $\log(I/I_0)$ versus $\gamma^2 G^2 \tau^2 \left\{ \frac{2}{3}\tau + \Delta \right\}$, the diffusion coefficient can be extracted by taking the slope. As an example, we measured there the diffusion coefficient of normal water and heavy water at 150 MHz and 23.05 MHz, respectively. The gradient was adjusted to $G = 52$ T/m in order to find the right value for the self-diffusion coefficient of normal water at 25 °C and then, the self-diffusion coefficient of heavy water was measured. Figure 4.8 exhibits the values for these two experiments. The diffusion coefficient found for heavy water is in good agreement with the values in the literature [AJ76].

4.2.4.3 Application to porous media

There are other sequences than a stimulated spin echo to measure diffusion. However, this sequence is particularly interesting for the following reason. Contrary to a classical Hahn echo, it contains an evolution time during which the T_2 relaxation is stopped and spins have the opportunity to explore by diffusion a distance ($\sqrt{6D\Delta}$ assuming a Fickian diffusion) which can be chosen by adjusting the experimental parameter Δ. Let us take the example of a porous

medium with a typical pore size a. As long as $\sqrt{6D\Delta} < a$, one expect to measure the diffusion coefficient of spins in bulk. However, as soon as $\sqrt{6D\Delta}$ becomes comparable to a, then spins start to feel the restriction due to the pore wall. As they cannot move further, their apparent diffusion coefficient is smaller. Thus, by measuring the apparent diffusion coefficient for various Δ, it is possible to extract some physical parameters such as the pore-size distribution and the tortuosity [HV02, MSS93].

4.2.5 A need for a localized study

To follow the drying process, the simplest study can be performed on the bulk material. However, to actually discriminate drying and hydration mechanisms, the monitoring of the total water in the sample versus time is not sufficient. Due to the anisotropy of the evaporation process, it is necessary to follow the distribution and evolution of water within the pore system not only in time but also in space. This justifies the combination of NMR relaxation with MRI (Magnetic Resonance Imaging) techniques. As all of the evaporation occurs at the paste/air interface, 1D-profiling methods are the most adequate tool. When dealing with cement paste, the MRI technique must rely on a stable and large gradient to overcome the rapid relaxation rates (see Table 4.3). This reduces the techniques of choice to the ones involving strong static gradients, such as STRAY Field Imaging (STRAFI). Indeed, there is already a significant body of literature concerning the study of cement paste using high-field STRAFI from superconducting magnets [McD97, NRS$^+$96, BGM$^+$98, BBM$^+$05, Nun06], but never as a function of the temperature and humidity, which however influences deeply the drying. Alternatively, some authors have chosen to use single sided permanent magnets with lower fields and static gradients such as the GarField [MMM$^+$07a, MAMM07] or the NMR-MOUSE™ [BPC08].
Here, we apply the two complementary NMR profiling methods the STRAFI and the NMR-MOUSE™ to the setting of a cement paste for studying the simultaneous effects of self-desiccation and evaporation by varying the temperature and humidity conditions.

4.3 Respective role of hydration and evaporation during drying of a cement paste

4.3.1 Materials and methods

4.3.1.1 Hardware

The principles of the profile NMR-MOUSE™ PM25 and the STRAFI experiments have been described in chapters 2 and 3, respectively.

MOUSE setup

The profile NMR-MOUSE™ PM25 mounted on its lift fits a $38 \times 38 \times 38$ cm^3 box and can easily be introduced in a commercial temperature and humidity cabinet (see Fig. 4.9A). This cabinet (model LHU-113) was provided by ESPEC™. To measure the effective relaxation rate T_2, we used a CPMG detection sequence [HG00] with an echo time of 140 μs which was the shortest echo time we could achieve to scan the sample until a depth of 20 mm over the magnet. Each echo from the train was recorded independently so T_2 can also be extracted either by exponential fit or Inverse Laplace Transformation.

STRAFI setup

The conventional STRAFI setup is completed by a humidity and temperature control (see Fig. 4.9B). The temperature is controlled by a classical NMR temperature unit manufactured by Eurotherm™. A thermocouple placed close to the sample allows the regulation of a heater inside a dewar positioned at the bottom of the probe. The range of temperatures which can be

A) 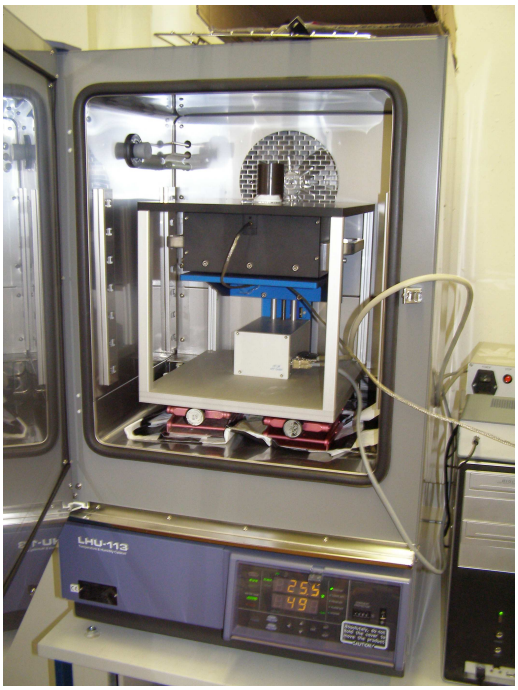 B) 

Figure 4.9: A) Picture of the profile NMR-MOUSE™ used. It was inserted inside a temperature and humidity cabinet manufactured by ESPEC™. The sample sits at the top of the black plate. B) Picture of the STRAFI setup. The sample is placed at the top of an alumina rod driven by a stepper motor. Both humidity and temperature are regulated.

achieved stands between 20 °C (ambient temperature) and 80 °C. The humidity is regulated by manually mixing dry air with water saturated air obtained using bubblers. This setup allows reaching humidity levels from 10 to 70 % rH.

Similarly to the NMR-MOUSE™, a CPMG detection train with an echo time of 40 μs was used to measure the effective relaxation rate T_2. Each echo from the train was recorded independently so T_2 can also be extracted either by exponential fit or Inverse Laplace Transformation.

4.3.1.2 Preparation of the white cement paste

The white cement has been provided by Saint-Gobain Recherche (white cement CEM II) and was used as received. The cement paste was prepared with a standard water/cement ratio equal to 0.4. In the case of experiments using the NMR-MOUSE™, the paste was prepared in a conventional 250 mL plastic beaker, directly placed on the plate above the sensor. During STRAFI studies, the water and cement mixture was cast into a 10 mm glass tube. The unsealed tube was then introduced inside our home-made probe in the glass cylinder used to guide the sample and where humidity and temperature are regulated. The origin of time is fixed at the moment when cement and water are put together.

4.3.2 Complementarity of the NMR-MOUSE™ and STRAFI profiles

The determination of the porous structure of cement by proton NMR requires the measurement of the signal decay (see Eqn. 4.6). This measurement is performed using the CPMG sequence. The first echo obtained is removed as its amplitude is shifted due to the presence of the gradient [GP95]. The obtained decay is then either fitted by multi-exponential functions or inverted using inverse Laplace transform (ILT) algorithm. Due to the fine dependence of T_2 on pore sizes (see Table 4.4), three T_2's (or distributions of T_2's) are usually expected in white ce-

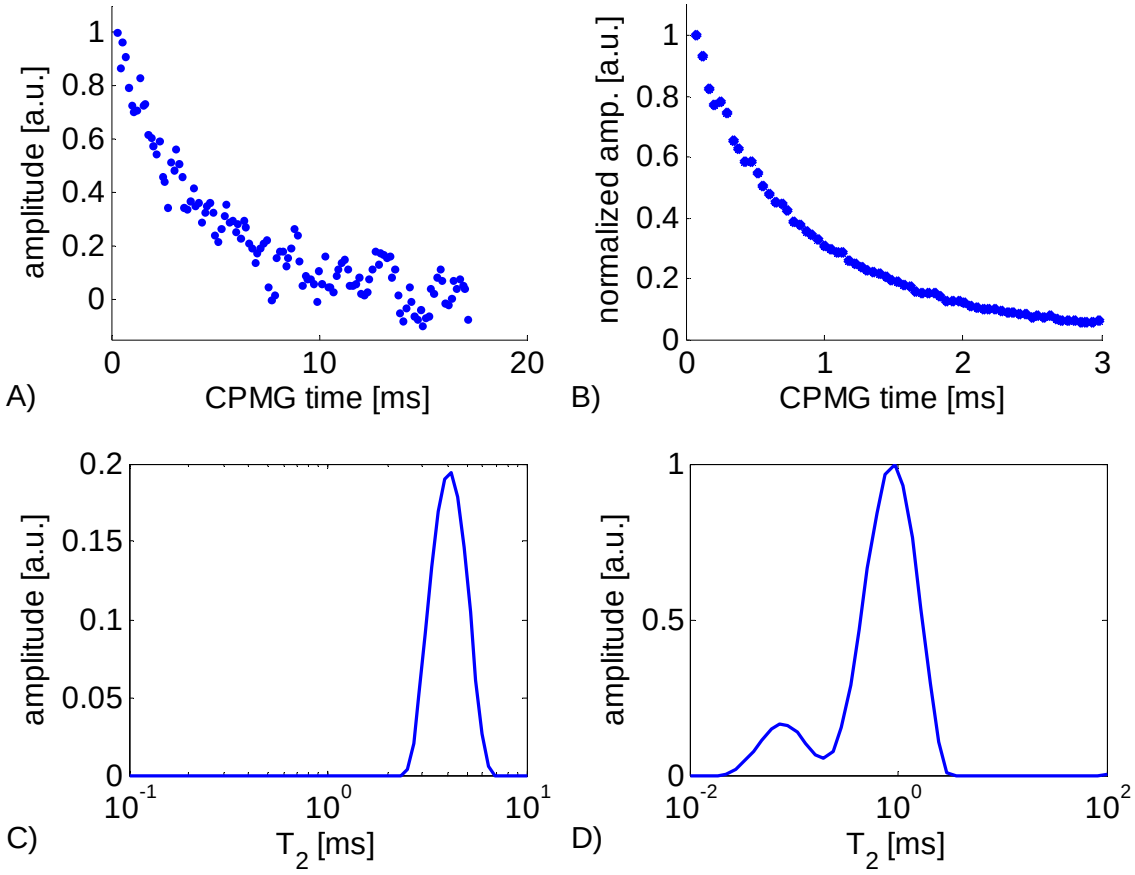

Figure 4.10: CPMG decays and associated T_2 distributions of white cement prepared with a ratio water/cement equal to 0.4. after 8 hours of drying. A) CPMG decay obtained using the NMR-MOUSE™. The echo time was set to 140 μs and the number of echoes to 128. The repetition time was 1 s. and the number of scans 512. This led to an experimental time of about 8.5 minutes. B) CPMG decay obtained using STRAFI. The echo time was 40 μs and the number of echoes 400. Here are displayed only the first 64 echoes. The repetition time was 1 s. and the number of scans is 512, leading to an experimental time of 8.5 min. C) T_2 distribution obtained from the ILT of the CPMG decay displayed on A). D) T_2 distribution obtained from the ILT of the CPMG decay displayed on B).

ment paste. These correspond to free water (water in capillary pores), "gel" water and structural water in the hydrates, respectively. Figure 4.10 exhibits typical CPMG decays of a white cement paste obtained using the NMR-MOUSE™ (A) and STRAFI (B). Both decays correspond to a drying of 8 hours. The associated ILT's are exhibited in Figure 4.10C and D, respectively. In the case of the NMR-MOUSE™, the distribution of the T_2's are mono-modal. The single peak is attributed to free water. However, the echo time of the NMR-MOUSE™ (140 μs) does not allow to see relaxing species with a T_2 shorter than a few hundreds of microseconds. Thus, "gel" water and structural water are naturally filtered out when white cement is measured with this tool. On the contrary, the T_2 distribution recorded by STRAFI is bimodal (see Fig. 4.10D). This can be achieved because the echo time in the CPMG detection is much shorter (40 μs). The two peaks are attributed to free water ($T_2 \approx 1$ ms) and "gel" water (around $T_2 \approx 100$ μs). Still the structural water (T_2 expected around 10 μs) cannot be seen by STRAFI. As a consequence, this preliminary study shows that we dispose of two complementary tools. The NMR-MOUSE™ being sensitive to long T_2's, is a simple indicator for capillary water content gradients within

white cement due to transfer to the interface such as during evaporation. The STRAFI being sensitive to "gel" water is expected to provide more information about the porous structure.

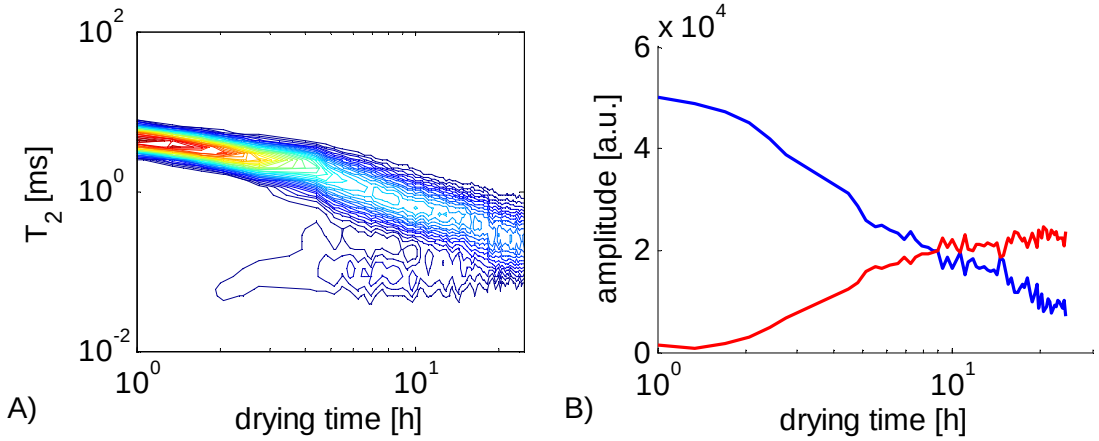

Figure 4.11: A) T_2 distribution of a white cement prepared with a water/cement ratio of 0.4. This distribution is the result of a numerical ILT of CPMG decays measured by STRAFI at a fixed height within the sample. The CPMG train contains 400 echoes and the echo time is 40 μs. Using a recycle delay of 1 s and 1024 scans, one point was measured every 17 min. The color code reveals the intensity of each peak in the Laplace distribution. B) Amplitude of the two populations evidenced by the ILT exhibited in a). This amplitude was obtained by double exponential fitting of the CPMG decay. The blue (resp. red) curve represents the population with long (resp. short) T_2.

4.3.3 Evolution of the porous structure of white cement

4.3.3.1 1D experiment

Study at a single position

To follow the evolution of the porous structure of white cement, a sample of white cement paste was prepared and measured by STRAFI using a CPMG detection train. This measurement was performed at a single height within the sample in order to accumulate more scans and obtain a better signal-to-noise ratio necessary for a good ILT. The experiment was performed in one day and a decay was measured every 17 minutes. Afterwards, each decay was numerically inverted to provide the T_2 distribution versus the hydration time (Fig. 4.11A) and a double exponential fit was performed. The amplitude of the two decays is displayed in Figure 4.11B. During the first 4 hours of hydration, a single T_2 can be realistically defined with a good level of confidence and the distribution can be considered as mono-modal, going from a T_2 of 4.5 ms at time $t = 0$, to 2 ms at $t = 5$ hours. After a hydration time of 10 h, the amplitude of the population with the long T_2 decreases below the amplitude of the population with short T_2. This corresponds to the setting time of the paste and the formation of the percolating C−S−H gel network. The long T_2 value shortens progressively from 1 ms down to 400 μs between 10 hours and 20 hours while the shorter T_2 is constant at about 150 μs.

Previous work [MKMM05] helps us to clearly attribute each kind of water with the porous structure (see Table 4.4). For example, the T_2 of 5 ms observed at a drying time of about 6 hours can be attributed to capillary pores of radius $r \approx 120$ nm. When T_2 is equal to 1 ms, this has previously been attributed to pores of radius $r = 16$ nm. The short T_2 of 150 μs corresponds to the gel C−S−H nanopores of a few nanometers. However, the T_2 of the chemically bound water (10-30 μs [BBM$^+$05], CH, and structural water of C−S−H) is not observed in the previous

analysis. Actually, it can be partially observed by displaying the first point of the CPMG echo train which is usually removed as it is known to be weighted by a factor 2/3 due to the presence of the magnetic field gradient [HG00, GP95]. Usually, the first echo of the CPMG appears with a lower intensity than the second. When studying cement, we noticed that the first echo occurring 30 μs after the first pulse, is much more intense than the others. This is interpreted as the contribution of the chemically bound water in cement hydrates which has not completely relaxed yet. In order to stabilize the analysis, we chose to remove the first point before processing the data in Figure 4.11 as well as in the following analysis.

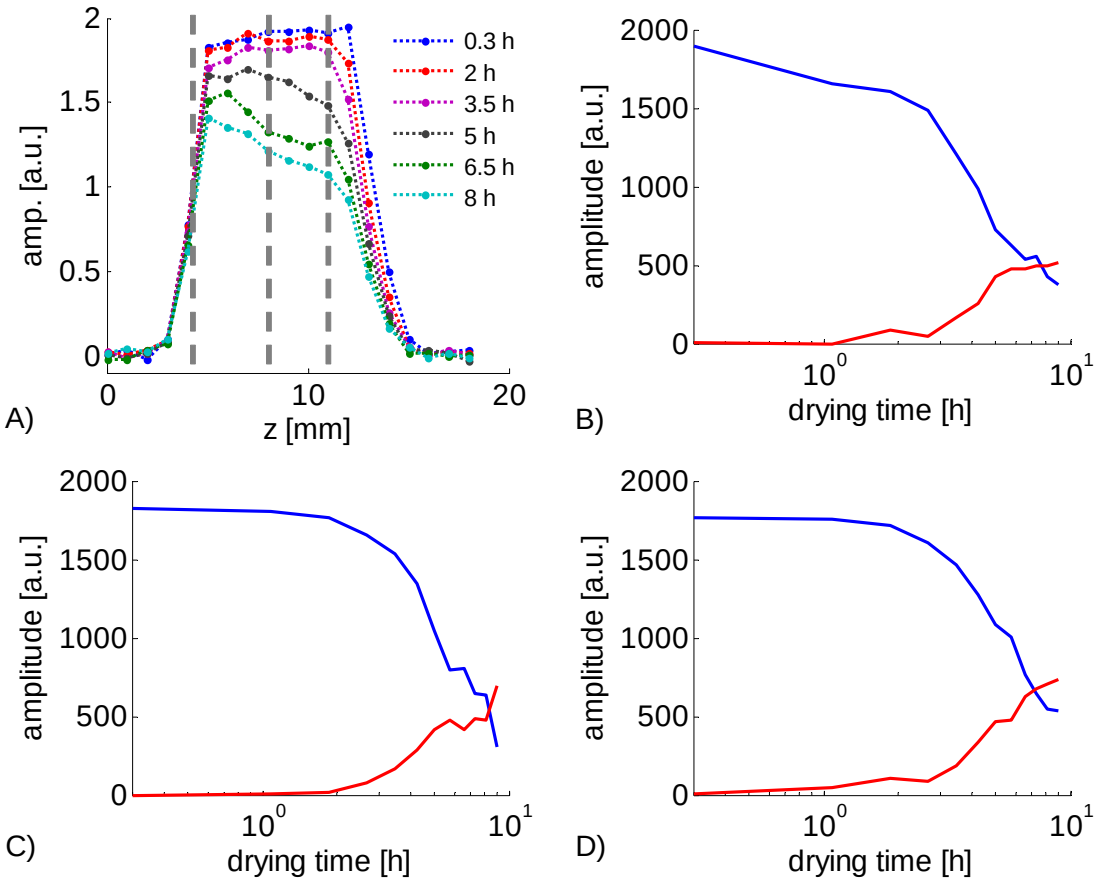

Figure 4.12: A) Profiles measured by STRAFI at various hydration time following the preparation of a sample of white cement (w/c = 0.4) at 25 °C and 30 %rH. These profiles were measured using a CPMG detection train with an echo time of 40 μs. For the profiles, only the first echo was processed. The recycling delay was 1 s and the number of scans 64 in order to complete the 19 points of the profile in 20 min. The vertical grey dotted lines correspond to the position were a double exponential fit was performed. The amplitude of the long T_2 (blue solid line) and short T_2 (red solid line) versus the hydration time are exhibited in plots (B), (C) and (D).

Spatially resolved study

The advantage of the experiment presented here is the clear attribution of the different kinds of water which successively appear in the material. It also evidences the discrete characteristics of the developing porous network with time. The interesting new result is that it can be performed with spatial resolution. An example of this kind of analysis is depicted in Figure 4.12. Figure 4.12A exhibits profiles of white cement measured at various hydration times using only the first echo of the CPMG echo train. At 25 °C and 30 %rH, a gradient in the distribution of water

is clearly induced along the sample. To know if this drying effect affects or not the kinetics of structuring of the material, a T_2 analysis similar to the one of Figure 4.11B was performed at various heights in the sample (at the bottom, the middle and at the top, positions depicted by the vertical grey dotted lines in Figure 4.12A). The comparison of the kinetics of emergence of the population with the short T_2 (red curve) and the decrease of the population with long T_2 at these various positions (Figure 4.12B, C and D) shows that the kinetics of the structuring is not affected by the drying.

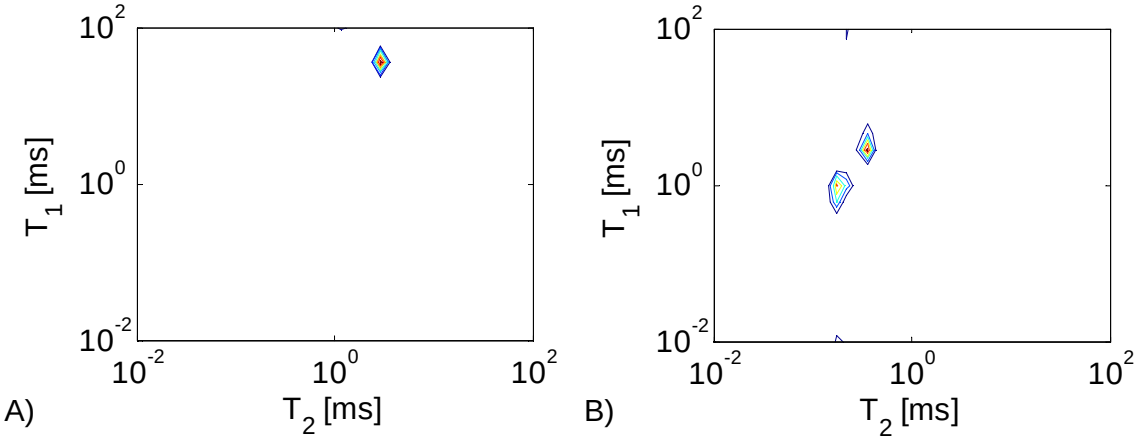

Figure 4.13: 2D T_1-T_2 NMR experiment performed by STRAFI at a single height in a sample of white cement (w/c = 0.4). The hydration time was (A) 6 h and (B) 4 days. The NMR sequence was a saturation recovery sequence (T_1 encoding) followed by a CPMG detection with a mixing time τ. The CPMG train consisted of 200 echoes with an echo time of 34 μs. The mixing time was set to vary logarithmically from 10 μs to 30 ms in 20 steps. Using a recycling delay of 1 s and 256 scans for each τ increment, the time to measure the full 2D map was close to 1h.

4.3.3.2 2D experiment

The previous 1D preliminary study performed by STRAFI at a single height can be completed by 2D T_1-T_2 NMR experiments which can be adapted for use in inhomogeneous magnetic field [HBS06] and some applications to the study of cement pastes are reported [MMM$^+$07a, MMM$^+$07b]. The sequence we used is a saturation recovery sequence [MHK71] followed by a mixing time τ varying logarithmically [CPB11] and a CPMG detection train. A T_1-T_2 2D NMR experiment was carried at a fixed position in the middle of the paste. The 2D experiment was analyzed with a 2D inverse Laplace transformation adapted to the study of T_1-T_2 correlation [SVH$^+$02]. In Figure 4.13 are displayed the T_1-T_2 maps of a white cement paste (w/c = 0.4) for different hydration times. After 6 hours of hydration (Fig. 4.13A), the 2D correlation map of the white cement exhibits a single spot (T_1 = 33 ms and T_2 = 2.5 ms). At this time, the porous network appears to be a continuous phase completely percolated. After 4 days (see Fig. 4.13B), two peaks are observed : the first at T_1 = 2 ms and T_2 = 400 μs and another at T_1 = 800 μs and T_2 = 150 μs. At the time scale of the experiment, no exchange peak is observed for a 4 days hydration, thus the two porous networks observed at that stage are almost disconnected or at least the exchange rate between the two networks is too long compared to the experimental time (see chapter 5). The water in large pores is converted after 4 days into water in smaller pores with T_1 = 2 ms and T_2 = 400 μs. The new peak at T_1 = 800 μs and T_2 = 150 μs corresponds to water in the nanopores of the C−S−H gel which is by now fully structured. This interpretation supports the discrete interpretation of the pore structure.

It can be noticed that the peaks are on a diagonal line $T_1 = 5T_2$. Following the work of McDonald et al [MKMM05] forecasting the T_2/T_1 dependence as a function of the magnetic field, this ratio at 137 MHz is expected between 0.2 and 0.4 assuming that the correlation time τ_m characterizing the 2D diffusion of protons on the pore surface is equal to 1.3 ns as stated by Barberon et al [BKP+03]. Thus, the dependence we found is consistent with the literature and shows that the behaviour of the water molecules follows the theory assessed in sections 4.2.2 and 4.2.3.

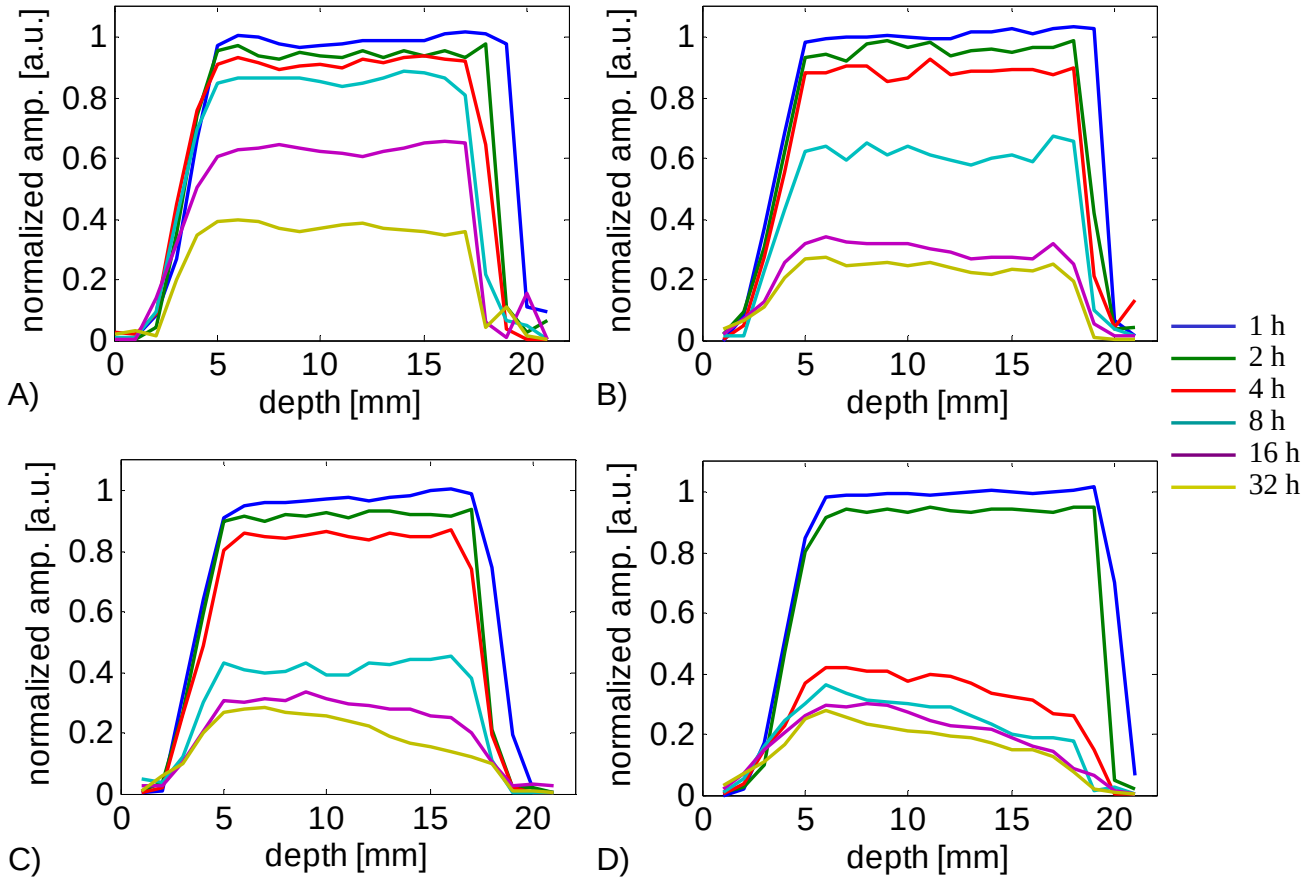

Figure 4.14: Profiles obtained using the NMR-MOUSE™ at various hydrating times and various temperatures: (A) 5 °C, (B) 20 °C, (C) 25 °C and (D) 35 °C on a white cement paste hydrated with a w/c ratio equal to 0.4. The profiles were measured over a range of 22 mm with a step of 1 mm. For each temperature, a profile was measured at exponentially spaced intervals of time: 1 h, 2 h, 4 h, 8 h, 16 h and 32 h, corresponding to the 6 downwards solid lines (blue, green, red, cyan, purple and yellow) of each plot. For each point of the profile, a CPMG detection train with an echo time of 140 μs was applied. Until a drying time of 4 h, 128 echoes were used in the CPMG train, the recycle delay was 1 s and the number of scans 48, leading to a total experimental time of 18 min. Beyond 4 h, the number of echoes was changed to 64, the recycle delay to 0.7 s and the number of scans to 128, so the total experimental time was 33 min. The amplitudes reported in the plots are the amplitudes obtained from a single exponential fit of the CPMG decay.

4.3.3.3 Conclusion of the STRAFI experiment

The experiments performed by STRAFI complement each other and global conclusions can be drawn. First of all, from Figure 4.11A and Figure 4.13B, it appears that the relaxation time $T_2 = 150$ μs is invariant. The exchange with the network is weak. Indeed, if we attribute this value of T_2 to the 2 nm pore ("gel" water), then, this T_2 value is constant because the S/V ratio of the interlayer is fixed. Indeed, despite of this water being part of a pore, the size of the pore is constant in the C−S−H. Moreover, this T_2 component appears lately in the hydration process. Considering the experiment from Figure 4.11, it appears that the long T_2 value is decreasing continuously from $T_2 = 4$ ms down to $T_2 = 400$ μs which is consistent with the evolution of the T_1-T_2 correlation maps (Fig. 4.13). These values are similar to those found by Holly et al. [HRHP07] for a white cement hydrated with a w/c ratio equal to 0.42.

Besides getting access to the dynamics of the formation of the porous structure of white cement through the observation of the water distributions at a single position, STRAFI allows to perform the same kind of study throughout the sample. Here, we showed for example (see Fig. 4.12) that the kinetics of the porous structure of white cement is constant throughout the sample, even when drying induced a gradient of water in the sample.

4.3.4 Temperature effect visited by the NMR-MOUSE™

4.3.4.1 Profile analysis

Figure 4.14 displays the NMR profiles obtained under 60% relative humidity at different hydration time and temperatures for a white cement paste. The sample was 22 mm thick and evaporation was allowed only on the upper face of the sample at the position $z = 22$ mm. Two types of behaviour can be distinguished depending on temperature. Below 25 °C, the profiles remain essentially flat except for a small region at the air interface of a few millimeters which is getting dryer and dryer. The boundary of this region defines a front which progresses inward as drying proceeds. Above 25 °C, the behaviour is the same during the first hours, however, behind the front, the profiles appear progressively tilted toward the air interface. This is clearly an effect of drying. To interpret these data, it is important to remember that the NMR-MOUSE™ setup is only sensitive to T_2's larger than 400 μs (see Fig. 4.10). This means that in a cement paste, the NMR-MOUSE™ profiles only the capillary water. From these considerations, we can conclude that below 20 °C, the amount of free water remains homogeneously distributed behind the drying front during hydration and drying except at a millimeter close to the air interface where the capillary pores appear totally desaturated. These observations are consistent with the results already observed by Bohris et al. [BGM+98] and are interpreted as follows. Drying by evaporation is very effective next to the air interface where there is almost no free water. On the contrary, in the bulk of the sample, the amount of free water decreases due to drying and hydration but remains homogeneously distributed. The porous cement network allows an efficient redistribution of the capillary water by capillary forces throughout the sample despite the unilateral evaporation. Behind the drying front, the drying mechanism is thus consistent with a funicular regime [BS90].

Above 25 °C, the situation appears significantly altered. Although a funicular drying mechanism can still be postulated at the beginning, after a certain time (4 hours for instance at 35 °C), the amount of free water varies across the depth of the paste. At these temperatures, the porous network in the paste is too dense to allow a timely capillary water transfer. The drying mechanism changes to a pendular regime [BS90] around 25 °C which could be due either to a more efficient evaporation, or to the formation of a denser cementitious matrix (percolation correlates with total pore volume), or even to the interplay of both since water availability influences the matrix density.

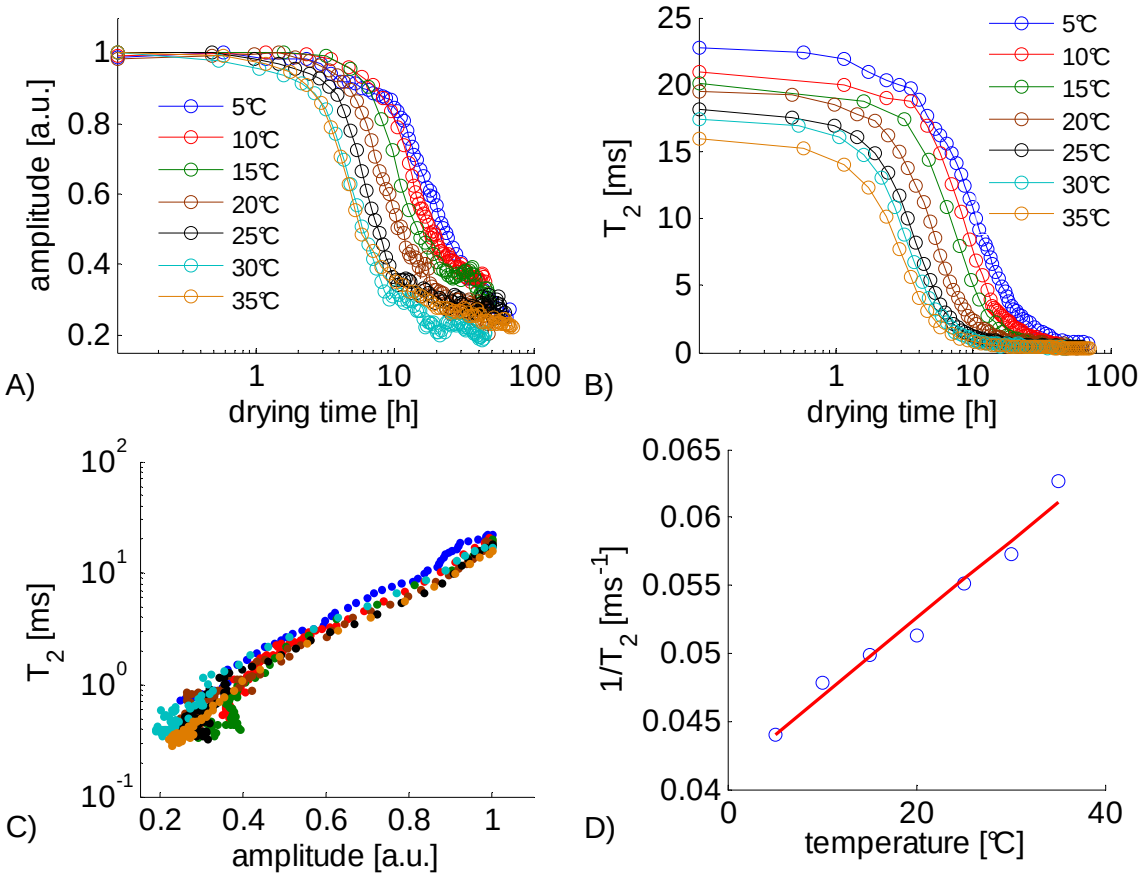

Figure 4.15: Amplitudes and T_2 relaxation rates as function of the drying time measured with the NMR-MOUSE™ at a single height in a sample of white cement (w/c = 0.4). For these measurements, a CPMG detection train with an echo time of 140 μs was used. Until a drying time of 4 h, 128 echoes were used in the CPMG train, the recycle delay was 1 s and the number of scans 256, leading to a total experimental time of 4 min. Beyond 4 h, the number of echoes was changed to 64, the recycle delay to 0.7 s, and the number of scans to 512, so the total experimental time was 6 min. The amplitudes and T_2's reported in the plots are obtained from single exponential fits of the CPMG decays. A) Evolution of the amplitudes versus the hydration time at various temperatures. B) Evolution of T_2's versus the hydration time at various temperatures. C) Correlation between amplitudes and T_2's at various temperatures. D) Correlation between the T_2's measured at the initial drying time and the temperature.

4.3.4.2 T_2 analysis and porous morphology

Figure 4.15A and B exhibits the evolution of the amplitude and T_2 at various temperatures measured with the NMR-MOUSE™ along the hydration time of white cement paste. The temperature affects drastically the kinetics of the setting of the cement paste. If one defines the setting as the inflexion point of the curve amplitude versus drying time (Fig. 4.15A), we can see that it occurs at a drying time of about 20 h at 5 °C whereas it occurs at about 5 h at 35 °C. This results is consistent with what is found in the literature [KD92]. This evolution can be alternatively seen through the observation of the T_2 along the drying time (Fig. 4.15B). Indeed, it exhibits a similar behaviour. However, one can notice that the temperature affects not only the kinetics of T_2's but also their values. Figure 4.15D shows a linear dependence of $1/T_2$ measured at the initial drying time as a function of the temperature. This is interpreted as

an effect of the temperature on the diffusion coefficient of water. Indeed, in a CPMG sequence performed in the presence of a uniform magnetic field gradient G, the apparent T_2 can be written as a function of the diffusion coefficient D [Kim97]:

$$\frac{1}{T_2^{\text{app}}} = \frac{1}{T_2} + D \cdot \frac{\gamma^2 G^2 t_{\text{E}}^2}{12} \tag{4.10}$$

where γ is the gyromagnetic ratio and t_{E} is echo time of the CPMG. One notices that $1/T_2$ increases with the temperature. This is mainly due to the linear increase of the self-diffusion coefficient D with temperature.

When T_2 (Fig. 4.15B) is plotted as a function of the amplitude (Fig. 4.15A), one can see that all curves can merge on a single master curve (Fig. 4.15C) and this for all the temperatures between 5 and 35 °C. The analysis of such a master curve shows that it follows a power law with an exponent equal to 3. We do not have any interpretation for this exponent at the moment as we would expect an exponent 1/3 in the case where the pores can be considered as spherical.

Here, we showed that the NMR-MOUSE™ is a very powerful method allowing to observe simply the effect of the drying and its consequence on the distribution of free water within the sample. It acts as a natural filter to exclusively observe the distribution of free water in white cement pastes. However, the disentanglement of drying and hydration effects requires the use of the complementary tool STRAFI.

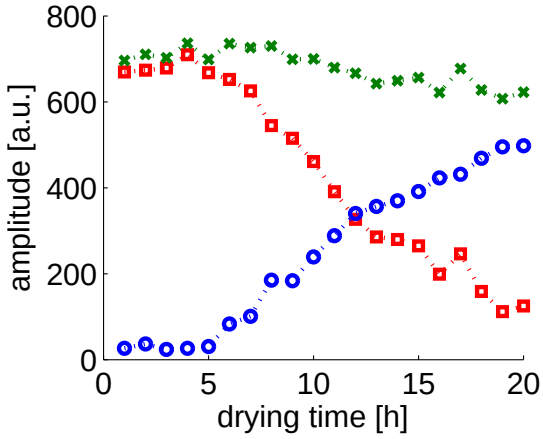

Figure 4.16: Evolution of free (red squares) and "gel" (blue circles) water along the hydration time of a white cement paste (w/c = 0.4) at 22 °C under 100% rH measured by STRAFI. The observed slice is in the bulk. The sum of both the free and the "gel" water is represented by the green line.

4.3.5 Effect of the relative humidity on the drying profiles

At this stage, it can be argued that the NMR signal is not sensitive to the total amount of water. As we have seen before, CH and hydroxyl groups in the C−S−H have very short T_2 values (a few tens of microseconds typically). If a part of the Portlandite NMR signal is missed, the observed total amount of water should decrease with the hydrating time, even without any drying effect. In order to check this and obtain an evaluation of the missing signal, the paste was hydrated in a confined environment so that no water is lost (experiment at 100%rH) and measured by STRAFI. The result is displayed in Figure 4.16. In this figure, one can see that the green curve slightly decrease with time. This decrease corresponds to a loss of 15% of the initial

amplitude in 20 hours of hydration. This effect is attributed to the conversion of free water into chemically combined water (CH and C−S−H) whose T_2 is too short to be recorded.

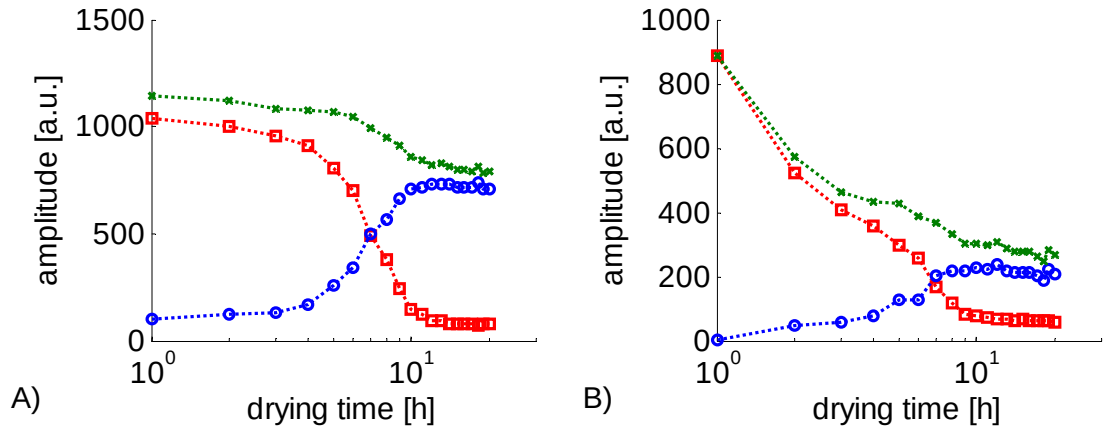

Figure 4.17: Evolution of the weight of the long (red squares) and short (blue circles) T2 component along the hydrating time for two positions in a profile of a white cement paste (w/c = 0.4) obtained at 22 °C with a relative humidity of 20%. The green curve corresponds to the total water in the sample (free and "gel" water). A) is obtained from a slice in the bulk of the paste, and B) is obtained at the surface (less than 1 mm from the surface).

To follow the influence of the humidity level on the dessication of white cement paste, STRAFI profiles were acquired along the hydrating time at 22 °C and a relative humidity of 20%. For each position of the profile, the CPMG signal was fitted by a two exponential decay. The amplitude of both exponentials along the hydrating time at two positions in the profile is displayed Figure 4.17. The effect of the drying is clearly evidenced. In the bulk (Fig. 4.17A), the decrease of free water (red squares) mainly corresponds as expected to a conversion of free water into "gel" water. The setting of the cement paste is observed at the hydrating time $t = 7$ hours. Figure 4.17B evidences a marked drying effect. Before a hydrating time of 5 hours, the free water (red squares) strongly decreases because of evaporation. As a consequence, after the setting time, the weak amount of remaining free water is converted into "gel" water, and the drying rate is slowed down. As a noteworthy result, the behavior obtained for the bulk is the same for all the positions in the paste. This is clearly consistent with the results obtained with the NMR-MOUSE™ (see Fig. 4.14): below 25 °C, the effect of the drying is effective up to a distance of 1 mm from the surface. For deeper positions in the paste, the water transport throughout the sample yields to a homogeneous repartition of the water in the paste. It can be noticed that the total amount of free water in the bulk is slowly decreasing: indeed, it appears that before the setting of the paste, the bulk is slowly and homogeneously drying.

Conclusion

In this part, we investigated the curing of cement using the tools developed in the previous chapters. The knowledge of the distribution of water between its various states (chemically bound, in C−S−H "gels" or in capillary pores) and this in a localized manner allows us to understand the structuring of the porous network which develops as cement is drying. By spatially resolved NMR imaging, we evidence the progressive evolution of the microstructure of white cement paste under different conditions of temperatures and humidity. In particular, by combining the NMR-MOUSE™ and STRAFI, we managed to disentangle drying from hydration during the progressive setting of the cement paste. The spatially resolved aspect of these techniques is of major interest as it could potentially indicate areas where stress occurs in the material leading to crack formation.

Bibliography

[AJ76] J.A. Akai and J. Jonas. *J. Solution Chem.*, 5(8):563–574, 1976.

[BBM+05] J. Boguszynska, M.C.A. Brown, P.J. McDonald, J. Mitchell, M. Mulheron, J. Tritt-Goc, and D.A. Verganelakis. *Cem. Concr. Res.*, 35(10):2033–2040, 2005.

[BET38] S. Brunauer, P.H. Emmett, and E. Teller. *J. Am. Chem. Soc.*, 60(2):309–319, 1938.

[BGM+98] A.J. Bohris, U. Goerke, P.J. McDonald, M. Mulheron, B. Newling, and B. Le Page. *Magn. Reson. Imaging*, 16(5-6):455–461, 1998.

[BGT59] F.G. Buttler, L.S.D. Glasser, and H.F.W. Taylor. *J. Am. Ceram. Soc.*, 42(3):121–126, 1959.

[BKP+03] F. Barberon, J.-P. Korb, D. Petit, V. Morin, and E. Bermejo. *Phys. Rev. Lett.*, 90(11):116103, 2003.

[BPC08] B. Blümich, J. Perlo, and F. Casanova. *Progr. Nucl. Magn. Reson. Spectr.*, 52(4):197–269, 2008.

[BQK+00] D.P. Bentz, D.A. Quenard, H.M. Kunzel, J. Baruchel, F. Peyrin, N.S. Martys, and E.J. Garboczi. *Mater. Struct.*, 33(227):147–153, 2000.

[BS90] C.J. Brinker and G.W. Scherer. *Sol-Gel Science : The Physics and Chemistry of Sol-Gel Processing*. Academic Press, 1990.

[BT79] K.R. Brownstein and C.E. Tarr. *Phys. Rev. A*, 19(6):2446–2453, 1979.

[Cal91] Paul T. Callaghan. *Principles of Nuclear Magnetic Resonance Microscopy*. Oxford Science Publications, 1991.

[CPB11] F. Casanova, J. Perlo, and B. Blümich. *Single-Sided NMR*. Springer, 2011.

[Der69] E. Derouane. *Bull. Soc. Chim. Belges*, 78(1-2):111, 1969.

[FR08] P. Faure and S. Rodts. *Magn. Reson. Imaging*, 26(8):1183–1196, 2008.

[Fra08] A. Franceschini. *Elaboration de nanocomposites ciment-polymère, basés sur des interactions covalentes entre des polymères greffés silanes et les hydrates C−S−H.* PhD thesis, Université Pierre et Marie Curie (Paris), 2008.

[FRE98] M. Francois, G. Renaudin, and O. Evrard. *Acta Crystallogr., Sect. C: Cryst. Struct. Commun.*, 54(9):1214–1217, 1998.

[GddLS+09] C. Giraudeau, J.-B. d'Espinose de Lacaillerie, Z. Souguir, A. Nonat, and R. Flatt. *J. Am. Ceram. Soc.*, 92(11):2471–2488, 2009.

[GHH+79] R.J. Gummerson, C. Hall, W.D. Hoff, R. Hawkes, G.N. Holland, and W.S. Moore. *Nature*, 281(5726):56–57, 1979.

[Gir09] C. Giraudeau. *Interactions organo - aluminates dans les ciments. Intercalation de polyméthacrylates-g-PEO dans l'hydrocalumite.* PhD thesis, Université Pierre et Marie Curie (Paris), 2009.

[GM81] R.J. Good and R.S. Mikhail. *Powder Technol.*, 29(1):53–62, 1981.

[GP95] G. Goelman and M.G. Prammer. *J. Magn. Reson.*, 113(1):11–18, 1995.

[GPC+00] J. Greener, H. Peemoeller, C.H. Choi, R. Holly, E.J. Reardon, C.M. Hansson, and M.M. Pintar. *J. Am. Ceram. Soc.*, 83(3):623–627, 2000.

[GS91] S.J. Gregg and K.S.W. Sing. *Adsorption, Surface Area, and Porosity.* Academic Press, 1991.

[GSG+07] E. Gallucci, K. Scrivener, A. Groso, M. Stampanoni, and G. Margaritondo. *Cem. Concr. Res.*, 37(3):360–368, 2007.

[HBS06] M. D. Hürlimann, L. Burcaw, and Y. Q. Song. *J. Colloid Interface Sci.*, 297(1):303–311, 2006.

[HG00] M.D. Hürlimann and D.D. Griffin. *J. Magn. Reson.*, 143(1):120–135, 2000.

[HGGS07] B.H. Haha, E. Gallucci, A. Guidoum, and K.L. Scrivener. *Cem. Concr. Res.*, 37(8):1206–1214, 2007.

[HJS94] W.P. Halperin, J.Y. Jehng, and Y.Q. Song. *Magn. Reson. Imaging*, 12(2):169–173, 1994.

[HRHP07] R. Holly, E.J. Reardon, C.M. Hansson, and H. Peemoeller. *J. Am. Ceram. Soc.*, 90(2):570–577, 2007.

[HV02] M.D. Hürlimann and L. Venkataramanan. *J. Magn. Reson.*, 157(1):31–42, 2002.

[Jen00] H.M. Jennings. *Cem. Concr. Res.*, 30(1):101–116, 2000.

[KD92] K.O. Kjellsen and R.J. Detwiler. *Cem. Concr. Res.*, 22(1):112–120, 1992.

[Kim97] R. Kimmich. *NMR Tomography Diffusometry Relaxometry.* Springer, 1997.

[KMM+07] J.-P. Korb, P.J. McDonald, L. Monteilhet, A.G. Kalinichev, and R.J. Kirkpatrick. *Cem. Concr. Res.*, 37(3):348–350, 2007.

[KMMM07a] J.-P. Korb, L. Monteilhet, P.J. McDonald, and J. Mitchell. *Cem. Concr. Res.*, 37(3):295–302, 2007.

[KMMM07b] J.-P. Korb, L. Monteilhet, P.J. McDonald, and J. Mitchell. *Cem. Concr. Res.*, 37(3):303–309, 2007.

[MAMM07] P. J. McDonald, P.S. Aptaker, J. Mitchell, and M. Mulheron. *J. Magn. Reson.*, 185(1):1–11, 2007.

[McD97] P.J. McDonald. *Prog. Nucl. Magn. Reson. Spectrosc.*, 30:69–99, 1997.

[MHK71] J.L. Markley, W.J. Horsley, and M.P. Klein. *J. Chem. Phys.*, 55(7):3604–3605, 1971.

[MKMM05] P. J. McDonald, J. P. Korb, J. Mitchell, and L. Monteilhet. *Phys. Rev. E*, 72(1), 2005.

[MM93] P.K. Mehta and P.J.M. Monteiro. *Concrete : Structure, Properties and Materials.* Prentice-Hall, 1993.

[MMM+07a] P. J. McDonald, J. Mitchell, M. Mulheron, P. S. Aptaker, J. P. Korb, and L. Monteilhet. *Cem. Concr. Res.*, 37(3):303–309, 2007.

[MMM+07b] P. J. McDonald, J. Mitchell, M. Mulheron, L. Monteilhet, and J. P. Korb. *Magn. Reson. Imaging*, 25(4):470–473, 2007.

[MSS93] P.P. Mitra, P.N. Sen, and L.M. Schwartz. Short-time behavior of the diffusion coefficient as a geometrical probe of porous media. *Phys. Rev. B*, 47(14):8565–8574, Apr 1993.

[Non04] A. Nonat. *Cem. Concr. Res.*, 34(9):1521–1528, 2004.

[NRS+96] T.G. Nunes, E.W. Randall, A.A. Samoilenko, P. Bodart, and G. Feio. *J. Phys. D: Appl. Phys.*, 29(3):805–808, 1996.

[Nun06] T.G. Nunes. *Advanced Materials Forum Iii, Pts 1 and 2*, chapter Influence of grain size on the setting of Portland cement: a stray-field magnetic resonance imaging study, pages 1633–1637. Trans. Tech. Publications LTD, 2006.

[NWN04] N. Nestle, B. Walaszek, and M. Nolte. *J. Magn. Reson.*, 168(1):46–52, 2004.

[Par81] L.J. Parrott. *Cem. Concr. Res.*, 11(5-6):651–658, 1981.

[PPL+05] A. Plassais, M.P. Pomiès, N. Lequeux, J.-P. Korb, D. Petit, F. Barberon, and B. Bresson. *Phys. Rev. E*, 72(4):041401, 2005.

[RBJ94] R.L. Rarick, J.I. Bhatty, and H.M. Jennings. *Materials Science of Concrete IV*, chapter Surface Area Measurement using Gas Sorption: Application to Cement Paste, pages 1–36. American Ceramic Society, 1994.

[RCP+06] D.G. Rata, F. Casanova, J. Perlo, Demco D.E., and B. Blümich. *J. Magn. Reson.*, 180(2):229–235, 2006.

[RFE99] G. Renaudin, M. Francois, and O. Evrard. *Cem. Concr. Res.*, 29(1):63–69, 1999.

[Ric08] I.G. Richardson. *Cem. Concr. Res.*, 38(2):137–158, 2008.

[SG88] K.L. Scrivener and E.M. Gartner. Microstructural gradients in cement paste around aggregate in particles. In *Bonding in Cementitious Composites, Mater. Res. Soc. Symp. Proc. 114*, pages 77–86, 1988.

[SNID04] E. Sakai, Y. Nikaido, T. Itoh, and M. Daimon. *Cem. Concr. Res.*, 34(9):1669–1673, 2004.

[SPPP87] K.L. Scrivener, H.H. Patel, P.L. Pratt, and L.J. Parrott. Analysis of phases in cement paste using backscattered electron images. In *Microstructural Development During Hydration of Cement, Mater. Res. Soc. Symp. Proc. 85*, pages 67–75, 1987.

[SRS93] J. Strange, M. Rahman, and E. Smith. *Phys. Rev. Lett.*, 71(21):3589–3591, 1993.

[SVH+02] Y.-Q. Song, L. Venkataramanan, M.D. Hurlimann, M. Flaum, P. Frulla, and C. Straley. *J. Magn. Reson.*, 154(2):261–268, 2002.

[Tay90] H.F.W. Taylor. *Cement Chemistry.* Academic Press, 1990.

[TJ08] J. Thomas and H. Jennings, 2008. `http://iti.northwestern.edu/cement/index.html`.

[VLYX96] D. Viehland, J.-F. Li, L.-J. Yuan, and Z. Xu. *J. Am. Ceram. Soc.*, 79(7):1731–1744, 1996.

[VPK02] R.M.E. Valckenborg, L. Pel, and K. Kopinga. *J. Phys. D: Appl. Phys.*, 35(3):249–256, 2002.

[VRM10] A. Valori, V. Rodin, and P.J. McDonald. *Cem. Concr. Res.*, 40(9):1375–1377, 2010.

[VSH02] L. Venkataramanan, Y. Q. Song, and M. D. Hurlimann. *Ieee Transactions on Signal Processing*, 50(5):1017–1026, 2002.

[Was21] E.W. Washburn. *Phys. Rev.*, 17(3):273–283, 1921.

[Web11] Weber®, 2011. `http://www.weber.fr/preparation-des-sols/le-guide-weber/notices-produits/les-mortiers-et-liants-pour-chapes/weberniv-fluid.html`.

[Woe61] D. E. Woessner. *J. Chem. Phys.*, 34(6):2057–2061, 1961.

[ZB57] J.R. Zimmerman and W.E. Brittin. *J. Phys. Chem.*, 61(10):1328–1333, 1957.

Chapter 5

Multi-site exchange NMR

In section 4.3.3.2, we briefly introduced multi-dimensional relaxation experiments. The idea is to evidence the dynamic behaviour of species moving from one environment to another. The knowledge of the presence of such motions within a material already provides valuable information about its internal structure, but the quantitative evaluation of the exchange rates involved within these motions is even more interesting.

Two-dimensional relaxation exchange NMR is in many ways similar to 2D frequency exchange NMR, except that the encoding times are comparable to the exchange time. This fact prevents the straightforward analysis of the cross peaks intensities in terms of joint probability densities, and quantitative information and understanding can only be obtained by comparison with simulated spectra. Practically, retro-fitting a simulated data set to an experimental one is shown to allow the determination of the experimental relaxation and exchange parameters. This point is illustrated by studying a model system consisting of interstitial water exchanging within a pack of spherical silica particles.

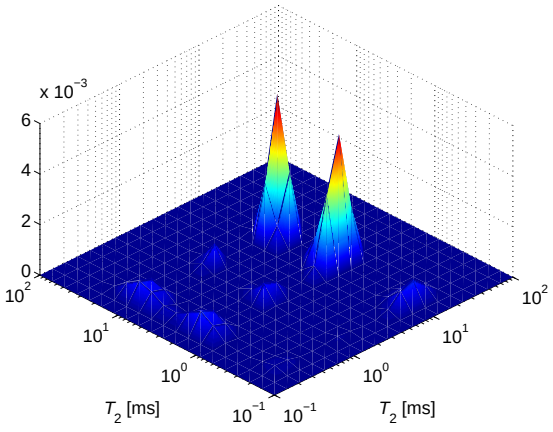

Figure 5.1: Example of a non-symmetric three-site 2D correlation map

5.1 Introduction

2D Fourier Transform frequency exchange NMR spectroscopy has been used for a long time now. It allows to discriminate the sites in terms of their chemical shifts in an NMR spectrum. However, it remains experimentally demanding as, to measure a chemical shift spectrum, a highly homogeneous magnetic field is needed, which requires a sophisticated magnet. Yet, the nuclear magnetic response of a molecule to a particular environment is not characterized solely by a chemical shift but also by a rate of decay. Conceptually, the chemical shift scale can be replaced by a relaxation or a diffusion scale, so that the occupancy of the different sites is obtained not by the structure of the frequency distribution but instead by the distribution of relaxation rates or diffusion coefficients. In practice, only three or four different sites can usually be resolved on a relaxation or diffusion scale, but this information can easily be obtained with simple magnets and inhomogeneous fields. This concept of relaxation exchange NMR is not new [KH86, LLSH93] but it gained recent popularity with the development of a stable 2D inverse Laplace transformation (ILT) algorithm [VSH02], a development reminiscent of Fourier NMR which gained momentum only once the fast Fourier Transformation algorithm had been mastered by the NMR community [CAG$^+$07, EA54]. After having briefly explained the principle of the 2D exchange spectroscopy, we will present our work on muti-site relaxation exchange NMR.

5.2 General theory of n-site exchange

5.2.1 Introduction

Nuclei with spin resonate at a characteristic frequency when placed in a magnetic field, hence NMR spectroscopy. In the simplest case, an isolated spin-1/2, this will give rise to a single, very sharp resonance. The resonance position is sensitive to the magnetic environment. This is one of the reasons why NMR is so useful. Since we routinely resolve resonances that differ by fractions of a part per million (ppm), many fine details of the chemical environment of the nucleus are revealed. If some dynamic process takes a given nucleus from one magnetic environment to a different one, the NMR spectrum will be affected. The ways that chemical exchange affects NMR spectra are very diverse, but the basic mechanism is similar. The study of chemical exchange has been extensively studied [Bai03, McC58, EBW87, Mac98] for 50 years so we will focus on the main results.

5.2.2 What do we call site exchange?

What we call "site" is a given magnetic environment. This is defined by all the interactions that determine the resonant behaviour (frequency and relaxation, chemical shielding, scalar coupling, quadrupole coupling for spins with quantum numbers greater than 1/2, etc). Then, a process carries a nucleus from one site to another. It can be intramolecular (rotation around bounds, chair-chair interchange (the typical example is cyclohexane), scrambling of ligands in a coordination complex, ...) or intermolecular (exchange of a proton on a OH or COOH group with a water molecule, ...).

5.2.3 Kinetics and thermodynamics

Exchange involves the passing of the molecule through a transition state, at the top of a kinetic barrier (see Fig. 5.2). Measurements of the rate as a function of temperature or other parameters are one of the few ways of experimentally determining the height of the barrier. The dependence of reaction rate k on temperature T was empirically described by Arrhenius [Lai65] in the following equation:

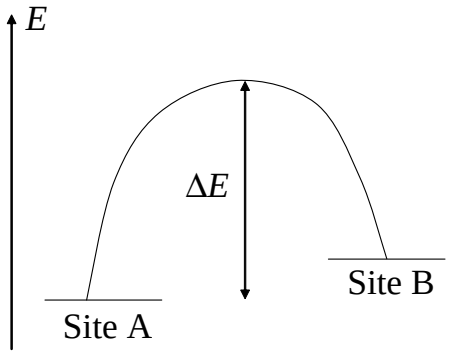

Figure 5.2: Sketch of two sites separated by barrier ΔE

$$k = A \exp\left(-\frac{\Delta E}{RT}\right) \tag{5.1}$$

In this equation, A is the pre-exponential factor, R is the gas constant and ΔE is the energy of activation. Later, Eyring put this relation on a firmer theoretical basis. Eyring's equation gives the rate constant as:

$$k = \frac{k_B T}{h} \exp\left(\frac{\Delta G}{RT}\right) \tag{5.2}$$

In this equation, k_B is Boltzmann's constant, h is Planck's constant and ΔG is the free energy of activation. The rate we measure is the rate of transfer from one site, A, to the other, B. However, the system is in dynamic equilibrium, so there is a reverse rate as well:

$$\mathrm{A} \underset{k_r}{\overset{k_f}{\rightleftharpoons}} \mathrm{B} \tag{5.3}$$

If the two sites do not have equal populations, then the ratio of the forward and reverse rates are related to the equilibrium constant, K by:

$$K = \frac{[A]}{[B]} = \frac{k_f}{k_r} = \exp\left(\frac{\Delta G}{RT}\right) \tag{5.4}$$

Thus, the measurement of the exchange rates provides the energy of the exchange barrier.

5.2.4 Bloch equations

Consider a system with N sites. These sites can be interconverted through chemical exchange or communicate through intra- or intermolecular cross-relaxation. The NMR signal $s(t)$ results from the superposition of all the magnetization components:

$$s(t) = \sum_{i=1}^{N} M_i(t) \tag{5.5}$$

The evolution of these N magnetization components, brought together in the magnetization vector $\boldsymbol{M}(t)$, under both relaxation and exchange is governed by the the following coupled differential equation system:

$$\frac{\mathrm{d}}{\mathrm{d}t}[\boldsymbol{M}(t) - \boldsymbol{M}^{\mathrm{eq}}] = -\mathbf{L}[\boldsymbol{M}(t) - \boldsymbol{M}^{\mathrm{eq}}] \tag{5.6}$$

where $\boldsymbol{M}^{\mathrm{eq}}$ is the magnetization at the equilibrium. $\boldsymbol{M}^{\mathrm{eq}} = 0$ for transverse magnetization and $\boldsymbol{M}^{\mathrm{eq}} = \boldsymbol{M}^0$ for longitudinal magnetization.

$$\mathbf{L} = \imath\,\boldsymbol{\Omega} + \mathbf{R} + \mathbf{K} \tag{5.7}$$

$\boldsymbol{\Omega}$ is a diagonal matrix with the frequency corresponding to each site. $\mathbf{R}$ is a diagonal matrix of relaxation rates ($R_k^{(1,2)} = 1/T_{(1,2)^k}$). $\mathbf{K}$ is an off-diagonal exchange matrix which mixes the magnetization components. Eqn. 5.6 has the familiar solution :

$$\boldsymbol{M}(t) - \boldsymbol{M}^{\mathrm{eq}} = \exp\{-\mathbf{L}(t - t_0)\}[\boldsymbol{M}(t_0) - \boldsymbol{M}^{\mathrm{eq}}] \tag{5.8}$$

The exponential operator can be understood as a time evolution operator which produces the magnetization state at time t given the magnetization state at time t_0. To evaluate this time evolution operator $\mathbf{U}(t)$, it is necessary to diagonalize $\mathbf{L}$ with the help of the rotation matrix $\mathbf{Q}$:

$$\mathbf{U}(t - t_0) = \mathbf{Q}\exp\{-\mathbf{Q^{-1}LQ}(t - t_0)\}\mathbf{Q^{-1}} \tag{5.9}$$

5.2.5 The exchange matrix

In the most general case, the exchange matrix $\mathbf{K}$ can be written:

$$\mathbf{K} = \begin{bmatrix} k_{11} & -k_{12} & \cdots & -k_{1n} \\ -k_{21} & k_{22} & \cdots & -k_{2n} \\ \vdots & \vdots & \ddots & \vdots \\ -k_{n1} & -k_{n2} & \cdots & k_{nn} \end{bmatrix}$$

where k_{ij} is the exchange rate between sites i and site j. As $\mathbf{K}$ only mixes magnetization components and preserves the total magnetization, detailed mass balance requires that whatever amount of magnetization is lost in one component has to be recovered from other components, i.e.:

$$\mathbf{K}\boldsymbol{M}^{\mathrm{eq}} = 0 \tag{5.10}$$

For example, for magnetization component M_1, we can write

$$k_{11}M_1^{\mathrm{eq}} - \sum_{j=2}^{n} k_{1j}M_j^{\mathrm{eq}} = 0 \tag{5.11}$$

By similar arguments, whatever total amount of magnetization is received by one of the magnetization components from other magnetization components has to be restored to them. For example, for magnetization component M_1,

$$\sum_{j=2}^{n} k_{1j}M_j^{\mathrm{eq}} = \sum_{i=2}^{n} k_{i1}M_1^{\mathrm{eq}}. \tag{5.12}$$

This, with the help of the previous equation, leads to:

$$k_{11} - \sum_{i=2}^{n} k_{i1} = 0 \tag{5.13}$$

so that the column sums of $\mathbf{K}$ vanish.

Let us take the example of a three sites system. By applying the mass balance to each of the three components, 6 equations are obtained. Furthermore, the total amount of magnetization exchanged is necessarily conserved. Consequently, of the initial nine parameters k_{ij}, only four remain independent. In the general case of n-site exchange, the kinetic matrix is determined by $(n-1)^2$ independent parameters. Note that the rates k_{ij} apply to the forward kinetics from state i to state j, so that the rates k_{ji} apply to the reverse kinetics from state j to state i. We remind from Eqn. 5.4 that the associated equilibrium constant K_{ij} which is defined by the ratio $[M_j]/[M_i]$ of concentrations is given by

$$K_{ij} = \frac{[M_j]}{[M_i]} = \frac{k_{ij}}{k_{ji}} \tag{5.14}$$

5.2.6 Free induction decay in response to a single excitation pulse

Given the state of the magnetization at time t_0 after an excitation pulse, the transverse magnetization at time t_1 later is given by Eqn. 5.8:

$$\boldsymbol{M}(t_1 + t_0) = \exp\{-\mathbf{L}(t_1 + t_0)\}\boldsymbol{M}(t_0) \tag{5.15}$$

The apparent formal simplicity of this equation is misleading. Since we are dealing with an exponential of a non-diagonal matrix, the prediction of the decay of the total transverse magnetization, or equivalently of the intensities and positions of the peaks is not trivial. It involves the determination of the eigenvalues and eigenvectors of the exponential operator as formally stated in Eqn. 5.9, a task which can be performed analytically only if the number of sites i remains limited and is not possible when dealing with unknown continuous distributions of sites.

5.2.7 The two-site case

In the simple case, where only two sites a and b are considered, the calculation can be done by explicit inversion [MKMM06, FS09]. Eqn. 5.8 becomes:

$$\boldsymbol{M} = \begin{bmatrix} M_\mathrm{a} \\ M_\mathrm{b} \end{bmatrix}$$

Under these conditions, the coupled Bloch equation 5.6 can be rewritten in a matrix form :

$$\frac{\mathrm{d}}{\mathrm{d}t}\begin{bmatrix} M_\mathrm{a} \\ M_\mathrm{b} \end{bmatrix} = -\mathbf{L}\begin{bmatrix} M_\mathrm{a} \\ M_\mathrm{b} \end{bmatrix}$$

Let us assume for simplicity (which is always possible by adjusting the nominal frequency of the spectrometer) that the Larmor frequencies of these sites are at $\pm\delta$. The matrix $\mathbf{L}$ can be expanded in three matrix. $\mathbf{\Omega}$ is the frequency matrix :

$$\mathbf{\Omega} = \begin{bmatrix} \omega_a & 0 \\ 0 & \omega_b \end{bmatrix} = \begin{bmatrix} \delta & 0 \\ 0 & -\delta \end{bmatrix}.$$

The relaxation matrix $\mathbf{R}$ is given by

$$\mathbf{R} = \begin{bmatrix} R_\mathrm{a}^{1,2} & 0 \\ 0 & R_\mathrm{b}^{1,2} \end{bmatrix},$$

and the exchange matrix $\mathbf{K}$ can be written upon balancing the magnetization as

$$\mathbf{K} = \begin{bmatrix} k_\mathrm{a} & -k_\mathrm{b} \\ -k_\mathrm{a} & k_\mathrm{b} \end{bmatrix},$$

where $k_\mathrm{b} = k_\mathrm{ab}$ and $k_\mathrm{a} = k_\mathrm{ab} \cdot M_\mathrm{b}/M_\mathrm{a}$.

To express the exponential of the matrix $\mathbf{L}$ (Eqn. 5.15), it is necessary to calculate its eigenvalues $\lambda_\pm^{1,2}$:

$$\lambda_+^{1,2} = \frac{-(R_\mathrm{a}^{1,2} + R_\mathrm{b}^{1,2} + k_\mathrm{a} + k_\mathrm{b}) + \sqrt{(R_\mathrm{b}^{1,2} + k_\mathrm{b} - R_\mathrm{a}^{1,2} - k_\mathrm{a})^2 + 4k_\mathrm{a}k_\mathrm{b} - 4\delta(\delta + \imath(R_\mathrm{a}^{1,2} + k_\mathrm{a} - R_\mathrm{b}^{1,2} - k_\mathrm{b}))}}{2}$$

$$\lambda_-^{1,2} = \frac{-(R_\mathrm{a}^{1,2} + R_\mathrm{b}^{1,2} + k_\mathrm{a} + k_\mathrm{b}) - \sqrt{(R_\mathrm{b}^{1,2} + k_\mathrm{b} - R_\mathrm{a}^{1,2} - k_\mathrm{a})^2 + 4k_\mathrm{a}k_\mathrm{b} - 4\delta(\delta + \imath(R_\mathrm{a}^{1,2} + k_\mathrm{a} - R_\mathrm{b}^{1,2} - k_\mathrm{b}))}}{2}$$

From this point, one should separate chemical exchange NMR spectroscopy from relaxation exchange NMR. Chemical exchange NMR has been extendedly treated in the literature ([Bai03, JMBE79, EBW87]). In the context of porous media, the chemical species are often the same but their magnetic environments differ. Thus, their frequencies may be the same but not the relaxation rates. Here, we will focus mainly on this second aspect.

5.2.8 Two-site relaxation exchange NMR

If only relaxation times and not frequencies are considered, the $\mathbf{L}$ matrix is limited to the sum of the $\mathbf{R}+\mathbf{K}$ matrix and the eigenvalues becomes [MKMM06]:

$$\lambda_+^{1,2} = \frac{-(R_\mathrm{a}^{1,2}+R_\mathrm{b}^{1,2}+k_\mathrm{a}+k_\mathrm{b})+\sqrt{(R_\mathrm{b}^{1,2}+k_\mathrm{b}-R_\mathrm{a}^{1,2}-k_\mathrm{a})^2+4k_\mathrm{a}k_\mathrm{b}}}{2}$$
$$\lambda_-^{1,2} = \frac{-(R_\mathrm{a}^{1,2}+R_\mathrm{b}^{1,2}+k_\mathrm{a}+k_\mathrm{b})-\sqrt{(R_\mathrm{b}^{1,2}+k_\mathrm{b}-R_\mathrm{a}^{1,2}-k_\mathrm{a})^2+4k_\mathrm{a}k_\mathrm{b}}}{2}$$

To calculate the exponential of the matrix $\mathbf{L}$ that is of the evolution operator of the magnetization (Eqn. 5.8), it is necessary to diagonalize it. The needed rotation matrix $\mathbf{Q}$ can be deduced from the eigenvectors. Experimentally, the eigenvalues of the $\mathbf{R}+\mathbf{K}$ matrix are the coordinates of the peaks of the distribution of the exponential decay rates obtained by the numerical approximation of the solution of the inverse Laplace problem. The intensities of the peaks can be obtained analytically from the rotation matrix $\mathbf{Q}$ [MKMM06], but, to stay more general, we prefer a numerical solution.

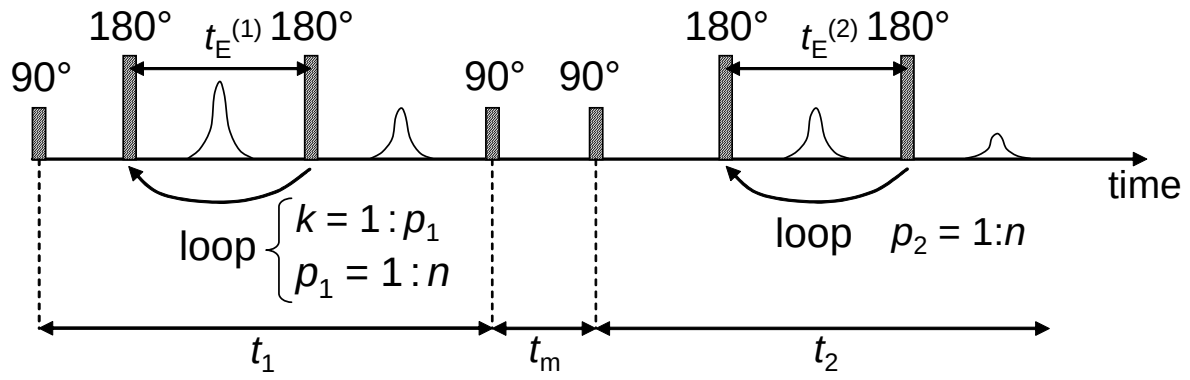

Figure 5.3: Pulse sequence for a T_2-T_2 exchange experiment.

5.2.9 Magnetization evolution in T_2-T_2 experiment

As an example, the time evolution of the magnetization is examined for a T_2-T_2 exchange experiment with a mixing period during which the magnetization is stored along the direction of the magnetic field and experiences T_1 relaxation.

5.2.9.1 T_2-T_2 Exchange Pulse sequence

A sketch of the Fig. T_2-T_2 exchange pulse sequence is exhibited on Figure 5.3. Following a $\pi/2$ read pulse at time t_0, a CPMG sequence of p_1 π pulses equally spaced by $t_E^{(1)}$ is applied during a first evolution period t_1. The transverse magnetization is encoded according to T_2 during t_1. It is then stored along the direction of the magnetic field with the help of a $\pi/2$ pulse where it subsequently relaxes with T_1 during the mixing time t_m. After the mixing time, a $\pi/2$ read pulse returns the magnetization to the transverse plane and its T_2 decay is followed for a second time in the detection period t_2 by recording the amplitude of each echo from a second CPMG sequence of n π pulses equally spaced by $t_E^{(2)}$. This sequence is repeated varying p_2 between 1 and n, resulting in an n^2 time-domain matrix. After ILT, one obtains a 2D T_2-T_2 correlation map.

5.2.9.2 Evolution of the magnetization during a T_2-T_2 experiment

The magnetization after the mixing time tm follows from Equation 5.15 :

$$\boldsymbol{M}(t_{\mathrm{m}}+t_1+t_0)-\boldsymbol{M}^0=\exp\Big\{-[\mathbf{R}^{(1)}+\mathbf{K}](t_{\mathrm{m}})\Big\}(\boldsymbol{M}(t_1+t_0)-\boldsymbol{M}^0). \tag{5.16}$$

During the evolution period t_1 and the detection period t_2 the magnetization is given by

$$\boldsymbol{M}(t_1+t_0)=\exp\Big\{-[\mathbf{R}^{(2)}+\mathbf{K}](t_1+t_0)\Big\}\boldsymbol{M}(t_0), \tag{5.17}$$

and

$$\boldsymbol{M}(t_2+t_{\mathrm{m}}+t_1+t_0)=\exp\Big\{-[\mathbf{R}^{(2)}+\mathbf{K}](t_2)\Big\}\boldsymbol{M}(t_{\mathrm{m}}+t_1+t_0). \tag{5.18}$$

The last three equations combine into

$$\begin{aligned}\boldsymbol{M}(t_2+t_{\mathrm{m}}+t_1+t_0) &= \exp\Big\{-[\mathbf{R}^{(2)}+\mathbf{K}](t_2)\Big\}\Big[\exp\Big\{-[\mathbf{R}^{(1)}+\mathbf{K}](t_{\mathrm{m}})\Big\}\\ &\quad\Big(\exp\Big\{-[\mathbf{R}^{(2)}+\mathbf{K}](t_1+t_0)\Big\}\boldsymbol{M}(t_0)-\boldsymbol{M}^0\Big)+\boldsymbol{M}^0\Big]\end{aligned} \tag{5.19}$$

5.2.10 Statistical interpretation of peak intensities in the slow exchange limit

5.2.10.1 Introduction

In 2D Fourier exchange NMR experiments, the fast exchange limit may apply during the mixing time so that relaxation can be neglected during t_m, while the slow exchange limit applies during the evolution and detection times. This situation is never encountered in 2D relaxation exchange NMR. Only the following three cases may be encountered. Their corresponding evolution operators are given in Table 5.1.

Table 5.1: Evolution operators of the three cases susceptible to occur in a usual 2D relaxation exchange NMR. The time periods t_1, t_m and t_2 are defined in Figure 5.3. For the T_2-T_2 exchange experiment schematized in Figure 5.3, $\mathbf{R}$ stands for $\mathbf{R}^{(1)}$ during t_m and for $\mathbf{R}^{(2)}$ during t_1 and t_2.

	$U(t_1)$	$U(t_{\mathrm{m}})$	$U(t_2)$
Case (1)	$\exp\{-[\mathbf{R}]t_1\}$	$\exp\{-[\mathbf{R}+\mathbf{K}]t_{\mathrm{m}}\}$	$\exp\{-[\mathbf{R}]t_2\}$
Case (2)	$\exp\{-[\mathbf{R}+\mathbf{K}]t_1$	$\exp\{-[\mathbf{K}]t_{\mathrm{m}}\}$	$\exp\{-[\mathbf{R}+\mathbf{K}]t_2$
Case (3)	$\exp\{-[\mathbf{R}+\mathbf{K}]t_1$	$\exp\{-[\mathbf{R}+\mathbf{K}]t_{\mathrm{m}}\}$	$\exp\{-[\mathbf{R}+\mathbf{K}]t_2$

- The exchange is slow during the evolution periods, which means that the time scale of exchange is long compared to the time scale of relaxation, and pure relaxation encoding is possible during the evolution periods. Consequently, there is no fast exchange during the mixing period.

- The exchange is fast compared to relaxation. Then the fast exchange limit is satisfied during the mixing time. In this case, the mixing period involves only exchange but not relaxation, while the evolution and detection periods encode both, relaxation and exchange.
- The exchange rate is commensurate with the relaxation rates, and both must be considered during the evolution, mixing, and detection periods.

Only in the first case can the 2D relaxation cross peaks be analyzed in terms of exchange kinetics, although not in a simple manner. Being in the slow exchange limit during evolution means that one can measure the relaxation rate R_i at time t and identify it with the magnetization of the corresponding site M_i. In this case, the slow exchange limit applies to the t_1 and t_2 encoding periods, and Eqn. 5.19 simplifies to

$$\begin{aligned} \boldsymbol{M}(t_2 + t_\mathrm{m} + t_1 + t_0) &= \exp\Big\{ -\mathbf{R}^{(2)} t_2 \Big\} \Big[\exp\Big\{ -[\mathbf{R}^{(1)} + \mathbf{K}](t_\mathrm{m}) \Big\} \\ &\quad \Big(\exp\Big\{ -\mathbf{R}^{(2)}(t_1 + t_0) \Big\} \boldsymbol{M}(t_0) - \boldsymbol{M}^0 \Big) + \boldsymbol{M}^0 \Big] \end{aligned} \tag{5.20}$$

As the relaxation matrix $\mathbf{R}^{(2)}$ is diagonal, the magnetization of a particular site i at the end of the evolution period is obtained as

$$M_i(t_1 + t_0) \approx \exp\{ -R_i^{(2)} t_1 \} M_i(t_0) = \exp\{ -t_1/T_{2,i} \} M_i(t_0) \tag{5.21}$$

After the mixing time tm, one obtains from Eqn. 5.15,

$$M_j(t_\mathrm{m} + t_1 + t_0) - M_j^0 = \sum_i \Big\{ \Big[\exp\{ -(\mathbf{R}^{(1)} + \mathbf{K}) t_\mathrm{m} \} \Big]_{ji} (M_i(t_1 + t_0) - M_i^0) \Big\}, \tag{5.22}$$

while similarly to what occurred during the evolution period t_1, only T_2 is encoded during the detection period t_2,

$$M_j(t_2 + t_\mathrm{m} + t_1 + t_0) \approx \exp\{ -R_j^{(2)} t_2 \} M_j(t_\mathrm{m} + t_1 + t_0) = \exp\{ -t_2/T_{2,j} \} M_j(t_\mathrm{m} + t_1 + t_0) \tag{5.23}$$

The resultant time-domain signal is then approximated by

$$\begin{aligned} M_j(t_2 + t_\mathrm{m} + t_1 + t_0) &\approx \exp\{ -t_2/T_{2,j} \} \Big[\sum_i \Big\{ \Big[\exp\{ -(\mathbf{R}^{(1)} + \mathbf{K}) t_\mathrm{m} \} \Big]_{ji} \\ &\quad \big(\exp\{ -t_2/T_{2,i} \} M_i(t_0) - M_i^0 \big) \Big\} + M_j^0 \Big] \end{aligned} \tag{5.24}$$

From there, it is apparent that after 2D inversion over t_1 and t_2, cross peaks arise at coordinates $(T_{2,i},\, T_{2,j})$ with amplitudes given by

$$M_{ij} = \big[\exp\{ -(\mathbf{R}^{(1)} + \mathbf{K}) t_\mathrm{m} \} \big]_{ij} M_i(t_0) \tag{5.25}$$

Therefore, when this slow exchange limit is fulfilled for the encoding and detection periods t_1 and t_2, the cross-peak amplitude represents the magnetization from site j that originated from site i before the mixing time t_m.

For the sake of understanding, the virtual case of fast exchange during the mixing is considered. Then we would have

$$\exp\{-(\mathbf{R}^{(1)}+\mathbf{K})t_{\mathrm{m}}\} \approx \exp\{-\mathbf{K}t_{\mathrm{m}}\} \tag{5.26}$$

In this limit, magnetization would have been conserved during the exchange and thus, upon normalization, could have been assigned to the probability of site occupancy. The cross peaks would then have mapped the joint probability of molecules or spins being at site j at time $t_0+t_1+t_{\mathrm{m}} \approx t_0+t_{\mathrm{m}}$, and at site i at time $t_0+t_1 \approx t_0$. This joint probability density can be expressed in terms of the conditional probability density of a spin being at site j knowing it started at time i following

$$M_{ji} = \langle R_j,(t_0+t_{\mathrm{m}})|R_i,t_0\rangle_{ji} M_i(t_0) \tag{5.27}$$

Consequently, comparing Eqns. 5.23 and 5.25, the exponential exchange operator could have been identified with the conditional probability matrix:

$$\exp\{-\mathbf{K}t_{\mathrm{m}}\} = \Big[\langle R_j,(t_0+t_{\mathrm{m}})|R_i,t_0\rangle_{ji}\Big], \tag{5.28}$$

and the cross-peak intensities would have directly mapped the elements of the exponential of the kinetic matrix, or equivalently of the conditional probability, as

$$M_{ji} = \langle R_j,(t_0+t_{\mathrm{m}})|R_i,t_0\rangle_{ji} M_i(t_0) = \Big[\exp\{-\mathbf{K}t_{\mathrm{m}}\}\Big]_{ji} M_i(t_0). \tag{5.29}$$

This means that the evolution of the intensities of the peaks with the length of the mixing period would have decayed according to the eigenvalues of the exchange matrix.

However, in reality, the fast exchange limit cannot be fulfilled during the mixing time when the slow exchange limit applies during the encoding times. As a result, magnetization is not conserved during the mixing time due to relaxation. Nevertheless, if all the sites had the same relaxation rate $R^{(1)}_{all}$, one could still write

$$\begin{aligned}\Big[\exp\{-(\mathbf{R}^{(1)}+\mathbf{K})t_{\mathrm{m}}\}\Big]_{ji} &= \exp\{-R^{(1)}_{all}t_{\mathrm{m}}\}\Big[\exp\{-\mathbf{K}t_{\mathrm{m}}\}\Big]_{ji} \\ &= \exp\{-t_{\mathrm{m}}/T_{1,\,all}\}\Big[\exp\{-\mathbf{K}t_{\mathrm{m}}\}\Big]_{ji},\end{aligned} \tag{5.30}$$

and the cross-peak intensities would still be a representation of the elements of the kinetic matrix albeit weighted by relaxation during the mixing time

$$\begin{aligned} M_{ji}(t_0+t_\mathrm{m}) &= \exp\{-R_{all}^{(1)}t_\mathrm{m}\}\langle R_j,(t_0+t_\mathrm{m})|R_i,t_0\rangle_{ji}M_i(t_0) \\ &= \exp\{-R_{all}^{(1)}t_\mathrm{m}\}\Big[\exp\{-\mathbf{K}t_\mathrm{m}\}\Big]_{ji}M_i(t_0). \end{aligned} \tag{5.31}$$

Nevertheless, 2D relaxation exchange NMR is of interest only when the sites relax differently, so that the case above is not pertinent. In general, even in the slow exchange limit, one cannot go further than writing

$$\begin{aligned} M_{ji}(t_0+t_\mathrm{m}) &= \Big[\exp\{-(\mathbf{R}^{(1)}+\mathbf{K})t_\mathrm{m}\}\Big]_{ji}M_i(t_0) \\ &= \Big[\mathbf{Q}\exp\{-\mathbf{Q}^{-1}(\mathbf{R}^{(1)}+\mathbf{K})\mathbf{Q}t_\mathrm{m}\mathbf{Q}^{-1}\}\Big]_{ji}M_i(t_0) \end{aligned} \tag{5.32}$$

The other two cases (as explained at the beginning of this section, namely fast exchange versus relaxation and exchange commensurate with relaxation) are even more complex as magnetization is not conserved or follows multiple single relaxation paths. The evolution of magnetization must be predicted working back from the general equations 5.9 and 5.19. As a consequence, 2D relaxation-exchange maps cannot be interpreted in terms of conditional probability densities, and the observed decay rates are not associated with single site relaxation rates [MKMM06] [MKMM05].

5.2.11 Multi-site relaxation exchange

In the case of an interconnected system of more than two sites, tracking the general analytical expression of the rotation matrix $\mathbf{Q}$ in order to diagonalize the evolution operator becomes extremely tedious at best and close to impracticable in most cases. Furthermore, as the slow exchange limit is typically violated in relaxation exchange NMR, 2D exchange maps cannot simply be interpreted in terms of joint probability densities. At this stage of the discussion, since no obvious generalizations can be made from the two-sites analytical solution, it becomes clear that only numerical simulations which take relaxation and exchange into account at all time periods of the 2D exchange experiment can support the interpretation of the experimental data.

5.3 Numerical simulations

5.3.1 Introduction

The simulation procedure provides the opportunity to generate time-domain exchange data sets free of experimental noise which can be processed by one of the available so-called ILT algorithms in order to evaluate methods of extracting relaxation, exchange, and population parameters from the exchange maps. Given a chosen set of $\mathbf{K}$, $\mathbf{R}^{(2)}$ and $\mathbf{R}^{(1)}$ matrices and an initial magnetization vector $\boldsymbol{M}(t_0)$ which typically is proportional to the population of sites, the magnetization vector $\boldsymbol{M}(t_1+t_0)$ is calculated according to equation 5.17 for each site i and at each time $t_1 = p_1 t_\mathrm{E}^{(1)}$ with p_1 varying between 1 and n:

$$M_i(t_1+t_0) = M_i(p_1t_\mathrm{E}^{(1)}+t_0) = \sum_{j=1}^{n}\Big[\exp\{-(\mathbf{R}^{(2)}+\mathbf{K})(p_1t_\mathrm{E}^{(1)})\}\Big]_{ji}M_j(t_0) \tag{5.33}$$

This provides a 1D time domain data set for each site. Then for each value of p_1 the magnetization vector $\boldsymbol{M}(t_2 + t_\mathrm{m} + p_1 t_\mathrm{E}^{(1)} + t_0)$ is calculated according to equation 5.19 for each site j and at each time $t_2 = p_2 t_{\mathrm{E}^{(2)}}$ with p_2 running form 1 to n. Thus, for each site j, an individual n^2 2D data set is obtained in the time domain,

$$\begin{aligned} M_j(t_2 + t_\mathrm{m} + t_1 + t_0) &= M_j(p_2 t_\mathrm{E}^{(2)} + t_\mathrm{m} + p_1 t_\mathrm{E}^{(1)} + t_0) \\ &= \sum_{r=1}^{n} \Big[\exp\{ -(\mathbf{R}^{(2)} + \mathbf{K})(p_2 t_\mathrm{E}^{(2)}) \} \Big]_{jr} \\ &\qquad \Big\{ \sum_{i=1}^{n} \Big(\Big[\exp\{ -(\mathbf{R}^{(1)} + \mathbf{K}) t_\mathrm{m}) \} \Big]_{ri} \\ &\qquad\qquad (M_i(p_1 t_\mathrm{E}^{(1)}) - M_i^0) \Big) + M_r^0 \Big\} \end{aligned} \tag{5.34}$$

Finally, the simulated 2D data set is the sum of the individual 2D data sets for each site j,

$$S(t_1,\, t_\mathrm{m},\, t_2) = S(p_1 t_\mathrm{E}^1,\, t_\mathrm{m},\, p_2 t_\mathrm{E}^2) = \sum_{j=1}^{n} M_j(p_2 t_\mathrm{E}^{(2)},\, t_\mathrm{m},\, p_1 t_\mathrm{E}^{(1)}). \tag{5.35}$$

This 2D time domain array simulates the data from the 2D relaxation-exchange NMR experiment [LLSH93]. Finally, the 2D T2-T2 exchange map is obtained by 2D Inverse Laplace Transform (ILT) of this array.

5.3.2 The problem of the ILT

5.3.2.1 Introduction

Although relaxation exchange and chemical exchange both come from the same formal equation (Eqn. 5.6), 2D Laplace NMR [HV02, MJ93, CM94, SD05] did not develop as early as the spectroscopic study of motion by 2D Fourier exchange NMR. The inversion of the data from the time domain into the relaxation rate domain involves the ill-defined ILT [VSH02, HBS06, Son06] which generates artefacts which are not as well understood as the ones coming from the Fourier transformation used to recover the frequency space from the temporal signal in Fourier NMR. Moreover, the numerical ILT is very consuming in terms of CPU, thus computing an ILT as proposed by Venkataramanan [VSH02] has only recently become possible.

5.3.2.2 1D case

Depending on the physico-chemical environments, species exhibit various relaxation times T following a distribution $A(T)$. At this point, there is no discrimination between longitudinal relaxation and transverse relaxation. Then, the relaxation signal $s(t)$ measured is the sum of the decay from all sites :

$$s(t) = \int A(T) \exp\Big\{ -\frac{t}{T} \Big\} \mathrm{d}T + \epsilon(t) \tag{5.36}$$

where $\epsilon(t)$ represents the noise of the signal which plays a major role in the numerical inversion. The objective is to estimate $A(T)$ subject to nonnegativity constraint ($A(t) \geq 0$). Note that by similarity with conventional two-dimensional spectroscopy, we shall call $A(T)$ the spectrum of $s(t)$.

Practically, relaxation decays are measured using multi-pulse sequences leading to a discrete measurement of the decay. This results in a discrete sampling of the "reciprocal space". So, the continuous form of the previous equation must be turned in a discrete form :

$$s(t_i) = \sum_{p=1}^{N} A(T_p) \exp\Big\{ - \frac{t_i}{T_p} \Big\} + \epsilon_i. \tag{5.37}$$

The general procedure to invert the data and determine the distribution $A(T)$ consists in applying a non-negative least square algorithm [LH74]. The idea is to minimize the following expression:

$$\chi^2 = \sum_{i=1}^{n} \Big[s(t_i) - \sum_{p=1}^{N} A(T_p) \exp\Big\{ - \frac{t_i}{T_p} \Big\} \Big]^2 \tag{5.38}$$

However, a small change in $s(t)$, due to the noise, may result in a large change in $A(T)$. The problem is said to be ill-conditioned. The strategy adopted to solve this problem is to add a so-called regularization function. The new function to minimize is [BBF98] :

$$\chi^2 = \sum_{i=1}^{n} \Big[s(t_i) - \sum_{p=1}^{N} A(T_p) \exp\Big\{ - \frac{t_i}{T_p} \Big\} \Big]^2 + \frac{1}{\alpha} \sum_{p=2}^{N-1} \Big[A(T_{p+1}) - 2A(T_p) + A(T_{p-1}) \Big]^2 \tag{5.39}$$

where α is the smoothing parameter. If one rewrite this expression in a matrix way, we obtained:

$$\chi^2 = ||S - \mathbf{U}A||^2 + \frac{1}{\alpha} ||A"||^2 \tag{5.40}$$

S is a vector with the n components of $s(t_i)$. $\mathbf{U}$ is a $n \times N$ matrix of the $\exp(t_i/T_p)$. N and the T_p's are fixed for the processing, so $\mathbf{K}$ is a known matrix. A is a vector of N components containing the amplitudes corresponding to the T_p. This is the vector to be determined.

5.3.2.3 2D case

At two dimensions, the problem is slightly more complex. The signal which is measured can be written as :

$$s(t_1, t_2) = \iint \exp\Big\{ - \frac{t_1}{T} \Big\} \exp\Big\{ - \frac{t_2}{T'} \Big\} A(T, T') \mathrm{d}T \, \mathrm{d}T' + \epsilon(t_1, t_2) \tag{5.41}$$

The integral part of this expression is known as a Fredholm integral of the first kind. The discrete expression is :

$$s(t_1^i, t_2^j) = \sum_{p=1}^{N} \sum_{q=1}^{N\prime} \exp\Big\{ -\frac{t_1^i}{T_p} \Big\} \exp\Big\{ -\frac{t_2^j}{T_q'} \Big\} A(T_p, T_q') + \epsilon(t_1^i, t_2^j) \tag{5.42}$$

Thus, in the matrix form, the quantity to minimize is:

$$\chi^2 = ||\mathbf{S} - \mathbf{U}\mathbf{A}\mathbf{U}'||^2 + \frac{1}{\alpha}||\mathbf{A}"||^2 \tag{5.43}$$

where $\mathbf{U}$ and $\mathbf{U}'$ are the the matrix of the $\exp(t_i/T_p)$ and $\exp(t_j/T_q')$ respectively.

From there, this 2D problem can be reduced to 1D problem by considering the following transformation [VSH02]:

- the $n \times m$ matrix $\mathbf{S}$ is lexicographically ordered into a vector $\tilde{S}$ (all the element of $\mathbf{S}$ are regarded as a single vector preserving its shape from before)
- the $N \times N'$ matrix $\mathbf{A}$ undergoes the same treatment to give the vector $\tilde{A}$
- the tensor product of matrices $\mathbf{U}$ and $\mathbf{U}'$ leads to $\tilde{\mathbf{U}}$ (containing each element of $\mathbf{R}$ multiplied by each element of $\mathbf{U}'$!)

Thus, the 2D problem takes the form:

$$\chi^2 = ||\tilde{S} - \tilde{\mathbf{U}}\tilde{A}||^2 + \frac{1}{\alpha}||\tilde{A}"||^2 \tag{5.44}$$

which has the same form as the 1D equation 5.40.

However, compare to the 1D case, the 2D case treated through a straightforward reduction to 1D is very demanding in terms of computer memory and speed and has been accomplished only on dedicated calculators [EWJH91]. To be used on desktop computers, the size of the data must be cut down. The solution proposed by Venkataramanan et al. [VSH02] is to use a Singular Value Decomposition (SVD) of $\mathbf{U}$ and $\mathbf{U}'$ before the 2D to 1D conversion in order to compress the data. The SVD's of $\mathbf{U}$ and $\mathbf{U}'$ are

$$\mathbf{U} = \mathbf{W}_\mathbf{U}\mathbf{\Sigma}_\mathbf{U}\mathbf{V}'_\mathbf{U} \tag{5.45}$$
$$\mathbf{U}' = \mathbf{W}_{\mathbf{U}'}\mathbf{\Sigma}_{\mathbf{U}'}\mathbf{V}'_{\mathbf{U}'} \tag{5.46}$$

Here, $\mathbf{\Sigma}_\mathbf{U}$ and $\mathbf{\Sigma}_{\mathbf{U}'}$ are diagonal matrices with the singular values in a decreasing order along the diagonal. The matrices $\mathbf{W}_\mathbf{U}$, $\mathbf{V}_\mathbf{U}$, $\mathbf{W}_{\mathbf{U}'}$ and $\mathbf{V}_{\mathbf{U}'}$ are unitary. Because of the form of the kernels $\mathbf{U}$ and $\mathbf{U}'$, the singular values as a function of their respective position along the diagonal decay quickly toward zero. Thus, the algorithm can be limited to the subspace spanned by the typically 8-10 largest singular values for each of the kernels [SVH+02]. In this way, Venkataramanan [VSH02] shows that the matrix $\mathbf{S}$ is reduced to $\hat{\mathbf{S}}$ through the following transformation:

$$\hat{\mathbf{S}} = \mathbf{W}'_\mathbf{R}\mathbf{S}\mathbf{W}_{\mathbf{R}'} \tag{5.47}$$

Then, the transformation from 2D to 1D presented before (Equation 5.44) leads to a χ^2 minimization with a reasonable number of variables.

5.3.2.4 Algorithm used

There are various algorithms available on the market. The most famous and probably the oldest is the program CONTIN written by Provencher [Pro82a, Pro82b]. We used a software developed by the group of Prof. P.T. Callaghan and based on the method of Venkataramanan [VSH02, CM94, WM89, SS95].

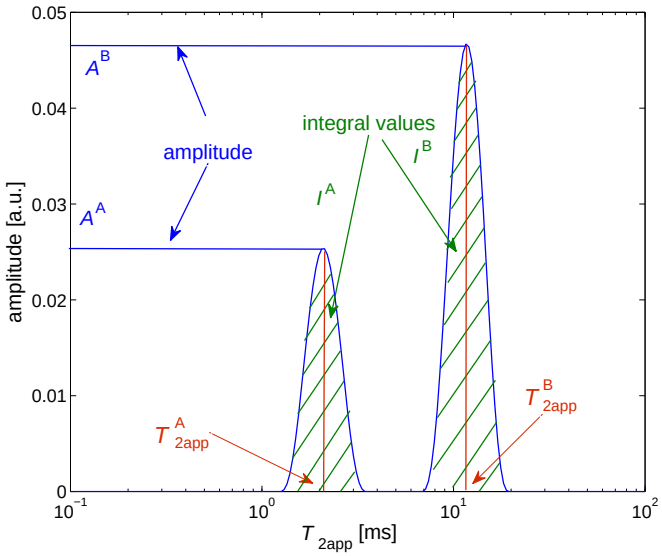

Figure 5.4: Notation for 1D relaxation time distributions of two exchanging sites.

5.3.3 Procedure for 1D simulations

As a preparatory check for 2D exchange data simulations, and to gain prior insight into relaxation-exchange NMR, 1D CPMG data are analyzed. Time-domain data sets were generated for two-site exchanges using Eqn. 5.35

$$S_{1D}^{twosites}(t_1,\, t_m,\, t_2) = S_{1D}^{twosites}(p_1 t_E^1,\, t_m,\, p_2 t_E^2) = M_A(p_2 t_E^{(2)},\, t_m,\, p_1 t_E^{(1)}) + M_B(p_2 t_E^{(2)},\, t_m,\, p_1 t_E^{(1)}) \tag{5.48}$$

and subsequently converted into distributions of relaxation times by ILT. The notation used in Eqn. 5.34 is the following (Fig. 5.4):

- $T_{2\,app}^A$, $T_{2\,app}^B$ denote the coordinates of the peaks on a transverse relaxation times scale obtained by ILT of the simulated data.
- A^A, A^B denote the amplitudes of the peaks in the relaxation time distribution of peaks A and B, respectively, calculated from the simulated data by ILT.
- I^A, I^B denote the areas of the ILT peaks of sites A and B, respectively.

The input parameters chosen for the 1D simulations are summarized in Table 5.2. The exchange time, e.g. the inverse of the exchange rate, is varied between 0.01 and 500 ms. For these parameters, 1D relaxation decays were simulated and inverted by ILT to extract the $T_{2\,app}$ coordinates of the peaks in the relaxation time distributions, the peak amplitudes, and the peak integrals. The results are summarized graphically in Figs. 5.5A and B.

Table 5.2: Input parameters for simulations of 1D T_2 distributions.

Parameter	Value
T_2^{A}	2.5 ms
T_2^{B}	25 ms
A^{A}	0.5
A^{B}	0.5

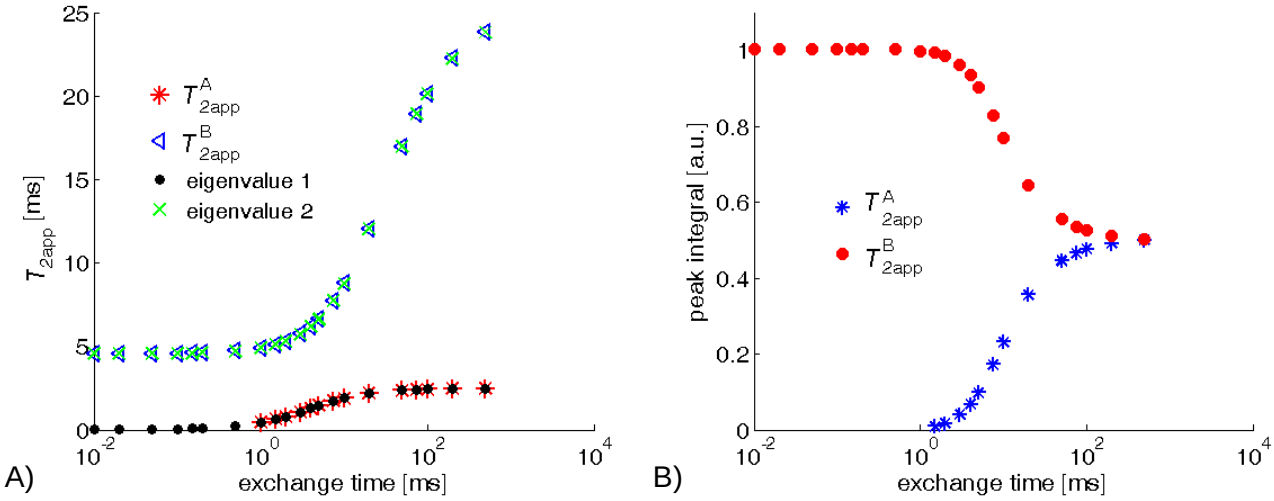

Figure 5.5: Results of 1D simulations for two-site exchange. A) Apparent relaxation times derived from relaxation time distributions and eigenvalues of the $\mathbf{R} + \mathbf{K}$ matrix. B) Peak integrals of relaxation time distributions.

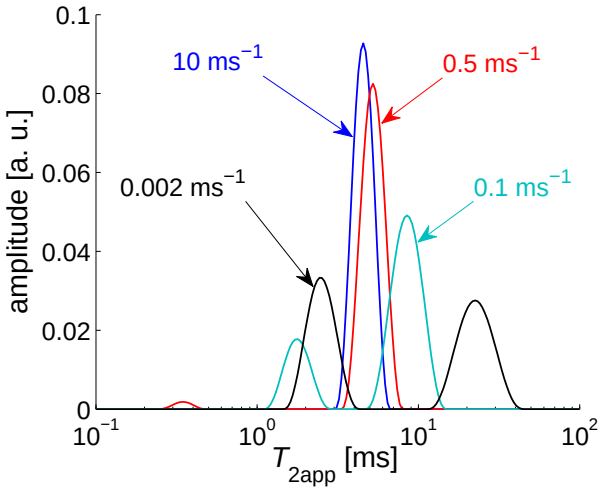

Figure 5.6: Examples of 1D spectra of two-site exchange for fast exchange ($k = 10$ ms^{-1}), two intermediate exchanges ($k = 0.5$ ms^{-1}, $k = 0.1$ ms^{-1}) and slow exchange ($k = 0.002$ ms^{-1}).

5.3.4 Results of 1D simulations

The influence of the exchange rate on the peak integrals and peak positions is illustrated in Figs. 5.5 and 5.6. When the exchange time becomes short compared to the relaxation times, one of the peaks grows at the expense of the other. For an exchange time lower than 1 ms, only a single peak is observed, and the peak integral corresponds to the number of spins from both sites (Fig. 5.5B). On the other hand, when the exchange time is at least ten times longer than the longest relaxation time, the peak integrals provide the correct population values. For shorter exchange times, the population of the peak with the longer relaxation time is overestimated and that of the other is underestimated. This observation is in line with the analytical predictions [MMM$^+$07, MKMM06].

To verify that these results were not an artefact of the ILT algorithm, the simulated relaxation curves were fitted with two exponential decay functions. The fit results confirmed that the peak integrals of the relaxation time distributions correspond to the amplitudes of the exponential fit functions. The amplitudes follow exactly the same pattern as the peak integrals, validating the use of peak integrals in the analysis of relaxation-time distributions to quantify spin populations.

It is emphasized that the relaxation times extracted from the maxima of the relaxation time distributions are apparent relaxation times, corresponding to the eigenvalues of the sum of the exchange and relaxation matrices and as such are strongly affected by the exchange rate (Fig. 5.6). An exchange time one hundred times longer than the longest T_2 component is required to obtain an unbiased estimate of T_2. Shorter exchange times lower the apparent transverse relaxation times. When the exchange approaches infinity, the shorter apparent T_2 value tends toward zero while the longer one shifts toward a value corresponding to the population weighted average of the relaxation rates, namely slightly below 5 ms in the present case.

In the intermediate exchange region between the fast and the slow exchange limits, the apparent relaxation times $T_{2\,\mathrm{app}}$ follows the eigenvalues of the $\mathbf{R}+\mathbf{K}$ matrix (Fig. 5.5A). The excellent agreement between the eigenvalues and the apparent relaxation times shows that, as expected from equation 5.6, the apparent relaxation times are indeed given by the eigenvalues of the $\mathbf{R}+\mathbf{K}$ matrix. To anticipate the discussion on 2D exchange experiments, we note that a 1D relaxation time distribution can be understood in terms of a projection of a 2D distribution onto one axis, and thus that the peaks in 2D distributions will be shifted by exchange along the relaxation-time axis in the same way as those in 1D distributions.

The results reported so far have all been simulated with one set of T_2 values, i.e. with $T_2^{\mathrm{A}} = 2.5$ ms and $T_2^{\mathrm{B}} = 25$ ms. Similar results were obtained with other choices of relaxation times as input variables. The dependences of the amplitudes and apparent relaxation times on the exchange time are similar in all cases, which corroborates the conclusions derived above. Moreover, if T_2 is replaced by T_1, the results of this study do not change. The T_1 values are affected by the exchange in the same way as the T_2 values.

5.3.5 2D simulations: two-site exchange

The time-domain data for two-site exchange were transformed to 2D exchange maps (Fig. 5.7) by 2D ILT. The 2D distributions exhibit two diagonal peaks and two off-diagonal peaks which reveal the exchange between the two sites. Depending on the exchange time and the exchange rate, one diagonal peak is observed for fast exchange, two diagonal peaks for slow exchange, and additional cross-peaks for intermediate exchange. As relaxation during the mixing period complicates the analysis of peak integrals (see Eqn. 5.19), simulations with the longitudinal relaxation time on (T_1 finite) and off (T_1 infinite) are compared. Simulations performed in this way with the parameters specified in Table 5.3 produced the exchange maps of Figure 5.7. The mixing time was set equal to the exchange time in each case except in the last case. When the exchange is very fast (bottom left), the exchange map exhibits a single peak in accordance with the 1D study. When the exchange time is increased and becomes comparable to the relaxation

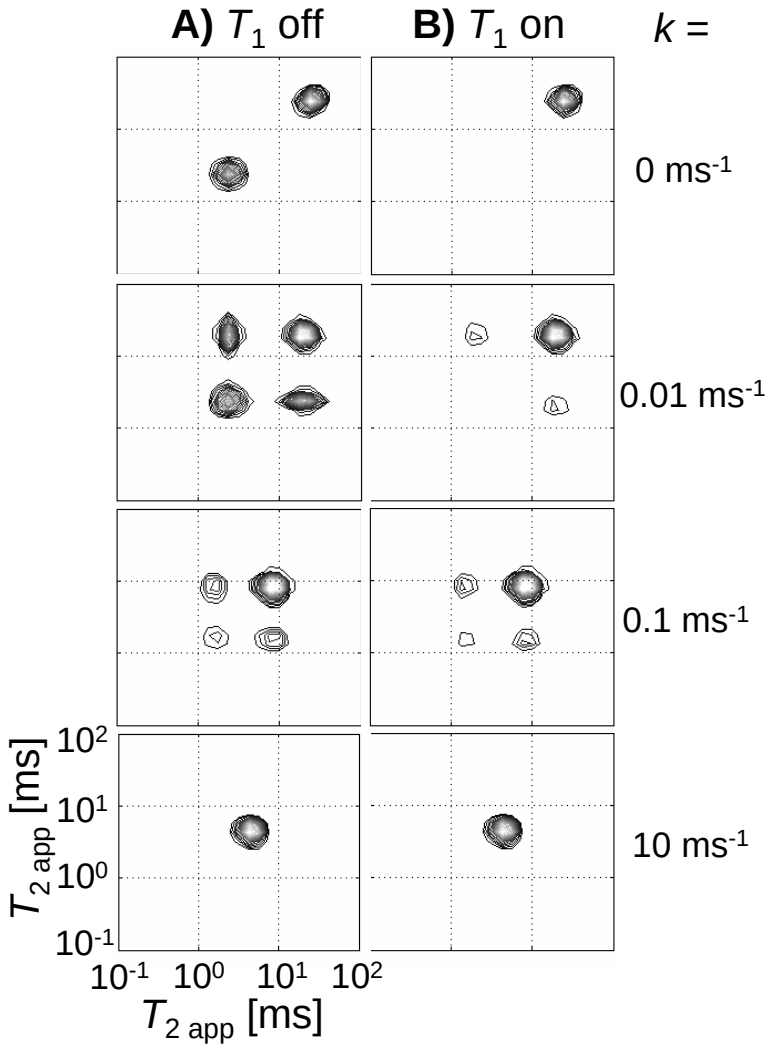

Figure 5.7: 2D distributions for two-site exchange simulated with the parameters of Tab. III with different exchange rates in the limit of infinite longitudinal relaxation times (A), and with longitudinal relaxation times equal to 6 times the transverse relaxation times (B).

times, cross peaks appear as well as two distinct diagonal peaks (bottom right, top left). When the exchange time becomes long, i.e. about ten times the longest value of T_2, the exchange is too slow to be seen and the cross peaks disappear (top right).

The peak intensities corresponding to the peak integrals in the 2D maps vary with the mixing time t_{m}. The diagonal peaks decay (Fig. 5.8A and B) and the cross-peaks initially grow exponentially with the mixing time t_m (Fig. 5.8C and D). This has been simulated for two-site exchange with $T_2 = 1$ ms and 10 ms for the two sites (Fig. 5.8). Without relaxation during the mixing time, the cross-peak intensity growths exponentially towards a dynamic equilibrium value (Fig. 5.8C). The time constants of the cross-peak build-up were determined via exponential fits. They are found to correspond to the inverse of the non-zero eigenvalue of the exchange matrix $\mathbf{K}$, i.e. to the input parameters $1/k_1 = 50$ ms and $1/k_2 = 100$ ms used in the simulations. As longitudinal relaxation has been turned off in the simulation, any change of peak intensity can indeed only be due to the exchange, so that the peak intensities can only change by mixing between the two populations.

Table 5.3: Parameters used to produce the exchange maps of Figure 5.7

Parameter	Value
T_2^{A}	2.5 ms
T_2^{B}	25 ms
T_1^{A}	Infinite, 15 ms
T_1^{B}	Infinite, 150 ms
k_1	10 ms^{-1}
k_2	0.1 ms^{-1}
k_3	0.01 ms^{-1}
k_4	0 ms^{-1}
A^{A}	0.5
A^{B}	0.5

When longitudinal relaxation is included during the mixing time t_{m}, the cross-peaks intensity goes to zero for long mixing times (Fig. 5.8D), and only when the longitudinal relaxation times are of the order of the exchange time and much larger than the transverse relaxation times did the cross peaks become intense. The build-up of the cross-peak intensity is no longer determined by the non-zero eigenvalue of the exchange matrix $\mathbf{K}$, as its growth is now affected by the T_1 relaxation of both sites.

5.3.6 2D simulations: three-site exchange

The results obtained for two-site exchange simulations did follow the known analytical solutions recalled in section 5.2.7 [MMM$^+$07, MKMM05, MKMM06]. To date, there is no published analytical solution for the case of relaxation and exchange between more than three sites. However, this case can be modelled with Eqn. 5.19. There is a fundamental difference between two- and n-site exchanges. For two-sites, the exchange maps are symmetric (if both dimensions are acquired with the same evolution times) as mass balance requires the forward and backward exchange to be identical. When exchange takes place between more than two sites, detailed mass balance applies to the overall exchange but not to subsets consisting of only two of the n sites, so that asymmetric exchange maps can arise. Figure 5.9 shows two simulated maps for three-site exchange, one symmetric (left) and the other one not (right). To obtain a symmetric map, all exchange times have to have the same value, whereas they differ strongly in the non-symmetric case.

5.3.7 2D simulations: noise and baseline artefacts

A further source of asymmetry in experimental data sets can be linked to the sensitivity of the numerical method used to approximate the inverse Laplace problem (the ILT algorithm) to noise and baseline artefacts [MKMM06]. To prove this point, a constant baseline and zero-mean Gaussian white noise with a standard deviation equal to a percentage of the maximum value of the simulated 2D data sets without any noise were added to the simulated data. The corresponding exchange maps derived by 2D ILT were analyzed for the peak integrals and the peak coordinates in the T_2-T_2 space (Fig. 5.10). Figure 5.10A, quantifies the effect noise on the peak integrals. The amplitude of the noise strongly affects the value of the integrals. As the peak integrals also depend on both the exchange rate and the longitudinal relaxation times, the accuracy with which exchange rates and longitudinal relaxation times can be determined is affected by the noise. The peak positions can also be shifted on the T_2-T_2 map in the presence of noise (Fig. 5.10B). This effect is not negligible as, remarkably, one of the diagonal peaks shifts away from the diagonal when the noise level is only just above 2%. Nonzero baselines

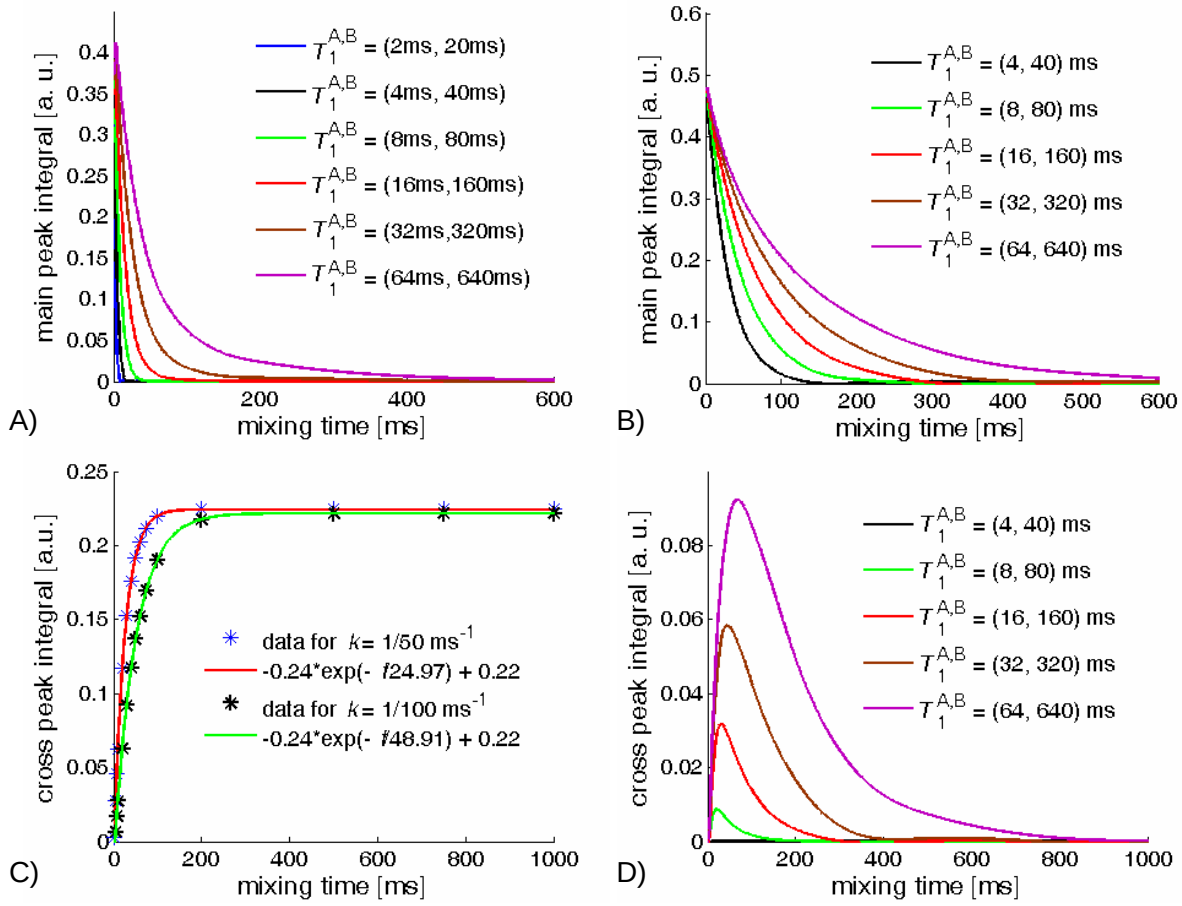

Figure 5.8: Evolution of peak integrals with the mixing time t_m in 2D maps for two-site exchange. A) Integrals of the diagonal peaks with the short relaxation time T_2 for various longitudinal relaxation rate. B) Integrals of the diagonal peaks with the long relaxation time T_2 for various longitudinal relaxation rate. C) Integral of cross peaks without longitudinal relaxation during the mixing time. D) Integral of cross peaks with longitudinal relaxation during the mixing time. The cross-peak build-up shown on C) was simulated two exchange times $1/k_1 = 50$ ms and $1/k_2 = 100$ ms. The exchange time for the curves on D) is $1/k_2 = 100$ ms.

also produce similarly strong artefacts in the peak intensities (c) and the peak positions (d). As shown in Figure 5.10C and 5.10D, a baseline offset of 2% is sufficient to produce asymmetric exchange maps.

5.4 Applications

The formalism to simulate 2D relaxation exchange maps was tested by modeling experimental maps for two-site exchange to extract relaxation and exchange parameters. Silica particles were synthesized according to the Stöber reaction [GJLH03] as this procedure is known to yield monodisperse particles which are good candidates for simple two-site exchange when saturated with water. The two relaxation sites are expected to be the bulk water in the intersticial space of the close packed structure on the one hand, and the water on the surface and within the micropores of the silica particles on the other hand.

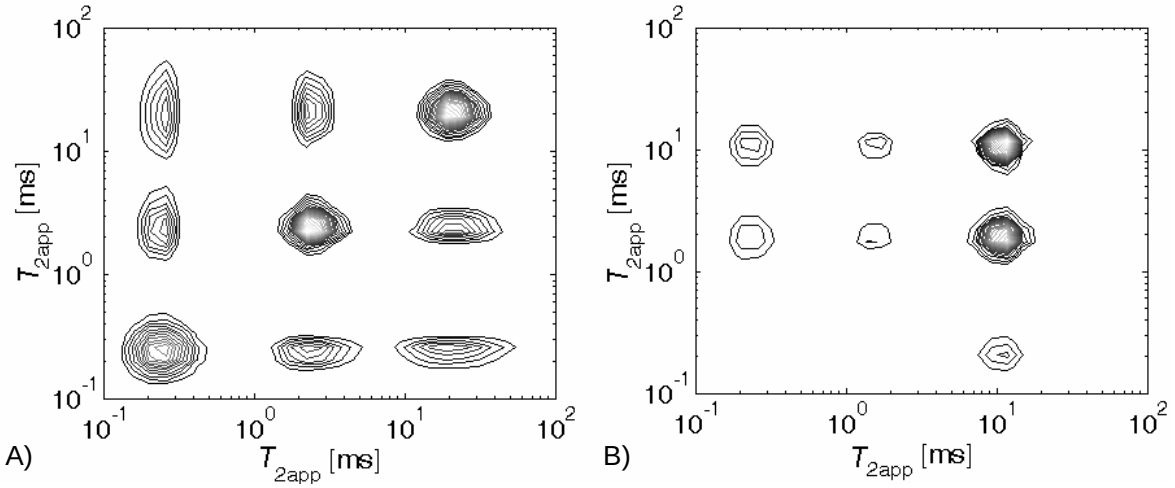

Figure 5.9: 2D maps for three-site exchange. A) Symmetric map with $1/k_{12} = 1/k_{13} = 1/k_{23} = 1/k_{32} = 250$ ms. B): Asymmetric map with $1/k_{12} = 400$ ms, $1/k_{13} = 20$ ms, $1/k_{23} = 3000$ ms, $1/k_{32} = 10$ ms. The longitudinal relaxation times were set to 4 times the corresponding transverse relaxation times.

5.4.1 Synthesis of silica particles

Silica particles were synthesized according to the Stöber reaction [SFB68]. For the particle synthesis, 60 mL of tetraethoxysilane ($Si(OC_2H_5)_4$), 405 mL of NH_3 at 25% in solution and 1.5 L of ethanol were mixed together. The Stöber synthesis is described by the following chemical reactions [GJLH03] :

- first, the ammonia NH_3 is ionized in water :

$$NH_3 + H_2O \longrightarrow NH_4^+ + OH^-$$

- second, the tetraethoxysilane is hydrolysed :

$$Si(OC_2H_5)_{4-x} + xH_2O \longrightarrow (HO)_xSi(OC_2H_5)_{4-x} + xC_2H_5OH$$

- then, a alcohol condensation leads to

$$Si(OC_2H_5)_4 + (OH)Si(OC_2H_5)_3 \longrightarrow (OC_2H_5)_3Si{-}O{-}Si(OC_2H_5)_3 + C_2H_5OH$$

- finally, the reaction product $(OC_2H_5)_3Si{-}O{-}Si(OC_2H_5)_3$ can undergo new alcohol condensation (from both sides) to lead finally to a polymer of silica SiO_2.

At the end of the reaction, the particles were washed first with ethanol and a second time with water, and their size was determined with a scanning electronic microscope (see Figure 5.11) to be 500 nm with a standard deviation of 40 nm.

5.4.2 1D measurements

Figure 5.12 depicts the transverse (A) and longitudinal magnetization build-up (B) curves measured by the CPMG sequence and the saturation recovery method respectively. As expected, the system exhibits two apparent transverse relaxation times T_2 which correspond to two different sites, but only a single apparent relaxation time T_1. Considering the results obtained in the 1D

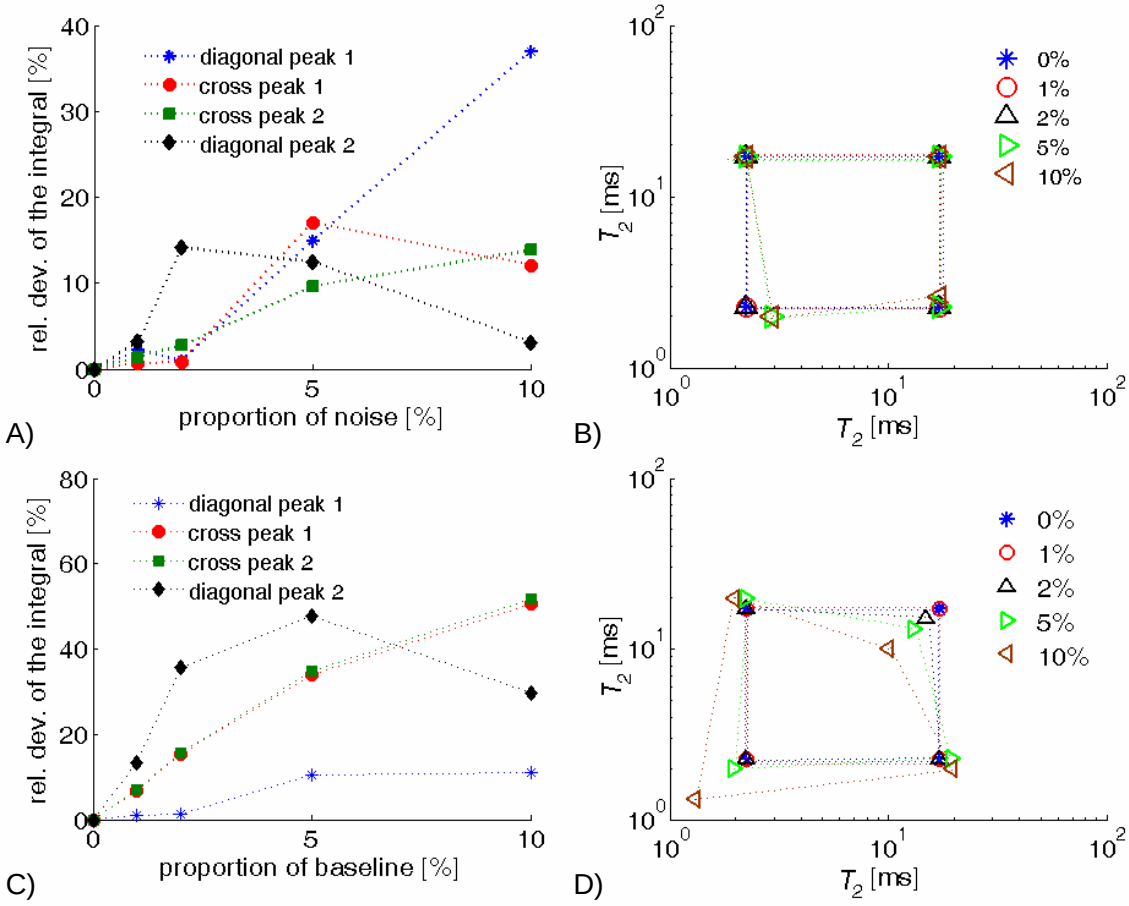

Figure 5.10: Effects of the noise (A and B) and baseline offset (C and D) on the peak intensities (A and C) and peak coordinates (B and D). The relative deviation of the integrals from the value in the absence of noise is given in percent. The baseline offset is specified relative to the maximum value of the original time-domain 2D data set.

simulations (see section 5.3.4), we can conclude from the observation of a single T_1 that the exchange time is small compared to the spin-lattice relaxation time. In this case, the single apparent T_1 corresponds to the nonzero eigenvalue of the $\mathbf{R}^{(1)} + \mathbf{K}$ matrix. Thus, we have already an idea of the other of magnitude of the exchange rate, which is a good indication for the choice of relevant parameters such as the mixing time.

5.4.3 Fitting of the experimental 2D data

5.4.3.1 Fitting procedure

T_1-T_2 correlation and T_2-T_2 exchange experiments were performed with a homemade Halbach-Magnet operating at a 21.85 MHz ^{1}H frequency. Using the algorithm described in section 5.2.8, 2D time data set were simulated for two-site exchange with six different mixing times (0 ms, 10 ms, 30 ms, 50 ms, 70 ms, 90 ms). A simplex algorithm [NM65] was used to match the input parameters of the simulation with the experimental data for each mixing time. The data were first fitted directly in the time domain in order to avoid any artefact from the ILT. The fitting procedure is described on Figure 5.13. The fit parameters are summarized in Tab. 5.4.

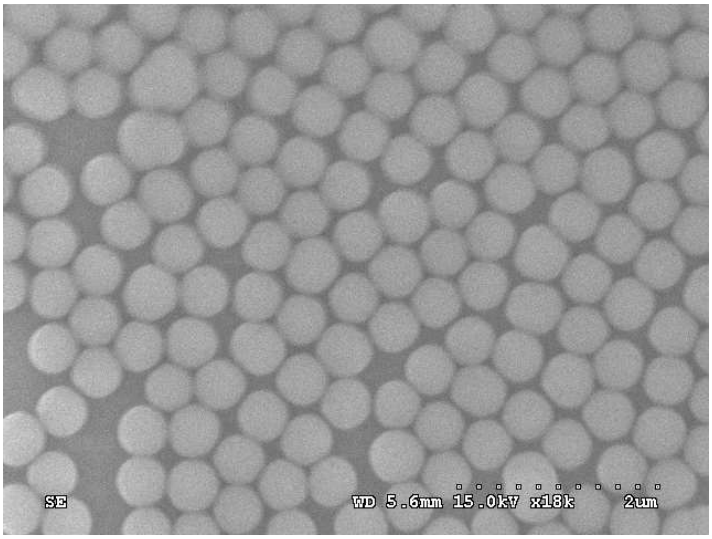

Figure 5.11: Picture of silica particles made from the Stöber reaction. The particles were first deposited on a wafer of silicium. Then, a gold layer was deposited in a Ar plasma to increase the contrast.

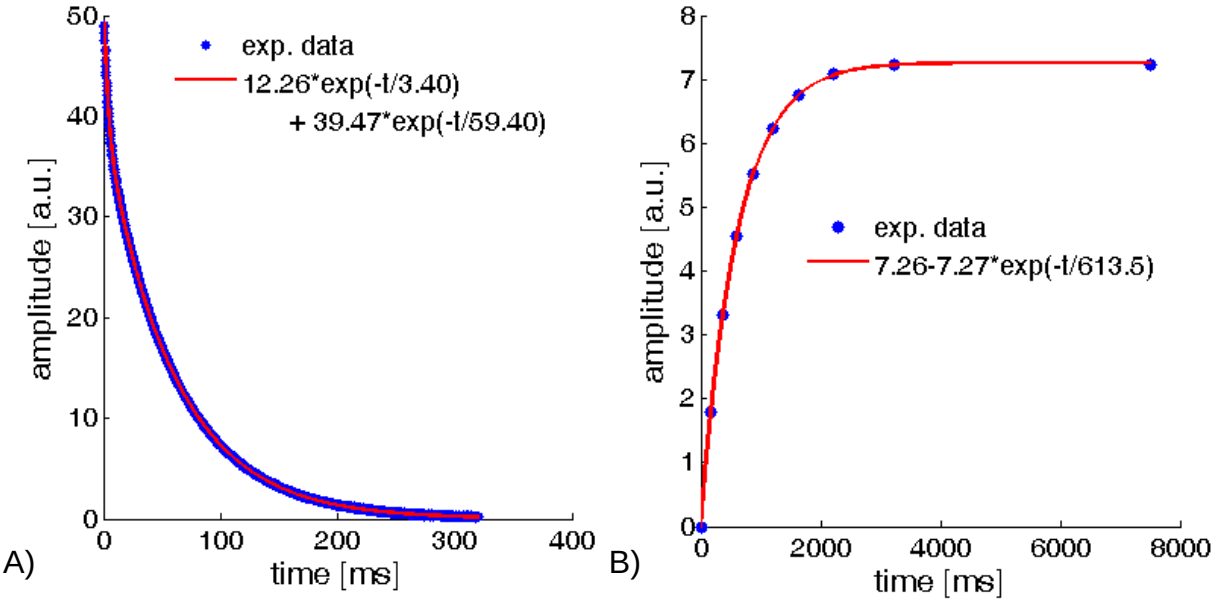

Figure 5.12: Water saturating silica particles. A) Transverse magnetization decay. B) Longitudinal magnetization build-up.measurements of water saturating silica particles.

5.4.3.2 Comparison of simulated and experimental data

The first remark is that, although this is beyond the point of this study, the ratio of the observed amplitudes is 3.3. This is one order of magnitude below the expected value considering only the ratio between the interstitial space and the microporous volume. With a close packing volumetric density of 0.74 and a porous volume within the particles of about 0.6% (a common value for Stöber silica)[STD02], one should get a ratio of 43. There is thus a significant contribution of the surface water to magnetization M^{A}.

Figure 5.14 shows the results obtained after ILT with a mixing time of 70 ms. One (a) is obtained by inverting the experimental data set, and the other one (b) by inverting the best-fit

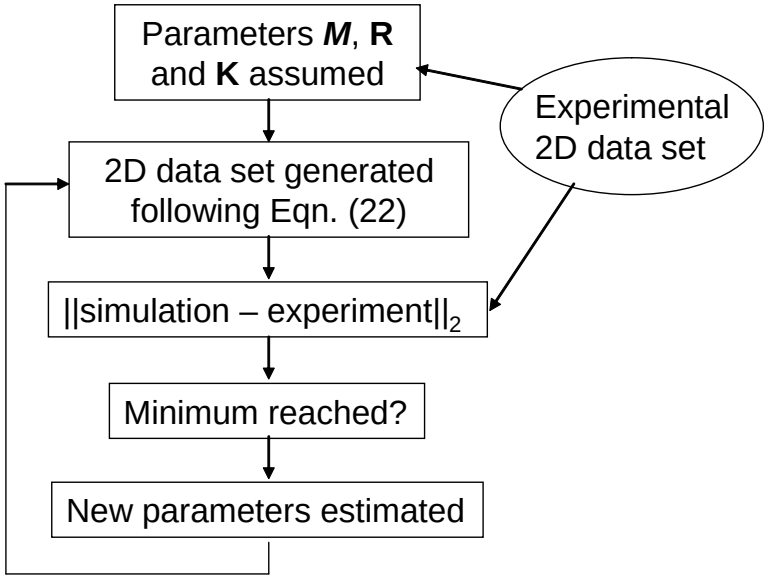

Figure 5.13: Flowchart demonstrating the procedure used to fit the experimental data. At each iteration, the simplex algorithm is used to estimate a new set of parameters minimizing the least-squares misfit of measured and experimental data points.

Table 5.4: Fit parameters obtained by the simplex algorithm described on figure 5.13

Parameter	Value
M^{A}	5.5
M^{B}	18.4
T_2^{A}	3.9 ms
T_2^{B}	103.5 ms
T_1^{A}	610 ms
T_1^{B}	630 ms
k	$1/110$ ms^{-1}

simulated data set. The peaks of the simulated maps are broader than the experimental ones. This is interpreted as a regularization artefact of the ILT procedure. To verify the quality of the fit, the evolution of the peak integrals with the mixing time (ranging between 0 and 90 ms) for both simulated and experimental maps are compared in Figure 5.15. Except for a discrepancy concerning the diagonal peak 1 at low mixing time, Figure 5.15 exhibits satisfactory agreement between the mixing time dependence of the peak intensities observed experimentally and the ones simulated using the parameters obtained by fitting the 2D data set. Thus, fitting experimental 2D time domain data sets with simulated ones allows to unravel relaxation from exchange and obtain the true (ie unbiased by the exchange) T_2 values which are quite different from the apparent one obtained by simple 1D fits (Fig. 5.12A). Unfortunately, in the experimental system under study, it has not been possible to extract real T_1 values as the exchange time was too short to distinguish them.

In support of the exchange analysis, the T_1-T_2 correlation map was measured and compared to the simulated one obtained with the fit parameters presented in Tab. 5.4 (Fig. 5.16). The small peak in the experimental map at low T_1 (around 40ms) is likely to be noise and does not carry any meaning as the 1D fit of Fig. 5.12A clearly indicated a single T_1.

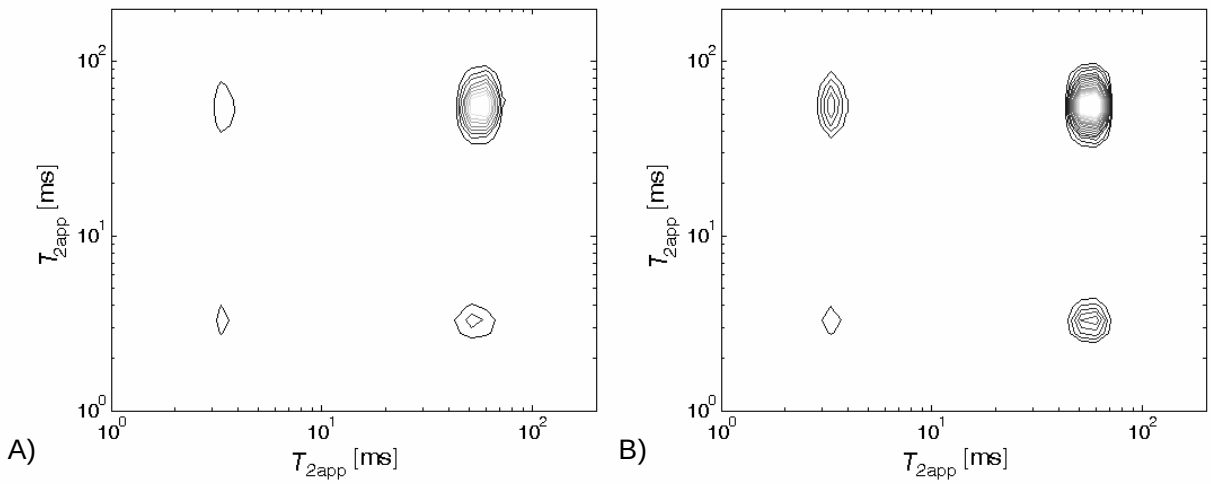

Figure 5.14: Experimental (A) and simulated (B) T_2-T_2 exchange spectrum of silica particles with the parameters of Tab. 5.4 for a mixing time of 70 ms.

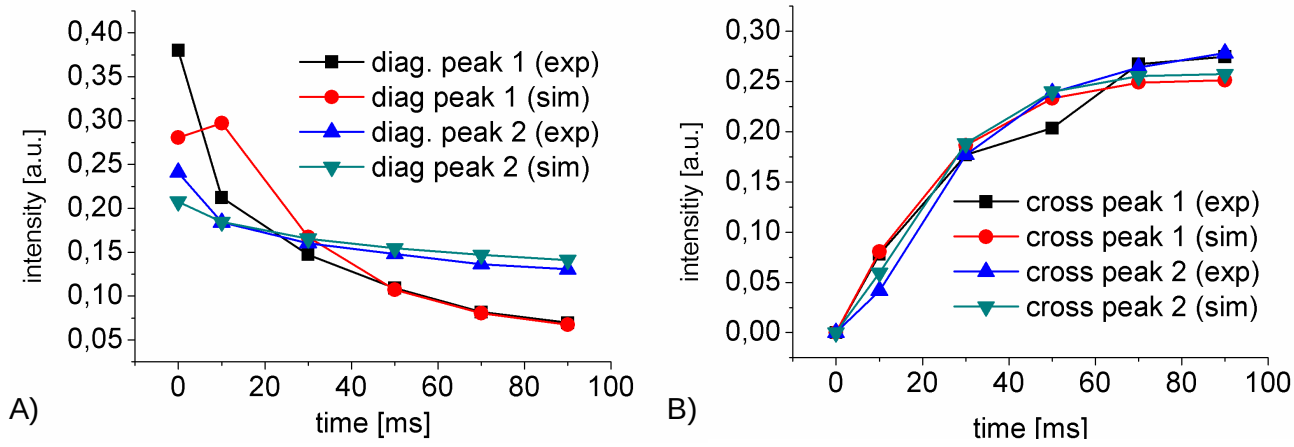

Figure 5.15: Comparison between the integrals of diagonal (A) and cross (B) peaks obtained by simulation and experiment versus the mixing time.

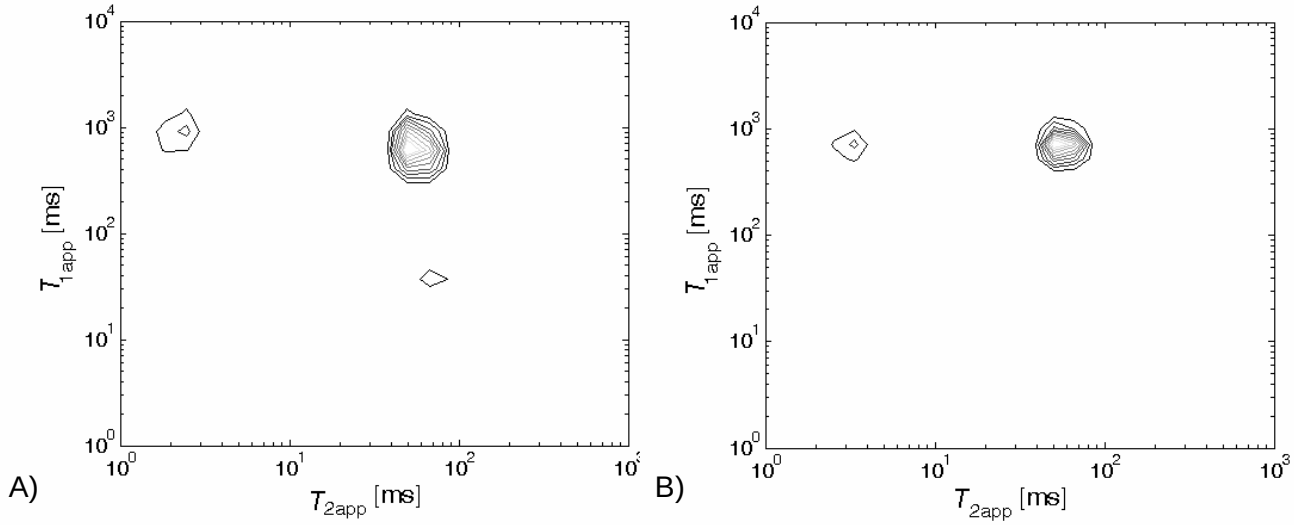

Figure 5.16: Experimental (A) and simulated (B) T_1-T_2 correlation map of water saturated silica particles derived with the parameters of Tab. 5.4.

Conclusion

Since a few years, multi-dimensional relaxation experiments have been developed to study the dynamics of the exchange between sites. Although exchange between these sites can be qualitatively evidenced by the presence of cross peaks in 2D correlation maps, its quantitative study is more complicated especially when the fast exchange limit is not fulfilled. In this chapter, we proposed a general method to extract numerically the exchange kinetics parameters by retro-fitting the experimental data. In particular, the simulations allowed us to propose a source of asymmetry, which is often observed experimentally as well as a source for the shift of peaks. As an example, two sites were identified for a model porous medium made of water in a saturated dense packing of silica particles with a narrow particle size distribution. However, although the theoretical framework allows the study of n discrete-site systems, its use is limited in practice to the case of four or five sites. Otherwise, the number of independent parameters becomes too large. On the other hand, it provides a first step towards the study of continuous distributions of sites such as in cementitious materials.

Bibliography

[Bai03] A.D. Bain. *Progr. Nucl. Magn. Reson. Spectr.*, 43(3-4):63–103, 2003.

[BBF98] G.C. Borgia, R.J.S. Brown, and P. Fantazzini. *J. Magn. Reson.*, 132(1):65–77, 1998.

[CAG+07] Paul T. Callaghan, Christoph H. Arns, Petrik Galvosas, Mark W. Hunter, Ying Qiao, and Kate E. Washburn. *Magn. Reson. Imaging*, 25(4):441–444, 2007.

[CM94] P. T. Callaghan and B. Manz. *J. Magn. Reson. Ser. A*, 106(2):260–265, 1994.

[EA54] R. R. Ernst and W. A. Anderson. *Rev. Sci. Instrum.*, 37(1):93–102, 1954.

[EBW87] R. R. Ernst, G. Bodenhausen, and A. Wokaun. *Principles of Nuclear Magnetic Resonance in One and Two Dimensions*. Oxford University Press, 1987.

[EWJH91] A.E. English, K.P. Whittall, M.L.G. Joy, and R.M. Henkelman. *Magn. Reson. Med.*, 22(2):425–434, 1991.

[FS09] M. Fleury and J. Soualem. *J. Colloid Interface Sci.*, 336(1):250–259, 2009.

[GJLH03] D. L. Green, S. Jayasundara, Y-F. Lam, and M.T. Harris. *J. Non-Cryst. Solids*, 315(1-2):166–179, 2003.

[HBS06] M. D. Hürlimann, L. Burcaw, and Y. Q. Song. *J. Colloid Interface Sci.*, 297(1):303–311, 2006.

[HV02] M.D. Hürlimann and L. Venkataramanan. *J. Magn. Reson.*, 157(1):31–42, 2002.

[JMBE79] J. Jeener, B. H. Meier, P. Bachmann, and R. R. Ernst. *Solid State Nucl. Magn. Reson.*, 71(11):4546–4553, 1979.

[KH86] R. M. Kroeker and R. M. Henkelman. *J. Magn. Reson.*, 69(2):218–235, 1986.

[Lai65] K.J. Laidler. *Chemical Kinetics*. McGraw-Hill, New York, 1965.

[LH74] C.L. Lawson and R.J. Hanson. *Solving Least Squares Problems*. Prentice-Hall, Englewood Cliffs, New Jersey, 1974.

[LLSH93] Jing Huei Lee, Christian Labadie, Charles S. Springer, and Gerard S. Harbison. *J. Am. Chem. Soc.*, 115(17):7761–7764, 1993.

[Mac98] R.S. Macomber. *A Complete Introduction to Modern NMR Spectroscopy*. Crystal Dreams Pub, 1998.

[McC58] H.M. McConnell. *J. Chem. Phys.*, 28(3):430–431, 1958.

[MJ93] K. F. Morris and C. S. Johnson. *J. Am. Chem. Soc.*, 115(10), 1993.

[MKMM05] P. J. McDonald, J. P. Korb, J. Mitchell, and L. Monteilhet. *Phys. Rev. E*, 72(1), 2005.

[MKMM06] L. Montheillet, J.-P. Korb, J. Mitchell, and P.J. McDonald. *Phys. Rev. E*, 74(6), 2006.

[MMM+07] P. J. McDonald, J. Mitchell, M. Mulheron, P. S. Aptaker, J. P. Korb, and L. Monteilhet. *Cem. Concr. Res.*, 37(3):303–309, 2007.

[NM65] J. A. Nelder and R. Mead. *Computer Journal*, 7(4):308–313, 1965.

[Pro82a] S.W. Provencher. *Comput. Phys. Commun.*, 27(3):229–242, 1982.

[Pro82b] S.W. Provencher. *Comput. Phys. Commun.*, 27(3):213–227, 1982.

[SD05] B. Q. Sun and K. J. Dunn. *J. Magn. Reson.*, 172(1):152–160, 2005.

[SFB68] W. Stöber, A. Fink, and E. Bohn. *J. Colloid Int. Sci.*, 26(1):62, 1968.

[Son06] Y. Q. Song. Resolution and uncertainty of laplace inversion spectrum. In *8th International Bologna Conference on Magnetic Resonance in Porous Media*, pages 445–448, Bologna, ITALY, Sep 10 2006. Elsevier Science Inc.

[SS95] C. Straley and L. M. Schwartz. Transverse relaxation in random bead packs: Comparison of experimental data and numerical simulations. In *3rd International Meeting on Recent Advances in MR Applications to Porous Media*, pages 999–1002, Louvain, Belgium, Sep 03-06 1995. Pergamon-Elsevier Science Ltd.

[STD02] M. Szekeres, J. Toth, and I. Dekany. *Langmuir*, 18(7):2678–2685, 2002.

[SVH+02] Y.-Q. Song, L. Venkataramanan, M.D. Hurlimann, M. Flaum, P. Frulla, and C. Straley. *J. Magn. Reson.*, 154(2):261–268, 2002.

[VSH02] L. Venkataramanan, Y. Q. Song, and M. D. Hurlimann. *Ieee Transactions on Signal Processing*, 50(5):1017–1026, 2002.

[WM89] K. P. Whittall and A. L. Mackay. *J. Magn. Reson.*, 84(1), 1989.

CONCLUSION

In this thesis, novel NMR techniques have been developed and applied to the study of cementitious materials. The main difficulties when investigating these materials arise from the shortness of their relaxation rates and their strong internal field gradient. Not only, do they result in a loss of resolution but a part of the water embedded within the materials may not be imaged. To overcome this difficulty, we developed our own NMR imaging probes. The original design of these probes adapts them to the particular geometry involved in STRAFI experiments but also exhibits the specifications of solid-state NMR probes which are good efficiency allowing the use of short pulse lengths and short dead times to implement the short echo times required for the quantitative investigation of fast relaxing species.

The probes developed in chapter 1 were then involved in a full STRAFI setup. The purpose of this experiment is to exploit a strong and static gradient to perform fast measurements of cementitious materials and avoid the image blurring due to the internal field gradients. In classical MRI experiments, the gradient coils are designed to generate the desired magnetic field in the zone of interest. Here, as it is static and cannot be changed, it was necessary to adapt our experimental setup to it. Thus, the region of the gradient exhibiting the properties required for high resolution imaging was theoretically determined and experimentally mapped. Afterwards, a procedure to finely orientate our sample against the direction of the gradient was implemented in order to achieve a resolution of 5 μm over a 10 mm wide sample. The monitoring of dynamic process such as the drying of mortar dessication over long periods (a few days) also required the implementation of automatic and synchronized running of the NMR spectrometer, the displacement of the sample, the processing and the displaying of the data. For that purpose, the conventional NMR setup was fitted into a larger system including external computers and acquisition cards allowing an automatic control of the spectrometer coupled to real-time processing of the data.

The major drawback of this powerful tool for the study of cementitious materials is that experiments are necessarily performed ex-situ, which means that samples cannot be measured on field and must fit the experimental setup. This limitation was solved by the use of low-field unilateral NMR sensors. Although this family of sensor is less sensitive and cannot image short relaxation rates, it can be used on-site to image semi-infinite sample such as a wall. Two single-sided sensors, namely the Profile MOUSE and the Fourier MOUSE were developed and used for that purpose. The existing Profile MOUSE was adapted to the study of thick layers (20 mm) of cementitious materials. Pulse program and processing methods were developed for the monitoring of mortar desiccation over a few days. In parallel, a need for a sensor allowing fast measurements on relatively thin layers (a few millimeters) appeared. For that purpose, we developed the Fourier MOUSE. This sensor is based on the use of a moderate gradient (typically ten times lower than the analogous Profile MOUSE) to excite the full depth range in a single shot and then make use of the Fourier Transformation to reconstruct the profile. To achieve this, the original field of a U-shaped magnet was carefully tailored using shim magnets to cancel the natural field inhomogeneities. With this sensor, a profile of 2 mm was obtained with a resolution of 25 μm in a few tens of a second.

The aim of the second part of the thesis is to apply the tools presented in the instrumental part to the study of cementitious materials. In these materials, water can be found in three

forms. Either it is chemically bound in hydrate forms, confined in C−S−H interlayers or it is free in the porous structure. These three states can be discriminated from their relaxation rates. The use of STRAFI allowed us to quantitatively and locally follow the growth of the porous structure of cement pastes. Thanks to its sensitivity to short relaxation rates, the study of the ratio of water confined in C−S−H and free in pores lead to the disentanglement of pure drying from self-dessication. In parallel, the Profile MOUSE turned out to be a natural and selective filter to monitor exclusively the free water. In particular, the impact of the curing temperature and humidity on the dessication of the cement paste was investigated. For example, it was found that at 60% of relative humidity and at 25 °C, the distribution of free water is constant over the sample. However, over 25 °C, a hydric gradient occurs which might lead to non uniform stress distribution within the sample and eventually to crack formation.

The static view of water in its three states within cementitious materials is not completely true. Indeed, even at the time scale of the measurement, a part of the free water is in exchange with the water in C−S−H. This exchange can be evidenced by using relaxation exchange NMR sequences (T_2-T_2 or T_1-T_2). A theoretical and numerical study of multi-site relaxation exchange NMR allowed us to show how the exchange can affect the measurement of the relaxation rates. Besides the bias induced by exchange on the relaxation rates, we proposed a procedure to extract from these measurements the kinetic parameters of the exchange which are the meaningful parameters. We also propose an origin for the presence of non symmetric 2D T_2-T_2 correlation maps often encountered when studying complex systems. As an example, we studied a model porous medium consisting of a pack of silica beads. Using our method, we managed to determine the exchange rate between the bulk water present in interstitial space and water interacting with the surface of the beads.

The development of STRAFI as a fundamental tool in the understanding of the porous structure in combination with the Profile MOUSE to perform on-site measurements turned out to be valuable in the study of cementitious materials. The next stage is to use them as systematic tools to observe the impact of cement additives on the porous structure and the dessication. The idea would be to correlate them with the presence or absence of cracks. The influence of the type of substrate is another way to explore. Indeed, these tools exhibit a resolution which allows them to finely look at the interface between the substrate and the paste. Finally, most of our work took place in the laboratory. It could be interesting to benefit from the portable aspect of the Profile MOUSE and perform measurements directly on-site.

Appendix A

Effects of diffusion

A.1 Phase differences due to diffusion

When a spin is moving in a magnetic field gradient, it explores an area where the Larmor frequency varies. So, in the rotating frame, the spin is getting a phase difference reflecting its motion inside the gradient. As this motion is random, the acquired phase difference is also random. Then, what is observed is the sum of every phase difference due to diffusion of every spin through the magnetic gradient.

A.1.1 Calculation of the phase term due to diffusion [DS54] [CP54] [HH56]

In the rotating frame at ω_0, the moment $\boldsymbol{m}(t)$ of a spin diffusing through areas where Larmor pulsations is $\omega(t)$ can be written :

$$\boldsymbol{m}(t) = \boldsymbol{m}(t_0) \cdot \exp\left(\imath \int_{t_0}^{t} (\omega(t) - \omega_0)\mathrm{d}t\right) \tag{A.1}$$

The relaxation term was deliberately removed as it is taken to be diffusion independent. It will be added again at the end. Let us consider that the spin is originally at a position where the Larmor pulsation is equal to ω. Then, the phase term can be expressed as the sum of the phase difference if the spin was fixed and a random term taking into account the diffusion:

$$\int_{t_0}^{t} (\omega(t) - \omega_0)\mathrm{d}t = [\omega - \omega_0] \cdot (t - t_0) + \phi_{t_0,\,t} = \Delta\omega \cdot (t - t_0) + \phi_{t_0,\,t} \tag{A.2}$$

where $\phi_{t_0,\,t}$ is the random phase shift acquired due to diffusion by this spin from t_0 to t. Then, the moment $\boldsymbol{m}$ of the diffusing spin can be rewritten:

$$\boldsymbol{m}(t) = \boldsymbol{m}(t_0) \cdot \exp\left(\imath(\Delta\omega \cdot (t - t_0) + \phi_{t_0,\,t})\right) \tag{A.3}$$

The vector $\boldsymbol{m}$ can be separates into two parts :

$$\boldsymbol{m}(t) = U(t) + \imath V(t) \tag{A.4}$$

with

$$U(t) = U(t_0) \cdot \exp\Big(\imath\Big(\Delta\omega(t-t_0)\Big)\Big) \cos(\phi_{t_0,t}) \tag{A.5}$$

$$V(t) = V(t_0) \cdot \exp\Big(\imath\Big(\Delta\omega(t-t_0)\Big)\Big) \sin(\phi_{t_0,t}) \tag{A.6}$$

The determination of the whole magnetization required the integration on all spins, ie an integration on all values of $\Delta\omega$ and all $\phi_{t_0,t}$. To do so, the distribution of and $\phi_{t_0,t}$ is required. In practice, since we are only interested in the amplitude at the top of the echo, $\Delta\omega$ plays no role. So we can simply omit it from the calculation. In the case of free diffusion, the distributions $P(\phi_{t_0,t}, t-t_0)$ and $Q(\delta\omega)$ are Gaussian:

$$P(\phi_{t_0,t}, t-t_0) = \frac{1}{\sqrt{2\pi\langle\phi^2_{t_0,t}\rangle}} \exp\Big(-\frac{\phi^2_{t_0,t}}{2\langle\phi^2_{t_0,t}\rangle}\Big) \tag{A.7}$$

Let us integrate on $\phi_{t_0,t}$:

$$\begin{aligned}
\int_{-\infty}^{+\infty} U(t)\,\mathrm{d}\phi_{t_0,t} &= U(t_0)\int_{-\infty}^{+\infty} P(\phi_{t_0,t}, t-t_0)\,\cos(\phi_{t_0,t})\,\mathrm{d}\phi_{t_0,t} \\
\int_{-\infty}^{+\infty} V(t)\,\mathrm{d}\phi_{t_0,t} &= V(t_0)\int_{-\infty}^{+\infty} P(\phi_{t_0,t}, t-t_0)\,\sin(\phi_{t_0,t})\,\mathrm{d}\phi_{t_0,t}
\end{aligned}$$

Using the two following classical integrals:

$$\int_{-\infty}^{+\infty} \cos(ax)\; e^{-b^2x^2}\mathrm{d}x = \frac{\sqrt{\pi}}{b}\; e^{-a^2/4b^2} \tag{A.8}$$

$$\int_{-\infty}^{+\infty} \sin(ax)\; e^{-b^2x^2}\mathrm{d}x = 0 \tag{A.9}$$

it is possible to calculate the integral of U and V taking $a=1$ and $b^{-2} = 2\,\langle\phi^2_{t_0,t}\rangle$:

$$\begin{aligned}
\int_{-\infty}^{+\infty} U(t)\,\mathrm{d}\phi_{t_0,t} &= \frac{U(t_0)}{2}\cdot\exp\Big(-\frac{\langle\phi^2_{t_0,t}\rangle}{2}\Big) \\
\int_{-\infty}^{+\infty} V(t)\,\mathrm{d}\phi_{t_0,t} &= 0
\end{aligned}$$

Keeping in mind that this expression is only correct at the summit of the echo, the magnetization can be written :

$$M_{x'}(t_\mathrm{E}) = \frac{M_{x'}(t_0)}{2}\; \exp\Big(-\frac{\langle\phi^2_{t_0,t}\rangle}{2}\Big) \tag{A.10}$$

$$M_{y'}(t_\mathrm{E}) = 0 \tag{A.11}$$

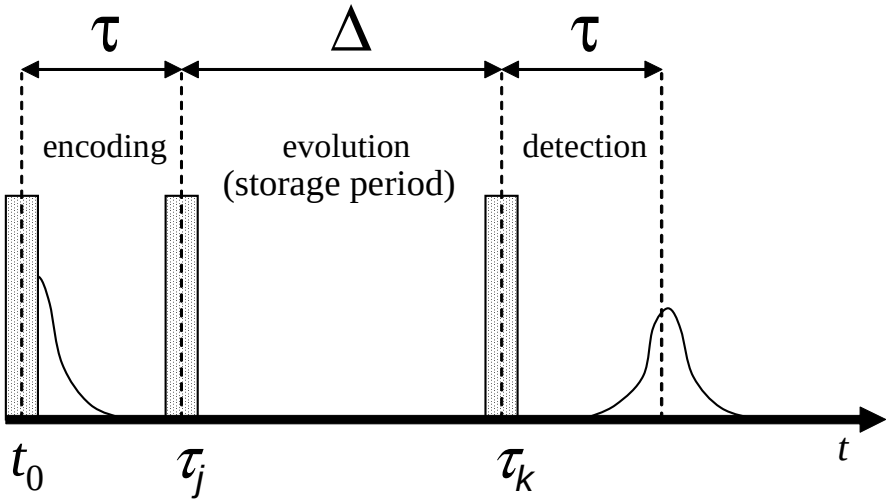

Figure A.1: Stimulated echo sequence used for self-diffusion coefficient measurement. Each pulse is a 90^o pulse.

A.1.2 Phase calculation for a stimulated spin echo [Woe61]

The calculation of $\phi_{t_0,t}$ for a stimulated spin echo (see Fig. A.1) is performed breaking the time down into equal intervals δt. $t_0 = 0$ is the time of the first pulse. The second pulse takes place at time $\tau_j = j\,\delta t$ and the third one at time $\tau_k = k\,\delta t$. One should notice at this point that during the storage period, the phase of the magnetization is not affected by the diffusion. The magnetization only goes from a frequency ω_j to a frequency ω_k but the integral of the random phase shift is equal to zero. Let us calculate the integral random phase shift for a molecule diffusing in a constant gradient G. In the general case, after n steps, the phase shift $\phi_{t_0,t}$ can be written as:

$$\phi_{t_0,t} = \gamma G(d_1\,\delta t + d_2\,\delta t + \cdots + d_i\,\delta t + \cdots + d_n\,\delta t) \tag{A.12}$$

where γ is the gyromagnetic ratio. The d_i are the displacement along the direction of the gradient from the initial position at the ith time increment. With a stimulated spin echo sequence, one can write

$$\phi_{t_0,t} = \gamma G\big(-(d_1\,\delta t + \cdots + d_j\,\delta t) + (d_{k+1}\,\delta t + \cdots + d_n\,\delta t)\big) \tag{A.13}$$

If we write:

$$\begin{aligned} d_2 &= d_1 + (d_2 - d_1) \\ d_3 &= d_1 + (d_2 - d_1) + (d_3 - d_2) \\ &\vdots \\ d_n &= d_1 + (d_2 - d_1) + (d_3 - d_2) + \cdots + (d_n - d_{n-1}) \end{aligned}$$

then, the phase shift can be written:

$$\begin{aligned}\phi_{t_0,t} &= \gamma G\delta t\Big\{(n-k-j)d_1+\sum_{u=1}^{u=j-1}(n-k-j+u)[d_{u+1}-d_u]+\cdots \\ &\quad \cdots+(n-k)\sum_{v=j}^{k}[d_{v+1}-d_v]+\sum_{w=1}^{n-k-1}w\cdot[d_{w+1}-d_w]\Big\} \end{aligned} \tag{A.14}$$

In the case of free diffusion, each $(d_{i+1}-d_i)$ is a normally distributed independent variable. Thus, $\phi_{t_0,t}$ is a linear combination of stochastic variable and its dispersion is :

$$\begin{aligned}\langle\phi_{t_0,t}^2\rangle &= \gamma^2G^2\delta t^2\Big\{(n-k-j)^2\langle d_1^2\rangle+\sum_{u=1}^{u=j-1}(n-k-j+u)^2\langle[d_{u+1}-d_u]^2\rangle+\cdots \\ &\quad \cdots+(n-k)^2\sum_{v=j}^{k}\langle[d_{v+1}-d_v]^2\rangle+\sum_{w=1}^{n-k-1}w^2\langle[d_{w+1}-d_w]^2\rangle\Big\} \end{aligned} \tag{A.15}$$

Moreover, according to diffusion theory, we can write:

$$\langle d_1^2\rangle=\langle[d_2-d_1]^2\rangle=\cdots=\langle[d_n-d_{n-1}]^2\rangle=2D\delta t \tag{A.16}$$

so, the previous equation can be written

$$\langle\phi_{t_0,t}^2\rangle=2\gamma^2G^2D\delta t^3\Big\{(n-k-j)^2+\sum_{u=1}^{u=j-1}(n-k-j+u)^2+(k-j+1)\cdot(n-k)^2+\sum_{w=1}^{n-k-1}w^2\Big\} \tag{A.17}$$

$$\langle\phi_{t_0,t}^2\rangle=2\gamma^2G^2D\delta t^3\Big\{\sum_{u=0}^{u=j-1}(n-k-j+u)^2+(k-j+1)\cdot(n-k)^2+\sum_{w=1}^{n-k-1}w^2\Big\} \tag{A.18}$$

$$\langle\phi_{t_0,t}^2\rangle=2\gamma^2G^2D\delta t^3\Big\{\sum_{p=1}^{p=n-k-1}p^2-\sum_{p=1}^{p=n-k-j-1}p^2+(k-j+1)\cdot(n-k)^2+\sum_{p=1}^{n-k-1}p^2\Big\} \tag{A.19}$$

We can notice that if $N\gg1$, then,

$$\sum_{p=1}^{N}p^2=\frac{N(N+1)(2N+1)}{6}\approx\frac{N^3}{3}. \tag{A.20}$$

Thus, we can write

$$\begin{aligned}\langle\phi_{t_0,t}^2\rangle &= 2\gamma^2G^2D\delta t^3\Big\{\frac{(n-k-1)^3}{3}-\frac{(n-k-j-1)^3}{3}+\cdots \\ &\quad \cdots+(k-j+1)\cdot(n-k)^2+\frac{(n-k-1)^3}{3}\Big\} \end{aligned} \tag{A.21}$$

$$\begin{aligned}\langle\phi_{t_0,t}^2\rangle &= \frac{2}{3}\gamma^2G^2D\Big\{2(t-\tau_k)^3-(t-\tau_k-\tau_j)^3+\cdots \\ &\quad \cdots+3(\tau_k-\tau_j)\cdot(t-\tau_k)^2\Big\} \end{aligned} \tag{A.22}$$

A.2 Calculation of the attenuation due to diffusion

The stimulated spin echo appears at $t = \tau_j + \tau_k$. So, the phase term in Eqn. A.21 becomes :

$$\langle \phi^2_{t_0,t} \rangle = 2\gamma^2 G^2 D \tau_j^2 \left\{ \frac{2}{3}\tau_j + (\tau_k - \tau_j) \right\} \tag{A.23}$$

Thus, the magnetization at the maximum of the echo is :

$$\begin{aligned} M_{x'}(t) &= \frac{M_{x'}}{2}(t_0)\ \exp\left(-\gamma^2 G^2 D \tau_j^2 \left\{ \frac{2}{3}\tau_j + (\tau_k - \tau_j) \right\} \right) \\ M_{y'}(t) &= 0 \end{aligned}$$

If we call τ the time between the two first pulses and Δ between the second and the third pulse, then the signal attenuation can be written:

$$\frac{I}{I_0} = \frac{1}{2} \exp\left(-\gamma^2 G^2 D \tau^2 \left\{ \frac{2}{3}\tau + \Delta \right\} \right) \tag{A.24}$$

Taking the relaxation again into account, the whole attenuation can be written.

$$\frac{I}{I_0} = \frac{1}{2} \exp\left(-\gamma^2 G^2 D \tau^2 \left\{ \frac{2}{3}\tau + \Delta \right\} - \frac{2\tau}{T_2} - \frac{\Delta}{T_1} \right) \tag{A.25}$$

Bibliography

[CP54] H.Y. Carr and E.M. Purcell. *Phys. Rev.*, 94(3):630–641, 1954.

[DS54] T.P. Das and A.K. Saha. *Phys. Rev.*, 93(4):749–756, 1954.

[HH56] B. Herzog and E.L. Hahn. *Phys. Rev.*, 103(1):148–168, 1956.

[Woe61] D. E. Woessner. *J. Chem. Phys.*, 34(6):2057–2061, 1961.

List of Figures

List of Tables

Zusammenfassung
Die Entwicklung von Materialien mit Hochleistungszement in Bezug auf ihre mechanischen Eigenschaften, Festigkeit oder Durchlässigkeit, erfordern ein gutes Verständnis ihrer porösen Struktur. Magnetische Resonanztomographie (MRT) ist als zerstörungsfreies Verfahren eine ausgezeichnete Methode zur Untersuchung der Wasserverteilung und des Feuchtetransports durch das Material. Doch aufgrund einer PorengröSSenverteilung über mehrere GröSSenordnungen und das Vorhandensein von paramagnetischen Verunreinigungen, erfordert die Anwendung von MRT auf diese Materialien den Einsatz von hohen Magnetfeldgradienten und eine schnelle Datenerfassung. Zu diesem Zweck haben wir zwei Techniken entwickelt. Für Labormessungen eignet sich STRAFI um die Auswirkung von Temperatur und Feuchtigkeit nicht nur auf die Wasserverteilung innerhalb der Materialien, sondern auch auf ihre poröse Struktur und damit auf deren Funktion zu charakterisieren. Die NMR-MOUSE™, ein tragbares Instrument, das bei niedrigem Feld arbeitet, erlaubt es, die Trocknung von zementhaltigen Materialien direkt vor Ort verfolgen. Sie bietet sich als interessantes Instrument für den industriellen Einsatz an. SchlieSSlich erlaubte uns die Implementierung einer Methode zum Verständnis des Magnetisierungsaustauschs zwischen verschiedenen Orten in porösen Medien Austauschraten zu quantifizieren und damit Information über die Porosität und die Porenkonnektivität zu erhalten.

Résumé
L'élaboration de matériaux cimentaires aux propriétés extrêmes en terme de tenue mécanique, de durabilité, voire de perméabilité, nécessite la compréhension précise du développement de leur structure poreuse. L'aspect non destructif de l'Imagerie par Résonance Magnétique (IRM) en fait une méthode de choix pour l'étude de la distribution et des transferts hydriques au sein de ces matériaux. Cependant, le caractère multi-échelle de ce matériau et la présence d'impuretés paramagnétiques requièrent des performances particulières en termes d'intensité de gradient de champ magnétique et de rapidité d'acquisition. C'est dans cet objectif que nous avons développé deux techniques IRM complémentaires. Le STRAFI permet de suivre, au laboratoire, l'effet des conditions de température et d'humidité sur la distribution d'eau à travers le matériau mais également sur l'évolution de sa structure poreuse, élément décisif pour les performances de ce dernier. La NMR-MOUSE™, version bas champ mais portative de l'IRM, permet un suivi du séchage des matériaux cimentaires directement sur-site, ce qui en fait un outil de choix dans un contexte industriel. Enfin, la mise au point d'une méthode d'analyse multi-dimensionnelle dans les milieux poreux nous a permis de mettre en évidence les constantes de temps impliquées dans l'échange de matière entre les différents types de pores présents dans le matériau, ce qui permet d'obtenir des informations sur sa porosité et la connectivité de ses pores.

Abstract
The development of high performance cementitious materials in terms of mechanical properties, sustainability and permeability requires a good understanding of their porous structure. As a non-destructive tool, Magnetic Resonance Imaging (MRI) is a method of choice for studying water distribution and hydric transfer throughout the material. However, due to a pore-size distribution over a few orders of magnitude and the presence of paramagnetic impurities, MRI applied to these materials requires the use of high magnetic field gradient systems and fast acquisition rates. For this purpose, we developed two techniques. Performed ex-situ, STRAFI allows to follow the effect of temperature and humidity on the water distribution within the material but also its impact on the porous structure and thus on the material performances expected. The NMR-MOUSE™, acting at low field and being portable, allows us to follow the drying of cementitious materials directly on-site. As such, it appears as an interesting tool for industrial use. Finally, the implementation of a method to understand multi-site exchange NMR experiments in porous media allowed us to quantify the exchange rates involved between various pores within the materials, which provides information about the porosity and connectivity of the porous structure.